

**The Search for Higgs Boson Production in Association
with a Top-Quark Pair in pp Collisions at $\sqrt{s} = 8$ TeV in
the Lepton Plus Jets Final State**

John Garland Wood
Charlottesville, VA

B.S., The University of California, Berkeley, 2008

A Dissertation presented to the Graduate Faculty
of the University of Virginia in Candidacy for the Degree of
Doctor of Philosophy

Department of Physics

University of Virginia
May, 2015

Abstract

The most important goal of the Large Hadron Collider (LHC) is to elucidate the mechanism of electroweak symmetry breaking. The Higgs mechanism is thought to be a prime candidate for this, which consequently predicts the existence of an additional particle, the Standard Model (SM) Higgs boson. The newly discovered boson announced on July 4th, 2012, with a mass of ~ 125 GeV/c^2 , has so far been shown to be consistent with a SM Higgs boson. However, the final confirmation of this new particle as the SM Higgs depends on subsequent measurements of all of its properties. The observation of this new particle in association with top-quark pairs would allow the couplings of this particle to top and bottom quarks to be directly measured. $t\bar{t}H$ with Higgs decaying to $b\bar{b}$ is an excellent channel to explore due to the dominant branching ratio of Higgs to $b\bar{b}$ and the kinematic handle the $t\bar{t}$ system offers on the event. However, it presents a plethora of difficult challenges due to a low signal to background ratio and uncertainties on kinematically similar SM backgrounds. This work discusses the search for Higgs boson production in association with a top-quark pair in pp collisions at $\sqrt{s} = 8$ TeV, collected by the Compact Muon Solenoid (CMS) experiment at the LHC. The search has been performed and published in two stages. The first analysis used the first 5.1 fb^{-1} , and was followed up by the second analysis with the full 2012 dataset, using a total integrated luminosity of 19.5 fb^{-1} .

We approve the dissertation of John Garland Wood.

Date of Signature

Supervisor: Prof. Christopher Neu

Committee Member: Prof. Hank Thacker

Committee Member: Prof. Edward Murphy

PhD Committee Chair: Prof. Craig Group

Contents

Contents	iv
List of Figures	viii
List of Tables	xx
Acknowledgements	xxiii
1 Introduction	1
2 Theoretical Background	4
2.1 An Overview of Quantum Field Theory	4
2.2 Abelian Gauge Theories of Particle Interactions	7
2.3 Non-Abelian Gauge Theories of Particle Interactions	9
2.4 The Higgs Mechanism in an Abelian Theory	12
2.5 The Higgs Mechanism in a non-Abelian Theory	14
2.6 Glashow Weinberg Salam Theory	16
2.7 The Standard Model of Particle Physics	22
2.8 Higgs Production in pp Collisions at the LHC	25
2.9 $t\bar{t}H$ Production in pp Collisions at the LHC	27
2.10 Background Processes to $t\bar{t}H$	28
2.11 Potential BSM Effects on $t\bar{t}H$ production	31
3 The Large Hadron Collider	33
3.1 The LHC Accelerator Complex	35
3.2 LHC Magnets	43
3.3 LHC RF Technology	49
3.4 The LHC Cryogen System	52
3.5 The LHC Vacuum System	53

4 The Compact Muon Solenoid	55
4.1 The Tracker	57
4.1.1 The Silicon Pixel Detector	59
4.1.2 The Silicon Strip Detector	61
4.2 The Electromagnetic Calorimeter	64
4.2.1 Vacuum Photo-Triodes	68
4.2.2 Test Rig at UVa	69
4.2.3 Results of UVa Tests	70
4.3 The Hadronic Calorimeter	73
4.4 Muon Chambers	78
4.5 Data Collection Overview	82
5 Particle Reconstruction at CMS	86
5.1 Iterative Tracking	86
5.2 Calorimeter Clustering	87
5.3 Calorimeter Energy Calibration	88
5.4 Linking	90
5.5 Physics Object Reconstruction	91
5.5.1 Muon Reconstruction	91
5.5.2 Electron Reconstruction	92
5.5.3 Charged Hadron Reconstruction	93
5.5.4 Photon and Neutral Hadron Reconstruction	93
5.5.5 Jet Reconstruction	94
5.5.6 Missing Transverse Energy Reconstruction	96
6 Analysis I: The first 5.08 fb^{-1} of 8 TeV data	98
6.1 Data and Simulated Samples	100
6.1.1 Data Samples	101
6.1.2 Signal Samples	102
6.1.3 Background Samples	102
6.1.4 MC pileup reweighting	103
6.1.5 Additional Pileup Corrections	104
6.2 Event Selection	106
6.2.1 Event cleaning	106
6.2.2 Trigger	107
6.2.3 Muon Selection	107

6.2.4	Electron Selection	108
6.2.5	Lepton selection and trigger efficiencies	109
6.2.6	Jet selection	110
6.2.7	<i>b</i> -tagging selection	111
6.2.8	Lepton + Jets Selection	114
6.3	Multivariate Analysis	117
6.3.1	Artificial Neural Network Overview	118
6.3.2	MVA Input Variables, Data to Monte Carlo Comparisons	122
6.3.3	MVA Output, Data to Monte Carlo Comparisons	140
6.4	Systematic Uncertainties	142
6.5	Statistical Methods	148
6.6	Results and Conclusions	151
7	Analysis II: The Complete 19.5 fb⁻¹ of 8 TeV data	153
7.1	Data and Simulated Samples	153
7.1.1	Data Samples	154
7.1.2	Signal Samples	154
7.1.3	Background Samples	154
7.1.4	MC pileup reweighting	155
7.1.5	Top <i>p</i> _T Reweighting	156
7.2	Event Selection	157
7.2.1	<i>b</i> -tag discriminant reweighting	158
7.2.2	Lepton + Jets Selection	159
7.3	Multivariate Analysis	160
7.3.1	Boosted Decision Tree Overview	160
7.3.2	MVA Input Variables, Data to Monte Carlo Comparisons	162
7.3.3	MVA Output, Data to Monte Carlo Comparisons	177
7.4	Systematic Uncertainties	177
7.5	Statistical Methods	185
7.6	Results and Conclusions	187
8	Analysis Improvements	189
8.1	aMC@NLO, MadSpin, and Pythia8 Monte Carlo	189
8.2	Analysis Techniques Under Development	191
9	Conclusions and Summary	195

Bibliography	198
List of Acronyms	212

List of Figures

1.1	The CMS experiment has observed a new boson at $m \sim 125 \text{ GeV}/c^2$	2
1.2	A Feynman diagram of the $t\bar{t}H$ process, with Higgs $\rightarrow b\bar{b}$, and the $t\bar{t}$ -system decaying semi-leptonically	3
2.1	Leading and Next to Leading Order Feynman diagrams for the coulomb scattering process	6
2.2	The global average of α_s , the QCD coupling constant [1].	7
2.3	A visual representation of the Higgs potential [2]	12
2.4	Experimental milestones of the Standard Model	24
2.5	Higgs production cross-sections at the LHC, for 7-14 TeV pp collisions	25
2.6	Feynman diagrams for the three largest Higgs production modes at the LHC . .	26
2.7	Feynman diagram for $t\bar{t}H$ production	27
2.8	Feynman diagrams for the semileptonic $t\bar{t}H$ process and its irreducible background, $t\bar{t} + b\bar{b}$	28
2.9	Feynman diagrams for the $t\bar{t}W$ and $t\bar{t}Z$ background processes	29
2.10	Feynman diagrams for the single t s,t, and tW background processes	29
2.11	Feynman diagrams for the W, Z plus jets, and diBoson (WW, WZ, ZZ) production.	30
2.12	Measurements of $t\bar{t}H$ backgrounds at CMS [3]	30
2.13	The cancellation of the divergent Higgs mass from a loop of top-quarks is cancelled by a loop of supersymmetric top-quarks, stop-quarks [4],	32
3.1	Aerial view of the LHC complex, spanning the French-Swiss border [5]	33
3.2	Integrated Luminosity delivered to the CMS experiment from 2010-12 [6]	35
3.3	The LHC accelerator complex, taking protons from a bottle of Hydrogen at the Linac2, all the way to the LHC ring [7]	36
3.4	Features of the Linac2, the first stage of acceleration in the LHC injection chain	37
3.5	Features of the PS booster, the second stage of the LHC injection chain	38
3.6	Features of the PS, the third stage of the LHC injection chain	41

3.7	Features of the SPS, the fourth and final stage of the LHC injection chain	42
3.8	The LHC ring is divided into eight octants [8]	44
3.9	The single turn injection scheme. A septum magnet makes the initial alignment. The kicker magnet times the injection and makes the final alignment. Bumper magnets align the LHC beam with the injected beam [9]	45
3.10	Layout of Interaction Region 8, where one proton beam is injected into the LHC ring. A transfer line from the SPS bring a proton in from the right. In green, a septum magnet aligns the beam horizontally with the LHC. In blue, a kicker magnet makes the final vertical alignment into the LHC, and is timed to fill one of the 400 MHz buckets of the RF capture system [8]	45
3.11	The initial filling of 6 batches of protons from the PSB to the PS, leaves 12 empty buckets in the PS bunch structure. The rise time of the SPS magnet creates an additional gap in the SPS bunch structure. Additional gaps emerge due to the rise time of the LHC injection and dumping kicker magnets [8]	46
3.12	Features of the dipole magnets used in the LHC	47
3.13	Features of the dipole magnets used in the LHC	48
3.14	Features of the 400 MHz superconducting RF system used in the LHC	49
3.15	A klystron uses a weak RF signal coupled to a resonance cavity to bunch an electron beam, which in turn creates an amplified RF signal as it passes through a second resonance cavity tuned to the same frequency [10].	50
3.16	One of sixteen 300 kW, 400 MHz klystrons that power the superconducting RF cavities that accelerate the proton beam [11].	51
3.17	Layout of the five cryogenic islands, which are home to the eight facilities that provide liquid helium to the LHC [12]	52
3.18	Features of the 4.5 K refrigeration system [13]	52
3.19	Cross section schematic of the cryogenic distribution system in the LHC tunnel [8]	53
3.20	Beam screen for the LHC, with slits to allow for easy pumping of residual gas molecules in the beam-pipe [14].	54
4.1	A cutaway diagram of the CMS detector. Two humans are present at the bottom of the image to provide scale [15].	55
4.2	A slice of the CMS detector showing how various particles interact and deposit energy. The trajectory of charged particles is measured in the tracker; electrons and photons deposit most of their energy in the ECAL; charged and neutral hadrons deposit most of their energy in the HCAL; the muon chambers measures the trajectory of muons or long-lived charged particles [16].	56

4.3 A side view of the tracker. The pixel detector is the innermost sub-system, with three concentric rings of detectors in the barrel, and two in the endcap. The tracker inner barrel (TIB) is a silicon strip detector, with four concentric rings. The tracker inner disks (TID) are three layers deep. The tracker outer barrel (TOB) is six concentric rings and the tracker end caps (TEC) are nine layers deep [15].	58
4.4 A head-on view of the beam-line and barrel components of the tracker [17].	58
4.5 The three barrel and two disk layers of the silicon pixel tracker provide coverage of $ \eta < 2.5$ [15].	59
4.6 The readout electronics chain for the pixel detector [15].	60
4.7 In 2012 pp collisions at $\sqrt{s} = 8$ TeV, the pixel detector performed with a resolution of $11.8 \mu\text{m}$. The above is a plot of the residual difference between a pixel and the results of a fit to a particle track [18].	61
4.8 A silicon strip module, with two $500 \mu\text{m}$ thick sensors [15].	62
4.9 Schematic of the readout sequence of the silicon strip detector [15].	63
4.10 Measurements of the performance of the silicon strip track using pp collisions from 2011 at $\sqrt{s} = 7$ TeV	63
4.11 Layout of the ECAL sub-detector [15]	64
4.12 Typical Lead Tungstate crystal, with APD attached to the rear face in the left frame, and a VPT attached in the right frame [15].	64
4.13 A simulation of the evolution of a electromagnetic shower being initiated by an electron entering the center of the front face [19].	65
4.14 A module of 500 crystals (25 crystals wide by 20 crystal tall) [15].	66
4.15 Schematic of the On-Detector Readout for the ECAL [15].	67
4.16 A section of the ECAL end-cap, a Dee. Two Dees form a disk with an inner bore for the beam-line to pass through. 5x5 modules, or supercrystals, are mounted in preparation for installation at CMS [15].	68
4.17 Vacuum Photo-Triode devices used in the ECAL end-caps (EE)	68
4.18 Features of the UVa VPT test stand	71
4.19 3 runs of 5 VPTs, exposed to blue LED light, and fit to a sum of two exponentials.	72
4.20 3 runs of 5 VPTs, exposed to orange LED light, and fit to a sum of two exponentials.	73
4.21 Longitudinal cross-section of the HCAL with the four sub-systems labeled [15].	74

4.22 Closeup of the HCAL barrel section. The center section of each of the 18 wedges are labeled, optical cables lay across the joint of the center and staggered edge sections of each wedge. The blue lines show the approximate azimuthal division of the wedge [15].	75
4.23 Over 1 million Russian shells of military artillery were re-processed in the construction of the HCAL [20]	76
4.24 Optical readout chain of the HCAL scintillator tiles [15].	76
4.25 HCAL endcap, 18 azimuthal divisions of alternating layers of brass and plastic scintillator [15].	77
4.26 Longitudinal cross-section of the HCAL forward calorimetry, the HF [15].	77
4.27 Longitudinal cross-section of one of the 5 wheels of the muon system. Drift tubes are placed in 4 concentric layers, with 2 being placed inside the return yoke of the magnet, and 12 azimuthal divisions [15].	79
4.28 A cross-section view of a drift cell. The anode wire is held at 3600 V, creating a potential difference with the walls. Electric field lines are shown in blue [15].	80
4.29 RPC layout for the barrel and endcaps	80
4.30 Exploded diagram of an RPC [21]	81
4.31 Cross-section of one quarter of the muon endcap system, with the 4 disks of CSC systems shown in red [15].	81
4.32 A CSC station with 7 layers, making 6 gas chambers. Cathode strips are shown in yellow, perpendicular to the vertical anode wires in orange [15].	82
4.33 A block diagram of the L1 trigger [15]	83
4.34 A schematic of the e/γ trigger algorithm [15].	83
4.35 Layout of the CMS DAQ [15]	84
 5.1 Results of the uncertainty on the ECAL intercalibration coefficients for the barrel (left) and endcaps (right) [22].	89
5.2 Instantaneous luminosity response to the crystals as measured by the laser and LED system. Additional crystal calibration constants are derived to normalize the crystal response over the range of collected data [23]	90
5.3 Results of using a χ^2 minimization procedure to estimate the neutral hadron energy contribution in the HCAL using simulated events[24]	91
5.4 Muon validation plots for the particle-flow reconstruction	92
5.5 Electron validation plots for the particle-flow reconstruction	93
5.6 The anti- kt jet clustering algorithm with distance parameter $R=1.0$ [25]	94

5.7	Commissioning of the particle-flow algorithm on jets, involved comparing the energy measured from charged hadron tracks, to energy measured in calorimeter clusters linked to the tracks [26].	95
5.8	A b -meson will travel a distance L_{xy} before decaying and creating a secondary vertex. The impact parameter, d_0 measures the longitudinal displacement of the two vertices [27].	96
6.1	This figure shows the breakdown of jet-to-parton assignments for the two jets with the minimum ΔR separation in the event for events with greater or equal 4 b -tagged jets.	99
6.2	Comparison of number of reconstructed vertices for data (black) and the $t\bar{t}$ MC sample before (blue) and after (red) pileup reweighting. After pileup reweighting, the MC matches the data well.	104
6.3	H_T distribution for 8 TeV lepton plus jet events with ≥ 4 jets and ≥ 2 tags shown for different amounts of pileup. The left-hand plot shows low pileup, the middle plot shows medium pileup, and the right-hand plot shows high pileup.	105
6.4	H_T distribution for 8 TeV lepton plus jet events with ≥ 4 jets and ≥ 2 tags. The left-hand plot shows the distribution before correction. The right-hand plot shows the distribution after correction. Note that the ratio in the right-hand plot is flatter than the left-hand plot.	106
6.5	Muon and electron ID, isolation selection and trigger efficiency scale factors in bins of p_T and η	110
6.6	Number of jets (left) and number of b -tagged jets (right) in data and simulation for events with ≥ 4 jets + ≥ 2 b -tags in the lepton+jets channel at 8 TeV. The background is normalized to the SM expectation; the uncertainty band (shown as a hatched band in the stack plot and a green band in the ratio plot) includes statistical and systematic uncertainties that affect both the rate and shape of the background distributions. The $t\bar{t}H$ signal ($m_H = 125 \text{ GeV}/c^2$) is normalized to $30 \times$ SM expectation.	117
6.7	A simple example of a MLP type ANN, with one layer of input neurons that make connections to a hidden layer, which is connected to the output layer [28]	118
6.8	The CFMlpANN architecture used in this analysis features two hidden layers, and 10 input variables for each jet/tag category (11 variables for the ≥ 6 jets, $\geq 4 b$ -tags category)	119
6.9	Comparisons of the testing and training samples used to optimize the CFMlpANN weights for each jet/tag category	121

6.10 Lepton + jets data/MC comparison for the ≥ 6 jets + 2 tag category. The uncertainty band includes statistical and systematic uncertainties that affect both the rate and shape of the background distributions.	127
6.11 Lepton + jets data/MC comparison for the ≥ 6 jets + 2 tag category. The uncertainty band includes statistical and systematic uncertainties that affect both the rate and shape of the background distributions.	128
6.12 Lepton + jets data/MC comparison for the 4 jets + 3 tag category. The uncertainty band includes statistical and systematic uncertainties that affect both the rate and shape of the background distributions.	129
6.13 Lepton + jets data/MC comparison for the 4 jets + 3 tag category. The uncertainty band includes statistical and systematic uncertainties that affect both the rate and shape of the background distributions.	130
6.14 Distributions of the five ANN input variables with rankings 1 through 5, in terms of separation, for the 5 jets + 3 b-tags category of the lepton+jets channel at 8 TeV. Definitions of the variables are given in the text. The background is normalized to the SM expectation; the uncertainty band (shown as a hatched band in the stack plot and a green band in the ratio plot) includes statistical and systematic uncertainties that affect both the rate and shape of the background distributions. The $t\bar{t}H$ signal ($m_H = 125 \text{ GeV}/c^2$) is normalized to the total background yield, for easier comparison of the shapes.	131
6.15 Distributions of the five ANN input variables with rankings 6 through 10, in terms of separation, for the 5 jets + 3 b-tags category of the lepton+jets channel at 8 TeV. Definitions of the variables are given in the text. The background is normalized to the SM expectation; the uncertainty band (shown as a hatched band in the stack plot and a green band in the ratio plot) includes statistical and systematic uncertainties that affect both the rate and shape of the background distributions. The $t\bar{t}H$ signal ($m_H = 125 \text{ GeV}/c^2$) is normalized to the total background yield, for easier comparison of the shapes.	132
6.16 Lepton + jets data/MC comparison for the ≥ 6 jets + 3 tag category. The uncertainty band includes statistical and systematic uncertainties that affect both the rate and shape of the background distributions.	133
6.17 Lepton + jets data/MC comparison for the ≥ 6 jets + 3 tag category. The uncertainty band includes statistical and systematic uncertainties that affect both the rate and shape of the background distributions.	134

6.18 Lepton + jets data/MC comparison for the 4 jets + 4 tag category. The uncertainty band includes statistical and systematic uncertainties that affect both the rate and shape of the background distributions.	135
6.19 Lepton + jets data/MC comparison for the 4 jets + 4 tag category. The uncertainty band includes statistical and systematic uncertainties that affect both the rate and shape of the background distributions.	136
6.20 Lepton + jets data/MC comparison for the 5 jets + 4 tag category. The uncertainty band includes statistical and systematic uncertainties that affect both the rate and shape of the background distributions.	137
6.21 Lepton + jets data/MC comparison for the 5 jets + 4 tag category. The uncertainty band includes statistical and systematic uncertainties that affect both the rate and shape of the background distributions.	138
6.22 Lepton + jets data/MC comparison for the ≥ 6 jets + 4 tag category. The uncertainty band includes statistical and systematic uncertainties that affect both the rate and shape of the background distributions.	139
6.23 Lepton + jets data/MC comparison for the ≥ 6 jets + 4 tag category. The uncertainty band includes statistical and systematic uncertainties that affect both the rate and shape of the background distributions.	140
6.24 The distributions of the CFMlpANN output for lepton+jets events at 8 TeV in the various analysis categories. Background-like events have a low CFMlpANN output value. Signal-like events have a high CFMlpANN output value. The background is normalized to the SM expectation; the uncertainty (shown as a hatched band in the stack plot and a green band in the ratio plot) includes statistical and systematic uncertainties that affect both the rate and shape of the background distributions. The $t\bar{t}H$ signal ($m_H = 125 \text{ GeV}/c^2$) is normalized to $30 \times \text{SM}$ expectation.	141
6.25 Comparison of the MVA discriminator for JES shift upwards (red) and downwards (blue) relative to the nominal (black) shape for the $t\bar{t}H(120)$ signal (left) and the main background sample $t\bar{t} +$ light flavor (right). The plots shown are from the ≥ 6 jet ≥ 4 tag category in the lepton+jets channel. All plots are normalized to unit area.	143

6.26 Comparison of the MVA discriminator for b -tag scale factor shift upwards (red) and downwards (blue) relative to the nominal (black) shape for the $t\bar{t}H(120)$ signal (left) and the main background sample $t\bar{t}$ + light flavor (right). The plots are from the ≥ 6 jets + ≥ 4 tags category in the lepton+jets channel. All plots are normalized to unit area.	144
6.27 Comparison of the MVA discriminator for additional PU correction systematic upwards (red) and downwards (blue) relative to the nominal (black) shape for the $t\bar{t}H(120)$ signal (left) and the main background sample $t\bar{t}$ + light flavor (right). The plots are from the ≥ 6 jets + ≥ 4 tags category in the lepton+jets channel. All plots are normalized to unit area.	145
6.28 The rate and shape variations for selected categories due to the Q^2 uncertainty. . .	147
6.29 A dedicated CFMlpANN trained to isolate $t\bar{t} + b\bar{b}$ from $t\bar{t} + jets$. The left plot shows is for the case of nominal $t\bar{t} + b\bar{b}$ cross-section, the right plot shows the case for x2 $t\bar{t} + b\bar{b}$ cross-section. The left-most region of both plots is the most sensitive to the $t\bar{t} + b\bar{b}$ normalization, and shows no significant improvement in data to MC agreement, justifying the reasoning that an uncertainty larger than 50% is needed.	148
6.30 The expected and observed 95% CL upper limits on the signal strength parameter $\mu = \sigma/\sigma_{SM}$ for the lepton+jets channel using the 2012 dataset. These limits were extracted using the asymptotic method.	152
7.1 Comparison of number of reconstructed vertices for data (black) and the sum of all background MC samples before (red) and after (blue) pileup reweighting. After pileup reweighting, the MC matches the data well.	156
7.2 The scale factors from top differential cross section group, the fitting as well as the $\pm 1\sigma$ variations.	157
7.3 Leading jet p_T distribution for 8 TeV lepton plus jet events with ≥ 4 jets and ≥ 2 tags. The left-hand plot shows the distribution before top p_T reweighting. The right-hand plot shows the distribution after top p_T reweighting. Note that the ratio in the right-hand plot is flatter than the left-hand plot.	157
7.4 Comparison of yields for the different categories (top), number of jets (bottom left), and number of tagged jets (bottom right) in data and Monte Carlo for events with one lepton μ or e , ≥ 4 jets and ≥ 2 tags.	160
7.5 Example of a decision tree, which chooses a set of variables to cut on, in order to produce a region of events with high signal purity	161
7.6 Comparisons of the testing and training samples used to optimize the BDT weights for each jet/tag category	163

7.7 Data/MC comparisons for events with one lepton and ≥ 6 jets + 2b- tags. The uncertainty band includes statistical and systematic uncertainties that affect both the rate and shape of the background distributions.	167
7.8 Data/MC comparisons for events with one lepton and 4 jets + 3 b-tags. The uncertainty band includes statistical and systematic uncertainties that affect both the rate and shape of the background distributions.	168
7.9 Data/MC comparisons for events with one lepton and 5 jets + 3 b-tags. The uncertainty band includes statistical and systematic uncertainties that affect both the rate and shape of the background distributions.	169
7.10 Data/MC comparisons for events with one lepton and ≥ 6 jets + 3 b-tags. The uncertainty band includes statistical and systematic uncertainties that affect both the rate and shape of the background distributions.	170
7.11 Data/MC comparisons for events with one lepton and ≥ 6 jets + 3 b-tags. The uncertainty band includes statistical and systematic uncertainties that affect both the rate and shape of the background distributions.	171
7.12 Data/MC comparisons for events with one lepton and 4 jets + 4 b-tags. The uncertainty band includes statistical and systematic uncertainties that affect both the rate and shape of the background distributions.	172
7.13 Data/MC comparisons for events with one lepton and 5 jets + ≥ 4 b-tags. The uncertainty band includes statistical and systematic uncertainties that affect both the rate and shape of the background distributions.	173
7.14 Data/MC comparisons for events with one lepton and 5 jets + ≥ 4 b-tags. The uncertainty band includes statistical and systematic uncertainties that affect both the rate and shape of the background distributions.	174
7.15 Data/MC comparisons for events with one lepton and ≥ 6 jets + ≥ 4 b-tags. The uncertainty band includes statistical and systematic uncertainties that affect both the rate and shape of the background distributions.	175
7.16 Data/MC comparisons for events with one lepton and ≥ 6 jets + ≥ 4 b-tags. The uncertainty band includes statistical and systematic uncertainties that affect both the rate and shape of the background distributions.	176

7.17 Final BDT output for lepton + jet events. Background-like events have a low BDT output value. Signal-like events have a high BDT output value. The uncertainty band includes statistical and systematic uncertainties that affect both the rate and shape of the background distributions. The top, middle and, bottom rows are events with 4, 5, and ≥ 6 jets, respectively, while the left, middle, and right-hand columns are events with 2, 3, and ≥ 4 b-tags, respectively. The $t\bar{t}H$ signal ($m_H = 125$ GeV) is normalized to $30 \times$ SM expectation.	178
7.18 Comparison of the MVA discriminator for JES shift upwards (red) and downwards (blue) relative to the nominal (black) shape for the $t\bar{t}H(125)$ signal (left) and the main background sample $t\bar{t} + b\bar{b}$ (right). The plots are from the ≥ 6 jet ≥ 4 tag category in the lepton+jets channel. All plots are normalized to unit area.	179
7.19 Comparison of the MVA discriminator when shifting the light flavor contamination in the heavy flavor scale factor determination shift upwards (red) and downwards (blue) relative to the nominal (black) shape for the $t\bar{t}H(125)$ signal (top row) and $t\bar{t} + b\bar{b}$ and $t\bar{t} + \text{LF}$ background samples (middle row and bottom row respectively). The plots are from the LJ ≥ 6 jet ≥ 4 category. All plots are normalized to unit area.	180
7.20 Comparison of the MVA discriminator when shifting the heavy flavor contamination in the light flavor scale factor determination shift upwards (red) and downwards (blue) relative to the nominal (black) shape for the $t\bar{t}H(125)$ signal (top row) and $t\bar{t} + b\bar{b}$ and $t\bar{t} + \text{LF}$ background samples (middle row and bottom row respectively). The plots are from the LJ ≥ 6 jet ≥ 4 category. All plots are normalized to unit area.	180
7.21 Comparison of the MVA discriminator when shifting to account for the statistical uncertainty on the heavy flavor scale factor extraction. Two classes of distortion in the scale factor are considered: linear distortions (labeled “Stat. Error 1”) and nonlinear distortions (labeled “Stat. Error 2”). Both shift upwards (red) and downwards (blue) relative to the nominal (black) shape for the $t\bar{t}H(125)$ signal (top row) and $t\bar{t} + b\bar{b}$ and $t\bar{t} + \text{LF}$ background samples (middle row and bottom row respectively) are shown. The plots are from the ≥ 6 jet ≥ 4 category. All plots are normalized to unit area.	181

7.22 Comparison of the MVA discriminator when shifting to account for the statistical uncertainty on the light flavor scale factor extraction. Two classes of distortion in the scale factor are considered: linear distortions (labeled “Stat. Error 1”) and nonlinear distortions (labeled “Stat. Error 2”). Both shift upwards (red) and downwards (blue) relative to the nominal (black) shape for the $t\bar{t}H(125)$ signal (top row) and $t\bar{t} + b\bar{b}$ and $t\bar{t} + \text{LF}$ background samples (middle row and bottom row respectively) are shown. The plots are from the ≥ 6 jet ≥ 4 category. All plots are normalized to unit area.	181
7.23 Comparison of the MVA discriminator when shifting to account for the uncertainty on the charm jets scale factor extraction. Two classes of distortion in the scale factor are considered: linear distortions (labeled “Error 1”) and nonlinear distortions (labeled “Error 2”). Both shift upwards (red) and downwards (blue) relative to the nominal (black) shape for the $t\bar{t}H(125)$ signal (top row) and $t\bar{t} + c\bar{c}$ and $t\bar{t} + \text{LF}$ background samples (middle row and bottom row respectively) are shown. The plots are from the ≥ 6 jet ≥ 4 category. All plots are normalized to unit area.	182
7.24 Comparison of the MVA discriminator for shifts in top quark p_T reweighting upwards (red) and downwards (blue) relative to the nominal (black) shape for the $t\bar{t} + \text{LF}$ background (left) and the $t\bar{t} + b\bar{b}$ (right). The plots are from the ≥ 6 jets $+ \geq 4$ tags category in the lepton+jets channel. All plots are normalized to unit area.	183
7.25 Comparison of the MVA discriminator when shifting the Q^2 scale up and down by its uncertainties. Shown are the shift upwards (red) and downwards (blue) relative to the nominal (black) shape for the $t\bar{t} + b\bar{b}$ (top row) $t\bar{t} + b$ (middle row) and $t\bar{t} + \text{LF}$ (bottom) background samples. The plots are from the LJ ≥ 6 jet ≥ 4 category. All plots are normalized to unit area.	184
7.26 The expected and observed 95% CL upper limits on the signal strength parameter $\mu = \sigma/\sigma_{SM}$ for the lepton+jets channel using the 2012 dataset. These limits were extracted using the asymptotic method.	187
8.1 The number of reconstructed jets passing selection (left) and that have additionally been b -tagged (right) for $t\bar{t}H$, $t\bar{t} + \text{jets}$, and $t\bar{t} + b\bar{b}$ samples generated with the aMC@NLO and Pythia 8 framework	191
8.2 The invariant mass of the W boson in the $t\bar{t}$ decay for the case of the MC truth (red), correctly associated reconstructed jets (blue), and incorrectly associated reconstructed jets (green)	192

8.3	The cosine of the angle between the momentum three-vectors for the b -quarks from the top decays (left), the lepton and the up-type W boson daughter (center), and the lepton and the down-type W boson daughter (right)	192
8.4	The difference in the ϕ coordinate between the momentum three-vectors for the b -quarks from the top decays (left), the lepton and the up-type W boson daughter (center), and the lepton and the down-type W boson daughter (right)	193
8.5	Jet times lepton charge, for the b -jet associated with the same top as the lepton. Green shows incorrectly associated reconstructed jets, blue shows correctly associated jets, and red is the MC truth	194

List of Tables

2.1	The quantum numbers Isospin and Hypercharge are assigned for each of the $SU(2)$ and $U(1)$ symmetries respectively	20
4.1	Fit Results for VPT Conditioning Studies at U.Va. and Brunel, Blue Reference LED	72
4.2	Fit Results for VPT Conditioning Studies at U.Va., Orange LED	73
6.1	The datasets analyzed for this analysis.	102
6.2	List of signal MC datasets and cross sections used to determine the SM expectation.	102
6.3	List of background MC datasets and cross sections used for normalization.	103
6.4	List of lepton+jets triggers	107
6.5	Tight and loose muon definition	108
6.6	Tight and loose muon definition	109
6.7	Jet definition	111
6.8	Jet Energy Resolution (JER) scale factors	111
6.9	Expected event yields in 5 fb^{-1} for signal and backgrounds in the $\mu+\text{jets}$ channel.	115
6.10	Expected event yields in 5 fb^{-1} for signal and backgrounds in the $e+\text{jets}$ channel.	115
6.11	Expected event yields in 5 fb^{-1} for signal and backgrounds in the $\mu+\text{jets}$ channel.	116
6.12	The ANN inputs for the nine jet-tag categories in the $8 \text{ TeV } t\bar{t}H$ analysis in the lepton+jets and dilepton channels. The choice of inputs is optimized for each category. Definitions of the variables are given in the text. The best input variable for each jet-tag category is denoted by \star	123
6.13	Summary of the systematic uncertainties considered on the inputs to the limit calculation. Except where noted, each row in this table will be treated as a single, independent nuisance parameter.	142
6.14	Relative yield change due to JES shift up/down for the ≥ 6 jets + ≥ 4 tags category in the lepton+jets channel.	143

6.15 Relative yield change due to b -tag scale factor shift up/down for the ≥ 6 jets + ≥ 4 tags category in the lepton+jets channel.	144
6.16 Cross section uncertainties used for the limit settings. Each column in the table is an independent source of uncertainty, except for the last column which represents uncertainties uncorrelated with any others. Uncertainties in the same column for two different processes (different rows) are completely correlated.	146
6.17 Expected and observed upper limits for SM Higgs for lepton + jets channel using the first 5.1 fb^{-1} of the 2012 dataset. These limits were extracted using the asymptotic method.	151
7.1 The datasets analyzed for this analysis.	154
7.2 List of signal MC datasets and cross sections used to determine the SM expectation.	154
7.3 List of background MC datasets and cross sections used for normalization.	155
7.4 Observed data event yields, expected event yields in 19.5 fb^{-1} for signal and backgrounds in the lepton+jets channel.	160
7.5 Event variables used in dilepton and lepton+jets BDT training and their descriptions.	164
7.6 BDT input variable assignments for the lepton+jets categories.	165
7.7 List of variables used as inputs in each of the ttbb/ttH BDTs. See table 7.5 for definitions.	165
7.8 Relative yield change due to JES shift up/down for the ≥ 3 tag category in the dilepton channel and the ≥ 6 jets + ≥ 4 tags category in the lepton+jets channel.	177
7.9 This table summarizes the rate effect of the six independent nuisance parameters that characterize the b -tag uncertainties. (Note: The b -tag rate uncertainties associated with JES variations are already included with the JES rate uncertainties in Table 6.14. The impact of statistical uncertainties is in the heavy-flavor and light-flavor scale factor extraction is incorporated using two separate nuisance parameters, as described above. The uncertainty labeled “Stat. Err. 1” represents statistical uncertainties resulting a linear distortion of the CSV scale factor, while the one labeled “Stat. Err. 2” corresponds to nonlinear distortions.	182
7.10 Relative yield change due to varying the top quark p_T reweighting. The “up” variation corresponds to apply twice as much correction to the top quark p_T distribution as the nominal, while the “down” correction corresponds to applying no correction to the default MC top quark p_T distribution.	183

7.11	Cross section uncertainties used for the limit settings. Each column in the table is an independent source of uncertainty, except for the last column which represents uncertainties uncorrelated with any others. Uncertainties in the same column for two different processes (different rows) are completely correlated.	184
7.12	This table summarizes the rate effect of shifting Q^2 scale uncertainty for Madgraph. Note that the shifts are made independently for the following topologies: $t\bar{t} + 0p$, $t\bar{t} + 1p$, $t\bar{t} + 2p$, $t\bar{t} + c\bar{c}$, $t\bar{t} + b$, and $t\bar{t} + b\bar{b}$	184
7.13	Summary for the of the systematic uncertainties considered on the inputs to the limit calculation. Except where noted, each row in this table will be treated as a single, independent nuisance parameter.	185
7.14	Specific effect of systematics on predicted background yields for events with ≥ 6 jets and ≥ 4 b-tags. Here we only consider the sum of the largest backgrounds, $t\bar{t} + lf$, $t\bar{t} + b$, $t\bar{t} + b\bar{b}$, and $t\bar{t} + c\bar{c}$. These three backgrounds account for 94% of all background events. The signal is 3.5% of the yield of the three main backgrounds. The signal fraction is directly comparable to the variations of the background in the table. The table shows that the signal is much smaller than many of the background variations.	186
7.15	Expected and observed upper limits for SM Higgs for lepton + jets channel using the 2012 dataset. These limits were extracted using the asymptotic method. . . .	187

Acknowledgements

First and foremost, the analysis described in this dissertation would be impossible without the thousands of individuals that have contributed to the design, construction, and commissioning of the Large Hadron Collider (LHC) and Compact Muon Solenoid (CMS) experiment. The countless years of passion and dedication that have been poured into these machines have resulted in the most sophisticated tools ever available to mankind to explore the frontiers of high energy physics. I am extremely grateful for the opportunity to participate in this collaboration and to contribute to the understanding of physics at the TeV energy scale.

I would like to thank Mike Arenton, Dave Cockerill and Alexander Ledovskoy for their tutelage and mentorship in regards to my studies with the UVa Vacuum Photo-Triode (VPT) rig. This project has been a critical to improving my understanding of electronics, firmware, and signal analysis, and has been both a challenging and exciting experience. I would also like to thank Thomas Anderson, Brian Franchise, Joseph Goodell, Al Tobias, and Evan Wolfe for all of their help in maintaining the 4 T magnet and ensuring the VPT rig has survived long enough to collect and analyze the data on these devices. I woud also like to thank Professors Brad Cox and Bob Hirosky of the CMS research group here at UVa for always challenging me to improve the VPT rig and analysis, while still providing me with all of the tools and input I needed to succeed.

The $t\bar{t}H$ analysis group at CMS has been provided an incredibly supportive environment to learn about particle physics and data analysis. I would like to thank Professor Kevin Lannon of the University of Notre Dame (ND) and Professors Richard Hughes and Brian Winer of the Ohio State University (OSU) for pushing the group as hard as possible while still maintaining a high level of quality for the work and studies presented each week. Additional thanks go out to the post-doctoral and graduate students at these Universities: Darren Puigh and Geoff Smith of ND and Jason Slaunwhite, Andrew Brinkerhoff, Wuming Luo, and Anna Woodard of OSU, without whom, this analysis would not have been published twice, nor would I be reflecting so fondly on a period of times that involved an intense set of deadlines and a lot of late nights.

To my fellow graduate students and good friends here at UVa: Thomas Anderson, Tanwa

Apornthip, Alexandre Arakelyan, Sana Deshmukh, Ryan Duve, Adam Fallon, Brian Francis, Joe Johnson, Manolis Kargiantoulakis, Micah Shiable, Julie Spencer, Niranjan Sridhar, Evan Wolfe, and too many more to list, you know who you are, thank you for so many wonderfully hazy nights that have helped me from going insane in graduate school. To my friends abroad: Supaksh Gupta, Kat Hunter, Ryan Karlsgodt, Kevin Karlsgodt, Ginny Morris, Mark Nicholson, Matt Pierce, Mikey Sheffield, Tyler Vickers, and the many others who also know who you are, thank you for continuing to be amazing friends throughout all these years apart.

I would like to give special thanks to Dr. Sarah Boutle, who has been an amazing mentor and friend. I owe so much of my understanding of particle physics, the LHC, and CMS to the countless conversations and coffee breaks we shared. I have been incredibly lucky to also have a role model of someone who has balanced a successful career as a scientist and still manages to maintain a caring, well-grounded personality with a great sense of humor, even during the most daunting and stressful of situations.

These acknowledgements would be incomplete without mention of Professor Chris Neu, who hooked me on studying particle physics at CMS during our first conversation together. Since then, I have had the privilege of being his student for the past six years. It has been an incredibly rewarding experience. Under his guidance, I have travelled around the world, analyzed and unblinded a historically significant dataset in the field of particle physics, and participated in one of the largest scientific collaborations in the history of mankind. I cannot thank him enough for everything I have learned, and for all of the amazing scientific opportunities he has provided.

I would like to acknowledge all of the love and support given to me by my family. Aunt Carolyn and cousin Gaylon, thank you for all of the Thanksgiving feasts, and for making me feel at home on the East Coast. Little sister, Carrie, thank you for always reminding me to keep an open heart and mind in all matters in life. Mom and Dad, thank for you encouraging me to follow my dreams and giving me every opportunity to do the things I love.

To the love of my life, Whitney Wegman, you have been the most incredible source of inspiration and happiness for me throughout the three and a half years we have been together at this point. I cannot have done this without all of your love and support.

¹ **Chapter 1**

² **Introduction**

³ On July 4th, 2012, the Compact Muon Solenoid (CMS) and A Toroidal LHC Apparatus (ATLAS)
⁴ experiments announced the discovery of a new boson of mass ~ 125 GeV [31][32]. The particle
⁵ has been shown to be increasingly consistent with the description of the boson predicted by
⁶ the Higgs mechanism of the SM, as measurements on its mass, width, and quantum numbers
⁷ are completed. Figure 1.1 shows a consistent mass peak between the $H \rightarrow ZZ$ and $H \rightarrow \gamma\gamma$
⁸ channels at the CMS experiment. However, there are several properties of this new boson, which
⁹ remain to be tested.

¹⁰ The Yukawa-coupling of the Higgs boson to the top quark in the SM is the largest coupling
¹¹ among the fundamental particles and is well predicted - thus offering an excellent test of the
¹² nature of the coupling of the Higgs to fermions, as well as a potential probe into physics Beyond
¹³ the Standard Model (BSM) that would alter this value from the SM prediction. The production
¹⁴ of the Higgs boson in association with top-quark pairs is the best production mode at the LHC
¹⁵ that offers direct access to the top-Higgs coupling. The dominant production mode of Higgs
¹⁶ at the LHC, gluon-gluon fusion, involves a triangle loop of strongly-coupled fermions, which
¹⁷ includes all of the other quarks, as well as the potential for BSM particles, and thus does involve
¹⁸ a pure top-Higgs coupling.

¹⁹ $t\bar{t}H$ production also has the ability to constrain some extensions of the SM that would not
²⁰ modify the Higgs branching fractions enough to be seen within current experimental precision.
²¹ Such models include Little Higgs models, models with extra dimensions, top-color models, and
²² composite Higgs models that introduce a vector-like top partner, a t' , that can decay to tH ,
²³ bW , or tZ states. Both $t't'$ and $t't$ production would produce a $t\bar{t}H$ final state, or one that is
²⁴ indistinguishable from it ($tHbW$). Upper limits on $t\bar{t}H$ production would also provide limits
²⁵ on the previously described models, which would be complementary to existing direct searches
²⁶ for t' particles, which attempt to reconstruct the t' resonance.

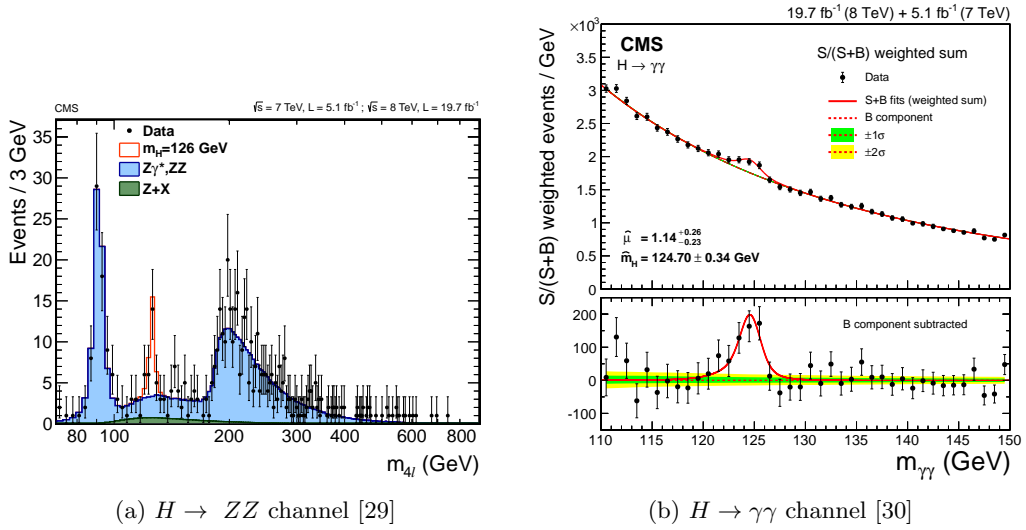


Figure 1.1: The CMS experiment has observed a new boson at $m \sim 125 \text{ GeV}/c^2$

The $t\bar{t}H$ channel has a rich set of possible final states. Each top quark will decay to a b quark and a W boson. The W boson will subsequently decay to two quarks, or a lepton and a neutrino. These decays are classified as either hadronic, semi-leptonic, or di-leptonic for zero, one, or both top quarks decaying leptonically respectively. The Higgs may decay to b quark, W , Z , τ , or γ pairs. In fact, this is one of the only production modes at the LHC which has access to every Higgs decay mode, as other production mechanisms are swamped by large backgrounds preventing measurements of all Higgs decay types.

The search is performed with the CMS experiment, a modern, general purpose particle detector capable of reconstructing and identifying hadronic jets, photons, electrons, muons, and tau leptons. The hermetic design, and its high precision and efficiency in reconstructing and tracking every particle in a pp collision, also makes it suitable for reconstructing missing transverse energy from the calculated momentum imbalance of all of the measured particles in the event. This missing transverse energy is often the signature of a neutrino, which is the only SM particle capable of escaping detection. The detector uses a 3.8 T axial magnetic field, produced by the solenoid it is named after, to bend charged particles as they travel through the detector. The measured curvature of their tracks allows the momentum of the particles to be calculated to a high precision. Tracks are formed and particles are reconstructed by a combination of sub-detector systems which work together to form the final final reconstructed image of each particle in the collision.

46 This thesis will focus on a semi-leptonic decay of the top quarks, with the Higgs decaying to
 47 a b -quark pair. Figure 1.2 is a Feynman diagram of the $t\bar{t}H$ process. The largest background to
 48 this process is top-quark pair production with extra jets originating from Initial State Radiation
 49 (ISR) or Final State Radiation (FSR) radiation, $t\bar{t} + \text{jets}$. The irreducible background is formed

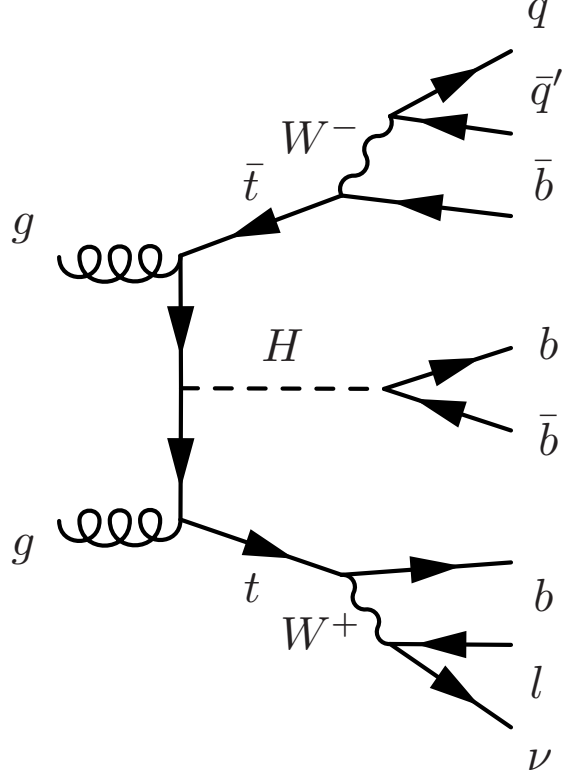


Figure 1.2: A Feynman diagram of the $t\bar{t}H$ process, with $H \rightarrow b\bar{b}$, and the $t\bar{t}$ -system decaying semi-leptonically

50 by top-quark pairs, where a gluon is radiated and decays to a b -quark pair, $t\bar{t} + b\bar{b}$. In addition
 51 to the large backgrounds, the high jet multiplicity in the $t\bar{t}H$ final state gives rise to a combina-
 52 torics problem in associating each jet with its role in the $t\bar{t}H$ system. This inevitably leads to
 53 misidentifying which jets are the decay product of the Higgs, and thus additionally smears out
 54 the resolution on the mass of the Higgs. Due to the similarity of the $t\bar{t} + b\bar{b}$ background and the
 55 combinatorics issue, no single variable is suitable for signal extraction. A Multi-Variate Analysis
 56 (MVA) technique is used in an attempt to isolate the $t\bar{t}H$ signal from the $t\bar{t} + jets$ background.
 57 The MVA provides a one-dimensional discriminant based on several input variables related to
 58 the kinematics of the event. This discriminant is then used to perform signal extraction and set
 59 upper-limits on $t\bar{t}H$ production. The results of two searches will be presented. The first result
 60 used the first 5.1 fb^{-1} of the 2012 dataset, with center of mass energy of 8 TeV, and was pub-
 61 lished in the Journal of High Energy Physics (JHEP), May 2013. The second result was update
 62 with the full 19.4 fb^{-1} 8 TeV dataset, and was published in JHEP, Spetember 2014.

⁶³ Chapter 2

⁶⁴ Theoretical Background

⁶⁵ The Standard Model (SM) of particle physics represents the sum of knowledge about the funda-
⁶⁶ mental particles and their interactions with each other. It is a Quantum Field Theory (QFT) that
⁶⁷ represents the interactions of each of the fundamental forces through the symmetry of a mathe-
⁶⁸ matical object known as a Lie group. It is the theory that dictates the rate that the $t\bar{t}H$ process
⁶⁹ is produced, as well as the kinematics of every particle involved. As such, its predictions are
⁷⁰ critical for modeling the characteristic signature of the $t\bar{t}H$ signal in the CMS detector, as well
⁷¹ as the background processes, like $t\bar{t} + b\bar{b}$ which leave a kinematically similar final-state signature.

⁷² 2.1 An Overview of Quantum Field Theory

⁷³ Quantum Field Theory (QFT) was developed out of the need for a relativistic description of
⁷⁴ quantum mechanics. Since the Einstein relation $E = mc^2$ allows for the creation of particle-
⁷⁵ antiparticle pairs, the single-particle description used in non-relativistic quantum mechanics,
⁷⁶ fails to describe this phenomenon [33]. The single-particle description additionally fails when
⁷⁷ considering that Heisenberg's uncertainty relation, $\Delta E \cdot \Delta t = \hbar$, allows for an arbitrary number
⁷⁸ of intermediate, virtual particles to be created. By quantizing a field representing a certain type
⁷⁹ of particle, multi-particle states are naturally described as discrete excitations of that field.

⁸⁰ Lorentz invariance, and the need to preserve causality, also define a fundamental relationship
⁸¹ between matter and antimatter. The propagation of a particle across a space-like interval is
⁸² treated equivalently to an anti-particle propagating in the opposite direction [33]. This is done
⁸³ so that the net probability amplitude for the particles to have an effect on a measurement occur-
⁸⁴ ring across a space-like interval cancel each other, thus preserving causality. This cancellation
⁸⁵ requirement additionally implies that the particle and anti-particle have the same mass, with
⁸⁶ opposite quantum numbers such as spin or electric charge.

87 The Lorentz transformations for a scalar field are different than for a field with internal de-
 88 grees of freedom, such as spin. A rotation on a vector field, will affect both its location, as well
 89 as its orientation [33]. This means the Lorentz invariant equation of motion describing a scalar
 90 field will have a different form than equations of motion for a field with non-zero spin. The most
 91 relevant equations describe the particles of SM, which contain spins of 0, 1/2, and 1. They are
 92 described by the Klein-Gordon, Dirac, and Proca equations respectively.

93

Klein-Gordon equation, for scalar (spin 0) fields

$$(\partial^2 + m^2)\phi = 0 \quad (2.1)$$

Dirac equation, for spinor (spin 1/2) fields

$$(i\gamma^\mu \partial_\mu - m)\psi = 0 \quad (2.2)$$

Proca equation, for vector (spin 1) fields

$$\partial_\mu(\partial^\mu A^\nu - \partial^\nu A^\mu) + m^2 A^\nu = 0 \quad (2.3)$$

94 With these equations, one can build a theory of free particles. The Lagrangian formulation is
 95 the most appropriate since all expressions are explicitly Lorentz invariant [33]. The Lagrangians
 96 for the Klein-Gordon, Dirac, and Proca equations are given as:

97

Klein-Gordon Lagrangian, for real and complex scalar fields

$$\begin{aligned} \mathcal{L} &= \partial_\mu \partial^\mu \phi^2 - \frac{1}{2} m^2 \phi^2 \\ \mathcal{L} &= (\partial_\mu \phi)^*(\partial^\mu \phi) - m^2 (\phi)^*(\phi) \end{aligned} \quad (2.4)$$

Dirac Lagrangian, for spinor fields

$$\mathcal{L} = i\bar{\psi}\gamma^\mu \partial_\mu \psi - m\bar{\psi}\psi \quad (2.5)$$

Proca Lagrangian, for vector fields

$$\mathcal{L} = -\frac{1}{4} F_{\mu\nu} F^{\mu\nu} + m^2 A^\nu A_\nu \quad (2.6)$$

98 where $F_{\mu\nu}$, is the field strength tensor, defined as $F_{\mu\nu} = \partial_\mu A_\nu - \partial_\nu A_\mu$

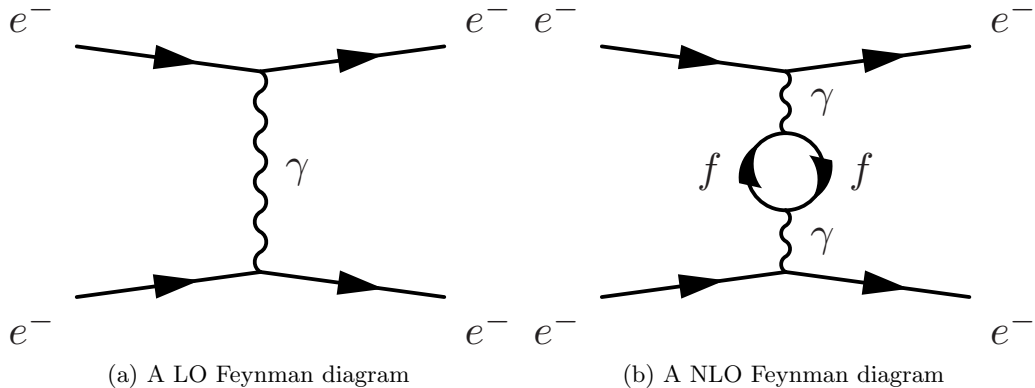


Figure 2.1: Leading and Next to Leading Order Feynman diagrams for the coulomb scattering process

Interactions are generated by coupling multiple fields together in a single term, such as
 $ieA_\mu\bar{\psi}\psi$ and treating it as a perturbation to the free-field theory. This implies every interaction
 between particles is carried out by a virtual mediating particle. When two electrons scatter off
 one another, they are really exchanging a virtual photon, the mediator of the electromagnetic
 force. The W^\pm and Z bosons mediate the weak force, while the gluons mediate the strong force.

$$\mathcal{L} = \mathcal{L}_{Free} + \mathcal{L}_{Interacting} \quad (2.7)$$

In order to calculate the probability and dynamics of two particles interacting with one another, an integral, constrained by energy and momentum conservation, over the phase space of outgoing particles and the scattering amplitude, \mathcal{M} , is evaluated. The scattering amplitude is calculated by using the propagator (Green's function of the free-particle theory) for the incoming, mediating, and outgoing particles, with an appropriate weighting function, or vertex factor, for each point the particles interact in the scattering process, and then integrating over the momentum of the mediating particle. Richard Feynman developed a set of rules for the writing down the propagators and vertex factors directly from the Lagrangian, and easily computing the scattering amplitude. He also introduced an elegant pictographic notation useful for visualizing particle interactions, known as Feynman diagrams.

With these tools, one can calculate the probability amplitudes of a given process occurring to Leading Order (LO) without any difficulties. However, when calculations in Next to Leading Order (NLO) are performed, and loop diagrams of virtual particles are considered, the probability amplitudes associated with a given process diverge to infinity. This occurs when one integrates over all of the possible momentum allowed by intermediate, loops of virtual particles, which due to Heisenberg's uncertainty principle, are allowed to take on any value of momentum. Figure 2.1 shows an example of a LO and NLO process.

¹²¹ The systematic removal of divergences from a theory is called renormalization. The di-

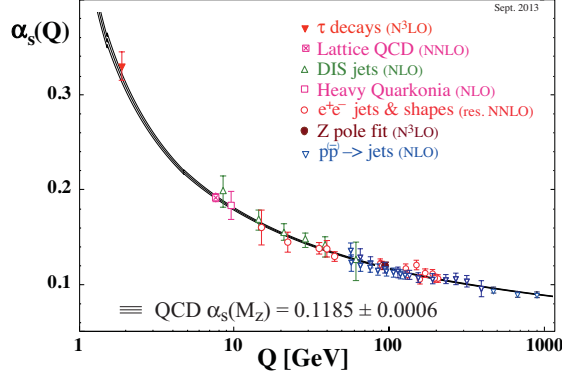


Figure 2.2: The global average of α_s , the QCD coupling constant [1].

vergences are absorbed into the definitions of the free parameters of the theory, making the parameters a function of the energy scale the process occurs at, instead of a constant. This allows for the calculations of fundamental processes to be completed, as long as the energy scale of the interaction is known. A modern interpretation of renormalization was provided by Kenneth Wilson [34] [35]. Instead of seeing the effects of high-momentum calculations after moving to NLO in perturbation theory, one uses an effective Lagrangian, computed by integrating out shells of momentum beginning at the energy cutoff of the theory, where the NLO effects begin to dominate. The dimensions of integration are then rescaled and the result of evaluating the integral over the momentum shell is absorbed into the definition of free parameters. The processes is iterated until the energy scale of the interaction is reached. The functional dependence of the parameters is then directly present in the resulting effective Lagrangian, instead of appearing suddenly when accounting for the one-loop contributions at NLO. Regardless of how strange this procedure may seem, the running of the coupling constant as a function of interaction energy has been validated experimentally time and time again, as shown in Figure 2.2 [1].

2.2 Abelian Gauge Theories of Particle Interactions

In 1930, Herman Weyl introduced the idea that the interactions between fields can be generated by requiring them to be invariant under gauge transformations of a local symmetry [36]. For electromagnetism, the local symmetry is that of the Lie group, $U(1)$. It is an abelian group, which has the property that the generators of the group symmetry commute with themselves. The $U(1)$ symmetry is invariant under phase rotations. By requiring local gauge invariance, the Lagrangian must be unchanged under the transformation:

$$\psi(x) \rightarrow e^{i\alpha(x)}\psi(x). \quad (2.8)$$

¹⁴³ Consider the Lagrangian for a free spin 1/2 particle:

$$\mathcal{L} = \bar{\psi}(i\gamma^\mu \partial_\mu - m)\psi \quad (2.9)$$

¹⁴⁴ The first term in the Lagrangian, involving the derivative, acts on $\psi(x)$, creating a new term in
¹⁴⁵ the Lagrangian, breaking its invariance under the local phase transformation.

$$\mathcal{L} \rightarrow \mathcal{L} - (\partial_\mu \alpha) \bar{\psi} \gamma^\mu \psi \quad (2.10)$$

¹⁴⁶ Thus, a new term must be added to the original Lagrangian to cancel out the term arising from
¹⁴⁷ the local phase transformation. This is achieved by defining the covariant derivative:

$$D_\mu = \partial_\mu + ieA_\mu \quad (2.11)$$

¹⁴⁸ where A_μ is a new vector field that transforms as follows:

$$A_\mu(x) \rightarrow A_\mu(x) - \frac{1}{e}\partial_\mu \alpha(x) \quad (2.12)$$

¹⁴⁹ The covariant derivative thus transforms like

$$\begin{aligned} D_\mu \psi(x) &\rightarrow [\partial_\mu + ie(A_\mu - \frac{1}{e}\partial_\mu \alpha)] e^{i\alpha(x)} D_\mu \psi(x) \\ &= e^{i\alpha(x)} [\partial_\mu + ie(A_\mu - \frac{1}{e}\partial_\mu \alpha + \frac{1}{e}\partial_\mu \alpha)] D_\mu \psi(x) \\ &= e^{i\alpha(x)} (\partial_\mu + ieA_\mu) \psi(x) \\ &= e^{i\alpha(x)} D_\mu \psi(x) \end{aligned} \quad (2.13)$$

¹⁵⁰ This covariant derivative transforms in the same way that $\psi(x)$ does, and the new locally gauge
¹⁵¹ invariant Lagrangian becomes

$$\begin{aligned} \mathcal{L} &= \bar{\psi}(i\gamma^\mu D_\mu - m)\psi - \frac{1}{4}F^{\mu\nu}F_{\mu\nu} \\ &= i\bar{\psi}\gamma^\mu \partial_\mu \psi - \bar{\psi}\gamma^\mu \psi A_{\mu u} - m\bar{\psi}\psi - \frac{1}{4}F^{\mu\nu}F_{\mu\nu} \end{aligned} \quad (2.14)$$

¹⁵² where

$$F^{\mu\nu} = (\partial^\mu A^\nu - \partial^\nu A^\mu) \quad (2.15)$$

¹⁵³ and $\frac{1}{4}F^{\mu\nu}F_{\mu\nu}$ is the kinetic energy term of the Proca equation for the new vector field.

¹⁵⁴ This new Lagrangian is identical to the QED Lagrangian, except it was derived beginning
¹⁵⁵ with a free Dirac theory and requiring the field to be locally gauge invariant under $U(1)$ trans-
¹⁵⁶ formations. This necessitated the introduction of a new vector field, A_μ , as well as an interaction

¹⁵⁷ term for it. This implies that the electromagnetic force can be represented by the requirement
¹⁵⁸ of local $U(1)$ symmetry on a free Dirac particle.

¹⁵⁹ It should be noted, that if the photon had mass, an additional term from the Proca equation
¹⁶⁰ would have to be added to the Lagrangian, $m^2 A_\mu A^\mu$. This term complicates the picture since
¹⁶¹ it is not invariant under local phase transformations, and cannot be compensated for through a
¹⁶² different choice of A_μ . This implies that the bosons of a gauge theory must be massless in order
¹⁶³ to preserve local gauge invariance.

¹⁶⁴ 2.3 Non-Abelian Gauge Theories of Particle Interactions

¹⁶⁵ In 1954, Yang and Mills worked to extend this idea to symmetries of different gauge groups [37].
¹⁶⁶ Their most important accomplishment was developing this procedure for non-abelian groups.
¹⁶⁷ These are groups where the transformation does not involve a simple variable $\alpha(x)$, but rather
¹⁶⁸ an entire matrix of dimension $n > 2$. These matrices do not commute with each other, and
¹⁶⁹ their work developed the procedure for applying local gauge invariance described above to the
¹⁷⁰ more complex, higher dimensional symmetries, such as $SU(2)$ and $SU(3)$. Consider the case of
¹⁷¹ $SU(2)$ symmetry. The theory is appropriate for describing the dynamics of two fermion fields,
¹⁷² represented as a doublet:

$$\psi = \begin{pmatrix} \psi_1(x) \\ \psi_2(x) \end{pmatrix} \quad (2.16)$$

¹⁷³ This will transform under the $SU(2)$ transformation as a two-component spinor:

$$\psi \rightarrow \exp\left(i\alpha^i \frac{\sigma_i}{2}\right) \psi \quad (2.17)$$

¹⁷⁴ where σ^i are the Pauli matrices:

$$\sigma^1 = \begin{pmatrix} 0 & 1 \\ 1 & 0 \end{pmatrix}, \sigma^2 = \begin{pmatrix} 0 & -i \\ i & 0 \end{pmatrix}, \sigma^3 = \begin{pmatrix} 1 & 0 \\ 0 & -1 \end{pmatrix} \quad (2.18)$$

¹⁷⁵ and have the commutation relation defined by:

$$\left[\frac{\sigma^i}{2}, \frac{\sigma^j}{2} \right] = i\epsilon^{ijk} \frac{\sigma^k}{2} \quad (2.19)$$

¹⁷⁶ Similar to the case of the $U(1)$ Abelian symmetry, in order to form a Lagrangian that is
¹⁷⁷ locally gauge invariant, three vector fields, A_μ^i , $i = 1, 2, 3$, are introduced, and coupled to ψ
¹⁷⁸ through the covariant derivative:

$$D_\mu = (\partial_\mu - igA_\mu^i \frac{\sigma^i}{2}) \quad (2.20)$$

¹⁷⁹ to ensure that the derivative covaries with the transformation, the fields, A_μ^i will transform like:

$$A_\mu^i \frac{\sigma^i}{2} \rightarrow A_\mu^i \frac{\sigma^i}{2} + \frac{1}{g}(\partial_\mu \alpha^i) \frac{\sigma^i}{2} + i \left[\frac{\alpha^i \sigma^i}{2}, A_\mu^i \frac{\sigma^i}{2} \right] \quad (2.21)$$

¹⁸⁰ The third term, which was absent from the abelian form of the transformation, is necessary to
¹⁸¹ account for the non-commutation of the Pauli matrices. This non-commutation also changes the
¹⁸² form of the field-strength tensor, $F_{\mu\nu}^i$:

$$F_{\mu\nu}^i = \partial_\mu A_\nu^i - \partial_\nu A_\mu^i + g\epsilon^{ijk} A_\mu^j A_\nu^k \quad (2.22)$$

¹⁸³ The entire $SU(2)$ invariant Lagrangian can then be written as:

$$\begin{aligned} \mathcal{L}_{Yang-Mills} &= -\frac{1}{4}F_{\mu\nu}^i F^{i\mu\nu} + \bar{\psi}(i\gamma^\mu D_\mu)\psi \\ &= -\frac{1}{4}F_{\mu\nu}^i F^{i\mu\nu} + \bar{\psi}(i\gamma^\mu \partial_\mu - igA_\mu^i \frac{\sigma^i}{2})\psi \end{aligned} \quad (2.23)$$

¹⁸⁴ This procedure generalizes to any continuous group of symmetries. The basic steps involve
¹⁸⁵ identifying the generators of the transformation:

$$\psi(x) \rightarrow e^{i\alpha^a t^a} \psi \quad (2.24)$$

¹⁸⁶ where t^a are a set of matrices with the commutation relationship:

$$[t^a, t^b] = if^{abc}t^c \quad (2.25)$$

¹⁸⁷ where f^{abc} is the structure constant for the group. The covariant derivative is then defined as:

$$D_\mu = \partial_\mu - igA_\mu^a t^a \quad (2.26)$$

¹⁸⁸ where the fields, A_μ^a , transform like:

$$A_\mu^a \rightarrow A_\mu^a + \frac{1}{g}\partial_\mu \alpha^a + f^{abc}A_\mu^b \alpha^c \quad (2.27)$$

¹⁸⁹ the field strength tensor is then formed as:

$$F_{\mu\nu}^a = \partial_\mu A_\nu^a - \partial_\nu A_\mu^a + f^{abc}A_\mu^b A_\nu^c \quad (2.28)$$

¹⁹⁰ and finally, the locally, gauge invariant Lagrangian will have the form:

$$\begin{aligned}\mathcal{L}_{\text{General, non-Abelian}} &= -\frac{1}{4}F_{\mu\nu}^a F^{a\mu\nu} + \bar{\psi}(i\gamma^\mu D_\mu)\psi \\ &= -\frac{1}{4}F_{\mu\nu}^a F^{a\mu\nu} + \bar{\psi}(i\gamma^\mu \partial_\mu - igA_\mu^a t^a)\psi\end{aligned}\quad (2.29)$$

In 1964, Murray Gell-Mann and George Zweig independently developed a model of hadron interactions that describe the spectrum of baryons and mesons in terms of combinations of fundamental particles, which Gell-Mann named quarks [38] [39] [40]. In their model, three quarks: u, d, s formed an $SU(3)$ flavor symmetry. However, this did not explain the appearance of only two and three-quark combinations, the mesons and baryons. It also could not explain the spin statistics of the baryons. The Δ^{++} , Δ^- , and Ω^- , particles all have uuu , ddd , sss quark combinations, respectively, with their spins aligned. That is to say, these baryons seem to violate the Pauli-exclusion principle since all three quarks seem to occupy the same quantum state simultaneously.

In 1964, O.W. Greenberg solved this problem by proposing that quarks also have an additional quantum number, color, that come in three types: red, green, blue [41]. The requirement that all stable hadrons be color neutral: either possessing equal amounts of all three colors in qqq combinations, or a $q\bar{q}$ pair sharing the same color, also explained the observation of only 2 and 3 quark combinations in experiments. These three colors form an $SU(3)$ symmetry, and is the gauge symmetry describing the interactions of quarks and leptons. This theory is known as Quantum Chromodynamics (QCD). Its derivation follows from the procedure outlined above.

This group has eight generators, known as the Gell-Mann matrices, and are defined as:

$$\begin{aligned}t^1 &= \frac{1}{2} \begin{pmatrix} 0 & 1 & 0 \\ 1 & 0 & 0 \\ 0 & 0 & 0 \end{pmatrix}, \quad t^2 = \frac{1}{2} \begin{pmatrix} 0 & -i & 0 \\ i & 0 & 0 \\ 0 & 0 & 0 \end{pmatrix}, \quad t^3 = \frac{1}{2} \begin{pmatrix} 1 & 0 & 0 \\ 0 & -1 & 0 \\ 0 & 0 & 0 \end{pmatrix} \\ t^4 &= \frac{1}{2} \begin{pmatrix} 0 & 0 & 1 \\ 0 & 0 & 0 \\ 1 & 0 & 0 \end{pmatrix}, \quad t^5 = \frac{1}{2} \begin{pmatrix} 0 & 0 & -i \\ 0 & 0 & 0 \\ i & 0 & 0 \end{pmatrix} \\ , t^6 &= \frac{1}{2} \begin{pmatrix} 0 & 0 & 0 \\ 0 & 0 & 1 \\ 0 & 1 & 0 \end{pmatrix}, \quad t^7 = \frac{1}{2} \begin{pmatrix} 0 & 0 & 0 \\ 0 & 0 & -i \\ 0 & -i & 0 \end{pmatrix}, \quad t^8 = \frac{1}{2\sqrt{3}} \begin{pmatrix} 1 & 0 & 0 \\ 0 & 1 & 0 \\ 0 & 0 & -2 \end{pmatrix}\end{aligned}\quad (2.30)$$

and a Lagrangian defined as:

$$\begin{aligned}\mathcal{L}_{QCD} &= -\frac{1}{4}G_{\mu\nu}^a G^{a\mu\nu} + \bar{\psi}(i\gamma^\mu D_\mu) \\ &= -\frac{1}{4}G_{\mu\nu}^a G^{a\mu\nu} + \bar{\psi}(i\gamma^\mu \partial_\mu - igA_\mu^a t^a)\end{aligned}\quad (2.31)$$

where t^a are the Gell-Mann matrices defined in equation 2.30 and the fields A_μ^a are the eight mediators of the QCD force, the *gluons*.

Like all non-abelian gauge theories, it is asymptotically free, meaning that the strength of the coupling constant, α_s , decreases as the momentum-transfer, Q in interaction increases. This allows the use of perturbation theory for high-momentum calculations, therefore allowing

214 calculations of hadronic-processes for experimental evaluation.

215 The idea of local gauge invariance was successful in describing the dynamics of QED and
216 QCD, which only contain massless gauge bosons. Theorists had long postulated that the weak
217 force was so weak because it was being facilitated by massive bosons, but adding a mass term
218 for a boson breaks the local gauge invariance. So, a tool was needed to reconcile the concept of
219 local gauge invariance, which works so well for the other forces, with the prospect of the weak
220 force being facilitated by massive gauge bosons.

221 2.4 The Higgs Mechanism in an Abelian Theory

222 In 1964 Peter Higgs introduced the idea that the gauge bosons can acquire their mass through
223 the breaking of an underlying symmetry [42]. In other words, the natural symmetry of the
224 Lagrangian describing a particular interaction could be different than the symmetry we observe
225 in nature. Consider an abelian example of complex scalar field theory, coupled to itself and to
226 an electromagnetic field [33].

$$\mathcal{L} = -\frac{1}{4}(F_{\mu\nu})^2 + |D_\mu\phi|^2 - V(\phi) \quad (2.32)$$

227 where $D_\mu = \partial_\mu + ieA_\mu$, is the familiar covariant derivative, and the Lagrangian is invariant under
228 the $U(1)$ transformation as described earlier. The potential term, $V(\phi)$ has the form

$$V(\phi) = -\mu^2\phi^*\phi + \frac{\lambda}{2}(\phi^*\phi)^2 \quad (2.33)$$

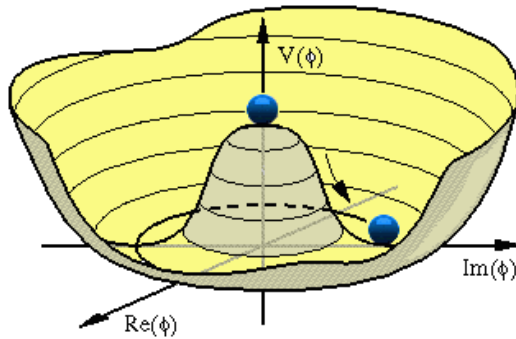


Figure 2.3: A visual representation of the Higgs potential [2]

229 if $\mu^2 > 0$ the shape of the potential no longer has a minimum at $\langle\phi\rangle = 0$. Figure 2.3 shows a plot
230 of the potential energy of ϕ in terms of each of its components. The new minimum potential
231 energy occurs at:

$$\langle \phi \rangle = \phi_0 = \left(\frac{\mu^2}{\lambda} \right)^{1/2} \quad (2.34)$$

232 and while the field has a ground state at the zero-potential point it is in an unstable equilibrium.
233 Any quantum fluctuation about this point will take the field into the lower-energy configuration
234 with a ground state about the new minimum. When the Lagrangian is expanded about equation
235 2.34, the field, ϕ is rewritten as:

$$\phi(x) = \phi_0 + \frac{1}{\sqrt{2}}(\phi_1(x) + i\phi_2(x)) \quad (2.35)$$

236 the potential term, $V(x)$, then becomes:

$$V(x) = -\frac{1}{2\lambda}\mu^4 + \frac{1}{2} \cdot 2\mu^2\phi_1^2 + \mathcal{O}(\phi_i^3) \quad (2.36)$$

237 where we can notice that ϕ_1 has acquired a mass term with, $m^2 = 2\mu^2$, while the scalar field
238 ϕ_2 remains massless, and is known as the Goldstone boson. The covariant derivative is also
239 transformed as:

$$|D_\mu \phi|^2 = \frac{1}{2}(\partial_\mu \phi_1)^2 + \frac{1}{2}(\partial_\mu \phi_2)^2 + \sqrt{2}e\phi_0 \cdot A_\mu \partial^\mu \phi_2 + e^2\phi_0^2 A_\mu A^\mu + \dots \quad (2.37)$$

240 where cubic and quartic terms of A_μ , ϕ_1 , and ϕ_2 have been dropped. The important term is the
241 last one, which can be interpreted as a mass term of the vector field, A_μ

$$\Delta \mathcal{L}_M = \frac{1}{2}m_A A_\mu A^\mu = e^2\phi_0^2 A_\mu A^\mu \quad (2.38)$$

242 where $m_A = 2e^2\phi_0^2$, has arisen from consequences of a non-zero vacuum expectation value of the
243 ϕ field. The remaining, massless Goldstone boson, ϕ_2 is not a physical particle, but rather a
244 consequence of the choice of gauge. This is illustrated when we can use the $U(1)$ gauge symmetry
245 to rotate the field $\phi(x)$ such that the field disappears.

$$\begin{aligned} \phi &\rightarrow \phi' = e^{i\alpha}(\phi_1 + \phi_2) \\ &= (\cos \alpha + i \sin \alpha)(\phi_1 + \phi_2) \\ &= (\phi_1 \cos \alpha - \phi_2 \sin \alpha) + i(\phi_1 \sin \alpha + \phi_2 \cos \alpha) \\ &= (\phi_1 - \phi_2 \tan \alpha) + i(\phi_1 \tan \alpha + \phi_2) \end{aligned} \quad (2.39)$$

246 Choosing $\alpha = -\tan \phi_2/\phi_1$ will make ϕ' a real quantity and eliminate its imaginary component,
247 ϕ'_2 . The Lagrangian can then be rewritten in terms of the rotated field ϕ' and see that the
248 massless boson is indeed removed from the theory.

$$\begin{aligned}\mathcal{L} = & \frac{1}{2}(\partial_\mu\phi'_1)(\partial^\mu\phi'_1) - \frac{1}{2} \cdot 2\mu^2\phi'_1\phi'_1 \\ & - \frac{1}{4}(F^{\mu\nu}F_{\mu\nu}) + \frac{1}{2} \cdot e^2\phi_0^2A_\mu A^\nu \\ & + \phi_0e^2\phi'_1A_\mu A^\mu + \frac{1}{2}e^2\phi'^2A_\mu A^\mu + \mathcal{O}(\phi'^3)\dots\end{aligned}\quad (2.40)$$

249 The degree of freedom that ϕ_2 represents, is absorbed as a longitudinal polarization of the
250 A_{mu} field, mathematically forbidden for massless gauge bosons, but necessary for massive bosons.

251 For this case of an abelian symmetry $U(1)$, it was shown that if a complex scalar field, which
252 interacts with itself and another vector field, can gain a non-zero vacuum expectation value. The
253 Lagrangian can be expanded about this new minimum, generating a mass term for the vector
254 field. One of the degrees of freedom of the original complex scalar field is then absorbed as a
255 longitudinal polarization state of the massive vector field.

256 2.5 The Higgs Mechanism in a non-Abelian Theory

257 Before describing the electroweak gauge theory of $SU(2) \otimes U(1)$, it will be helpful to see the
258 effects of the Higgs mechanism for the non-Abelian group, $SU(2)$ by itself. Consider an example
259 of an $SU(2)$ gauge field coupled to a scalar field that transforms like a real-valued vector under
260 $SU(2)$ transformations [33]. The field ϕ will have the form:

$$\phi = \begin{pmatrix} \phi_1 \\ \phi_2 \\ \phi_3 \end{pmatrix} \quad (2.41)$$

261 where the components, ϕ_i are real-valued fields. The $SU(2)$ transformation for this scalar field
262 will also look like:

$$\phi \rightarrow e^{i\alpha^i T^i} \phi \quad (2.42)$$

263 where the matrices, T^i are defined as:

$$iT^1 = \begin{pmatrix} 0 & 0 & 0 \\ 0 & 0 & 1 \\ 0 & -1 & 0 \end{pmatrix}, \quad T^2 = \begin{pmatrix} 0 & 0 & -1 \\ 0 & 0 & 0 \\ 1 & 0 & 0 \end{pmatrix}, \quad T^3 = \begin{pmatrix} 0 & 1 & 0 \\ -1 & 0 & 0 \\ 0 & 0 & 0 \end{pmatrix} \quad (2.43)$$

264 The Lagrangian for this field will feature a Higgs potential term along with the previously
265 mentioned $SU(2)$ gauge fields, A_μ^a coupled to the scalar field, ϕ , and is given by:

$$\mathcal{L} = -\frac{1}{4}F_{\mu\nu}^a F^{a\mu\nu} + |D_\mu\phi|^2 + \mu^2\phi^*\phi - \frac{\lambda}{4}(\phi^*\phi)^2 \quad (2.44)$$

266 where $F_{\mu\nu}^a$, the field strength tensor is defined as:

$$F_{\mu\nu}^a = (\partial_\mu A_\nu^a - \partial_\nu A_\mu^a) + g\epsilon^{abc} A_\mu^b A_\nu^c \quad (2.45)$$

²⁶⁷ and the covariant derivative is defined as:

$$D_\mu = (\partial_\mu + igA_\mu^a T^a)\phi \quad (2.46)$$

²⁶⁸ Similarly to the Abelian case, the Higgs potential will induce a spontaneous symmetry breaking,
²⁶⁹ and one of the components of the field ϕ will gain a vacuum expectation value. After this
²⁷⁰ breaking and expanding around the ground state potential, the field ϕ will have the form:

$$\phi = \frac{1}{\sqrt{2}} \begin{pmatrix} 0 \\ 0 \\ v+h \end{pmatrix} \quad (2.47)$$

²⁷¹ There has been no loss in generality in assuming this form since, similarly to the abelian case,
²⁷² we can use the gauge symmetry of $SU(2)$ to rotate the field into this configuration. Goldstone's
²⁷³ theorem tells us that we should expect two massive gauge bosons corresponding to the T^1 , and
²⁷⁴ T^2 generators, while the T^3 generator will correspond to a massless gauge boson, since ϕ is still
²⁷⁵ invariant under T^3 transformations.

²⁷⁶ As in the Abelian case, the mass terms for the gauge bosons are generated from the covariant
²⁷⁷ derivative term, $|D_\mu\phi|^2$

$$\begin{aligned} D_\mu\phi &= \frac{1}{\sqrt{2}} \left(\partial_\mu + gA_\mu^1 \begin{pmatrix} 0 & 0 & 0 \\ 0 & 0 & 1 \\ 0 & -1 & 0 \end{pmatrix} + gA_\mu^2 \begin{pmatrix} 0 & 0 & -1 \\ 0 & 0 & 0 \\ 1 & 0 & 0 \end{pmatrix} + gA_\mu^3 \begin{pmatrix} 0 & 1 & 0 \\ -1 & 0 & 0 \\ 0 & 0 & 0 \end{pmatrix} \right) \begin{pmatrix} 0 \\ 0 \\ v+h \end{pmatrix} \\ &= \frac{1}{\sqrt{2}} \begin{pmatrix} 0 \\ 0 \\ \partial_\mu \end{pmatrix} + \frac{gA_\mu^1}{\sqrt{2}} \begin{pmatrix} 0 \\ v+h \\ 0 \end{pmatrix} - \frac{gA_\mu^2}{\sqrt{2}} \begin{pmatrix} v+h \\ 0 \\ 0 \end{pmatrix} \\ &= \frac{1}{\sqrt{2}} \begin{pmatrix} g(v+h)A_\mu^1 \\ g(v+h)A_\mu^2 \\ \partial_\mu h \end{pmatrix} \end{aligned} \quad (2.48)$$

²⁷⁸ Therefore

$$|D_\mu \phi|^2 = \frac{1}{2} \partial_\mu h \partial^\mu h + \frac{g^2 v^2}{2} ((A_\mu^1)^2 + (A_\mu^2)^2) + \frac{g^2}{2} (h^2 + 2hv) ((A_\mu^1)^2 + (A_\mu^2)^2) \quad (2.49)$$

279 This theory produces two massive bosons, A_μ^1 and A_μ^2 , both with mass, $m_A = gv$. These
 280 fields have h , and h^2 couplings to the Higgs boson. The third gauge field, A_μ^3 , remains massless
 281 and is not coupled to the Higgs field. This model is beginning to resemble a description of
 282 electroweak physics; however, a third massive boson is necessary, as is a new gauge symmetry
 283 in order to generate it. That is the subject of the next section.

284 2.6 Glashow Weinberg Salam Theory

285 Glashow, Weinberg, and Salam published their theory unifying electromagnetic and weak forces
 286 in the 1960s [43] [44] [45]. It begins with the requirement of a $SU(2)_L \otimes U(1)$ symmetry
 287 and incorporates the Higgs mechanism to give mass to the gauge bosons of the weak force. As
 288 described earlier, the $U(1)$ symmetry requires introducing a vector field, which will be labeled B_μ ,
 289 and an interaction term, which is absorbed into the covariant derivative, D_μ . The transformation
 290 will also be parameterized with a quantum number, Y , known as hypercharge. The $SU(2)$
 291 symmetry requires the introduction of three new vector fields, which will be labeled $W_\mu^i, i =$
 292 1, 2, 3. The quantum number associated with this gauge group is isospin, and is determined
 293 by the T^3 operator, acting on an $SU(2)$ doublet on the third generator of the group. The
 294 $SU(2) \otimes U(1)$ transformation, $U(x)$, will then be given by:

$$U(x) = e^{i\alpha^a(x)\tau^a} e^{iY\alpha(x)} \quad (2.50)$$

295 where $\tau^a = \sigma^a/2$, the Pauli matrices, 2.18. These gauge fields will be coupled, via the covariant
 296 derivative, to a doublet of complex scalar fields ϕ , with hypercharge $Y = +1/2$. A Higgs potential
 297 will be added to generate the spontaneous symmetry breaking that will give mass to three of
 298 the gauge fields, and leave one massless. In order to preserve the $SU(2)_L \otimes U(1)$ symmetry, the
 299 new covariant derivative will take the form:

$$D_\mu = (\partial_\mu - igW_\mu^a \tau^a - \frac{i}{2}g'B_\mu) \quad (2.51)$$

300 The subscript L on $SU(2)_L$ refers to experimental observations of the weak force violating
 301 parity maximally, by only interacting with the left-handed chiral component of a field. Right
 302 versus left chirality is determined by whether the spin of a particle is aligned or anti-aligned
 303 with its direction of motion, and in general a particle is represented by a linear combination

of its right and left-handed components. This idea was first proposed by Chen Ning Yang and Tsung-Dao Lee, in the 1950s. Their ideas were validated by the experimental discovery of parity violation in 1957, through the beta decays of Cobalt 60 atoms by C.S Wu. That same year, Yang and Lee were awarded the Nobel Prize for their insight [46]. In this model, then, the left-handed components of the particles participate in the weak interaction and are formed into doublets, while the right handed components are singlets, and will only interact with the electromagnetic field, B_μ . The quantum numbers will be given by +1/2 for the upper component of the $SU(2)$ doublet, and -1/2 for the lower component. The fermion content of this theory is then given by:

$$\begin{pmatrix} \nu_L \\ e_L \end{pmatrix}, e_R \quad \begin{pmatrix} u_L \\ d_L \end{pmatrix}, u_R, d_R \quad (2.52)$$

where the right-handed neutrino, ν_R , has been omitted since it has zero charge, and isospin, and therefore does not participate in any of the interactions of this theory. The complete Lagrangian is given by a sum of free-particle terms for massless bosons, fermions, and Higgs scalar fields; the Higgs potential; and a Yukawa coupling term between the fermions and the Higgs, which generates their masses.

$$\mathcal{L}_{GWS} = \mathcal{L}_{BosonKE} + \mathcal{L}_{Higgs} + \mathcal{L}_{FermionKE} + \mathcal{L}_{Yukawa} \quad (2.53)$$

The Higgs potential will have the form:

$$\mathcal{L}_{Higgs} = (D_\mu \phi)^\dagger (D^\mu \phi) + \mu^2 \phi^\dagger \phi - \lambda (\phi^\dagger \phi)^2 \quad (2.54)$$

The Higgs potential will break the symmetry of the Lagrangian when one of the four degrees of freedom in the complex scalar doublet, ϕ , spontaneously acquires a vacuum expectation value. In this case, it will generate three massive gauge bosons, one massless gauge boson, and a massive scalar field. After gaining a vacuum expectation value, and expanding about this value, the scalar fields will have the form:

$$\langle \phi \rangle = \frac{1}{\sqrt{2}} \begin{pmatrix} 0 \\ v + h \end{pmatrix} \quad (2.55)$$

where no loss of generality has occurred since we are always able to rotate into this form through the appropriate gauge transformations, similar to what was described in the Abelian case. It should also be noted that this form is not invariant to any of the individual generators t^a , however ϕ will be invariant to a combination of $T^3 + Y$ generators. Per Goldstone's theorem, we should expect this linear combination of fields to be the massless vector boson after symmetry breaking.

The massless eigenstate will be the electromagnetic field, $A_\mu \sim A_\mu^3 + B_\mu$. The electric charge quantum number, Q , is then defined as

$$Q = T^3 + Y \quad (2.56)$$

322 As before, the generation of the masses for the gauge bosons are generated by the interaction
323 of their fields with the Higgs field via the covariant derivative.

$$\begin{aligned} D_\mu \phi &= \frac{1}{\sqrt{2}} \left(\partial_\mu - \frac{ig}{2} A_\mu^1 \begin{pmatrix} 0 & 1 \\ 1 & 0 \end{pmatrix} - \frac{ig}{2} A_\mu^2 \begin{pmatrix} 0 & -i \\ i & 0 \end{pmatrix} - \frac{ig}{2} A_\mu^3 \begin{pmatrix} 1 & 0 \\ 0 & -1 \end{pmatrix} \right) \begin{pmatrix} 0 \\ v+h \end{pmatrix} \\ &= \frac{1}{\sqrt{2}} \left(\left(\frac{g}{2}(v+h) A_\mu^2 \right) + i \left(\frac{g}{2}(v+h) A_\mu^1 \right) \right) \\ &\quad + \frac{1}{\sqrt{2}} \left(\partial_\mu + i \left(\frac{1}{2}(v+h)(gA_\mu^3 - g'B_\mu) \right) \right) \end{aligned} \quad (2.57)$$

324 Taking the dot product of this with its hermitian conjugate gives the $|D_\mu \phi|^2$ term:

$$\begin{aligned} |D_\mu \phi|^2 &= \frac{1}{2} \partial_\mu h \partial^\mu h + \frac{1}{2} \frac{g^2 v^2}{4} ((A_\mu^1)^2 + (A_\mu^2)^2) + \frac{v^2}{4} (gA_\mu^3 - g'B_\mu)^2 \\ &\quad + \frac{1}{2} g^2 4(h^2 + 2vh)((A_\mu^1)^2 + (A_\mu^2)^2) + \frac{1}{2} \frac{1}{4} (h^2 + 2vh)(gA_\mu^3 - g'B_\mu) \end{aligned} \quad (2.58)$$

325 From equation 2.58 we can identify three massive and one massless gauge bosons, corresponding
326 to the charged and neutral weak currents, and the electromagnetic current.

$$\begin{aligned} W_\mu^\pm &= \frac{1}{\sqrt{2}} (A_\mu^1 \mp i A_\mu^2) && \text{with mass } m_W = g \frac{v}{2}; \\ Z_\mu^0 &= \frac{1}{\sqrt{g^2 + g'^2}} (gW_\mu^3 - g'B_\mu) && \text{with mass } m_Z = \frac{v}{2} \sqrt{g^2 + g'^2}; \\ A_\mu &= \frac{1}{\sqrt{g^2 + g'^2}} (gW_\mu^3 + g'B_\mu) && \text{with mass } m_A = 0; \end{aligned} \quad (2.59)$$

327 where the last field, A_μ is absent from the covariant derivative term, but already identified as
328 the massless gauge boson of the theory due to its gauge invariance under a $T^3 + Y$ rotation.

329 Using these definitions the covariant derivative has the following form:

$$\begin{aligned} D_\mu &= \partial_\mu - \frac{ig}{\sqrt{2}} (W^+ T^+ + W^- T^-) \\ &\quad - \frac{i}{\sqrt{g^2 + g'^2}} Z_\mu^0 (gT^3 - g'Y) - \frac{gg'}{\sqrt{g^2 + g'^2}} A_\mu (T^3 + Y) \end{aligned} \quad (2.60)$$

330 where $T^\pm = \frac{1}{2}(\sigma^1 \pm \sigma^2)$. From this form, we can identify the fundamental electric charge, e , as

$$e = \frac{gg'}{\sqrt{g^2 + g'^2}} \quad (2.61)$$

331 The similarity in the forms between Z_μ^0 and A_μ suggest that their relationship can be ex-
 332 pressed in a simpler form, as the rotation of underlying gauge fields A_μ^3 and B_μ through the
 333 weak mixing angle, θ_W

$$\begin{pmatrix} Z_\mu^0 \\ A_\mu \end{pmatrix} = \begin{pmatrix} \cos \theta_W & -\sin \theta_W \\ \sin \theta_W & \cos \theta_W \end{pmatrix} \begin{pmatrix} A_\mu^3 \\ B_\mu \end{pmatrix} \quad (2.62)$$

334 where $\tan \theta_W = \frac{g'}{g}$. Expanding 2.62, we have the definitions of the Z_μ^0 and A_μ fields in terms of
 335 θ_W

$$\begin{aligned} Z_\mu^0 &= A_\mu^3 \cos \theta_W - B_\mu \sin \theta_W \\ A_\mu &= A_\mu^3 \sin \theta_W + B_\mu \cos \theta_W \end{aligned} \quad (2.63)$$

336 The weak mixing angle, θ_W , also provides a simple relationship between the W_μ^\pm and Z_μ^0 fields:

$$m_W = m_Z \cos \theta_W \quad (2.64)$$

337 The covariant derivative, D_μ is also rewritten in terms of the mass eigenstates of the gauge fields

$$D_\mu = (\partial_\mu - \frac{ig}{\sqrt{2}}(W_\mu^+ + W_\mu^- T^-) - \frac{ig}{\cos \theta_W} Z_\mu^0(T_3 - \sin^2 \theta_W Q) - ieA_\mu Q) \quad (2.65)$$

338 where $g = e/\cos \theta_W$. The square of the covariant derivative is then written as

$$\begin{aligned} |D_\mu|^2 &= \frac{1}{2}\partial_\mu h \partial^\mu h + \frac{1}{2}m_W^2 W_\mu^+ W^{\mu+} + \frac{1}{2}m_W^2 W_\mu^- W^{\mu-} + \frac{1}{2}m_Z^2 Z_\mu^0 Z^{\mu 0} \\ &+ \left(\frac{h^2}{v^2} + \frac{h}{v}\right)\left[\frac{1}{2}m_W^2(W_\mu^+ W^{\mu+} + W_\mu^- W^{\mu-}) + \frac{1}{2}m_Z^2 Z_\mu^0 Z^{\mu 0}\right] \end{aligned} \quad (2.66)$$

339

340

341 With the form of the covariant derivative in place, the fermionic kinematic term of the
 342 Lagrangian can be described. As mentioned earlier, the masses of the fermions in the model
 343 will be generated by the Yukawa interaction term with the Higgs, so this term only involves
 344 the covariant derivatives acting on the left-handed doublet and right-handed singlet states of
 345 this model. The quantum number assignments for the leptons, which are chosen in order to
 346 reproduce the known values of their electric charges, are shown in table 2.1. The values of these
 347 quantum numbers enter into the covariant derivative via the Z_μ^0 term of equation 2.65. The
 348 fermionic kinetic energy term of the Lagrangian is given by:

	ν_L	e_L	e_R	u_L	d_L	u_R	d_R
Isospin	+1/2	-1/2	0	+1/2	-1/2	0	0
Hypercharge	-1/2	-1/2	-1	+1/6	1/3	2/3	-1/3
Electric Charge	0	-1	-1	2/3	-1/3	2/3	-1/3

Table 2.1: The quantum numbers Isospin and Hypercharge are assigned for each of the $SU(2)$ and $U(1)$ symmetries respectively

$$\begin{aligned} \mathcal{L}_{Fermion} = & \bar{E}_L(i\gamma^u D_\mu)E_L + \bar{e}_R(i\gamma^u D_\mu)e_R \\ & \bar{Q}_L(i\gamma^u D_\mu)Q_L + \bar{u}_R(i\gamma^u D_\mu)u_R + \bar{d}_R(i\gamma^u D_\mu)d_R \end{aligned} \quad (2.67)$$

349 Expanding the covariant term for the left-handed electron shows its explicit coupling to the
 350 gauge boson fields.

$$\begin{aligned} \mathcal{L}_{E_L} = & \begin{pmatrix} \bar{\nu}_L & \bar{e}_L \end{pmatrix} \left(i\gamma^\mu (\partial_\mu - \frac{ig}{\sqrt{2}}(W_\mu^+ T^+ + W_\mu^- T^-) - \frac{ig}{\cos \theta_W} Z_\mu^0 (T^3 - \sin^2 \theta_W Q) - ie A_\mu Q) \right) \begin{pmatrix} \nu_L \\ e_L \end{pmatrix} \\ = & \bar{\nu}_L i\gamma^\mu \partial_\mu \nu_L + \bar{e}_L i\gamma^\mu \partial_\mu e_L + \frac{ig}{\sqrt{2}} W_\mu^+ \bar{\nu}_L \gamma^\mu e + \frac{ig}{\sqrt{2}} W_\mu^- \bar{e}_L \gamma^\mu \nu_L \\ & + \frac{ig}{\cos \theta_W} \bar{\nu}_L (1/2) \gamma^\mu \nu_L + \frac{ig}{\cos \theta_W} \bar{e}_L \gamma^\mu (-1/2 + \sin^2 \theta_W (+1)) e_L + (ie) \bar{e}_L \gamma^\mu A_\mu (-1) \end{aligned} \quad (2.68)$$

351 All of the terms will be combined with the final, spontaneously-broken GWS Lagrangian at the
 352 end of this section.

353 The final term to discuss in the theory, before combining all of the results, is the Yukawa
 354 interaction term between the fermion fields and the Higgs. For the electron, this term takes the
 355 form:

$$\begin{aligned} \mathcal{L}_{Yukawa} = & -\lambda_e \bar{E}_L \cdot \phi e_R - \lambda_e E_L \cdot \phi \bar{e}_R \\ = & -\frac{\lambda_e}{\sqrt{2}} (v + h) (\bar{e}_L e_R + e_L \bar{e}_R) \\ = & -\frac{\lambda_e v}{\sqrt{2}} (\bar{e}_L e_R + e_L \bar{e}_R) - \frac{\lambda_e}{\sqrt{2}} (\bar{e}_L e_R + e_L \bar{e}_R) h \end{aligned} \quad (2.69)$$

356 where the mass of the electron is identified as $m_e = \frac{\lambda_e v}{\sqrt{2}}$. In order to generate the masses
 357 of the particles, each fermion has its own unique λ value. So while the Higgs mechanism is
 358 able to generate the masses in a way that preserves the underlying $SU(2) \otimes U(1)$ symmetry,
 359 it does not explain the hierarchy of masses since each λ value is unique to each lepton. The
 360 second term in equation 2.69 is the coupling of the Higgs particle, h , to the fermions. The
 361 coupling is proportional to the mass of the particle. The largest of these is to the top quark,
 362 with $m_t = 173.21 \pm 0.51 \pm 0.71 \text{ GeV}$.

363 The Yukawa coupling for the quarks is necessarily modified when additional quarks besides

364 the u and d are added to the theory. This is because there can be additional coupling terms
 365 that mix generations. This occurs when the mass eigenstate of the quarks is not the same as the
 366 interaction eigenstate. The modification requires the expansion of the u_L and d_L components
 367 into a vector of left handed quarks. If we let

$$u_L^i = (u_L, c_L, t_L), \quad d_L^i = (d_L, s_L, b_L) \quad (2.70)$$

368 represent the up- and down-type quarks in the original weak interaction basis, then the vectors,
 369 u_L^i and d_L^i , can be defined as the diagonalized basis for the Higgs coupling. They are related
 370 through a unitary transformation.

$$u_L^i = U_u^{ij} u_L^{j'}, \quad d_L^i = U_d^{ij} d_L^{j'} \quad (2.71)$$

371 The interaction terms with the charged gauge boson currents must then be rewritten as

$$J_W^{\mu+} = \frac{1}{\sqrt{2}} \bar{u}_L^i \gamma^\mu d_L^i = \frac{1}{\sqrt{2}} \bar{u}_L^{i'} \gamma^\mu (U_u^\dagger U_d) d_L^{j'} = \frac{1}{\sqrt{2}} \bar{u}_L^{i'} \gamma^\mu V_{ij} d_L^{j'} \quad (2.72)$$

372 where V_{ij} is the 3x3 Cabibbo-Kobayashi-Maskawa (CKM) matrix describing the mixing among
 373 six quarks [47] [48]. It is an extension of the Glashow-Iliopoulos-Maiani mechanism, which was
 374 a 2x2 matrix that predicted the existence of a fourth quark, the charm quark [49]. The GIM
 375 mechanism was an attempt to suppress flavor-changing-neutral currents, which occur at LO in
 376 a three-quark model, but not in a four-quark model. The CKM matrix, however, was motivated
 377 by an attempt to explain CP violation in the weak interaction. At the time of its publication,
 378 the bottom and top quarks were not predicted. After these were discovered, they were awarded
 379 the nobel prize in physics in 2008.

380 At this point, all the of the pieces are ready to write down the GWS Lagrangian, after the
 381 Higgs mechanism has spontaneously broken the $SU(2) \otimes U(1)$ symmetry.

$$\begin{aligned} \mathcal{L}_{Unbroken} = & -\frac{1}{4} A_{\mu\nu}^a A^{\mu\nu a} - \frac{1}{4} F_{\mu\nu} F^{\mu\nu} \\ & + |D_\mu \phi|^2 + \mu^2 (\phi^\dagger \phi) - \lambda (\phi^\dagger \phi)^2 \\ & + \bar{E}_L (i\gamma^\mu D_\mu) E_L + \text{similar terms for } e_R, U_L, u_R, d_R \\ & - \lambda_e \bar{E}_L \cdot \phi e_R + h.c. + \text{similar terms for } e_R, U_L, u_R, d_R \end{aligned} \quad (2.73)$$

$$\begin{aligned}
\mathcal{L}_{GWS} = & -\frac{1}{4}(Z_{\mu\nu}^0)^2 - \frac{1}{2}(W_{\mu\nu}^+ W_{\mu\nu}^-) - \frac{1}{4}(F_{\mu\nu})^2 \\
& + ig \cos \theta_W ((W_\mu^- W_\nu^+ - W_\nu^- W_\mu^+) \partial^\mu Z^{0\nu} + W_{\mu\nu}^+ W^{-\mu} Z^{0\nu} + W_{\mu\nu}^- W^{+\mu} Z^{0\nu}) \\
& + ie ((W_\mu^- W_\nu^+ - W_\nu^- W_\mu^+) \partial^\mu A^\nu + W_{\mu\nu}^+ W^{-\mu} A^\nu - W_{\mu\nu}^- W^{+\mu} A^\nu) \\
& + g^2 \cos^2 \theta_W (W_\mu^+ W_\nu^- Z^{0\mu} Z^{0\nu} - W_\mu^+ W^{-\mu} Z_\nu^0 Z^{0\nu}) \\
& + g^2 (W_\mu^+ W_\mu^- A^\mu A^\nu - W_\mu^+ W^{-\mu} A_\nu A^\nu) \\
& + ge \cos \theta_W (W_\mu^+ W_\nu^- (Z^{0\mu} A_\nu + Z^{0\nu} A^\mu) - 2W_\mu^+ W^{-\mu} A^\nu) \\
& + \frac{1}{2}g^2 (W_\mu^+ W_\nu^-) (W^{+\mu} W^{-\nu} - W^{+\nu} W^{-\mu}) \\
& + \frac{1}{2}\partial_\mu h \partial^\nu h - v^2 \lambda h^2 + \frac{1}{2}m_W^2 W_\mu^+ W^{+\mu} + \frac{1}{2}m_W^2 W_\mu^- W^{-\mu} + \frac{1}{2}m_Z^2 Z_\mu^0 Z^{0\mu} \\
& + \left(\frac{h^2}{v^2} + \frac{h}{v}\right) \left(\frac{1}{2}m_W^2 (W_\mu^+ W^{+\mu} + W_\mu^- W^{-\mu}) + \frac{1}{2}m_Z^2 Z_\mu^0 Z^{0\mu}\right) - \lambda v h^3 - \frac{1}{4}\lambda h^4 \\
& + \bar{E}_L (i\gamma^\mu \partial_\mu) E_L + e_R^- (i\gamma^\mu \partial_\mu) e_R + \bar{Q}_L (i\gamma^\mu \partial_\mu) Q_L + u_R^- (i\gamma^\mu \partial_\mu) u_R + \bar{d}_R (i\gamma^\mu \partial_\mu) d_R \\
& + g(W_\mu^+ J_W^{\mu+} + W_\mu^- J_W^{\mu-} + Z_\mu^0 J_Z^\mu) + e A_\mu J_{EM}^\mu \\
& - \frac{\lambda_e v}{\sqrt{2}} (\bar{e}_L e_R + \bar{e}_R e_L) - \frac{\lambda_e h}{\sqrt{2}} (\bar{e}_L e_R + \bar{e}_R e_L) \\
& - \frac{\lambda_u v}{\sqrt{2}} (\bar{u}_L u_R + \bar{u}_R u_L) - \frac{\lambda_u h}{\sqrt{2}} (\bar{u}_L u_R + \bar{u}_R u_L) \\
& - \frac{\lambda_d v}{\sqrt{2}} (\bar{d}_L d_R + \bar{d}_R d_L) - \frac{\lambda_d h}{\sqrt{2}} (\bar{d}_L d_R + \bar{d}_R d_L)
\end{aligned} \tag{2.74}$$

where the currents of the electroweak interaction, $J_W^{\mu+}$, $J_W^{\mu-}$, J_Z^μ , J_A^μ are defined as:

$$\begin{aligned}
J_W^{\mu+} &= \frac{1}{\sqrt{2}} (\bar{\nu}_L \gamma^\mu e_L + \bar{u}_L^i \gamma^\mu V_{ij} d_L^j) \\
J_W^{\mu-} &= \frac{1}{\sqrt{2}} (\bar{e}_L \gamma^\mu \nu_L + \bar{d}_L^i \gamma^\mu V_{ij} u_L^j) \\
J_Z^\mu &= \frac{1}{\cos \theta_W} (\bar{\nu}_L \gamma^\mu (+1/2) \nu_L + \bar{e}_L \gamma^\mu (-1/2 + \sin^2 \theta_W) e_L + \bar{e}_R \gamma^\mu \sin^2 \theta_W e_R \\
&\quad + \bar{u}_L \gamma^\mu (1/2 - 2/3 \sin^2 \theta_W) u_L + \bar{u}_R \gamma^\mu (-2/3 \sin^2 \theta_W) u_R \\
&\quad + \bar{d}_L \gamma^{mu} (-1/2 + 1/3 \sin^2 \theta_W) d_L + \bar{d}_R \gamma^\mu (1/3 \sin^2 \theta_W) d_R) \\
J_{EM}^\mu &= e_{L,R}^- \gamma^\mu (-1) e_{L,R} + u_{L,R}^- \gamma^\mu (2/3) u_{L,R} + d_{L,R}^- \gamma^\mu (-2/3) d_{L,R}
\end{aligned} \tag{2.75}$$

382 2.7 The Standard Model of Particle Physics

The Standard Model of particle physics, extends the GWS model by incorporating the QCD interaction between the quarks and gluons. The symmetry of this theory is that of:

$$SU(3)_C \otimes SU(2)_L \otimes U(1)_Y \tag{2.76}$$

³⁸³ The Lagrangian of the model is given by

$$\mathcal{L}_{SM} = \mathcal{L}_{GWS} - \frac{1}{4} G_{\mu\nu}^a G^{a\mu\nu} + g_S C_\mu^a J_{QCD}^{a\mu} \quad (2.77)$$

³⁸⁴ where the current for the QCD interaction, $J_{QCD}^{a\mu}$ is defined as:

$$J_{QCD}^a = \bar{u}^i \gamma^\mu t^a u^i + \bar{d}^i \gamma^\mu t^a d^i \quad (2.78)$$

³⁸⁵ where t^a are the Gell-Mann matrices defined in equation 2.30. The field strength tensor for the
³⁸⁶ eight gluon fields, $G_{\mu\nu}^a$, is defined as

$$G_{\mu\nu}^a = (\partial_\mu C_\nu^a - \partial_\nu C_\mu^a) - g_S f^{abc} C_\mu^b C_\nu^c \quad (2.79)$$

³⁸⁷ The experimental evidence in favor of the SM is compelling. It has not only been able to
³⁸⁸ describe existing phenomena to great precision, but has also predicted the existence of new forms
³⁸⁹ of matter and interactions among fundamental particles. The UA1 [50] [51] and UA2 [52] [53]
³⁹⁰ experiments at CERN, under the leadership of Carlo Rubbia, discovered the W and Z bosons
³⁹¹ in 1983. The experiments observed a handful of events, in $p\bar{p}$ collisions, at $\sqrt{s} = 540$ GeV, and
³⁹² were able to measure the masses to be $M_W \sim 80$ GeV and $M_Z \sim 95$ GeV. This was the first
³⁹³ direct observation of the massive weak bosons predicted by the Glashow-Weinberg-Salam theory
³⁹⁴ of weak interactions.

³⁹⁵ In the following years, from 1989-2000, the Large electron-positron (LEP) collider at CERN
³⁹⁶ conducted precision measurements of the SM [54] [55]. Along with high-precision measurements
³⁹⁷ on the W, Z masses:

$$m_Z = 91.1875 \pm 0.0021 \text{ GeV} \quad (2.80)$$

$$m_W = 80.376 \pm 0.0033 \text{ GeV}$$

³⁹⁸ the experiment was also able to put stringent limits on the existence of more than three families of
³⁹⁹ leptons and quarks by measuring the width of the Z boson. Figure 2.4(a) shows the comparison
⁴⁰⁰ of two, three, and four family hypotheses to data.

⁴⁰¹ Another milestone for the Standard Model occurred in 1995 when the CDF [60] and D0 ex-
⁴⁰² periments [61] at the Tevatron announced the observation of the top quark, with $m_t \sim 176$ GeV,
⁴⁰³ in $p\bar{p}$ collisions at $\sqrt{s} = 1.8$ TeV. Figure 2.4(b) shows a plot from 2012, the latest top quark
⁴⁰⁴ mass measurements from CDF, which reports a $m_t = 173.18 \pm 0.56 \pm 0.75$ GeV. It was the
⁴⁰⁵ last quark predicted by the CKM matrix to be observed, and earned Makoto Kobayashi and
⁴⁰⁶ Toshihide Maskawa the nobel prize in 2008 for their work extending the quark sector to three

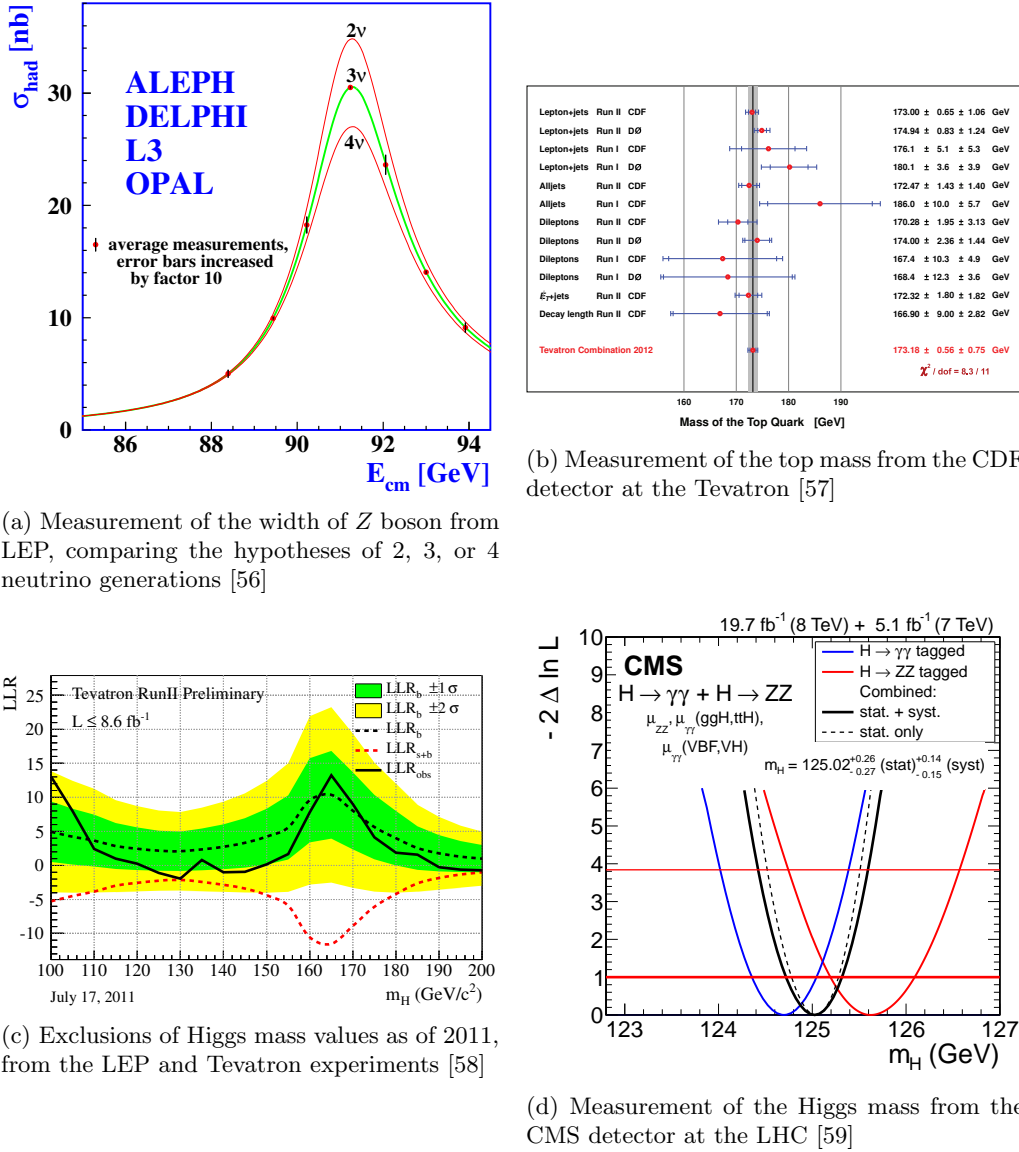


Figure 2.4: Experimental milestones of the Standard Model

407 families and parameterizing their electroweak mixing.

408 After the discovery of the top-quark, the last remaining particle that was predicted by the
 409 Standard Model, and remained to be observed was the Higgs Boson. Although the LEP and
 410 Tevatron experiments were unable to observe the Higgs, they were able to exclude a large range
 411 of possible masses [58]. The combined results of both experiments, as of 2011, only allowed the
 412 possible masses of $115 < m_{Higgs} < 155$ GeV, and $m_{Higgs} > 176$ GeV, as shown in figure 2.4(c).

413 Yet another milestone was reached in 2012, when the CMS and ATLAS detectors at CERN
 414 announced the observation of a new boson, with characteristics strikingly similar to the elusive
 415 Higgs boson of the SM. Figure 2.4(d) shows the latest measurement results on the mass from
 416 the $H \rightarrow \gamma\gamma$ and $H \rightarrow ZZ$ channels, with a $m_H = 125.02 \pm 0.27 \pm 0.15$ GeV. One of the
 417 most important remaining goals is to measure the couplings of this new boson to all of the other
 418 particles in the Standard Model. Of particular interest is the coupling to the top-quark, since it
 419 offers the largest value of the Higgs Yukawa coupling to measure. This offers a test of the nature
 420 of the coupling, as well as a probe into deviations from its value.

421 2.8 Higgs Production in pp Collisions at the LHC

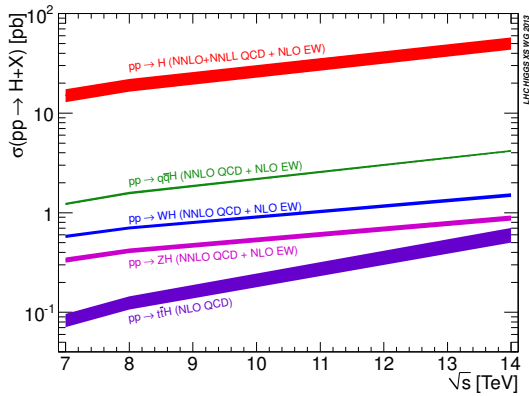


Figure 2.5: Higgs production cross-sections at the LHC, for 7–14 TeV pp collisions

422 The rest of the thesis will describe the search for Higgs-boson production in proton-proton
 423 collisions at the LHC, so it will be useful to understand the production mechanisms for the Higgs
 424 in this scenario. At the LHC collision energies 7 – 14 TeV, there are four dominant production
 425 mechanisms that produce Higgs events: gluon-gluon fusion (ggf), vector-boson fusion (vbf),
 426 associated production with vector bosons (VH), and associated production with top-quark pairs
 427 ($t\bar{t}H$). Figure 2.5 shows the relative cross sections for each of these mechanisms.

Gluon-gluon fusion, which proceeds via a heavy-quark loop [62], is the dominant production mechanism at the LHC. The QCD radiative corrections to the total cross section have been computed at the next-to-leading order (NLO) and at the next-to-next-to-leading order (NNLO

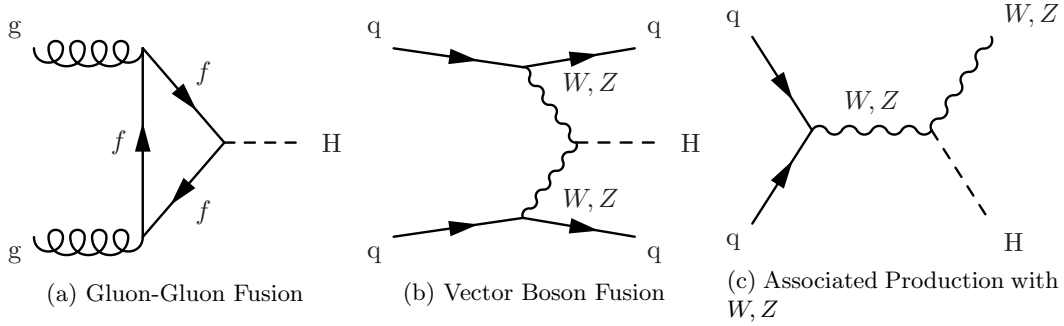


Figure 2.6: Feynman diagrams for the three largest Higgs production modes at the LHC

accuracy). The cross section for Higgs production at $m_H = 125$ GeV and $\sqrt{s} = 8$ TeV, the cross section is given as:

$$\sigma_{ggF} = 19.27 \pm \text{QCD Scale Unc.}^{+7.2\%}_{-7.8\%} \pm \text{PDF} + \alpha_S \text{ Unc.}^{+7.4\%}_{-6.9\%} \text{ pb}^{-1} \quad (2.81)$$

Figure 2.6(a) shows a Feynman diagram for this process. The triangle loop contains all strongly coupled fermions, which is dominated by the top-quark since its Yukawa coupling to the Higgs is the largest.

Vector-boson fusion proceeds through the fusion of W^+W^- or Z^0Z^0 gauge bosons [62]. The characteristic signature of the production mode is the associated production of two quarks, typically at a low angle relative to the proton beam. This process has been calculated to NNLO for QCD and NLO for electroweak (EW) corrections [62]. The cross section at $m_H = 125$ GeV and $\sqrt{s} = 8$ TeV is given as:

$$\sigma_{VBF} = 1.653 \pm \text{EW Unc.}^{+4.5\%}_{-4.5\%} \pm \text{QCD Scale Unc.}^{+0.2\%}_{-0.2\%} \pm \text{PDF} + \alpha_S \text{ Unc.}^{+2.6\%}_{-2.8\%} \text{ pb}^{-1} \quad (2.82)$$

Figure 2.6(b) shows a Feynman diagram for VBF production. The large coupling to the W, Z bosons helps to make this the sub-dominant production mechanism at the LHC. However, the gluon content of the proton at TeV energies is much larger than that of the valence quarks, thus the relative suppression.

The third largest production mechanism for Higgs bosons at the LHC is through associated production with a W or Z boson [62]. It has been calculated to NNLO for QCD and NLO for EW corrections. This process is also sometimes referred to as, "Higgstrahlung", since it resembles the bremsstrahlung process of an electron radiating a photon. The higher order electroweak corrections are similar to that of Drell-Yan, so much of the technology to compute the cross-section can be borrowed from existing EW calculations. The cross section for $m_H = 125$ GeV and $\sqrt{s} = 8$ TeV is:

$$\begin{aligned}\sigma_{WH} &= 0.7046 \pm \text{QCD Scale Unc.}^{+1.0\%}_{-1.0\%} \pm \text{PDF} + \alpha_S \text{ Unc.}^{+2.3\%}_{-2.3\%} \text{ pb}^{-1} \\ \sigma_{ZH} &= 0.4153 \pm \text{QCD Scale Unc.}^{+3.1\%}_{-3.1\%} \pm \text{PDF} + \alpha_S \text{ Unc.}^{+2.5\%}_{-2.5\%} \text{ pb}^{-1}\end{aligned}\quad (2.83)$$

442 Figure 2.6(c) shows the Feynman diagram for VH production. This channel is most useful for
443 identifying hadronic decays of the Higgs, since the associated gauge boson can decay to leptons,
444 giving a strong kinematic handle over backgrounds that would normally overwhelm a similar
445 search in the ggF channel.

446 **2.9 $t\bar{t}H$ Production in pp Collisions at the LHC**

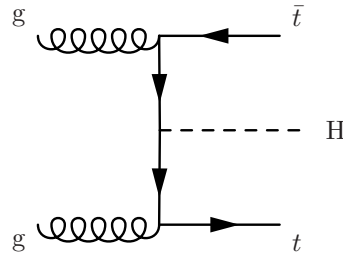


Figure 2.7: Feynman diagram for $t\bar{t}H$ production

447 The $t\bar{t}H$ production mode is the fourth-largest production mode at the LHC [62]. This pro-
448 duction mode has been calculated to NLO in QCD [63] [64] and has been studied recently with the
449 state of the art NLO tools using the aMC@NLO [65] and POWHEG (PYTHIA+HERWIG) [66]
450 frameworks. Studies have also been performed interfacing NLO QCD studies [67] with the
451 Sherpa parton shower framework [68]. Additional studies on the effects of spin correlations with
452 the aMC@NLO and Madspin framework have also been performed [69].

It has been found that the addition of NLO effects increases the cross-section relative to LO by $\sim 20\%$. The largest theoretical uncertainty comes from the variation of the renormalization and factorization scale, the QCD coupling α_S , and the PDF uncertainty. The renormalization and factorization scales are set to $\mu_R = \mu_F = (1/2)(m_T + m_T + m_H)$ and are varied by a factor of 2 to determine the cross-section's dependence on these parameters. Three different PDF sets, MSTW2008, CTEQ6.6, and NNPDF2.0 were used with the appropriate corresponding values of α_S to determine the combined effect of varying $\text{PDF} + \alpha_S$. The cross section for $m_H = 125 \text{ GeV}$ and $\sqrt{s} = 8 \text{ TeV}$ is given by:

$$\sigma_{ttH} = 0.1293 \pm \text{QCD Scale Unc.}^{+3.8\%}_{-9.3\%} \pm \text{PDF} + \alpha_S \text{ Unc.}^{+8.1\%}_{-8.1\%} \text{ pb}^{-1} \quad (2.84)$$

453 A search for the Higgs in this production mode is additionally challenging due to this large

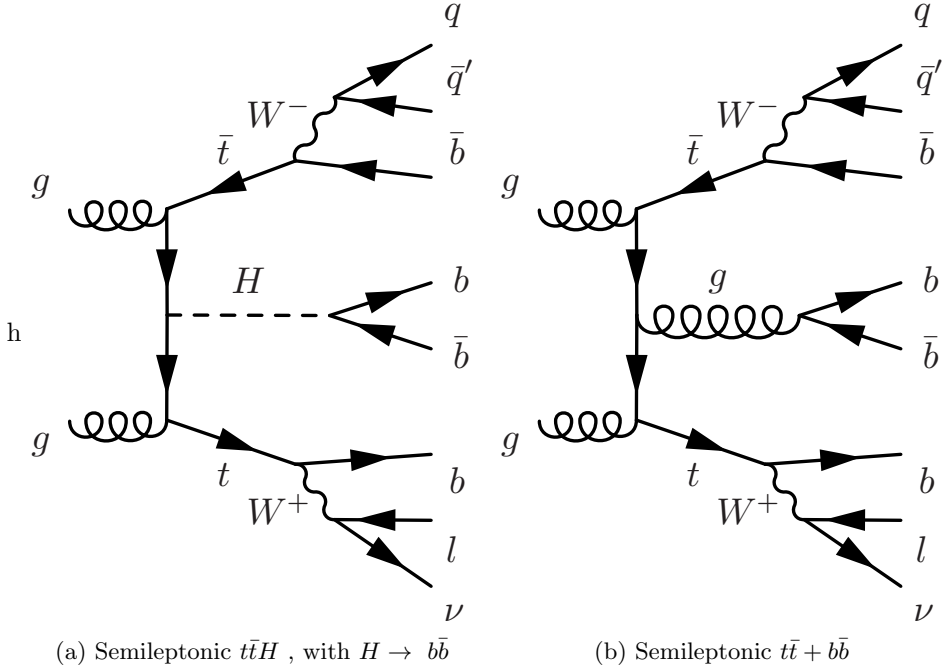


Figure 2.8: Feynman diagrams for the semileptonic $t\bar{t}H$ process and its irreducible background, $t\bar{t} + b\bar{b}$

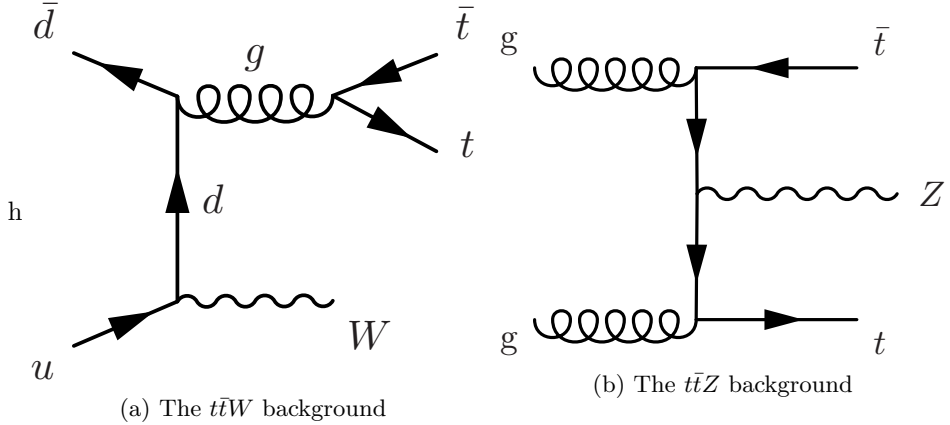
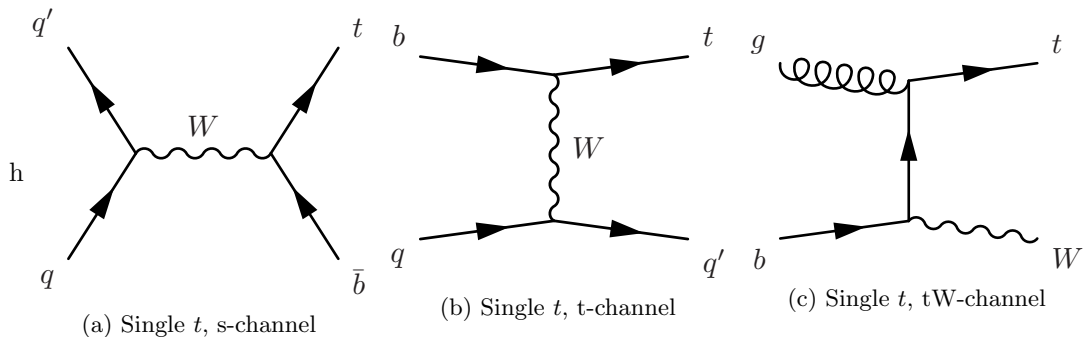
454 $\sim 10\%$ error on the theoretical cross-section. Figure 2.7 shows a Feynman diagram for this
455 process before the branching of the top-quarks or Higgs to final states.

456 When asking for the Higgs to decay to b -quark pairs, yet another complication arises when
457 trying to identify which b quarks came from a top decay or from a Higgs decay. For example,
458 in the semileptonic decay of top quarks, there will be four b quarks, and two light-flavor quarks
459 in the final state. This means there are 15 (six choose four) possibilities to associate quarks
460 to the top system. Although this is potentially constrained by b -tagging (more on this later),
461 and kinematic requirements (such as forming the top or W masses), the number of remaining
462 possibilities smears out the resolution on peaking variables such as the invariant mass of b -quark
463 pairs.

464 2.10 Background Processes to $t\bar{t}H$

465 The dominant background for $t\bar{t}H$ production of top-quark pairs with additional ISR/FSR jets,
466 $t\bar{t} + jets$. The irreducible component of this background occurs when the extra radiation
467 produces a final state with two additional b quarks, $t\bar{t} + b\bar{b}$. Figure 2.8 compares the Feynman
468 diagrams for the semileptonic decays of $t\bar{t}H$ and $t\bar{t} + b\bar{b}$.

469 Additional difficulties come from the theoretical uncertainty on the $t\bar{t} + b\bar{b}$ background [62].
470 The process has been calculated to NLO QCD in Sherpa [68] and OpenLoops [70] [71] [72].
471 These studies have shown that, depending on the event selection, and use of NLO PDF inputs,

Figure 2.9: Feynman diagrams for the $t\bar{t}W$ and $t\bar{t}Z$ background processesFigure 2.10: Feynman diagrams for the single t s,t, and tW background processes

472 the difference between LO and NLO calculations on the cross section can be anywhere from
 473 0.99% to 1.96%.

474 The light flavor component of the $t\bar{t} + jets$ background also enters in the selection when any
 475 of the jets from the $t\bar{t}$ system or extra radiation are misidentified as b jets. The cross-section
 476 for the $t\bar{t} + jets$ process is $\sim 245 \text{ pb}^{-1}$. This is a factor of 1800 compared to $t\bar{t}H$, so even if a
 477 b-tagging algorithm performs with a 1% mis-identification rate of light-jets, there will still be a
 478 large contribution from this process that will leave a very similar signature in the detector as
 479 $t\bar{t}H$.

480 The next largest background is the production of vector bosons in association with top-
 481 quark pairs, $t\bar{t}W$ and $t\bar{t}Z$. Figure 2.9 shows Feynman diagrams from these two processes. They
 482 have cross-sections of $\sigma_{ttW} = 0.249 \text{ pb}^{-1}$ and $\sigma_{ttZ} = 0.208 \text{ pb}^{-1}$, which are only a factor of ~ 2
 483 greater than the $t\bar{t}H$ process. These processes can enter the semileptonic $t\bar{t}H$ selection by a
 484 semileptonic $t\bar{t}$ decay, while the vector bosons decay to quarks, or through a hadronic $t\bar{t}$ decay,
 485 while the vector bosons decay to quarks, and in the case of $t\bar{t}Z$, one of the leptons is not
 486 identified in the reconstruction.

487 Single-top production is also an important background to consider in a search for $t\bar{t}H$ pro-
 488 duction. Figure 2.10 shows Feynman diagrams for this process. It does not have as large of a

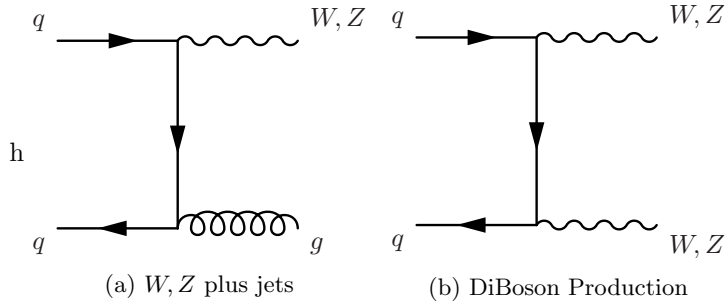


Figure 2.11: Feynman diagrams for the W, Z plus jets, and diBoson (WW , WZ , ZZ) production.

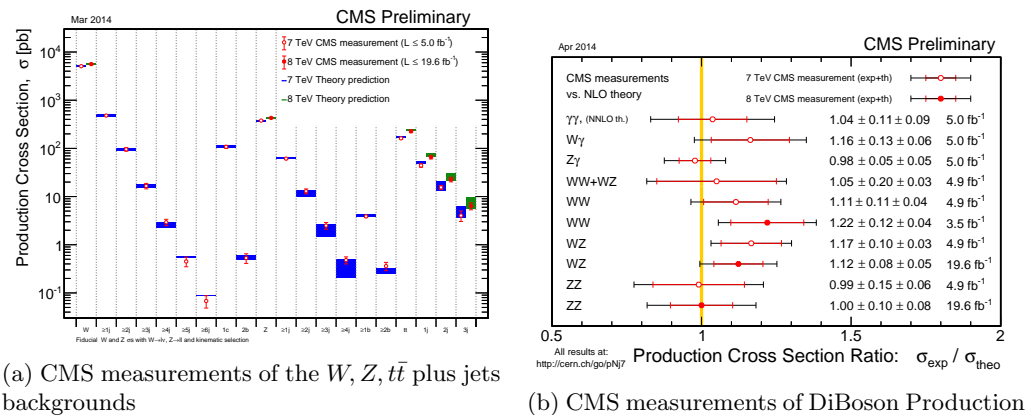


Figure 2.12: Measurements of $t\bar{t}H$ backgrounds at CMS [3]

489 contribution as the other backgrounds, since it requires additional radiation in order to have a
 490 similar final state jet multiplicity as $t\bar{t}H$. However, since a top-quark is still involved in the pro-
 491 cess, the final state kinematics of its decay products will be very similar. Single- t production has
 492 a cross section of $\sigma_t = 71.3 \text{ pb}^{-1}$, while single- \bar{t} production has a cross section of $\sigma_{\bar{t}} = 43.6 \text{ pb}^{-1}$,
 493 due to charge asymmetry of the valence quarks of the proton

The last backgrounds to consider are the electroweak production of W and Z bosons in association with jets, as well as WW , WZ , and ZZ pairs in association with jets. Figure 2.11 shows the Feynman diagrams for these processes, where the V , stands in for either a W or Z boson. For a semileptonic selection of $t\bar{t}H$ events, Z plus jets events enter from a misidentification of one of the leptons from the Z boson decay. Extra FSR/ISR radiation is also to leave a similar signature in the signal region of a $t\bar{t}H$ search, so it mainly contributes to control regions of the data.

All of these backgrounds, except for $t\bar{t} + b\bar{b}$, have been measured at CMS. With the exception of a small degree of tension in the WW cross-section measurement, all backgrounds are in good agreement with SM predictions. Figure 2.12(a) shows the results of CMS measurements on $V+jets$ and $t\bar{t} + jets$ backgrounds. Figure 2.12(b) shows the same, but for diboson production.

505 2.11 Potential BSM Effects on $t\bar{t}H$ production

506 The phenomenological motivation for the existence of physics beyond the Standard Model come
 507 from the observation of phenomenon or states of matter not described by the theory. Observations of the cosmic microwave background from the Plank telescope have estimated that only
 508 $\sim 5\%$ of the observable universe is composed of ordinary matter [73]. The remaining composition
 509 is divided between dark matter and dark energy ($\sim 27\%$, and $\sim 68\%$ respectively). Evidence for
 510 dark matter also comes from discrepancies between the observed rotational velocities of galaxies,
 511 and the observed mass distributions, suggesting the presence of an additional form of matter
 512 which does not interact electromagnetically [74].

514 Additionally, in 1998, the Super-Kamiokande experiment proved that neutrinos oscillated
 515 between flavors, implying indirectly that they also have mass [75]. This is something not de-
 516 scribed in the SM. Due to their neutral charge, these particles are extremely difficult to detect,
 517 so experiments have only been able to measure differences in the mass squared between the three
 518 mass eigenstates. In 2005, the KamLAND experiment reported $|\Delta m_{12}^2 = 0.000079 eV^2|$ [76]. In
 519 2006, the MINOS experiment reported $|\Delta m_{23} = 0.0027 eV^2|$ [77].

520 One of the largest theoretical problems with the SM comes from the mechanism which made
 521 it all possible, the Higgs. In equation 2.73 there are terms that couple the Higgs boson to itself,
 522 $-\lambda vh^3$, and $-\frac{1}{4}\lambda h^4$. When computing NLO effects, these terms lead to a divergence in the Higgs
 523 mass, when considering the effect of a loop of fermions on the Higgs propagator. The corrections
 524 are of the form $\Delta m_H = -\frac{\lambda_f^2}{8\pi^2} \Lambda_{UV}$, and are very large compared to the LO calculation. Where
 525 Λ_{UV} is the high energy cut off for the theory, which in the limit of a perfect theory, should
 526 extend to infinity. This is known as the hierarchy problem.

527 Beyond the Standard Model physics is a term that describes extensions of the Standard
 528 Model in order to describe the observed phenomenon. For the neutrino oscillations, a solution
 529 similar to CKM matrix has been proposed, the Pontecorvo Maki Nakagawa Sakata (PMNS)
 530 matrix. This proposes that the mass eigenstates of the neutrino are linear combinations of the
 531 weak eigenstates, allowing for the mixing of flavors. Current experiments now seek to measure
 532 the free parameters of this model.

533 Both the dark matter and hierarchy problems suffer in the fact that there is no clearly
 534 favored model, such as the PMNS matrix, to provide a theoretical solution. There are many
 535 models that describe this phenomenon, just none that are clearly favored. Out of the plethora
 536 of theories that attempt to solve these problems, supersymmetry (SUSY) is the most popular
 537 in the theoretical and experimental community. It suggests that there is a broken symmetry
 538 between fermions and bosons, and introduces a partner to each SM particle with a spin quantum

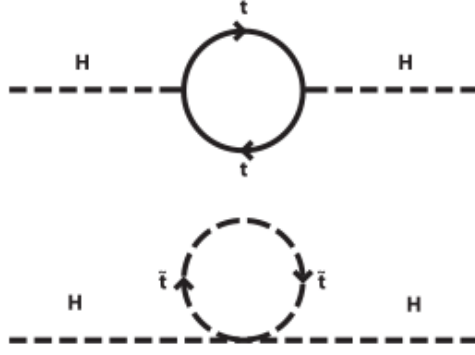


Figure 2.13: The cancellation of the divergent Higgs mass from a loop of top-quarks is cancelled by a loop of supersymmetric top-quarks, stop-quarks [4],

number less 1/2 [78]. For the hierarchy problem, this provides a set of particles to cancel out the divergences in the NLO corrections to the Higgs mass. Figure 2.13 shows the Feynman diagrams for a supersymmetric top-quark, or stop quark, that would cancel the divergent contribution from the SM top quark. Depending on the specific form of the SUSY model, the stop quarks can potentially couple directly or indirectly to the top quark, producing them at a higher rate during pp collisions. This would effect the number of observed events making it into the $t\bar{t}H$ selection.

A number of extensions to the SM also involve introducing new top-like particles into the theory. Vector-like quarks would be spin 1/2 particles that transform as triplets under the $SU(3)$ color group and whose left and right-handed components have the same color and electroweak quantum numbers [79]. These objects are common to several different types of models. Little Higgs models [80] [81] [82], models with extra dimensions [83] [84], top-color models [85], and composite Higgs models [86], include a vector-like top partner, t' that decays to a top-quark and either a Higgs, W , or Z particle. Both $t't'$ pair production and $t't$ production would yield the $t\bar{t}H$ final state, or at least one indistinguishable detector signature. $t\bar{t}H$ search can provide indirect limits on these models, by observing an excess or lack thereof of $t\bar{t}H$ events, without having to directly construct a t' resonance.

555 **Chapter 3**

556 **The Large Hadron Collider**



Figure 3.1: Aerial view of the LHC complex, spanning the French-Swiss border [5]

557 The Large Hadron Collider (LHC), is a superconducting, proton-proton, accelerator and
558 collider operated by the European Center for Nuclear Research (CERN) laboratory in Geneva,
559 Switzerland [8]. Figure 3.1 shows an aerial view of the LHC complex, with the main laboratory
560 campus being labeled as CERN, with four of the detector experiments being labeled as ALICE,
561 ATLAS, CMS, and LHCb. Three smaller experiments, not pictured, also use the LHC ring, and
562 are TOTEM, LHCf, and MOeDAL. It was designed to elucidate the mechanism of electroweak
563 symmetry breaking and explore TeV scale of particle physics. As such, it is required to produce
564 a large number of high center-of-mass energy events. The high center-of-mass energy allows the
565 creation of heavy particles, while a large luminosity allows for the creation of rare processes.
566 The number of events produced at a collider is a product of the luminosity of the collider and

567 the total cross-section for the objects being collided.

$$N_{events} = L\sigma_{event} \quad (3.1)$$

568 The cross-section, σ_{event} , can be estimated from the theory of the Standard Model as described
 569 in section 2.1 and validated by measurement at detectors, such as CMS, as shown in section 2.10.
 570 The luminosity is a control of the experiment, and for Gaussian distributed beams, is given by
 571 the equation:

$$L = \frac{N_b^2 n_b f_{rev} \gamma_r}{4\pi \epsilon_n \beta^*} F \quad (3.2)$$

572 The parameters of this equation and their value for the LHC is as follows:

- 573 • N_b - Number of particles per bunch, squared since there are two beams. The mechanism
 574 of achieving such high energies is based in Radio-Frequency (RF) cavity technology, which
 575 clusters the protons together into packets, which are all accelerated and collided together.
 576 For the LHC, $N_b = 1.15 \times 10^{11}$.

- 577 • n_b - Number of bunches per beam. The maximum design for the LHC allows for $n_b = 2808$
 578 bunches, however in practice, lower number of bunches have been run with in order to
 579 create more time between bunch crossings.

- 580 • f_{rev} - Revolution frequency of the protons in the LHC ring. This is determined by ring
 581 circumference, and for the LHC, $f_{rev} = 11.2$ kHz.

- 582 • γ_r - This is the relativistic gamma-factor, determined by the speed, and thus the center of
 583 mass energy of the collisions.

- 584 • ϵ_n - This is the normalized transverse emittance of the beam, which describes the RMS
 585 spread of the beam in its transverse plane. For the LHC $\epsilon_n = 3.75 \mu\text{m}$.

- 586 • β^* - Is the minimum of the β function, which is defined as the square of the transverse
 587 beam-size divided by ϵ_n . It is minimized at interaction regions, where the beams are being
 588 squeezed into the smallest region possible, to maximize the probability of protons colliding
 589 during each bunch crossing. For the LHC, $\beta^* = 0.55$

- 590 • F - This is the efficiency for having the two beams head-on, and is determined by the
 591 crossing angle at which the two counter-rotating beams meet each other.

592 The LHC is designed to deliver a maximum luminosity of $L = 10^{34}\text{cm}^{-2}\text{s}^{-1}$ to the CMS and
 593 ATLAS experiments, with a maximum center-of-mass energy of $\sqrt{s} = 14$ TeV.

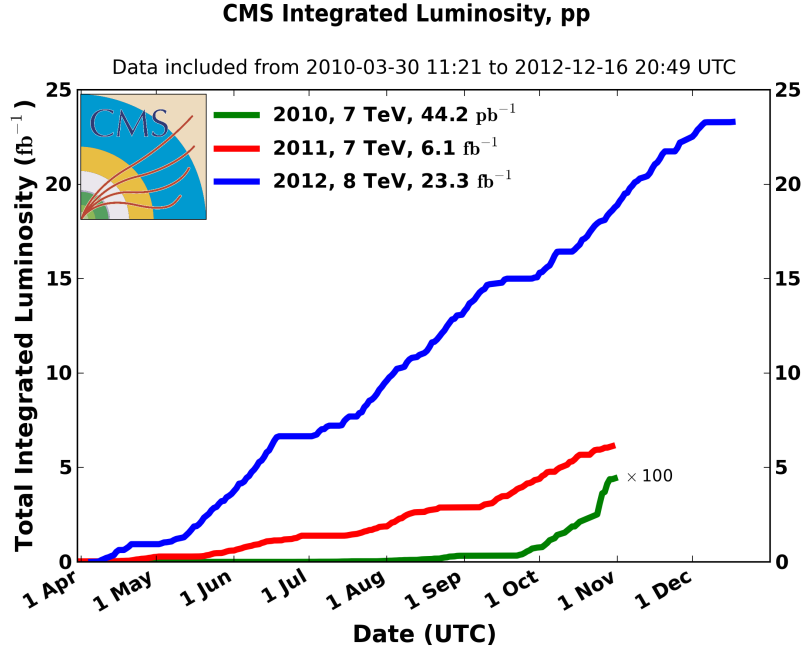


Figure 3.2: Integrated Luminosity delivered to the CMS experiment from 2010-12 [6]

594 In 2010-11, the LHC ran at center-of-mass energy, $\sqrt{s} = 7 \text{ TeV}$ and delivered $\sim 6 \text{ fb}^{-1}$ of
 595 data to the CMS experiment. In 2012, it ran at $\sqrt{s} = 8 \text{ TeV}$ and collected $\sim 23 \text{ fb}^{-1}$. Figure 3.2
 596 shows a diagram of the luminosity collected as a function of time for each year running.

597 The next sections will describe the LHC accelerator complex, the chain of events leading
 598 up to collisions of protons at the LHC, and the associated technologies that allow for the con-
 599 trol and operation of the high-energy, high-luminosity beams that allow the CMS and ATLAS
 600 experiments to search for heavy particles and rare-processes.

601 3.1 The LHC Accelerator Complex

602 The main LHC ring is a 26.7 km tunnel, that is 45 m to 170 m underneath the surface of the
 603 earth, with 1.4% slope towards Lake Leman. It extends across the French-Swiss border, into
 604 the French countryside. The tunnel was originally constructed between 1984 and 1989 for the
 605 Large Electron Positron (LEP) experiment that is famous for its precision measurements of
 606 several Standard Model parameters [8]. The choice to build the ring underground was driven by
 607 real estate costs, but the underground setting also provides natural radiation shielding from the
 608 beam-line and greatly reduces the impact of cosmic radiation on the detectors.

609 The LHC also utilizes the existing accelerator complex from the LEP experiment, which is
 610 shown in figure 3.3. The complex is composed a series of increasingly powerful accelerators that
 611 gradually increase the energy of the protons.

612 Protons are initially accelerated by the Linac2 linear accelerator up to 50 MeV [93] [94]. A

The LHC injection complex

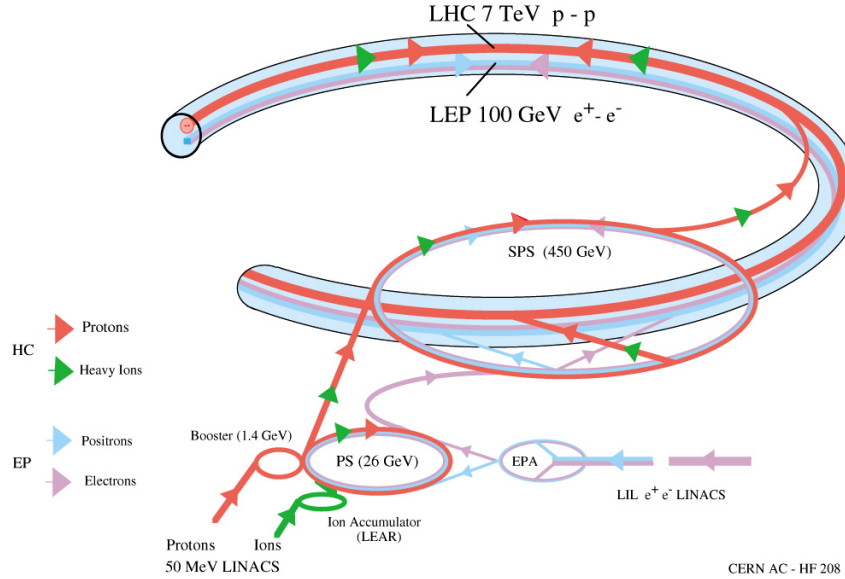


Figure 3.3: The LHC accelerator complex, taking protons from a bottle of Hydrogen at the Linac2, all the way to the LHC ring [7]

bottle of Hydrogen is attached to a duoplasmatron source. This device ionizes the Hydrogen, and creates a 300 mA beam of protons, through a high-voltage anode, and a geometry designed to focus and collimate the beam as it leaves the device. Figure 3.4(a) shows a schematic for this device, showing the gas input on the left, and proton beam leaving to the right. Figure 3.4(b) shows the actual device used in the Linac2 at CERN. The proton beam then enters the Radio-Frequency Quadrupole (RFQ) system, which accelerates and bunches the protons up to 750 keV. The RFQ is a waveguide with four flanges, which have been machined with a sinusoidal modulation in the longitudinal direction, which creates an standing electric wave in this direction, accelerating the protons. Figure 3.4(c) shows a schematic of this modulation, and figure 3.4(d) is a close-up image of this modulation in an actual RFQ. The last stage of acceleration is provided by three Alvarez tanks. Each Alvarez tank holds a series of electrically isolated cylinders, known as drift tubes, coaxial with the main tank, with gaps in between them. An alternating electric field is present in the gaps, and space between each drift tube and the walls of the tank. Protons passing through the center of the drift tubes feel no electric field, but the gaps are located such that, a proton will always see an accelerating field in the gap, and are thus receive a boost of energy from each gap as it traverses the length of the three tanks. Figure 3.4(e) shows an image of the inside of an Alvarez tank, and figure 3.4(f) shows the tanks at the Linac2 at CERN. The final product is a 180 mA, 50 MeV proton beam, which is steered to the Proton Synchrotron Booster for the next stage of acceleration.

The Proton Synchrotron Booster (PS booster) complex accelerates the protons up to 1.4

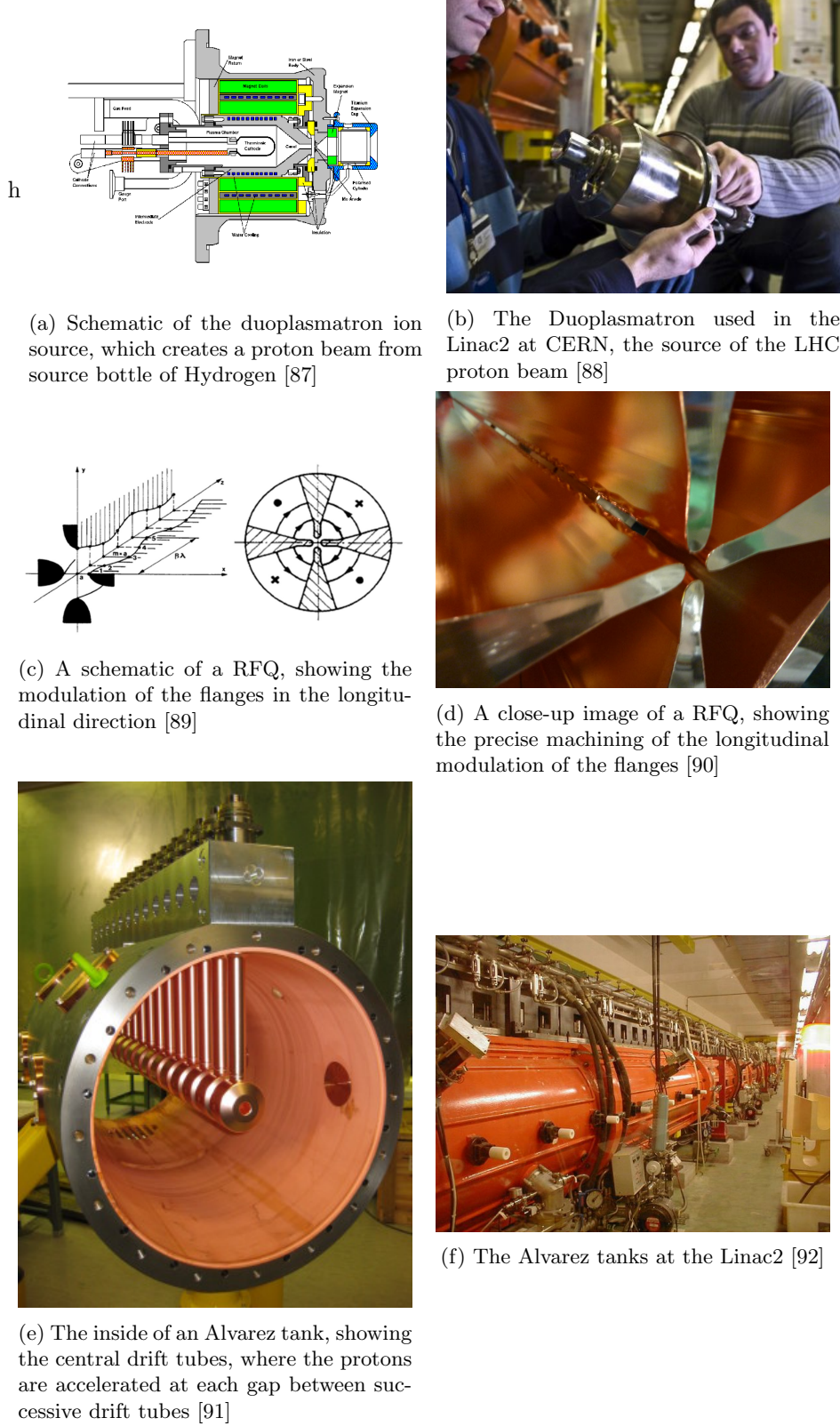


Figure 3.4: Features of the Linac2, the first stage of acceleration in the LHC injection chain

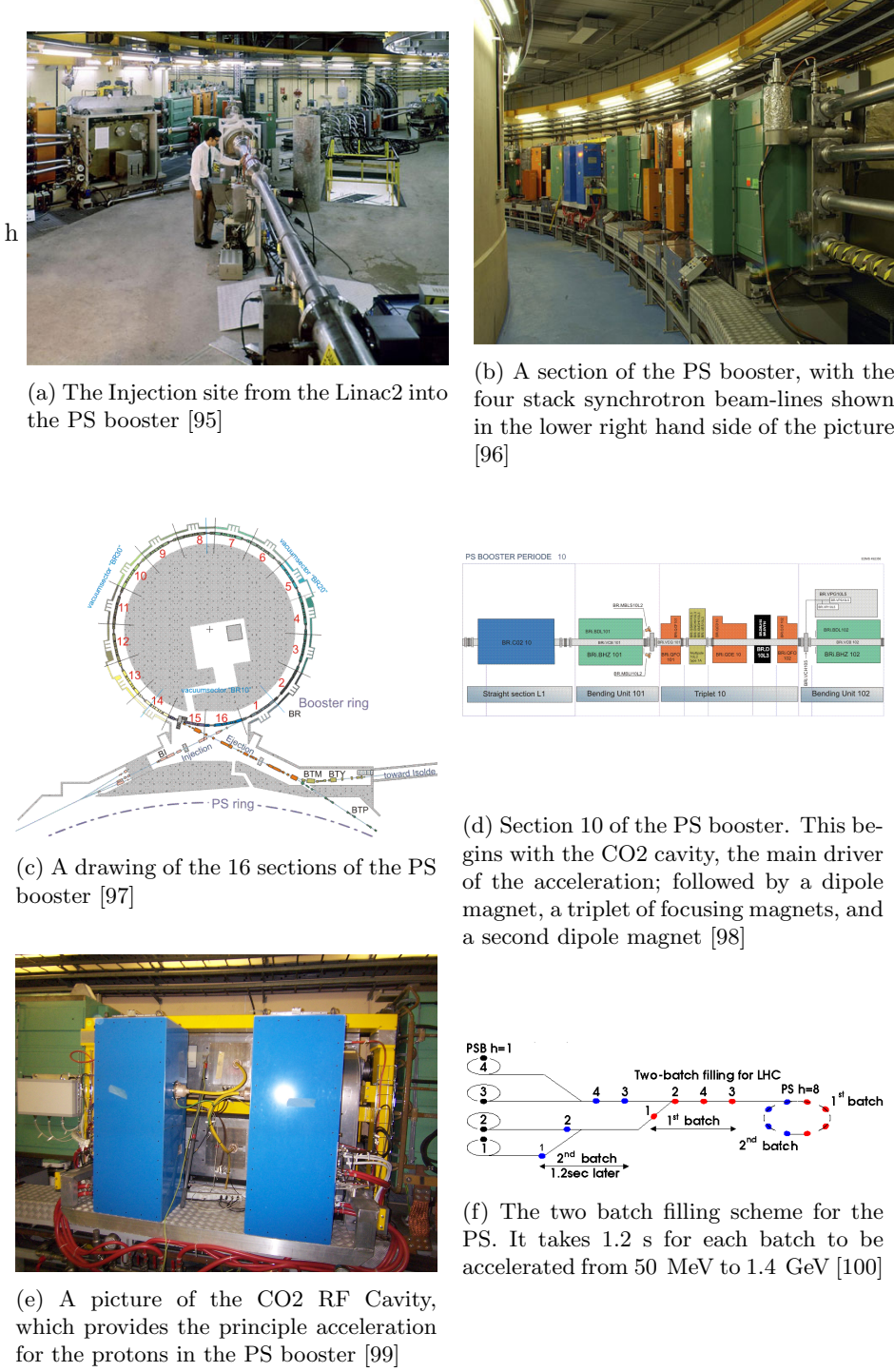


Figure 3.5: Features of the PS booster, the second stage of the LHC injection chain

633 GeV [93]. The complex takes the proton beam from the Linac2 and splits the beam into four
 634 separate, synchrotrons, stacked on top of one another. Figure 3.5(a) shows the injection site of
 635 the proton beam from the Linac2 into the PS booster. The right side of figure 3.5(b) shows the
 636 four synchrotron beam pipes stacked vertically on top one another. The splitting of the beam is
 637 done in order to reduce the effect of the space charge of the proton beam, which would increase
 638 the transverse emmitance beyond a tolerable degree. The PS booster uses thirty-two 0.87 T
 639 dipole magnets to bend the beams, and fourty-eight quadrupoles to focus the beam as it makes
 640 its way around each of the 50 m diameter rings. Each magnet is composed of a vertical stack of
 641 four magnets, one for each of the synchrotrons, and share a common yoke, allowing one power
 642 supply to provide the current to all of them in series [101]. The booster is divided into 16 arcs, as
 643 shown in figure 3.5(c). Each arc contains a bending dipole, 3 focusing quadrupoles, and a second
 644 bending dipole, followed by a straight section containing beam diagnostic, injection and ejection
 645 systems, and in three sections, the Radio-Frequency (RF) cavities, which is the mechanism of
 646 accelerating the beam [102]. Figure 3.5(d) shows the layout of the tenth arc, which also contains
 647 one of the RF cavities in the first section.

648 An RF cavity is a specially shaped, hollow conductor, that the beam passes through [103].
 649 The shape of the cavity determines the resonant frequency and harmonics (integer multiples of
 650 the fundamental frequency), of the standing electromagnetic fields that result when the cavity
 651 is driven by an alternating voltage source. The idea is to choose a resonant frequency such
 652 that the proton will always experience a positive electric field, and thus an acceleration, each
 653 time it passes through the RF cavity. This means that the revolution frequency of the proton
 654 must be equal to the fundamental frequency or harmonic of the RF cavity, $f_{RF} = n \times f_{rev}$, with
 655 $n = 1, 2, 3, \dots$. Eventually, the proton is accelerated up to an equilibrium speed and will enter
 656 the cavity just as the standing electric field is alternating through it's zero point. If arrives too
 657 early for this (moving too fast), then it will experience a negative electric force, a deceleration,
 658 which will eventually bring it back to the equilibrium revolution frequency, where it experiences
 659 zero net force. A diffuse beam of protons will be bunched into groups of protons through this
 660 effect as well, as the faster protons in the beams are decelerated, and the slower ones accelerated,
 661 until they all reach the same equilibrium revolution frequency. Driving the RF cavity with a
 662 harmonic, n , of the proton's revolution speed will thus create n bunches of protons. Each one of
 663 the potential n bunch positions is referred to as a bucket. In the case where a proton has to be
 664 accelerated through a wide range of energies, the frequency of the cavity must also increase to
 665 maintain synchronization with the proton revolution frequency.

666 Three types of RF cavities are used to accelerate the beam during each revolution. The first
 667 of the three types of RF cavities is the CO₂, with frequency range of 0.6 to 2.0 MHz and is used

668 to drive the $h = 1$ harmonic of the synchrotron, and is pictured in figure 3.5(e). The second type
 669 of cavity is the CO4 chamber, with a frequency range of 1.2 to 3.9 MHz, and drives the $h = 2$
 670 mode of the synchrotron. This second mode is capable of splitting the beam and creating two
 671 separate bunch structures. However, for LHC running, only one bunch is used, and is driven
 672 primarily by the $h = 1$ mode. The $h = 2$ mode is supplemental and is used to shape the beam. A
 673 third type of RF cavity, CO16, has a frequency range of 5 to 16 MHz, and is used to control the
 674 longitudinal shape of a bunch during acceleration. The beam leaves the PS booster and enters
 675 the PS in a two-batch filling scheme, taking only 1.2 s to accelerate a second batch of protons
 676 from 50 MeV to 1.4 GeV. This second batch enters just as the first batch has traveled to the
 677 opposite side of the PS ring. A schematic of this process is shown in figure 3.5(f). To achieve
 678 the 25 ns bunch spacing design of the LHC, only 6 bunches of proton beam need to be delivered
 679 to PS. This is achieved by either using a 4+2 or 3+3 filling scheme, in terms of the number of
 680 proton bunches delivered from the four possible synchrotrons.

681 The next stage is the Proton Synchrotron (PS), which will boost the protons up to 25
 682 GeV [93]. The layout is shown in figure 3.6(a). The ring has a circumference of 628 m, and
 683 uses 100 dipole magnets and 177 higher-order focusing magnets, to steer the beam around the
 684 ring. Figure 3.6(b) shows a picture of one of the dipole magnets used at the PS. In addition
 685 to providing acceleration up to 25 GeV, the PS forms the basis of the bunch structure that is
 686 eventually used in the LHC. The $h = 7$ harmonic is used to capture the 6 bunches of protons
 687 delivered from the PS booster, leaving a gap in the place of a seventh bunch. The beam is then
 688 split into three, by using three different RF cavities tuned to the $h = 7, 14, 21$ modes of the PS.
 689 Figure 3.6(c) shows a simulation of a proton bunch being divided into three over the course of
 690 25 ms. The $h = 21$ mode is then used to accelerate the protons to from 1.4 to 25 GeV using the
 691 20 MHz RF cavity. Each bunch is then split twice, using the $h = 21, 42, 84$ synchrotron modes,
 692 to create 72 bunches, spaced 25 ns apart, with a 320 ns gap for the 12 unused buckets of the
 693 $h = 84$ harmonic. This process is simulated in figure 3.6(d), over the course of 125 ms. The 320
 694 ns gap is created to account for the rise time of the kicker magnet, which ejects the beam out of
 695 the PS into the SPS. The entire splitting process is summarized in figure 3.6(e). For the case of
 696 50 ns bunch spacing, the final stage of splitting is not performed, and the $h = 21, 42$ modes are
 697 used to split the beam. Finally, in order to fit the bunches into the 200 MHz RF acceleration
 698 scheme of the SPS, the bunch length must be compressed from 11 ns to 4 ns. This is achieved
 699 by rotating the beam in the energy vs time phase space by sequential increases in voltage to
 700 the 40 MHz $h = 84$ mode, followed by an increase to the 80 MHz $h = 168$ mode. Figure 3.6(f)
 701 shows the result of this rotation - a distortion free ellipse with a smaller 4 ns spread, but a larger
 702 spread in the energy spectrum of the proton beam.

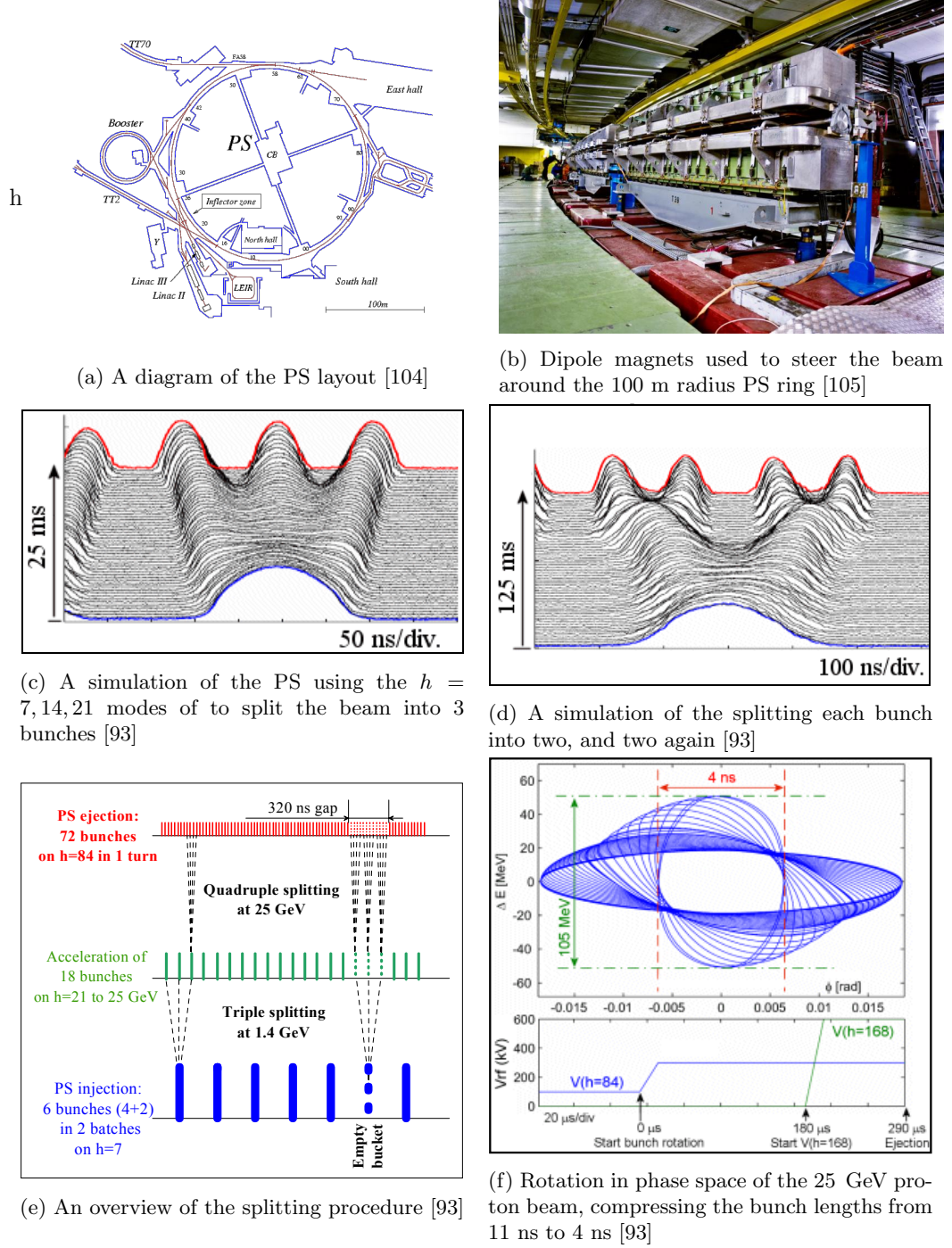


Figure 3.6: Features of the PS, the third stage of the LHC injection chain

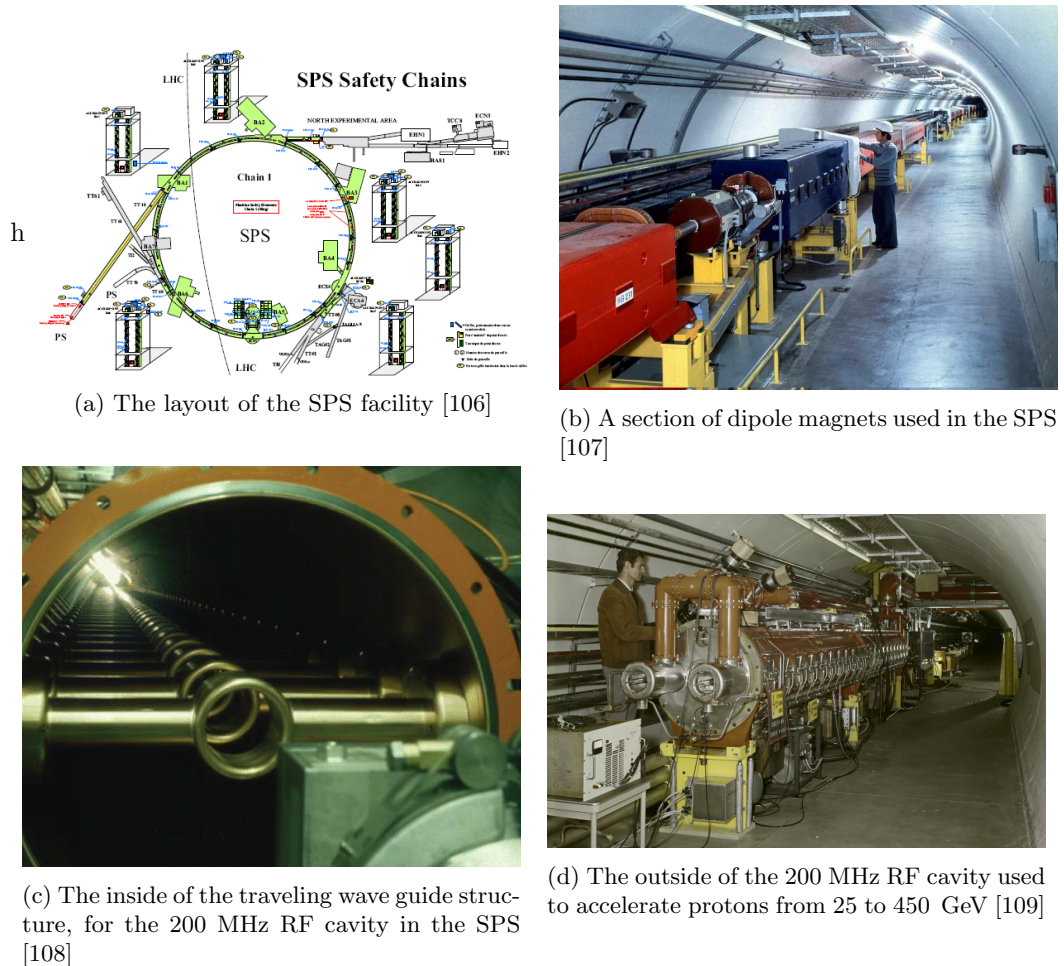


Figure 3.7: Features of the SPS, the fourth and final stage of the LHC injection chain

703 Next, the protons arrive at the Super Proton Synchrotron (SPS), where they will be acceler-
 704 erated to 450 GeV. The SPS is the last stage of acceleration before the protons are injected
 705 into the LHC. The layout is show in figure 3.7(a). It has a circumference of 7 km, and steers
 706 the proton beam with 744 dipole magnets, with 573 higher-order focusing magnets [110]. Figure
 707 3.7(b) shows one of the dipole magnets in the SPS tunnel. Like all the other synchrotrons in
 708 the injection chain, the acceleration is provided by RF cavities. A 200 MHz system of RF cavi-
 709 ties capture and fill the SPS by using 2-4 batches of 72 bunch proton beams from the PS [93].
 710 Although the relative change in frequency is small, the large degree of acceleration necessitates
 711 the use of a tunable RF cavity. The 200 MHz system has 2 sections of 4 traveling wave cavities
 712 in series, and another 2 sections of 5 cavities in series. Figure 3.7(c) shows the inside of this
 713 structure, which uses drift tubes to accelerate protons in the gaps between tubes, with horizon-
 714 tally mounted bars, spaced 374 mm [111] apart, determining the periodicity of the resonant RF
 715 field that builds up inside. The outside of the structure is shown in figure 3.7(d). An additional
 716 800 MHz system is used to control the transverse emmitance. It is also used to stabilize the
 717 beam-line and prevent coupled-bunch instabilities [93].

718 Finally, protons are injected into the LHC ring in one clockwise, and another counter-
 719 clockwise rotating beams. In order to work in the limited space of the existing LEP tunnel,
 720 the two beams are contained within a single mechanical and cryostat structure, with a dual-bore
 721 design for each of the beams. Here, each proton beam is accelerated to their final energy of 7
 722 TeV, moving at 99.9999991% the speed of light, before they meet head on, producing 14 TeV
 723 center-of-mass collisions.

724 The LHC ring itself is divided into eight octants, with eight straight sections that are located
 725 in front and behind each of the eight collision points, where the beams are made to cross and
 726 collide, as shown in figure 3.8. These crossings are known as interaction regions (IRs). Four
 727 of these points are currently being used by experiments. TOTEM has detectors on either side
 728 of the CMS experiment at one interaction region, known as point 5 (P5). LHCf has detectors
 729 on either side of ATLAS at point 1 (P1). MOeDAL has detectors near LHCb at point 8 (P8)
 730 and the ALICE detector is located at point 2 (P2). The following sections will cover the RF,
 731 magnet, cryogen, and vacuum technologies used in the LHC ring.

732 3.2 LHC Magnets

733 Several types of magnets are used in order to properly circulate and focus the proton beam as
 734 it makes its way around the 26.7 km long tunnel. A complete list of all types, can be found
 735 in the technical design report [112], as well as through CERN’s outreach web resources [113].

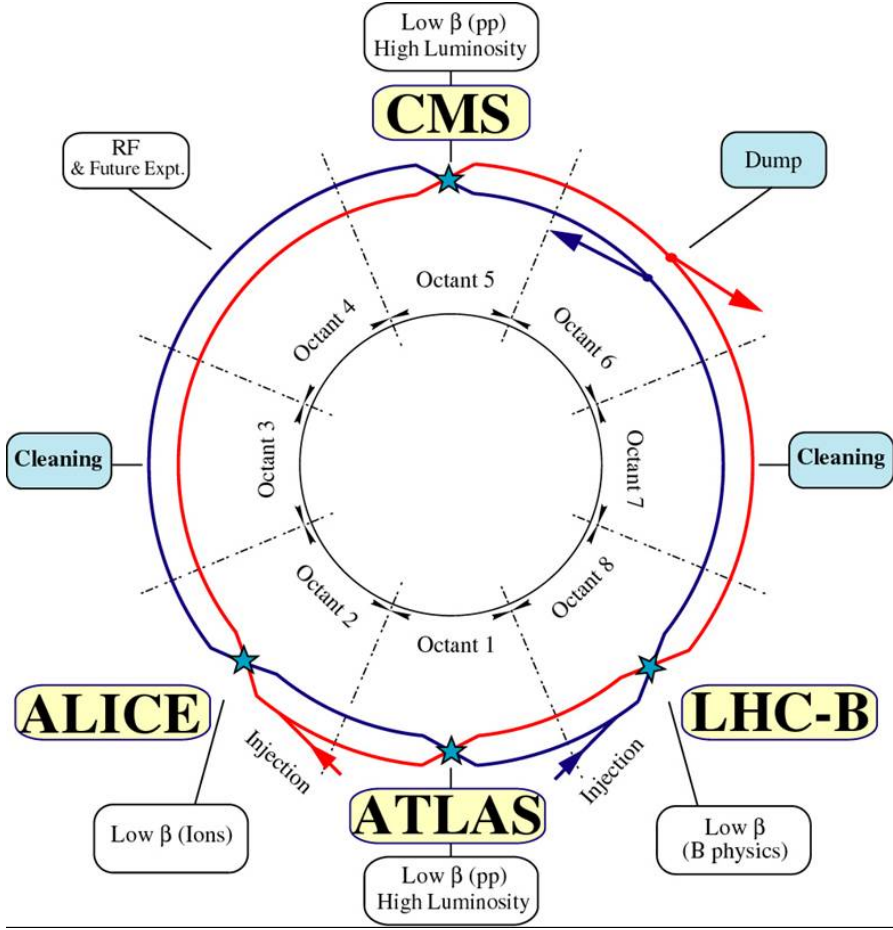


Figure 3.8: The LHC ring is divided into eight octants [8]

This section will give an overview of the a few of the critical subsystems: the septum and kicker magnets used for injection from the SPS, the dipole magnets used for bending the beam around the circumference of the ring, and the higher-order-pole magnets that are used for focusing the beam.

The injection and extraction of proton beams from one synchrotron to another involves three types of magnets, septums, kickers, and bumpers. Septum magnets contain a partition, or a septum, that provides a boundary between a high magnetic field region and a near-zero magnetic field region and are operated in DC or a slow-pulsed mode [114]. In case of injecting a beam of protons into a synchrotron, the target beam-pipe of the synchrotron passes through the low-field region, so the trajectory is unaffected by the high-field region, which bends the injection beam towards the synchrotron aligning it horizontally, with the target beam. The kicker magnet, is a fast-pulsed magnet and provides the timing selection in order to make a final vertical bend into the synchrotron orbit, and into the correct basket of the synchrotron bunch train [9]. Finally, bumper magnets make small bends to the beam and align it with the injection site. Figure 3.9 shows a schematic for this process, where a transfer line brings protons to a septum, which bends the beam to a kicker, which makes the final corrections to match the synchrotron orbit. For

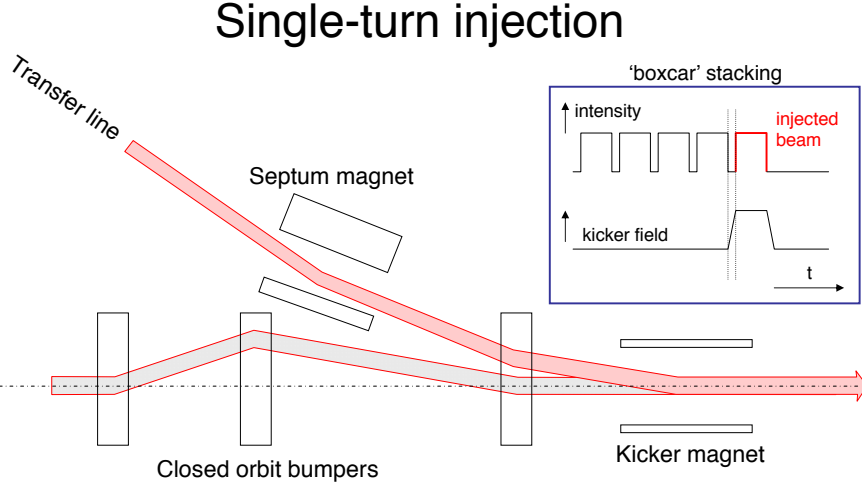


Figure 3.9: The single turn injection scheme. A septum magnet makes the initial alignment. The kicker magnet times the injection and makes the final alignment. Bumper magnets align the LHC beam with the injected beam [9]

752 extraction, the kicker magnet quickly displaces a portion of the beam, which is steered away by
 753 the septum, while the original beam passes through its low-field region unaffected.

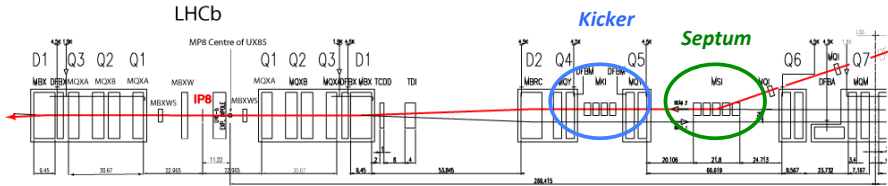


Figure 3.10: Layout of Interaction Region 8, where one proton beam is injected into the LHC ring. A transfer line from the SPS brings a proton in from the right. In green, a septum magnet aligns the beam horizontally with the LHC. In blue, a kicker magnet makes the final vertical alignment into the LHC, and is timed to fill one of the 400 MHz buckets of the RF capture system [8]

754 At the LHC, beam is injected at Interaction Regions (IR) 2 and 8 [8]. Two transfer lines bring
 755 the beam extracted from the SPS to ~ 150 m of the LHC ring. Five Labertson-type septum
 756 magnets, of field strength ~ 1 T, are used to deflect each of the transfer line beams 12 mrad
 757 to align the transfer beam horizontally with the LHC orbit. Then, four ~ 0.12 T MKI kicker
 758 magnets quickly deflect the beam 0.85 mrad to close the orbit with the LHC ring. Figure 3.10
 759 shows the layout of the injection point at IR 8. The green circle encloses the septum structure,
 760 which provides the horizontal alignment, and the blue encloses the kicker structure, which makes
 761 the final vertical alignment and synchronizes the injection of the beam into the LHC. The rise
 762 time for the field provided by the kicker magnets in the LHC and SPS determine the final bunch
 763 structure of the LHC. Figure 3.11 extends figure 3.6(e) showing how the rise times of the kickers
 764 that inject, or eject beam create gaps in the bunch structure of the LHC. The initial filling of
 765 the PS with 6 batches of protons from the PSB, leaves one initial bucket unused in the PS. After

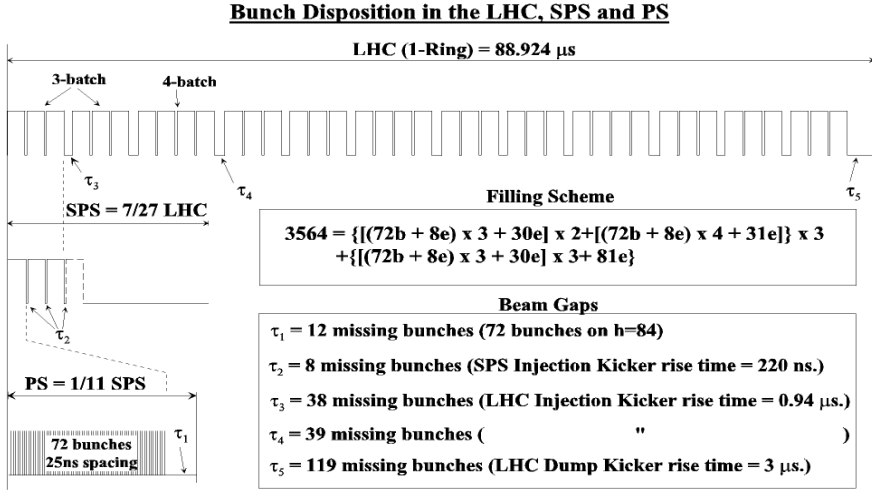


Figure 3.11: The initial filling of 6 batches of protons from the PSB to the PS, leaves 12 empty buckets in the PS bunch structure. The rise time of the SPS magnet creates an additional gap in the SPS bunch structure. Additional gaps emerge due to the rise time of the LHC injection and dumping kicker magnets [8]

766 the splitting of the beam into the 25 ns bunches, there 12 empty buckets at the of the PS bunch
 767 train. The SPS is filled with three to four of these trains, leaving an additional 8 25 ns buckets
 768 unfilled due to the 220 ns rise time of the SPS kicker magnet. These three to four trains are
 769 then injected into the LHC, where there are 38 or 39 bunch gaps due to the LHC injector 0.94
 770 μ s rise time. At the end of a full LHC orbit, 119 buckets are left empty to allow for the rise time
 771 of the beam dumping kicker magnet, used to remove beam from the LHC.

772 Once the beam is injected, the curved path around the circumference of the LHC is main-
 773 tained via 1232 superconducting dipole magnets. The superconducting material niobium-titanium,
 774 NbTi, is cooled to 1.9 K in order to produce the 8.33 T field. Figure 3.12(a) shows a cross-section
 775 view of one of the LHC dipoles. The dual-bore design of the beam-pipe is enclosed by an iron
 776 yoke, that serves as the cold mass to maintain the superconducting temperature, and provides
 777 a 195 mm gap between each beam. A close up picture of the non-magnetic collar and supercon-
 778 ducting coils are shown in figure 3.12(b). A simulation of the magnet in figure 3.12(c) shows the
 779 homogenous, vertical magnetic field produced in the center of the coil. Diagram 3.12(d) shows
 780 an exaggerated view of the 2812 m radius curvature of each dipole. However, since each dipole
 781 is only ~ 14 m in length, this curvature is hardly noticeable, as shown in a photo of an actual
 782 dipole magnet in a staging area at CERN, awaiting installation in figure 3.12(e).

783 Quadrupole, sextupole, octupole, and other multipole magnets are used to focus a single
 784 beam, as well as squeeze the two beams together. There are 392 quadrupole magnets on the
 785 LHC ring, each controlling the height and width of the beam. Figure 3.13(a) shows a schematic
 786 of a dual-bore quadrupole magnet, and figure 3.13(b) shows an actual quadrupole in a staging
 787 area before installation. Quadrupole magnets use four sets of coils to create a magnetic field that

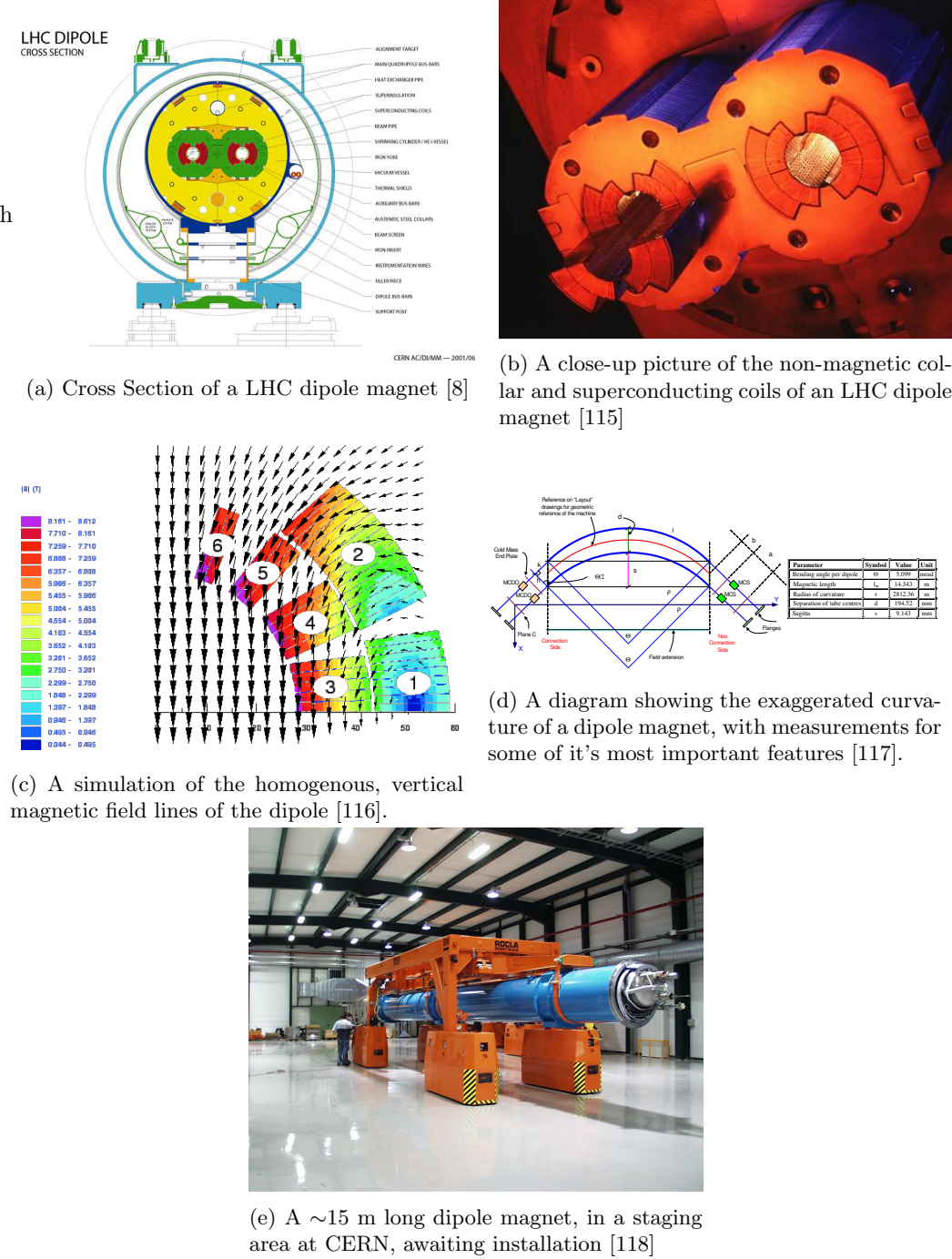


Figure 3.12: Features of the dipole magnets used in the LHC

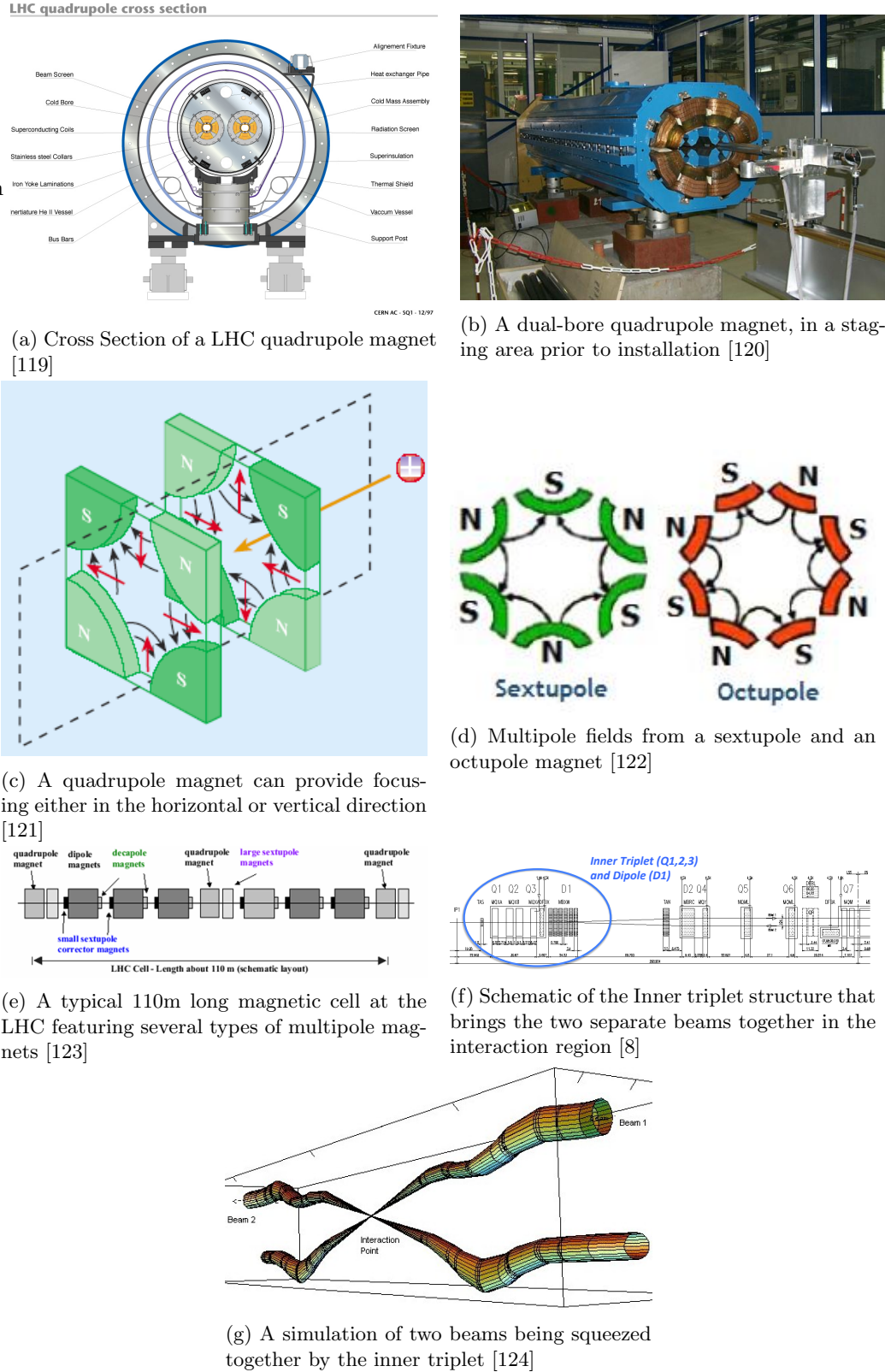


Figure 3.13: Features of the dipole magnets used in the LHC

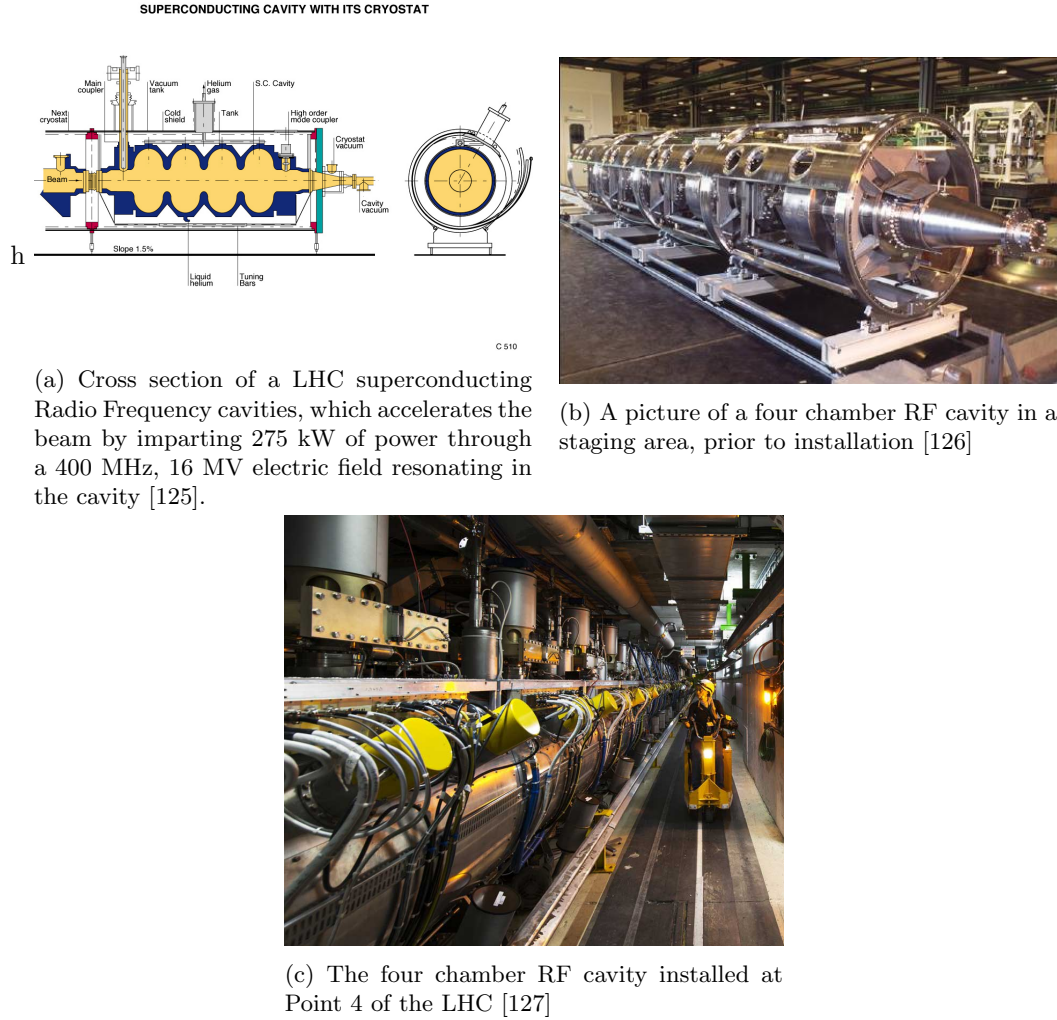


Figure 3.14: Features of the 400 MHz superconducting RF system used in the LHC

either squeezes the beam horizontally or vertically, as shown in figure 3.13(c). Finer corrections to the beam shape are made with the multipole magnets, since they are able to compress the beam from more than two axes. Figure 3.13(d) shows the fields lines of a sextupole and octupole magnet. A typical cell of magnets, 110 m long, in the LHC octant is shown in a diagram in figure 3.13(e), where the dipole, quadrupole and higher order magnets work in series to confine the protons to the LHC ring. Finally, a set of single bore magnets, known as an inner triplet, bring the two beams together into an interaction region. Figure 3.13(f) shows the arrangement of magnets that squeeze the beam together, while figure 3.13(g) shows a simulation of the beams being brought together to collide in the interaction region.

3.3 LHC RF Technology

The LHC uses a 400 MHz superconducting RF cavity system to capture and accelerate the beam from 450 GeV to 7 TeV [8]. Two independent system are used to provide 8 MV of RF voltage

at injection at 16 MV during equilibrium at 7 TeV and deliver 275 kW of power to each beam. This is provided by 16 niobium sputtered cavities, housed in 4.5 K refrigeration units, known as cryo-modules, at Point 4 of the LHC octant. The superconducting material covering the inside of the cavity has near-zero resistivity, which dissipates much less power and has a much narrower resonance width, or Q-factor, than a cavity made from normally conducting material. Figure 3.14(a) shows a schematic of a four cavity cryo-module. The beam pipe passes through the center of each chamber and longitudinal (left to right in the diagram) electric fields accelerate the protons each time they circulate the LHC ring. Figure 3.14(b) shows an actual four cavity module in a staging area prior to installation. In this picture, the resonance cavities are concealed underneath the cylindrical housing of the vacuum tank and cryostat. Figure 3.14(c) is a picture of the module installed at Point 4. The thin cylindrical structures extending off the top is the LHe intake valve and quench system. The thicker cylindrical structures are the waveguides that couple the cavities to the source of the electric field, the klystrons.

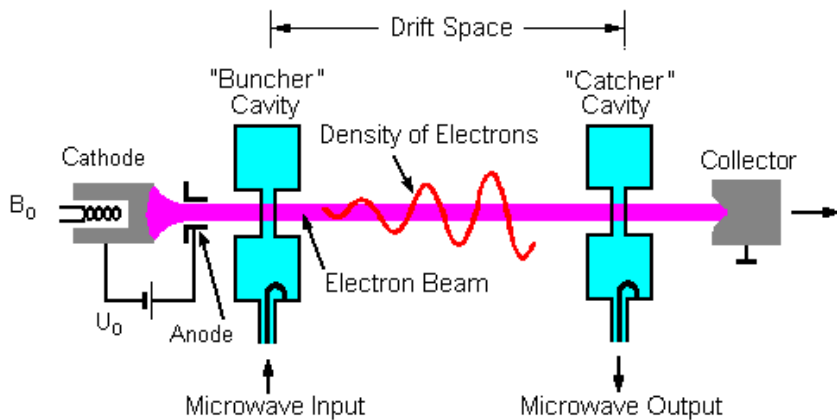


Figure 3.15: A klystron uses a weak RF signal coupled to a resonance cavity to bunch an electron beam, which in turn creates an amplified RF signal as it passes through a second resonance cavity tuned to the same frequency [10].

A Klystron is the source of RF power that builds up as a resonance in the cavities that accelerate the protons. Figure 3.15 shows a diagram of the basic operating principle. The device uses an anode to accelerate the thermionic emission of electrons off of a cathode material into one or more bunching cavities tuned to the frequency the device is designed to produce. This cavity is driven with a weak RF source, that groups electrons into bunches. Just as discussed for protons earlier, when electrons arrive at the entrance of the cavity at just the right time, it will experience the zero-point of the oscillation of the resonating electric field. If it arrives early or late, it is accelerated or decelerated and thus bringing it closer to its neighbors, and increasing the density of the beam. After passing through multiple chambers, the tightly bunched electrons enter a catcher cavity tuned to the same resonance frequency. As the electrons pass through at

823 this resonance frequency, standing electric waves are excited and quickly build up in the catcher
 824 cavity. The electron beam is thus used to amplify the original RF signal in the catcher cavity,
 825 which is then transported via waveguide to power the RF cavity used to accelerate the proton
 826 beam-line.

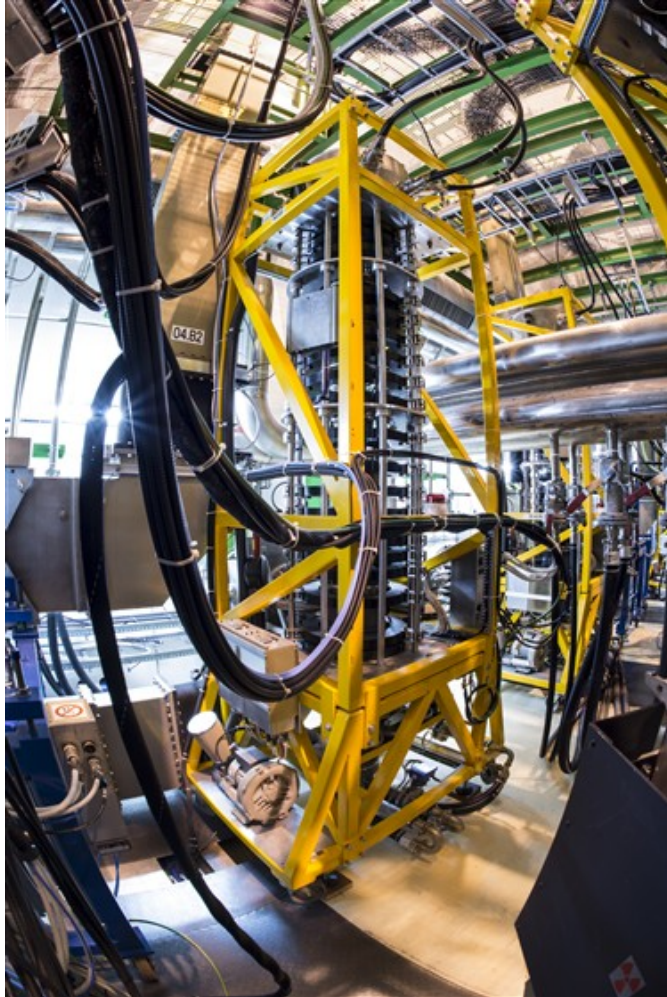


Figure 3.16: One of sixteen 300 kW, 400 MHz klystrons that power the superconducting RF cavities that accelerate the proton beam [11].

827 At the LHC, 16 400 MHz, 300 kW klystrons, work together to provide 4800 kW of power
 828 to the superconducting RF cavities [8]. They are also located at Point 4, in the UX45 service
 829 cavern adjacent to the RF cavities, about 6 m below the beam-line. An average of 22 m of
 830 waveguide is used to transport the power generated by the klystrons to the RF cavities. Figure
 831 3.16 shows a klystron installed at the LHC, and like most modern klystrons, it also utilizes a
 832 multi-bunching chamber design.

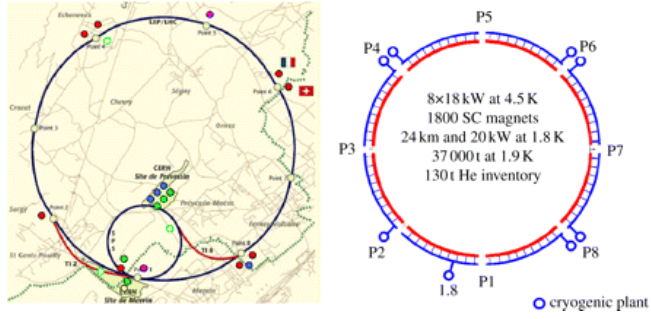


Figure 3.17: Layout of the five cryogenic islands, which are home to the eight facilities that provide liquid helium to the LHC [12]



(a) The compressor station for the 4.5 K refrigeration system

(b) The 4.5 K refrigeration system cold box, containing heat exchanging fins and turbines to cool the He

Figure 3.18: Features of the 4.5 K refrigeration system [13]

3.4 The LHC Cryogen System

The LHC is the largest cryogenic system in the world [128], as its operating temperature is 1.8 K, in order to produce the high-magnetic fields needed by the dipole magnets. Additionally, the acceleration mechanism, the RF cavities, are also superconducting, and must be cooled to 4.5 K. Over 120 tons of Helium are used as the cryogenic medium, since once it is cooled below 2.17 K, it becomes a superfluid, a phase of matter with a high thermal conductivity, making it ideal for refrigeration. Cryogenic and auxiliary equipment are concentrated into 5 "cryogenic islands" at Points 1,2,4,6, and 8 [8]. As shown in figure 3.17, Points 4,6, and 8 house two facilities each, making a total of eight, one for each octant of the LHC arc.

At each cryogenic plant, He is cooled to 80 K by circulating it through refrigeration equipment with liquid nitrogen in the heat exchangers[128]. Next, the He is brought to 4.5 K with refrigerators recovered from the LEP experiment [129]. The He gas is first compressed and allowed to expand, where it is cooled by losing energy through mechanical turbo-expanders that run at up to 140,000 rpm on helium-gas bearings, as shown in figure 3.18(a). The He is then liquified after passing through a vacuum sealed box containing heat exchangers and more turbo-

848 expanders [13]. The compressor for this system is pictured in figure 3.18(b). Finally, the liquified
 849 He is brought to 1.8 K with a refrigeration unit that uses a cold compression train to decrease
 850 the saturation pressure, and thus temperature as well.

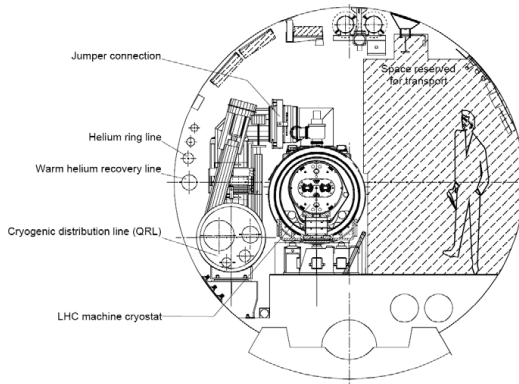


Figure 3.19: Cross section schematic of the cryogenic distribution system in the LHC tunnel [8]

851 In the LHC tunnel, a cryogenic distribution line runs parallel to the machine [129]. It consists
 852 of eight 3.2 km long cryostats, that contain the equipment to supply and recover helium with
 853 temperatures ranging from 4 K to 75 K. A total of 310 service modules, are used to control the
 854 system and provide safety mechanisms against pressure buildup and magnet quenching. Figure
 855 3.19 shows a cross section of the cryogen distribution system in the tunnel.

856 3.5 The LHC Vacuum System

857 The LHC is also the largest operational vacuum system in the world and is capable of achieving
 858 pressures lower than outer space [130]. Three different types of vacuum systems are used: one
 859 for insulating the helium distribution lines, another for insulating the dipole magnets, and a final
 860 ultra-high vacuum system for the beam pipe [8].

861 The vacuum systems for insulating the helium distribution and dipoles involves some 104
 862 km of piping and over 250,000 welding joints [130]. Pressure here is required to be kept at 10^{-1}
 863 mbar, but at cryogenic temperatures, pressures tend to equalize at a much lower level, to 10^{-6}
 864 mbar ($\sim 10^{-9}$ atm) [8].

865 The most stringent requirements come on the vacuum of the beam-pipe. The beam must
 866 minimize the number of interactions it has with any particles outside of the interaction region.
 867 A pressure of 10^{-10} to 10^{-11} mbar are maintained in the 54 km of beam-pipe [130]. Weeks of
 868 cryogenic pumping, eventually condenses gas trapped in the beam-pipe into a liquid that can be
 869 absorbed by the walls of the beam-pipe. The inside beam-pipe is also coated with a thin layer



Figure 3.20: Beam screen for the LHC, with slits to allow for easy pumping of residual gas molecules in the beam-pipe [14].

870 of a special substance developed at CERN, a titanium-zirconium-vanadium alloy, which absorbs
871 residual particles when heated. 780 ion pumps are used to remove the noble gases and methane,
872 which do not interact with the substance, which acts as its own distributed pumping system.
873 Room-temperature sections of the beam-pipe are also heated to 300^{deg} to be baked-out from the
874 outside. This is done to periodically remove any material which may have settled and become
875 trapped. Additionally, the beam-pipe is designed with a racetrack shape, which optimizes the
876 available aperture while leaving space for the cooling tubes, as shown in figure 3.20. Slits also
877 allow for gas molecules to be easily pumped out from inside its volume.

878 **Chapter 4**

879 **The Compact Muon Solenoid**

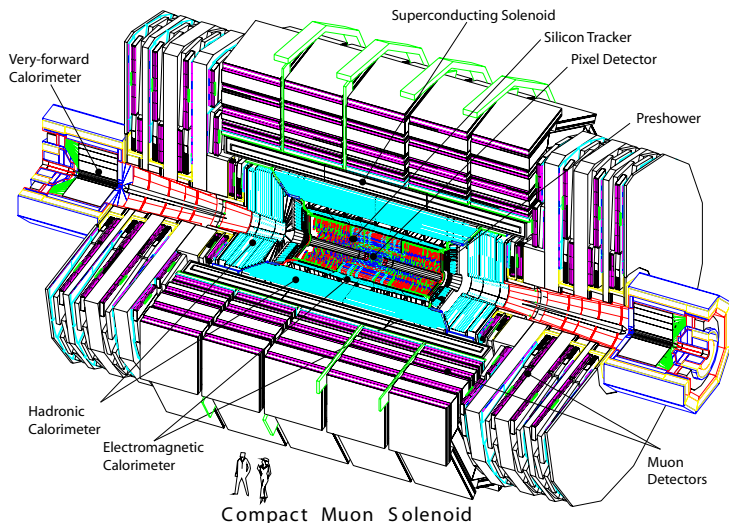


Figure 4.1: A cutaway diagram of the CMS detector. Two humans are present at the bottom of the image to provide scale [15].

880 The Compact Muon Solenoid (CMS) experiment is a general-purpose particle detector ca-
881 pable of performing a wide range of physics measurements at the TeV energy scale. It provides
882 hermetic, 4π , coverage surrounding the interaction region on Point 5 of the LHC octant, and
883 is capable of identifying and reconstructing charged and neutral hadrons, photons, electrons,
884 and muons directly. Tau leptons, are measured indirectly through a careful reconstruction of
885 its decay products. The hermetic coverage allows the detection of neutrinos by measuring a
886 momentum imbalance in a given collision. The detector is assembled in five sections and weighs
887 over 14,000 tons. The "Compact" part of the experiment's name comes from its relatively small
888 volume for a modern particle detector, with length of 28.7 m and a diameter of 15.0 m. Ironically,
889 this is as tall as most 4-5 story buildings and weights as much as \sim 7000 cars. Figure 4.1 shows
890 a cutaway drawing of the CMS detector. Unless otherwise stated, all technical information on

891 the CMS detector is taken from [15].

892 A right-handed coordinate system is used to measure particle positions within the detector.

893 The origin is centered at the nominal interaction point with the \hat{x} direction pointed towards the
 894 center of the LHC ring, the \hat{y} direction towards the sky, and the \hat{z} direction pointed counter-
 895 clockwise along the LHC ring towards Point 2 and the ALICE experiment. In the much more
 896 natural polar coordinates, \hat{r} , points radially outward from the interaction point, the azimuthal
 897 angle $\hat{\phi}$ is measured as the angle relative to the \hat{x} axis, and the polar angle, $\hat{\theta}$, is measured as
 898 the angle relative to the \hat{z} axis. An important Lorentz invariant position variable is the rapidity,
 899 y , and its approximation in terms of the polar angle, the pseudorapidity, η :

$$\begin{aligned} y &= \frac{1}{2} \ln \left(\frac{E + p_z c}{E - p_z c} \right) \\ \eta &= -\ln \left(\tan \frac{\theta}{2} \right) \end{aligned} \quad (4.1)$$

900 The psuedorapidity is useful since it is an approximately Lorentz invariant version of polar angle,
 901 which allows for a more intuitive understanding of the distribution of particles when boosting
 902 into different measurement reference frames. The component of the momentum transverse to
 903 the beam-line, p_T is the most common form of measuring the momentum, and is defined as

904 $p_T = |p| \cos \phi$.

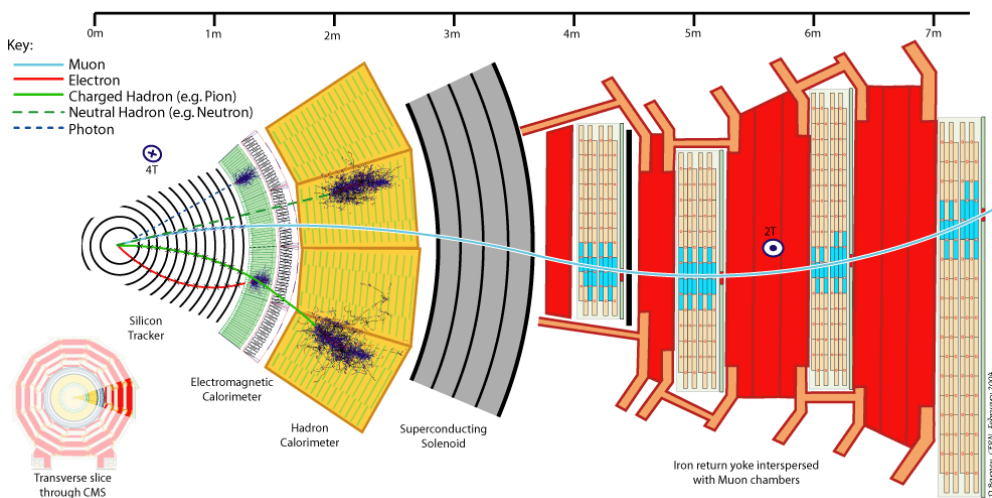


Figure 4.2: A slice of the CMS detector showing how various particles interact and deposit energy. The trajectory of charged particles is measured in the tracker; electrons and photons deposit most of their energy in the ECAL; charged and neutral hadrons deposit most of their energy in the HCAL; the muon chambers measures the trajectory of muons or long-lived charged particles [16].

905 CMS is composed of a system of sub-detectors, each specialized in measuring a certain type or
 906 characteristic of a particle. They are arranged approximately as concentric cylinders of increasing
 907 radius, wrapped around the interaction region of the pp collisions and an analogy is often made

908 between the layers of sub-detectors being similar to the layers of an onion. The closest sub-
 909 detector to the interaction region is the tracker system. It is an all silicon pixel and strip detector,
 910 with a high precision position resolution, which is used to identify the trajectory of charged
 911 particles close to the primary vertex of a collision. The Electromagnetic Calorimeter (ECAL) is
 912 the next layer, and is used to absorb energy of electromagnetically interacting particles. It uses
 913 lead-tungstate (PbWO_4) crystals which act as both the absorbing and scintillating medium for
 914 energy deposited by charged particles and photons as they pass through this sub-detector. The
 915 Hadronic Calorimeter (HCAL) uses brass and steel tiles to absorb energy and induce hadronic
 916 interactions, while a plastic scintillator material layered between the absorber tiles samples the
 917 energy of hadrons. The tracker, ECAL, and HCAL systems are all contained in the bore of the 3.8
 918 T solenoid from the CMS namesake. This device bends the trajectory of charged particles as they
 919 traverse the detector, and the curvature of this bend is used to obtain information on the charge
 920 and momentum of the measured particle. The muon system sits outside of the solenoid structure,
 921 and uses three types of detection systems: drift tubes (DTs), resistive strip chambers (RPCs)
 922 and cathode strip chambers (CSCs), which provide excellent timing and position resolution.
 923 The return yoke structure of the magnet also provides the mechanical support for the muon
 924 chambers. Figure 4.2 shows a slice of the CMS experiment showing how various particles interact
 925 and traverse the different sub-detector regions, as described above.

926 At center-of-mass energy of $\sqrt{s} = 14 \text{ TeV}$, the expected event rate is approximately 10^9
 927 events/second. This is too much information to store and analyze, and is mainly dominated
 928 by Standard Model QCD multi-jet production, a background for searches for new particles or
 929 physics. An online event selection, or trigger, must be used to reduce this rate to a manageable
 930 100 events/second. This is achieved through a combination of hardware, firmware, and software
 931 that provides a rough reconstruction of events in near real-time, and makes a decision about
 932 whether it meets a minimum set of criteria to be used in an analysis.

933 4.1 The Tracker

934 The innermost sub-detector is an all silicon pixel and strip tracker designed to provide precise
 935 and efficient measurement of the trajectories of charged particles and reconstruction secondary
 936 vertices necessary for identification of b -jets and τ leptons.

937 At peak LHC design luminosity of $10^{34} \text{ cm}^{-2} \text{ s}^{-1}$, and bunch spacing of 25 ns, there will be
 938 ~ 1000 particles from 20 overlapping pp collisions for each bunch crossing. This corresponds to a
 939 hit rate density of 1 MHz/mm² at a radius of 4 cm, 60 kHz/mm² at 22 cm, and 3 kHz/mm² at
 940 115 cm from the beam line. This large particle flux will also cause intense radiation damage to

detector components. These conditions necessitate the use radiation-hard silicon, with a high-granularity to create a low occupancy for each detector element, which are read out by fast electronics. Additional mitigation of the effects of radiation damage is taken by cooling and operating the entire detector to -10° C in order to maintain a signal to noise ratio of 10:1 for the sensors. After 10 years of running, it is anticipated that this will need to decrease to -27° in order to compensate for the accumulated damage.

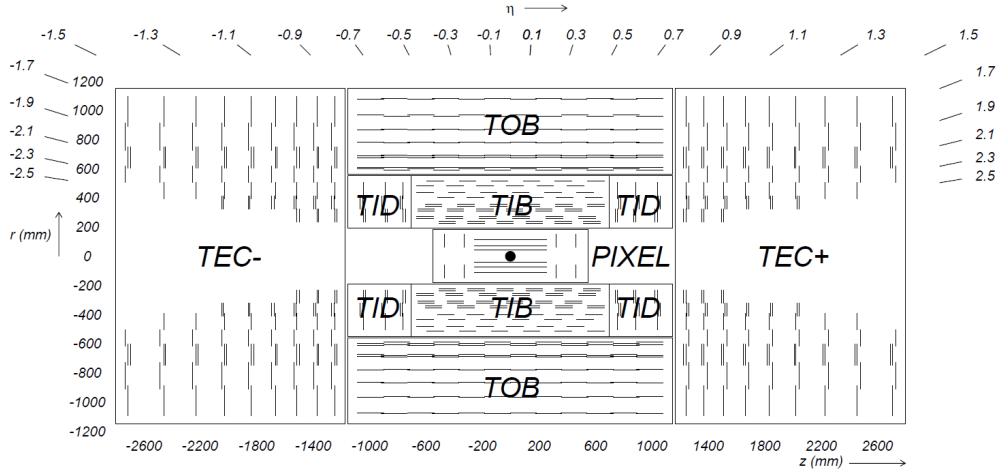


Figure 4.3: A side view of the tracker. The pixel detector is the innermost sub-system, with three concentric rings of detectors in the barrel, and two in the endcap. The tracker inner barrel (TIB) is a silicon strip detector, with four concentric rings. The tracker inner disks (TID) are three layers deep. The tracker outer barrel (TOB) is six concentric rings and the tracker end caps (TEC) are nine layers deep [15].

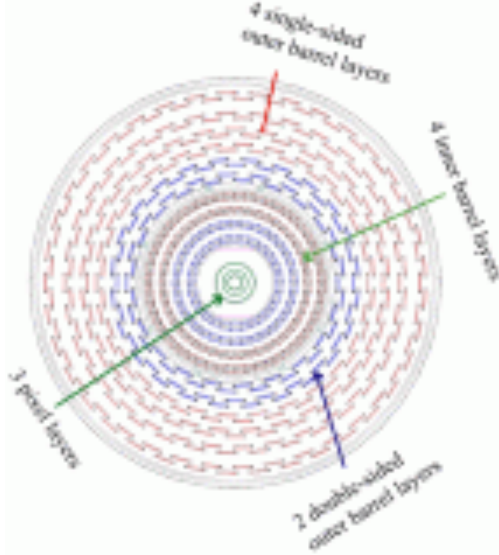


Figure 4.4: A head-on view of the beam-line and barrel components of the tracker [17].

The tracker has a cylindrical shape that surrounds the interaction region, with a length of 5.8 m and a diameter of 2.5 m. The large particle flux close to the beam-line requires the use of a pixel detector sub-system in the innermost region, from radius 4.4 cm to 10.2 cm from the

beam-line. The particle flux drops off sufficiently at larger radii to use silicon strip detectors, arranged into four different sub-systems: the tracker inner barrel (TIB), tracker inner disks (TID), tracker outer barrel (TOB) and tracker end caps (TEC), which extend to a radius of 1.2 m from the beam-line. Figure 4.3 shows a side view of the tracker layout and figure 4.4 shows a view down the beam-line of the barrel sections. The tracker has a total acceptance of $|\eta| < 2.5$.

There are competing factors for the radial length of the tracker. More layers allow for more samples of a particle's trajectory, giving a higher spatial precision, but more material means photons and hadrons are more likely to decay, and create a shower of particles that would better measured through the absorption of energy via calorimeters. The depth of the tracker varies from 0.4 to 1.8 radiation lengths, resulting in small degradation of the ECAL performance, since approximately half the photons will be converted to e^+e^- pairs.

4.1.1 The Silicon Pixel Detector

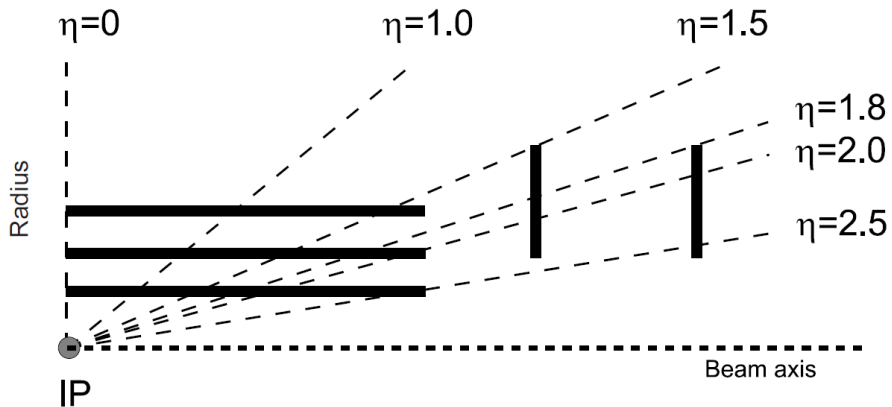


Figure 4.5: The three barrel and two disk layers of the silicon pixel tracker provide coverage of $|\eta| < 2.5$ [15].

The pixel detector consists of 66 million $100 \times 150 \mu\text{m}$ pixels, arranged in three concentric cylindrical layers of radius of 4.4, 7.3, and 10.2 cm from the beam line and two disc layers on either side of the barrel detectors. Figure 4.5 shows the eta coverage of the detector out to $|\eta| < 2.5$.

The sensor technology uses a n -on- n concept, where a high-dose n -implant is introduced onto a n -substrate with large resistance. A $p - n$ junction is made by the placement of a p -type semiconductor on the back side of the substrate. When a charged particle passes through the face of the substrate, between the $p - n$ junction, it liberates electrons from the silicon atoms, creating electron-hole pairs. The p -side has a voltage bias of 150 V in the barrel, and 300 V in the disks, that sweeps the pair apart, creating a current. Pixels are isolated from one another using a moderated p -spray in the barrel region, and open p -stops in the disks in order to create

an additional $p-n$ structure that acts like a diode to limit current flow between pixels. The 3.7 T magnetic field of the CMS solenoid also induces a Lorentz drift of the current in the $\hat{\phi}$ direction. This results in the current produced in one pixel being shared among multiple neighboring pixels. The charge collected by each of the multiple pixels are read-out, using an interpolation between pixels, resulting in a 15-20 μm spatial resolution on the trajectory of the charged particle - much smaller than the size of an individual pixel. In order to induce this effect in the disks (where the pixels are orientated perpendicular to the barrel), the pixels are angled 20° in the \hat{y} direction.

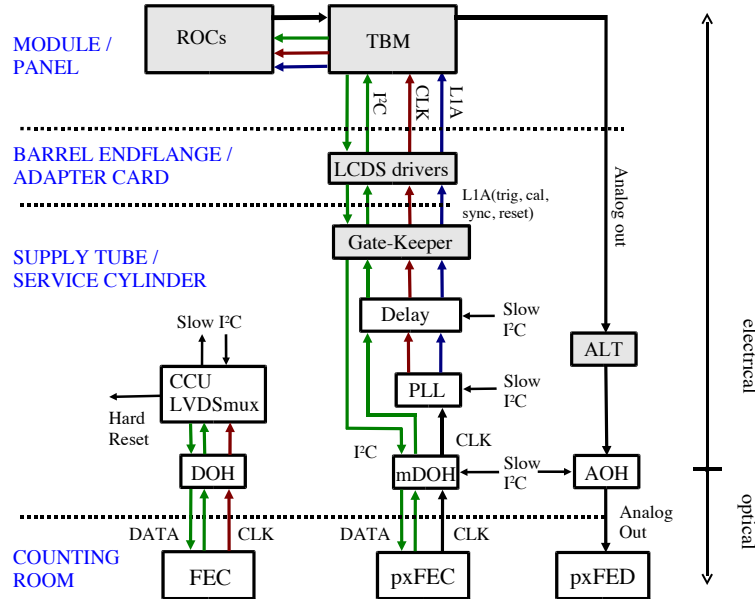


Figure 4.6: The readout electronics chain for the pixel detector [15].

The current created by the charged particle is collected by a readout chip (ROC) that is soldered with a bump bond type connection to the pixel. The ROC is a custom ASIC chip, that processes the signals for a grid of 52x80 pixels. It provides amplification, buffering, and zero suppression (threshold) of the charge from each pixel. Depending on the layer, 8-16 ROCs in the barrel, and 21-24 ROCs in the disks are connected and read-out by a single token bit manager (TBM) chip. This chip communicates information from the sensors to the trigger system, which is used to determine whether a given event is stored as data for analysis later. The pixel front end controller (pxFEC) interfaces with the ROC and TBM and provides central clocking and communicates to the CMS data acquisition system. The pixel front end digitizer (pxFED) converts the analog signals from the ROC and TBMs. A total of 40 pxFED (32 in the barrel and 8 in the disks) modules are used to read-out the entire pixel detector, and figure 4.6 shows a schematic of the pixel read-out chain.

The resolution of the pixel detector was measured in 2012 with $\sqrt{s} = 8 \text{ TeV}$ pp collision. The

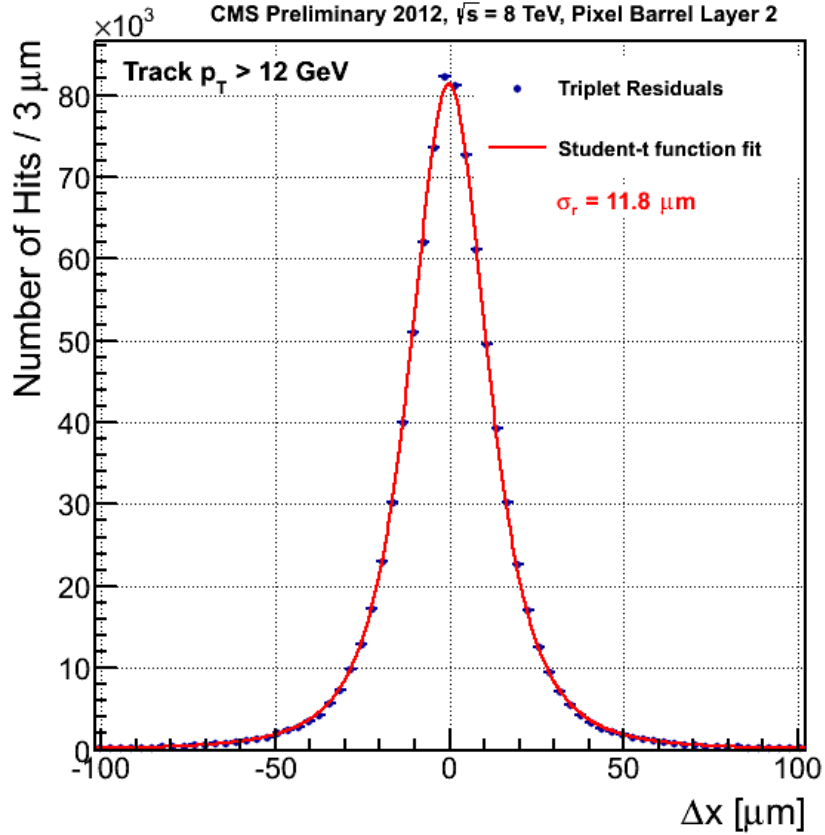


Figure 4.7: In 2012 pp collisions at $\sqrt{s} = 8$ TeV, the pixel detector performed with a resolution of $11.8 \mu\text{m}$. The above is a plot of the residual difference between a pixel and the results of a fit to a particle track [18].

993 residual distance between the hit position recorded by a pixel, and an interpolated track that
 994 uses that hit is plotted and fit with a student-t function in figure 4.7. For tracks with $p_T > 12$
 995 GeV, the pixel detector was found to have a spatial resolution of $11.8 \mu\text{m}$.

996 4.1.2 The Silicon Strip Detector

997 As shown in figure 4.3, the silicon strip tracking system has four components: the tracker inner
 998 barrel (TIB), tracker inner disks (TID), tracker outer barrel (TOB) and tracker end caps (TEC).
 999 A total of 15,148 detector modules are distributed among these systems, each with either one
 1000 $320 \mu\text{m}$ thick sensor, or two $500 \mu\text{m}$ thick sensors, making 24,244 sensors with an active area of
 1001 198 m^2 of silicon. A module with two sensors is shown in figure 4.8. Each sensor has either 512
 1002 or 768 strips since they are read out by two multiplexed 128-channel front end chips, making it
 1003 possible to only read out sensors in groups of 256. Each strip has a pitch that varies between 80
 1004 and $200 \mu\text{m}$ and lengths that vary between 10 and 25 cm. All in all, 9.3 million strips are used
 1005 in the silicon tracker.

1006 The TIB and TID provide radial coverage from 20 to 55 cm. The TIB has four barrel layers,

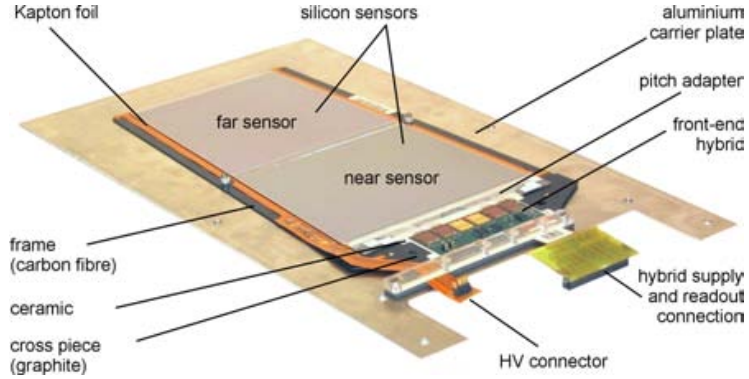


Figure 4.8: A silicon strip module, with two $500\ \mu\text{m}$ thick sensors [15].

with $80\ \mu\text{m}$ pitch strips on the first two layers, and $120\ \mu\text{m}$ strips on the outer two, giving a single point resolution of 23 and $35\ \mu\text{m}$ respectively. The strip pitch varies between 100 and $141\ \mu\text{m}$ in the three discs of the TID. The TOB surrounds the TIB/TID and is composed of six barrel layers that extend the tracker radius to $116\ \text{cm}$. It is composed of $500\ \mu\text{m}$ thick strip sensors, with pitches of $183\ \mu\text{m}$ in the first four layers and $122\ \mu\text{m}$ in the outer two layers. It provides 6 measurement points of the particle trajectory with a single point resolution of 53 (35) μm in the first four (last two) layers. Each TEC is made of 9 discs, each with 7 rings of strip detectors. The inner four rings of each disk use the single, $320\ \mu\text{m}$ thick strip modules, while the outer three rings use the double, $520\ \mu\text{m}$ thick strip modules. The average pitch varies between 97 to $184\ \mu\text{m}$ in each of the rings. In the first two layers of the TIB, the first two rings of the TID, the first two layers of the TOB, and rings 1 , 2 , and 5 in each disk of the TEC contain modules mounted back-to-back, with an angle of $100\ \text{mrad}$ between them to provide a two-dimensional measurement of a particle's trajectory.

Each of the strips is a single sided p -on- n type silicon sensor manufactured on 6 inch wafers, with a base material of n doped silicon. The front side of the wafer is implanted with a p^+ type semiconductor. A uniform n^+ implantation on the back forms the ohmic contact to $500\ \text{V}$. This forms a pn junction and when a charged particle passes through the face of the wafer, atoms in the junction are ionized and the $500\ \text{V}$ potential difference creates a current out of the resulting electron/hole pairs. This current is collected and processed through the read-out system.

A custom integrated circuit, the APV25, is used to amplify, shape, and buffer the signals produced from the silicon strips. It has 128 read-out channels, and samples the detector signals at the $40\ \text{MHz}$, suitable for the $25\ \text{ns}$ collisions. It is able to store data for up to $4\ \mu\text{s}$ to account

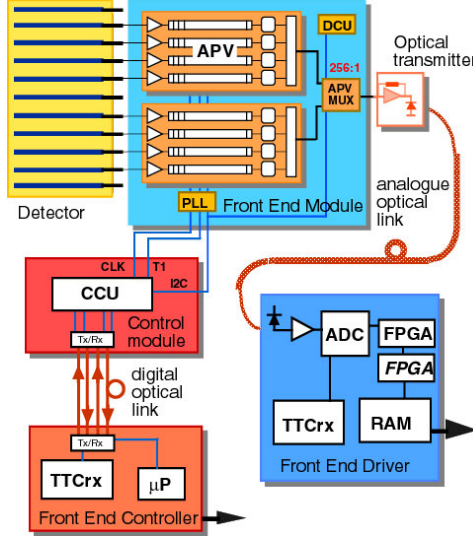


Figure 4.9: Schematic of the readout sequence of the silicon strip detector [15].

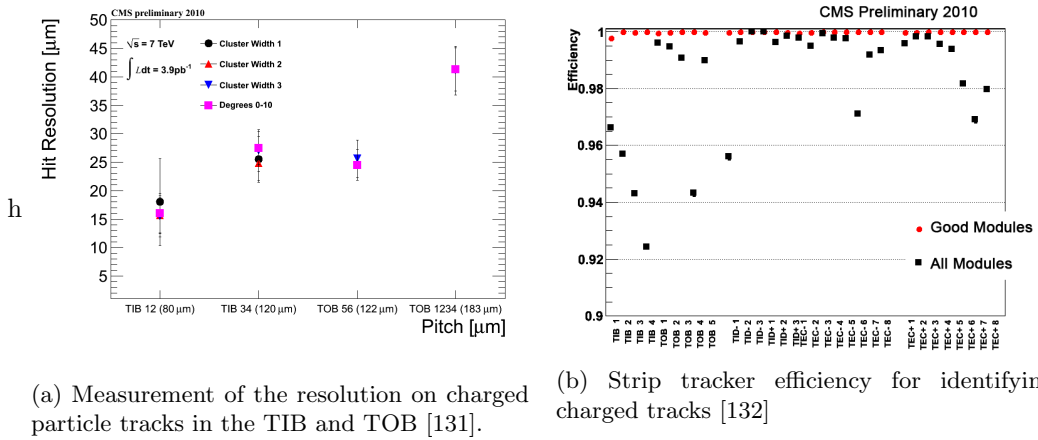


Figure 4.10: Measurements of the performance of the silicon strip track using pp collisions from 2011 at $\sqrt{s} = 7 \text{ TeV}$

for trigger latency. Two APV25 chips are linked with fiber optics to the Front End Driver (FED) system. Each FED receives data from 94 optical fibers, and digitizes them in parallel. The Front End Controller (FEC) transmits clock, trigger, and control data to the APV25s. The entire readout chain is shown in figure 4.9.

In 2011, the strip efficiency and resolution were measured from data in center-of-mass energy, $\sqrt{s} = 7 \text{ TeV}$ pp collisions. Figure 4.10(a) shows the resolution varying between 15-40 μm for the TIB and TOB detectors. Figure 4.10(b) shows the efficiency for reconstructing tracks with the strip tracker, which is well above 99% when only considering operational modules.

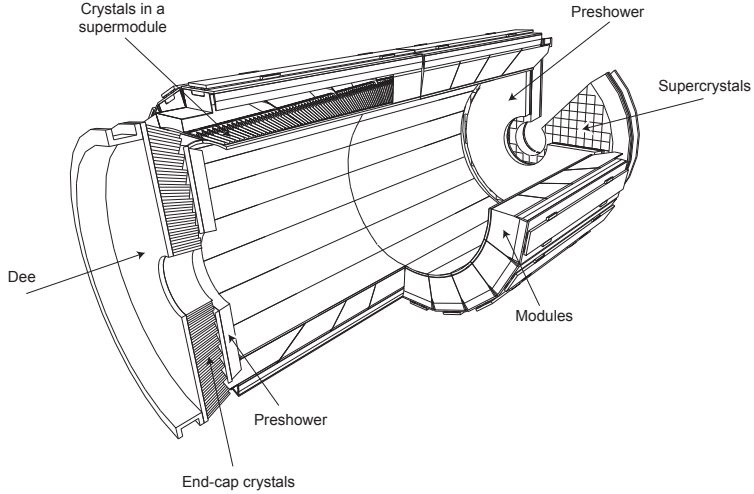


Figure 4.11: Layout of the ECAL sub-detector [15]

¹⁰³⁷ 4.2 The Electromagnetic Calorimeter

¹⁰³⁸ The Electromagnetic Calorimeter (ECAL) surrounds the inner tracker with 61,200 high density
¹⁰³⁹ lead tungstate (PbWO_4) crystals in the central barrel section, and 7,324 crystals in each of
¹⁰⁴⁰ the two endcaps. The crystals have a fast response, provide fine granularity, and are radiation
¹⁰⁴¹ resistant, making them ideal for the LHC environment and the physics goal of observing the
¹⁰⁴² Standard Model Higgs boson decay to two high energy photons. The primary background for
¹⁰⁴³ this process comes from neutral pions decaying to two photons, which is especially difficult when
¹⁰⁴⁴ the photons are close together and can potentially be reconstructed as a single high-energy
¹⁰⁴⁵ photon. This occurs most frequently in the endcaps, so an additional detector, the preshower,
¹⁰⁴⁶ provides additional spatial resolution with silicon microstrip detectors, similar to those in the
¹⁰⁴⁷ tracker. Figure 4.11 shows the layout of the ECAL.

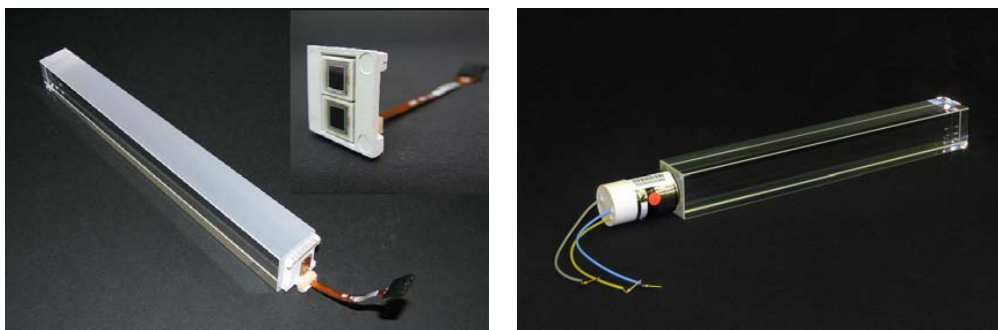


Figure 4.12: Typical Lead Tungstate crystal, with APD attached to the rear face in the left frame, and a VPT attached in the right frame [15].

¹⁰⁴⁸ Lead tungstate is an ideal material for electromagnetic calorimetry. Figure 4.12 shows a
¹⁰⁴⁹ typical crystal, with photomultipliers attached to the rear faces, which will be discussed later.

1050 The material has a high density, 8.28 g/cm^3 , giving it a large electromagnetic cross-section,
 1051 making it much more likely for a particle traversing the crystal to interact with one of the atoms
 1052 in its structure. When a particle interacts with the crystal, it does so by depositing energy into
 1053 its atoms, which excite the electrons that are bound to it. The atoms then relax by emitting
 1054 photons, in a process known as scintillation and the PbWO_4 crystals release 80% of their light
 1055 in the 25 ns LHC bunch crossing time. This light is collected by photomultipliers attached to
 1056 the rear face of the crystal and converted into an electrical signal. Read-out electronics amplify,
 1057 digitize, and buffer the signal until it can be stored as data or discarded.

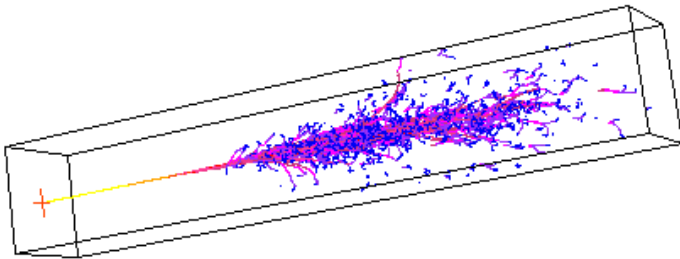


Figure 4.13: A simulation of the evolution of an electromagnetic shower being initiated by an electron entering the center of the front face [19].

1058 As a charged particle or photon begins to deposit energy, it begins a decay chain into many
 1059 lower energy photons and electrons, known as an electromagnetic shower. Electrons, being
 1060 bent by the CMS magnetic field, and multiple scattering off of the PbWO_4 crystals, create
 1061 bremsstrahlung photon radiation. Since the intensity of bremsstrahlung is inversely proportional
 1062 to the mass of the particle squared, particles heavier than electrons such as muons and hadrons
 1063 do not leave a large signature in the ECAL. Photons convert to e^+e^- pairs, which in turn create
 1064 additional bremsstrahlung. The crystals have a short radiation length, $X_0=0.89\text{cm}$, which is
 1065 the distance it takes an electron to deposit $1/e$ of its energy through bremsstrahlung, and $7/9$
 1066 of the mean free path of a high energy photon before it converts to an e^+e^- pair. A corollary
 1067 of the crystal's short radiation length is its small Moliere radius, 2.2cm , which is the radius of
 1068 a cylinder that encloses 90% of the electromagnetic shower's energy deposition. A typical
 1069 crystal has a front face that is $22\times 22 \text{ mm}^2$, a rear face of $26\times 26 \text{ mm}^2$, and a length of 230 mm ,
 1070 or $25.8 X_0$ radiation lengths. This means that a relatively small grid of crystals can be used to
 1071 fully collect the energy deposited by a high energy electron or photon. As previously mentioned,
 1072 heavier charged particles will not bremsstrahlung as much as electrons, and will travel through
 1073 the entire ECAL, depositing only a moderate fraction of their energy in the crystals. Figure 4.13
 1074 shows a simulation of an electromagnetic shower produced by an electron entering the front face
 1075 of a crystal.

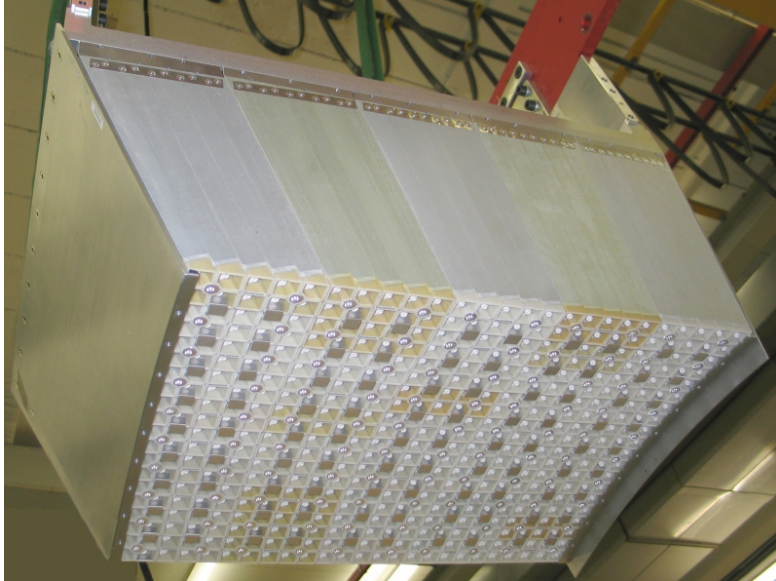


Figure 4.14: A module of 500 crystals (25 crystals wide by 20 crystal tall) [15].

The barrel of ECAL (EB) covers a psuedorapidity range of $|\eta| < 1.479$ with 61,200 crystals at a radius 1.29 m from the beam-line. The crystals are positioned in a quasi-projective geometry, such that their axes make a 3° angle with respect to the vector pointing to the nominal interaction point. This ensures that particles will not pass through the cracks and spaces between crystals, and are forced to interact with a portion of the ECAL. Crystals are assembled in groups of 400 or 500 into modules, as shown in figure 4.14 . Four of these modules are assembled into a supermodule contain 1700 crystals, and 36 supermodules make up the barrel region.

The crystals in the EB are read out by Avalanche Photo-Diode (APD) photomultipliers, shown in the left frame of figure 4.12. The APDs were manufactured by Hamamatsu and are a bulk *n*-type silicon material, with a *p*-type implanted on its surface to form a *pn*-junction. The operation principle is similar to that of tracker. When scintillation light from the lead tungstate crystals enters the face of the APD, it creates electron-hole pairs in the intrinsic region between the *p* implantation and the *n* bulk material. The APD is biased with 45 V, which creates a current from the electron-hole pairs and is the signal that a particle has created scintillation in the crystal. The APD provides a gain of 50 and has a quantum efficiency of 75%. Both the APDs and the PbWO₄ exhibit a strong temperature dependence, so the entire system is kept at 18° C with a water-based cooling system distributed throughout the barrel and end-caps.

The ECAL readout electronics are designed to read-out a 5×5 array of crystals, known as a trigger tower, in the EB, and a single supercrystal in the EE. Each trigger or tower or supercrystal consists of 5 Very Front End (VFE) boards, each connected to 5 APDs (VPTs), one Front End (FE) board, two (EB) or six (EE) Gigabit Optical Hybrids (GOHs), one Low Voltage Regulator (LVR) and a motherboard. Once triggered, the APD (or VPT in the EE) is sampled 10 times, at

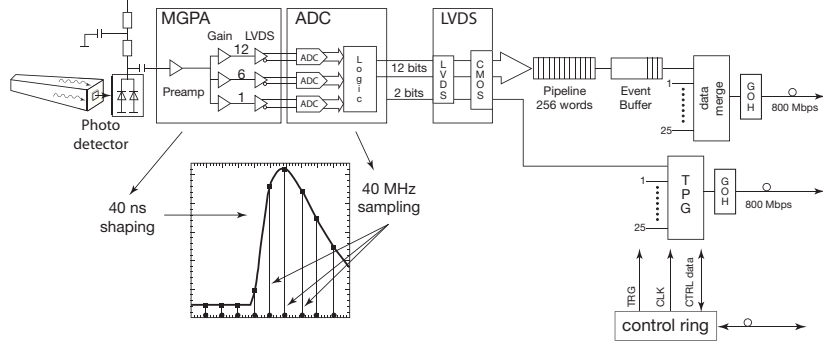


Figure 4.15: Schematic of the On-Detector Readout for the ECAL [15].

a 40 MHz sampling rate, and amplified by a multi-gain amplifier (MGPA), with nominal gains of 1, 6, and 12 contained on the VFE. These digitized samples are sent to the FE, where they are buffered until receiving a Level-1 trigger, where they are sent to the off-detector electronics Data Concentrator Card (DCC) via the GOHs. Figure 4.15 shows a schematic of the on-detector read-out.

In the barrel, the 5×5 trigger towers are divided in the 5 strips in the $\hat{\phi}$ direction. The energy deposits in these strips is summed by the FE cards and define the transverse energy of the tower. In the endcaps, supercrystals are divided into groups of five contiguous crystals of variable shape, known as psuedo-strips. The energy of these strips is performed by the FE, and the off-detector electronics use these to compute the transverse energy deposition.

The preshower detector sits in front of the ECAL end-caps and provides coverage from $1.653 < |\eta| < 2.6$. It is a two-layer sampling calorimeter. Lead radiators initiate electromagnetic showers from electrons and photons, and silicon strips are placed behind them to measure trajectories and deposited energy of passing particles. The total thickness is 20cm, which corresponds to a 2 radiation lengths in the first layer, and another radiation length in the second layer. 95% of photons are converted to e^+e^- pairs after the first layer. Each silicon sensor is composed of 31 strips, with thickness of $320 \mu\text{m}$ and are 1.9 mm in pitch. A front-end ASIC performs pre-amplification, shaping, voltage sampling, and communicates information to the trigger system to determine if data is stored or discarded. The structure is formed into Dees, and two Dees form a disk with a hole for the beam-line to pass through.

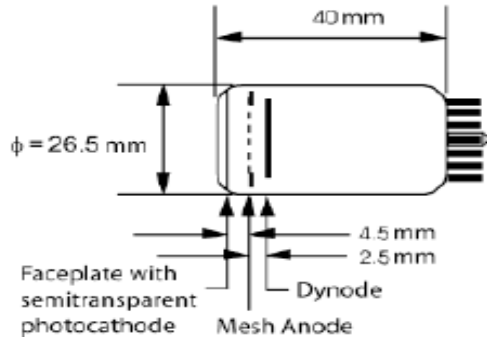
Behind the preshower is the ECAL end-cap (EE). It covers the psuedorapidity range of $1.479 < |\eta| < 3.0$, and sits a longitudinal distance of 315.4 cm from the nominal interaction point. Crystals are grouped into 5×5 modules known as supercrystals (SCs). Like the preshower, each endcap is divided into two sections, Dees, which form a disk with an inner bore for the beam line to pass through, as shown in figure 4.16. Each Dee holds 3,662 crystals, which are divided



Figure 4.16: A section of the ECAL end-cap, a Dee. Two Dees form a disk with an inner bore for the beam-line to pass through. 5x5 modules, or supercrystals, are mounted in preparation for installation at CMS [15].



(a) A picture of a VPT next to a standard size pen for scale [133]



(b) Schematic of a VPT showing characteristic dimensions [134]

Figure 4.17: Vacuum Photo-Triode devices used in the ECAL end-caps (EE)

₁₁₂₃ into 138 supercrystals, and 18 special partial-supercrystals for the inner and outer sections of
₁₁₂₄ the Dee.

₁₁₂₅ 4.2.1 Vacuum Photo-Triodes

₁₁₂₆ The photomultiplier used to readout the lead tungstate crystals in the EE is the Vacuum Photo-
₁₁₂₇ Triode (VPT), shown in the right frame of figure 4.17(a). Each device is 26.5mm in diameter
₁₁₂₈ and 40mm in length as shown in figure 4.17(b). It is a gain stage device. Photons from the
₁₁₂₉ lead tungstate scintillation light enter the front face of the VPT and liberate electrons from the
₁₁₃₀ grounded bi-alkali photocathode (SbKCs) via the photoelectron effect. The cathode material
₁₁₃₁ has a quantum efficiency of $\sim 20 - 25\%$. The photo-electrons are accelerated towards the mesh

1132 anode grid, which is held at 800 V. Approximately half the photo-electrons pass through the
1133 mesh and encounter a dynode plate held at 600 V. Electrons either collide with the dynode,
1134 liberating secondary electrons from the collision, or are turned around by the 200 V difference
1135 between anode and dynode. Electrons are thus constantly accelerated towards the anode, and
1136 create secondary electrons as they collide with the anode. The process repeats with the secondary
1137 electrons, creating an avalanche of charge near the anode. As these charges eventually recombine
1138 with the anode over the course of a few nanoseconds, the voltage of anode drops, signaling the
1139 device has detected a photon from the PbWO₄ crystals.

1140 The performance of the VPT is degraded over time by two effects associated with exposure to
1141 the scintillation light from the crystals. The first is loss of the vacuum inside the tube. Molecules
1142 from the air become ionized by the large voltages and the positive ions are accelerated towards
1143 the photo-cathode, which is damaged through the resulting collision. The second effect is the
1144 gradual depletion of photo-electrons from the bi-alkali cathode material. The result is a decrease
1145 in the current, and thus signal, produced by the anode. Both of these effects can be effectively
1146 modeled as the sum of two falling exponential functions. The University of Virginia has studied
1147 the performance of VPTs with respect to their light exposure rates over the course of several
1148 years in order to characterize the device's response and long-term behavior.

1149 4.2.2 Test Rig at UVa

1150 The University of Virginia (UVa) has continuously monitored four production VPTs operated
1151 at 800 V anode and 600 V dynode, in a 3.8 T field, at 15° to the tube axis, with photocath-
1152 ode currents of approximately 10 nA. This was done to simulate light exposure from the lead
1153 tungstate crystals in the forward regions of the ECAL end-caps, as well as provide an accelerated
1154 simulation of photocurrents that would be experienced in the larger eta regions. As described
1155 above, the light exposure is theorized to be the most significant cause of the loss of response
1156 in the VPT, known as burn-in. The amount of light that the device has been exposed to is
1157 measured in terms of the total number amount of charge liberated from the cathode, measured
1158 from the cathode current draw, and is known as the integrated charge. By operating at such
1159 high photocurrents, UVa is able to probe this burn-in effect in an attempt to understand the
1160 long term behavior of the VPT response to light.

1161 The University of Virginia is well suited to test these devices, since it operates a 3.8 T
1162 solenoid magnet, with a sufficiently large inner bore to accommodate a rig containing five (5)
1163 VPTs, LEDs, LED driving hardware, and amplifying equipment. The magnet itself was built
1164 by Oxford instruments and has an inner bore diameter of 0.4 m and an outer bore diameter of
1165 1.5 m. The inner bore is 0.13 m in height from the ground, and the magnet has a length of 1.5m

1166 along its z-axis, which is perpendicular to the normal of the floor.

1167 The VPTs were supplied with high voltage (800 V anode, 600 V cathode) from a CAEN
1168 High Voltage supply. This manufacturer also provides high voltage supplies for the VPTs used
1169 in CMS. They are preferable due to their stability, programmable user interface, and capacity
1170 to drive multiple VPTs simultaneously. A voltage separation between anode and cathode much
1171 larger than this is not recommended due to its potential do damage the device.

1172 The VPTs were pulsed with blue and orange LEDs at rates of 10 kHz, and 20 kHz, to capture
1173 the same features (frequency and rate) that light from the lead tungstate crystals would produce
1174 while collisions were occurring in the detector. The driving circuits are the same as those used in
1175 the LED system in the end-caps at point 5 (the location of CMS at CERN), with the exception
1176 that the current limiting resistors are larger. The driving circuits are Dallas Semiconductor
1177 DS1040Z-D70 Programmable One-Shot Pulse Generators. The TTL signals from the FPGA
1178 serve as a trigger for a Dallas Semiconductor pulse generator chip on the board that generates a
1179 30 nSec pulse, so there is no overlap in pulses generated by the VPT. The pulsing was also run
1180 in an on/off cycle of 16 hrs on, 8 hrs off to be consistent with the LHC beam fill cycle.

1181 The LED pulsing and data acquisition was automated via a PXI unit manufactured by Na-
1182 tional Instruments, which contains a FPGA card, a digital oscilloscope, and computer running
1183 Windows XP. The FPGA card was programmed with LabVIEW software which controlled LED
1184 pulse rate, low voltage power, and measurements of VPT signals. The data acquisition was
1185 triggered by means of a PIN diode placed next to the VPT. This served the dual purpose of in-
1186 dependent data triggering and also provided the means to correct fluctuations in the illumination
1187 provided by the LEDs.

1188 The current from the VPTs anode and cathode are ultimately routed to the PXI Crates
1189 switches, and then on to the crates DMM or oscilloscope via a preliminary amplification stage.
1190 The VPTs anode is connected directly to a Stephenson amplifier, which connects to a high-
1191 frequency switch. The PIN diode signal passes unmodified to that same high-frequency switch.
1192 The cathode signal cables connect to a distribution box near the PXI Crate. The distribution
1193 box then routes their signals to the terminal block on a low-frequency switch. All of these signals
1194 leave the rig over BNC cables before terminating at or adjacent to the PXI Crate. Figure 4.18
1195 highlights different components of the test stand at UVa.

1196 4.2.3 Results of UVa Tests

1197 The University of Virginia rig ran three sets of 5 VPTs for approximately 30 wks each in a
1198 3.8 T magnetic field under high light conditions from blue and orange frequencies to simulate
1199 a large light yield found in large eta regions of the end-cap. The large photocurrents allowed

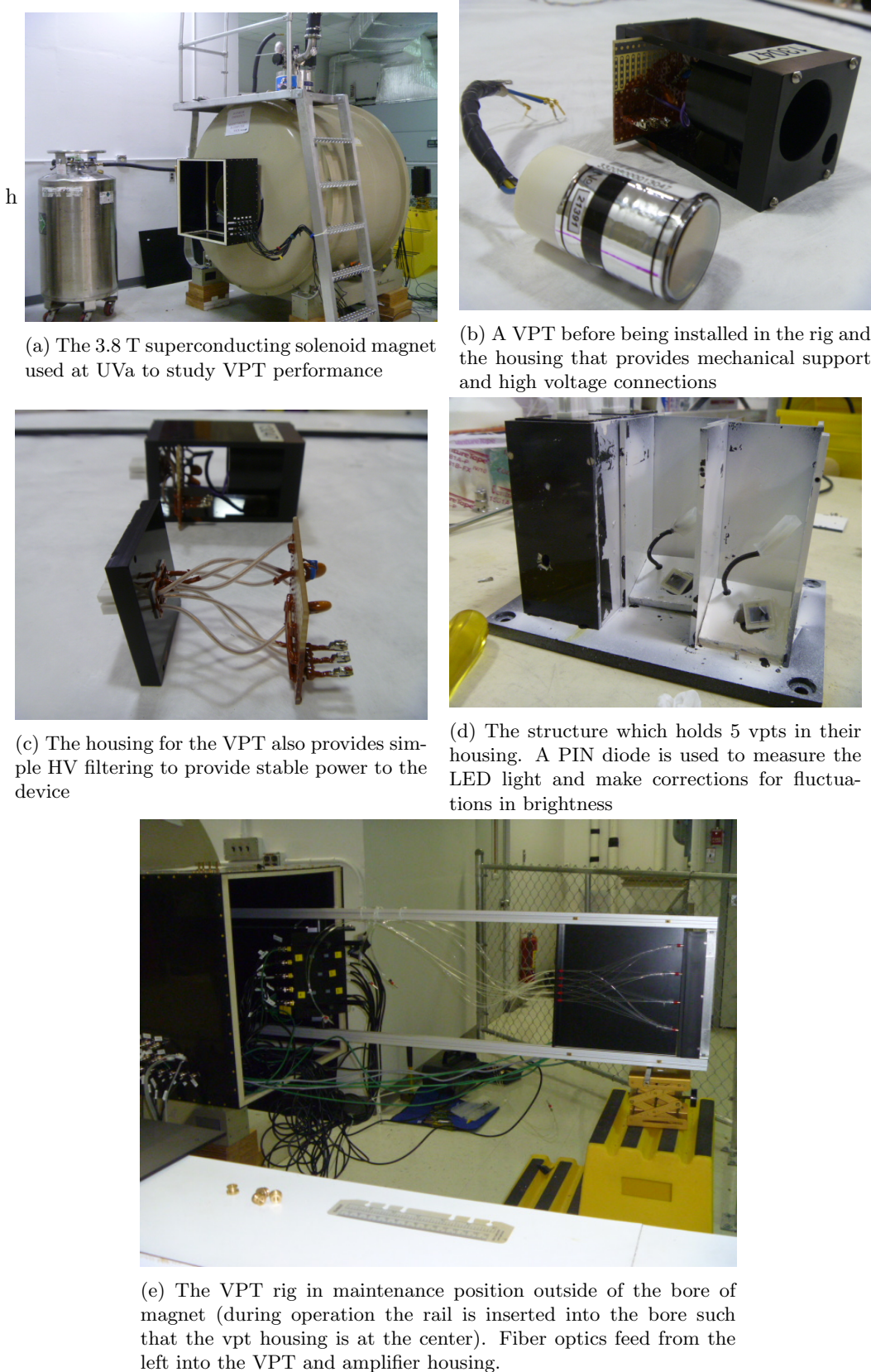


Figure 4.18: Features of the UVa VPT test stand

the collection of an integrated charge of ~ 48 mC for the largest gain VPT, and ~ 16 mC for the other three. All VPTs were characterized by an initial steep decline followed by a plateau region, which was fit with a double exponential function of the form

$$f(x) = A + B \exp(Cx) + D \exp(Ex) \quad (4.2)$$

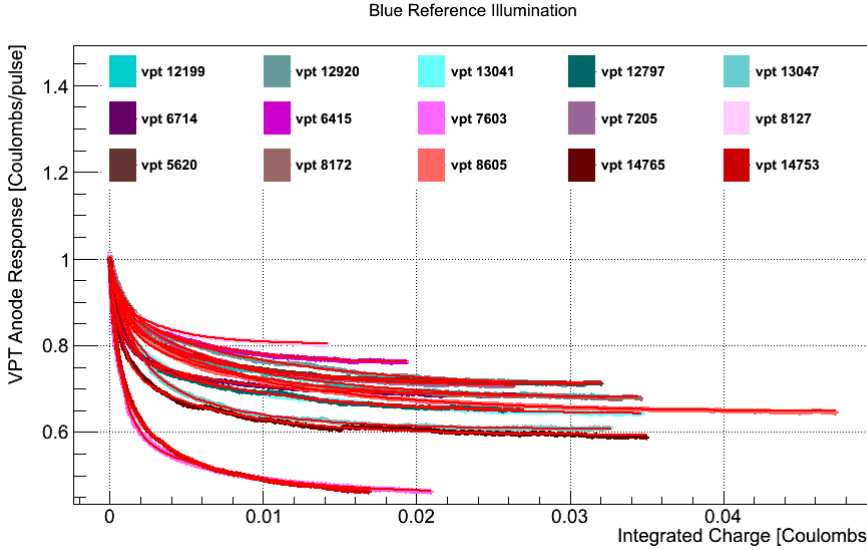


Figure 4.19: 3 runs of 5 VPTs, exposed to blue LED light, and fit to a sum of two exponentials.

Table 4.1: Fit Results for VPT Conditioning Studies at U.Va. and Brunel, Blue Reference LED

RIE Number	% Drop	χ^2/NDF	Pedestal	Fast exp Amplitude	Fast exp τ	Slow exp Amplitude	Slow exp τ
12199	30.1	1.20e+00	1.51e-09	3.42e-10	-8.84e-04	3.85e-10	-1.00e-02
12920	27.0	7.27e-01	1.72e-09	3.16e-10	-1.16e-03	4.03e-10	-1.05e-02
13041	33.5	8.46e-01	1.09e-09	3.43e-10	-1.20e-03	2.46e-10	-9.31e-03
12797	33.6	1.07e+00	6.39e-10	2.18e-10	-9.72e-04	1.31e-10	-9.87e-03
13047	38.1	1.06e+00	5.48e-10	1.98e-10	-1.40e-03	1.49e-10	-6.19e-03
6714	29.3	8.37e-01	1.55e-09	4.10e-10	-6.66e-04	2.48e-10	-6.11e-03
6415	23.6	1.28e-01	1.19e-09	1.54e-10	-6.55e-04	2.20e-10	-5.16e-03
7603	50.3	3.25e+00	1.44e-09	1.02e-09	-8.22e-04	4.87e-10	-6.72e-03
7205	29.4	4.53e-01	1.41e-09	2.14e-10	-5.68e-04	3.94e-10	-5.96e-03
8127	19.6	1.97e-01	1.71e-09	1.82e-10	-3.12e-04	2.35e-10	-3.30e-03
5620	27.4	4.57e+00	1.68e-09	2.85e-10	-5.20e-04	3.68e-10	-6.19e-03
8172	30.3	8.75e+00	8.32e-10	1.52e-10	-1.06e-03	2.27e-10	-6.87e-03
8605	32.1	6.94e+00	1.36e-09	3.33e-10	-8.97e-04	3.94e-10	-1.03e-02
14765	38.9	2.78e+01	3.47e-10	1.37e-10	-7.46e-04	9.24e-11	-6.77e-03
14753	52.9	2.53e+01	1.19e-09	7.45e-10	-5.86e-04	6.10e-10	-4.77e-03
Average	31.0	4.62e+00	1.17e-09	2.94e-10	-1.09e-03	1.66e-10	-3.07e-01

where A is a pedestal parameter, B is the amplitude of the fastest dropping exponential, C is the time constant of the fast dropping exponential, D is the amplitude of the slow dropping exponential, and E is the time constant of the fast exponential. The summary of the fit parameters for blue LED light is shown in table 4.1 and the summary of fit parameters for the orange LED light is shown in table 4.2. Plots of the VPT anode response versus integrated charge, and

1208 the associated fit for each of the devices is shown in figure 4.19 for blue LED exposure and in
 1209 figure 4.20 for orange LED exposure. Based on these findings, it can be concluded that the VPT
 1210 "burn-in" eventually reaches a plateau at about $\sim 70\%$ for blue LED exposure and $\sim 50\%$ for
 1211 orange LED exposure.

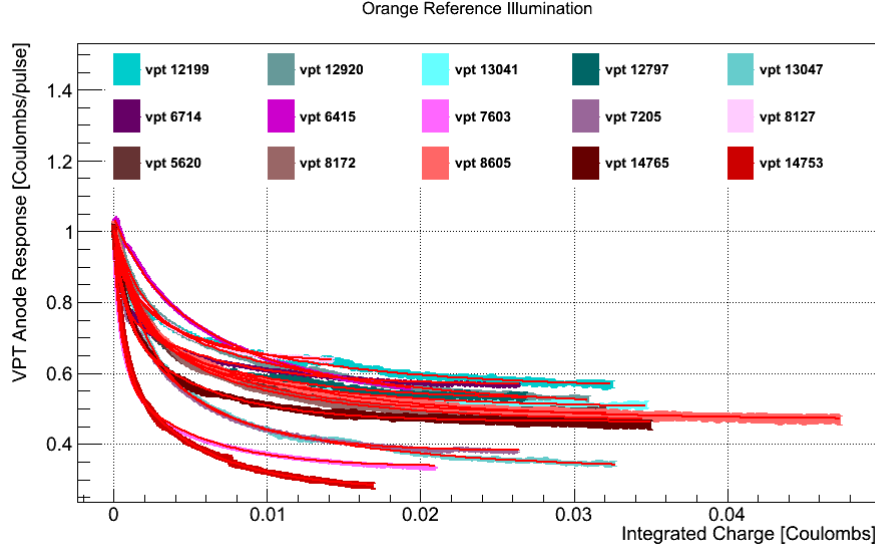


Figure 4.20: 3 runs of 5 VPTs, exposed to orange LED light, and fit to a sum of two exponentials.

Table 4.2: Fit Results for VPT Conditioning Studies at U.Va., Orange LED

RIE Number	% Drop	χ^2/NDF	Pedestal	Fast exp Amplitude	Fast exp τ	Slow exp Amplitude	Slow exp τ
12199	41.9	6.23e-01	4.23e-10	1.79e-10	-1.10e-03	1.76e-10	-1.10e-02
12920	45.3	1.84e-01	6.73e-10	3.24e-10	-1.67e-03	3.72e-10	-1.26e-02
13041	48.3	7.42e-01	2.75e-10	1.81e-10	-1.63e-03	1.04e-10	-1.02e-02
12797	46.4	5.05e-01	2.05e-10	1.14e-10	-1.23e-03	7.87e-11	-8.77e-03
13047	63.0	1.09e+00	1.34e-10	1.73e-10	-2.18e-03	1.07e-10	-1.16e-02
6714	43.4	1.43e+01	7.73e-10	3.29e-10	-4.49e-04	2.84e-10	-6.11e-03
6415	46.5	2.34e+01	4.41e-10	8.75e-11	-1.80e-03	3.47e-10	-7.95e-03
7603	64.8	3.20e+01	3.01e-10	3.42e-10	-5.42e-04	2.24e-10	-5.04e-03
7205	63.2	6.52e+01	1.94e-10	1.29e-10	-4.49e-04	2.16e-10	-5.13e-03
8127	39.4	2.24e+01	7.09e-10	1.54e-10	-2.08e-04	3.10e-10	-3.75e-03
5620	50.3	2.30e-01	4.07e-10	2.13e-10	-1.16e-03	2.37e-10	-7.79e-03
8172	51.7	1.56e-01	4.01e-10	2.73e-10	-1.91e-03	2.08e-10	-9.48e-03
8605	49.6	1.83e-01	2.39e-10	1.46e-10	-1.45e-03	1.33e-10	-1.12e-02
14765	53.3	3.08e-01	2.07e-10	1.27e-10	-8.55e-04	1.17e-10	-5.66e-03
14753	72.2	2.22e-01	1.94e-10	2.76e-10	-6.01e-04	2.47e-10	-5.06e-03
Average	52.0	1.08e+01	3.72e-10	2.03e-10	-1.15e-03	2.11e-10	-8.10e-03

1212 4.3 The Hadronic Calorimeter

1213 The Hadronic Calorimeter (HCAL) is divided into four sub-systems: the barrel (HB), the
 1214 endcap (HE), the outer calorimeter (HO), and the forward calorimeter (HF). It is especially
 1215 important for measuring hadronic jets and neutrinos by measuring an imbalance in energy trans-

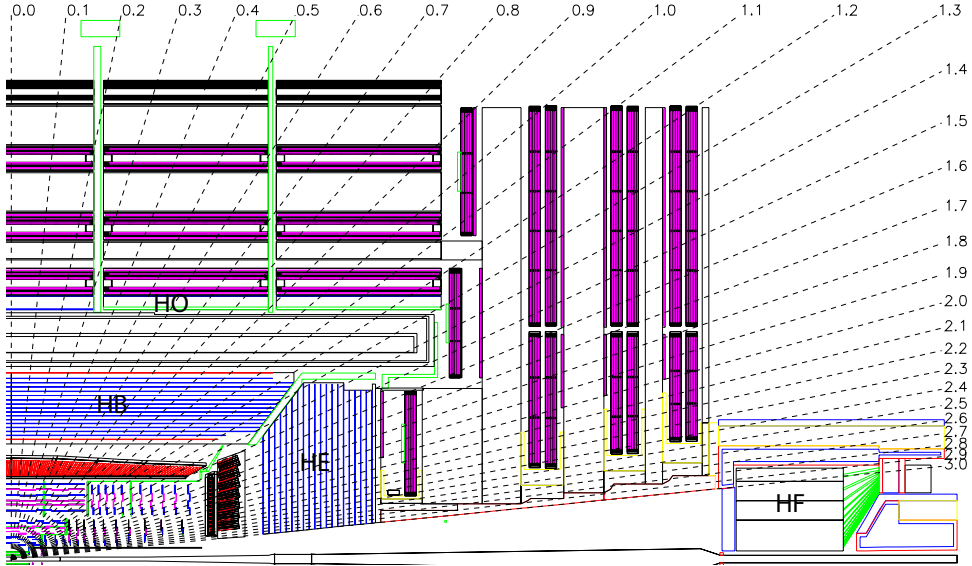


Figure 4.21: Longitudinal cross-section of the HCAL with the four sub-systems labeled [15].

verse to the beam-line. It provides coverage from $|\eta| < 3$ from the HB, HE, and HO, and the HF extends the coverage out to $|\eta| < 5.2$. A diagram of the longitudinal cross section is shown in figure 4.21.

The barrel section of the HCAL, the HB, is divided into two sections longitudinally, each with 18 identical azimuthal wedges wrapped around the beam-line. Each wedge has four azimuthal sections, with the center two sections aligned and each edge piece angled and staggered in a configuration that creates no projective dead material for the full radial extent of the HCAL. Figure 4.22 shows a closeup photograph of four wedges, where optical fibers are laid out across the seam that joins the staggered edge layers to the two aligned center layers, and blue lines highlight the four azimuthal divisions for a single wedge.

The HB is a sampling calorimeter, with each azimuthal section composed of 14 alternating layers of brass absorber plates, and layers plastic scintillator tiles, with steel plates on the top and bottom layers for structural support. Each quarter-barrel section of scintillator has 16 η divisions, giving a segmentation of $(\Delta\eta, \Delta\phi) = (0.087, 0.087)$. The brass absorber plates are C26000/Cartridge Brass. The material was chosen since the absorber material could not be distorted or bend under the stress of its own weight for at least 15 years of experimental running. Much of the material was purchased, but over a million Russian WW2 brass shell casings, designed to withstand the stresses of travel aboard 1940s Navy vessels, were melted down and processed into absorber tiles. Figure 4.23 shows members of the Russian Navy posing with some of the shells.

When a hadron passes through a wedge, the brass and steel plates absorb energy and ini-



Figure 4.22: Closeup of the HCAL barrel section. The center section of each of the 18 wedges are labeled, optical cables lay across the joint of the center and staggered edge sections of each wedge. The blue lines show the approximate azimuthal division of the wedge [15].

tiates the decay of the hadron into a number of lighter particles. These particles pass through the scintillator layer, which absorb energy from the interactions or collisions with the passing particles. The electrons of the scintillator become excited and relax by emitting a number of photons in the blue-violet range of the visible spectrum proportional to the amount of energy absorbed by the scintillator. These photons are absorbed by wavelength shifting fibers (WSFs), which re-emit the light in the green part of the visible spectrum. The WSFs are spliced into four clear fiber optical cables. These fibers transport the light from each of the layers to an optical decoding unit (ODU), which arranges the fibers into readout towers. A hybrid photodiode (HPD) converts this light into electric signals and is digitized by an ADC contained on the front-end electronics. The HPD is a photo-cathode, which converts light to electrons via the photoelectric effect, that sits above a silicon diode that amplifies the signal of the cathode. The HPD provides a gain of 2000 to the light signals received from the scintillator trays. The on-detector electronics communicate to the HCAL trigger/readout (HTR) boards, which communicate with the trigger system to decide whether to store the event as data or discard it.

The brass absorbing material has a nuclear interaction length, or the length necessary to reduce the number of charged particles in a hadron shower by $1/e$, of 16.42 cm, and a radiation length of 1.49 cm. This means that the HB will be able to contain a large part of most hadron showers produced at LHC energies, but a portion will still pass through the entire radial distance. The outer barrel layer, HO is designed to measure the remnants of the hadron shower. It sits



Figure 4.23: Over 1 million Russian shells of military artillery were re-processed in the construction of the HCAL [20]

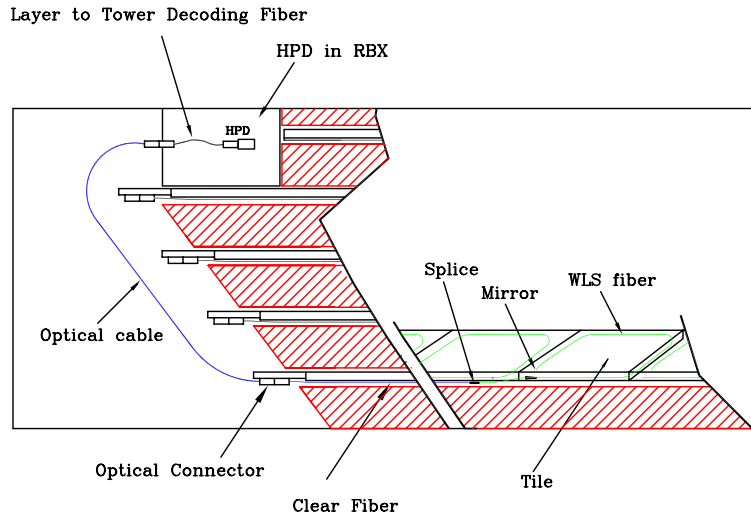


Figure 4.24: Optical readout chain of the HCAL scintillator tiles [15].

1256 outside of the solenoid magnet, using it as an absorber layer $1.4/\sin \theta$ interaction lengths. It
 1257 consists of 5 sections along the z-axis, which form rings around the beam-line. Each ring is a layer
 1258 of scintillator tiles at radial distance of 4.07m, except for the center ring. Since it corresponds
 1259 to the $\eta = 0$ ring, there is a minimum amount of absorber material in front of it. The central
 1260 ring is thus two layers of scintillator at radial distances 3.82 and 4.07 m, which sit on either side
 1261 of a 19.5cm thick piece of iron absorber.

1262 The endcap system, the HE, provide a substantial portion of the total η coverage, from
 1263 $1.3 < |\eta| < 3.0$, and contains $\sim 1/3$ of the final state particles in a collision. Like the HB, it is
 1264 a sampling calorimeter with alternating layers of brass and plastic. The demand for radiation
 1265 hardness, and the need for a non-magnetic material, lead to the same choice of C26000 cartridge

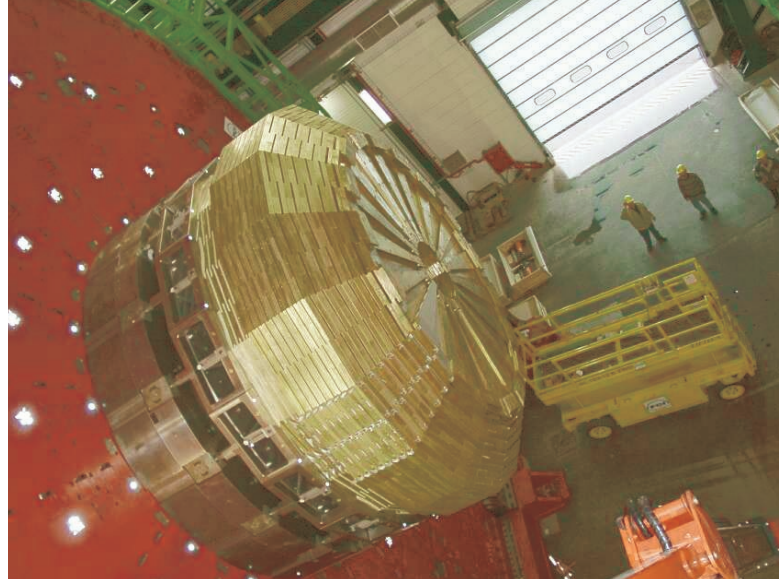


Figure 4.25: HCAL endcap, 18 azimuthal divisions of alternating layers of brass and plastic scintillator [15].

1266 brass found in the HB. It is also divided into 18 azimuthal wedges, and 16 η divisions, giving
 1267 it the same $(\Delta\eta, \Delta\phi) = (0.087, 0.087)$ segmentation. Figure 4.25 shows an image of a partially
 1268 assembled endcap before being installed.

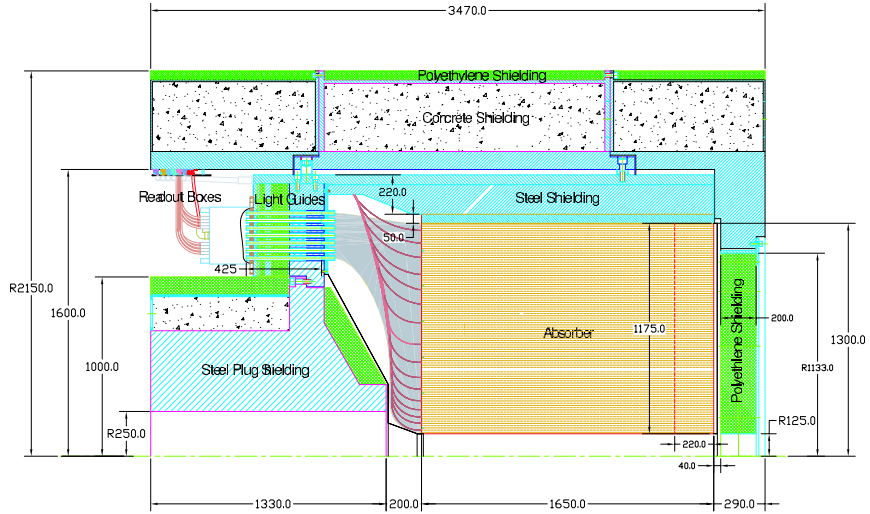


Figure 4.26: Longitudinal cross-section of the HCAL forward calorimetry, the HF [15].

1269 The forward calorimetry, HF, extends the HCAL coverage from $3.0 < |\eta| < 5.0$, and neces-
 1270 sarily must sit in the region of the detector with the largest particle fluxes and thus radiation
 1271 exposure. The HF is a cylindrical steel structure with an inner bore 12.5 cm from the beam line,
 1272 and a outer radius of 130.0 cm. It sits 11.2 m away from the nominal interaction point in the

¹²⁷³ \hat{z} direction. Like the HE, it has 18 azimuthal divisions on either side of the interaction point.
¹²⁷⁴ Relativistic particles that move through the steel generate Cherenkov light, which is collected
¹²⁷⁵ by radiation hard quartz fibers, which transport the light to HPDs which are readout in the
¹²⁷⁶ manner as described above. Since the detection mechanism is Cherenkov light, this sub-system
¹²⁷⁷ is primarily sensitive to the electromagnetic component of the hadronic shower. Figure 4.26
¹²⁷⁸ shows a cross-sectional view of the HF detector.

¹²⁷⁹ 4.4 Muon Chambers

¹²⁸⁰ In pp collisions, muons are only created through electroweak or exotic physics processes, making
¹²⁸¹ the detection of this particle an invaluable tool for reducing the large hadronic backgrounds
¹²⁸² produced at the LHC. The muon chambers, positioned furthest from the beam-line, sit behind
¹²⁸³ the ECAL and HCAL detectors, which absorb almost all of the hadronic activity from a collision.
¹²⁸⁴ They operate in a relatively low flux environment, allowing for robust measurement of their
¹²⁸⁵ kinematics, making it an excellent trigger system. One of the most important discovery channels
¹²⁸⁶ for the Higgs boson, involved the decay of the Higgs into two Z bosons, which decay to two pairs
¹²⁸⁷ of muons. Only 25 events were needed for a statistically significant observation in that channel,
¹²⁸⁸ since the backgrounds had been reduced to only 5 expected events and the muons had provided
¹²⁸⁹ high resolution on the invariant mass of the Higgs.

¹²⁹⁰ The muon chambers are composed of three types of gaseous detector technology: drift tubes
¹²⁹¹ (DTs), cathode strip chambers (CSCs), and resistive plate chambers (RPCs). In the muon barrel
¹²⁹² system (MB), where the magnetic field is uniform DTs provide η coverage, for $|\eta| < 1.4$, and
¹²⁹³ are supplemented by a system of RPCs that provide an independent trigger source and faster
¹²⁹⁴ timing resolution. In the muon endcap system (ME), where the magnetic field would degrade
¹²⁹⁵ the performance of DTs, a system of CSCs and RPCs provide η coverage from $1.4 < |\eta| < 2.4$.

¹²⁹⁶ The DTs are located in the MB system, which is divided into 5 longitudinal, cylindrical
¹²⁹⁷ sections around the beam-line, known as wheels. In each wheel there are 4 concentric layers of
¹²⁹⁸ drift tube stations, one on either side of the magnet return yoke, and two interspersed inside of
¹²⁹⁹ it. Each wheel is divided into 12 azimuthal sections, making 48 stations in the barrel, as shown
¹³⁰⁰ in figure 4.27. Each station on the first three (fourth) layers contain 3(2) superlayers, where
¹³⁰¹ each superlayer is made of a stack of 4 layers of rectangular drift cells, which are staggered
¹³⁰² by half a cell each. Two of the superlayers are oriented such that they are parallel to the
¹³⁰³ beam, measuring the muon in the $r - \phi$ plane. The first three layers contain a third superlayer,
¹³⁰⁴ orientated perpendicular to the beam, measuring a z component of the muon trajectory. Each
¹³⁰⁵ drift cell is a hollow 13×42 mm tube, with a relatively thick 1.5mm wall to provide isolation

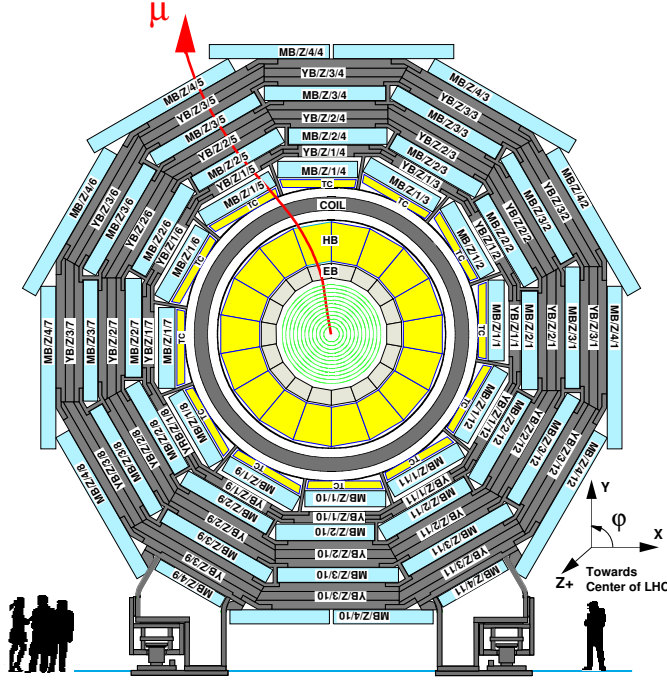


Figure 4.27: Longitudinal cross-section of one of the 5 wheels of the muon system. Drift tubes are placed in 4 concentric layers, with 2 being placed inside the return yoke of the magnet, and 12 azimuthal divisions [15].

1306 between adjacent cells. Each cell is filled with a mixture of 85% argon + 15% CO₂ gas mixture,
 1307 and contains an anode wire that is held at 3600 V that runs down the axis of the cell. The
 1308 walls of the cell are held at 1800 V or -1200 V depending on the wall. When a muon passes
 1309 through the chamber, it's charge ionizes molecules of the CO₂ gas, causing the electrons to drift
 1310 towards the anode wire, and the CO₂ ions drift towards the wall. As the electrons approach the
 1311 anode, they are accelerated and liberate secondary electrons from other CO₂ molecules, creating
 1312 an avalanche of electrons near the wire, resulting in a drop in voltage as they are collected. The
 1313 voltage drop is read out by front end electronics as a signal that a muon has passed through
 1314 the chamber. The Argon gas quenches the avalanche reaction, and the maximum drift time
 1315 for electrons in the gas is 380 ns. This long time scale necessitates the use of an additional,
 1316 fast-timing system, the RPCs. Figure 4.28 shows a cross-section view of a drift cell, including
 1317 electric field lines produced by the potential difference between the anode wire and the walls of
 1318 the drift cell.

1319 The resistive place chambers (RPCs) are the fast timing system chosen to supplement the
 1320 DTs in the barrel, and the CSCs in the endcaps. In the barrel, they are adhered to the top and
 1321 bottom of the first two layers of drift stations. In the outer two layers, they are only adhered
 1322 to the bottom of each station. Figure 4.29(a) shows the layout of the barrel RPC system. The
 1323 muon endcap system is composed of three disks on either side of the interaction point, and is

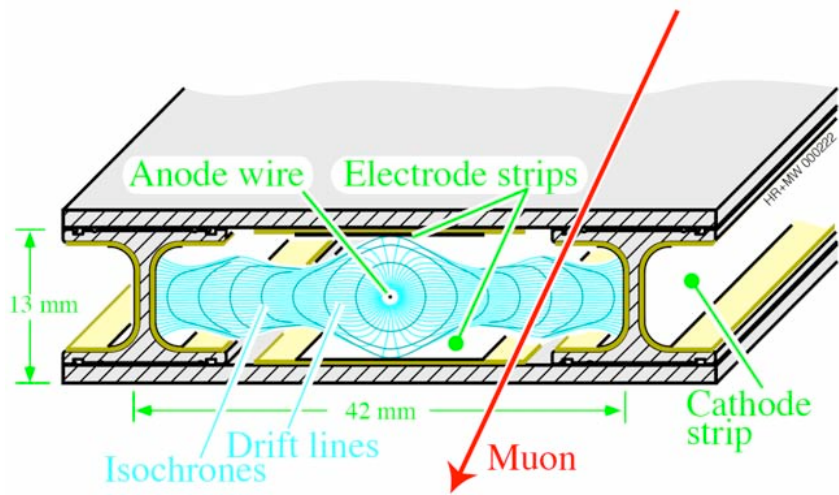
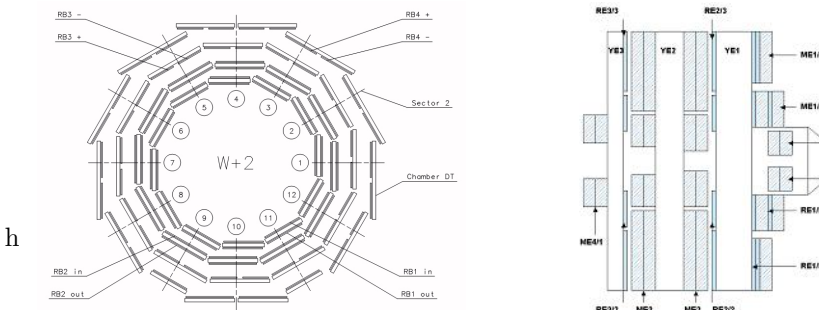


Figure 4.28: A cross-section view of a drift cell. The anode wire is held at 3600 V, creating a potential difference with the walls. Electric field lines are shown in blue [15].

1324 shown in figure 4.29(b). RPCs are mounted on the back of the CSC stations of the innermost
 1325 and outermost disks, and on the front of the CSC for the middle disk. Each RPC consists
 1326 of two plates of high resistance material, one held at a positive voltage, the anode, and the
 1327 other held at a negative voltage, the cathode. The volume between the plates is filled with
 1328 a gas similar to the drift tubes. When a muon passes between the plates, it ionizes the gas
 1329 molecules, and the electrons are accelerated towards the positive plate, creating an avalanche of
 1330 secondary electrons that combine with the positive plate creating a voltage drop that is read out
 1331 as a signal. The timing resolution achieved from the RPCs is less than the 25 ns LHC bunch



(a) A longitudinal cross-section of the muon barrel RPC system. RPCs are attached to the top and bottom of the first two layers of drift stations, and to the bottom of the outer two layers [15]

(b) Cross-section of muon endcap system. It is composed of three disks, with RPCs mounted on the back of CSC system on the first and last disks, and on the front of the CSC in the middle disk [15]

Figure 4.29: RPC layout for the barrel and endcaps

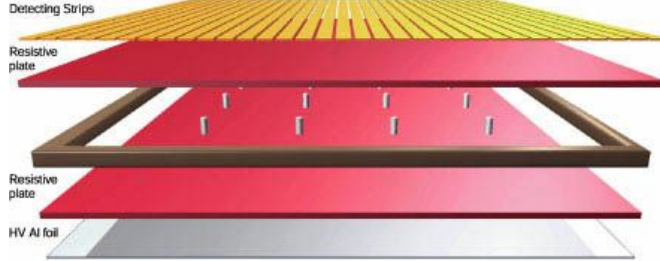


Figure 4.30: Exploded diagram of an RPC [21]

1332 crossing, supplementing the spatial resolution provided by the DTs in the barrel, and the CSCs
1333 in the endcap.

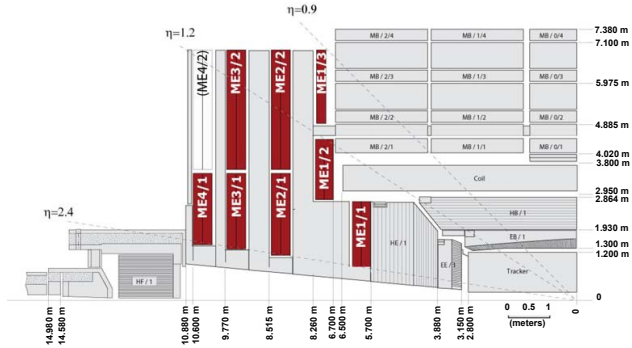


Figure 4.31: Cross-section of one quarter of the muon endcap system, with the 4 disks of CSC systems shown in red [15].

1334 In addition to RPCs, the muon endcap (ME) system, uses cathode strip chambers (CSCs)
1335 to provide additional spatial resolution on muons. Each endcap has 4 layers of CSCs, with a
1336 trapezoidal shape, with 468 cathode strip chambers distributed on each. Three groups of 72 are
1337 located on the inner disk, a group of 36 and a group of 72 in the second and third disk, and
1338 a group of 36 in the outer disk. Figure 4.32 shows the layout of a quarter section of the CSC
1339 system in the ME. A CSC station consists of 6 layers of gas chambers, where each chamber is
1340 an array of anode wires, held at a positive voltage, arranged perpendicular to cathode strips,
1341 held at negative voltage. The volume of the chamber is filled with a gas that is 40% Argon,
1342 50% CO₂, and 10% CF₄. When a muon passes through the volume, the gas is ionized, and now,
1343 since the anode and cathode strips are perpendicular, when the electrons and gas ions combine
1344 with the anode and cathode respectively, a 2-D measurement of the muon's position is recorded.
1345 Figure 4.32 shows a diagram of a CSC chamber with 7 layers to create the 6 gas chambers.

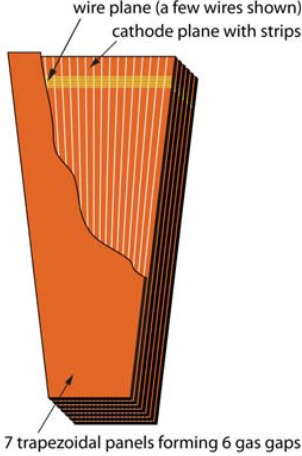


Figure 4.32: A CSC station with 7 layers, making 6 gas chambers. Cathode strips are shown in yellow, perpendicular to the vertical anode wires in orange [15].

¹³⁴⁶ 4.5 Data Collection Overview

¹³⁴⁷ The LHC is designed to deliver protons at 40 MHz, corresponding to a bunch crossing every 25 ns.
¹³⁴⁸ The majority of the interactions will be glancing, low-energy collisions, which do little to reveal
¹³⁴⁹ new phenomenon, and would be impossible to store for analysis. A trigger system is designed to
¹³⁵⁰ select interesting events with a large potential of revealing new physics. The rate is reduced in
¹³⁵¹ two steps through the Level-1 (L1) trigger, and the High-Level Trigger (HLT). The L1 trigger is
¹³⁵² composed of programmable electronics and hardware that buffers the data and perform simple
¹³⁵³ calculations on tracks and calorimeter energy deposits to determine whether an event should be
¹³⁵⁴ kept for analysis. This reduces the event rate from 40 MHz to 10 kHz. The HLT is a computer
¹³⁵⁵ farm of \sim 1000 computer processors, that perform a more sophisticated reconstruction of the
¹³⁵⁶ tracks and energy deposits, as well as more complicated calculations between reconstructed
¹³⁵⁷ objects. This stage reduces the rate to a much more manageable 100 Hz.

¹³⁵⁸ The L1 trigger is composed of local, regional, and global components. The process of deter-
¹³⁵⁹ mining whether to accept or reject the event begins by calculating Trigger Primitive Generators
¹³⁶⁰ (TPGs) based on calorimeter energy deposits, and tracks in the muon chambers. The entire
¹³⁶¹ process has a latency time of $3.2 \mu\text{s}$, which corresponds to the length of the LHC abort gap.
¹³⁶² Sufficiently large data buffers allow the storage of all the events processed during a bunch train,
¹³⁶³ meaning that CMS is capable of running with zero dead time due to detector readout latency.

¹³⁶⁴ In the ECAL a trigger tower consists of a 5×5 array of crystals. Front-end electronics on the
¹³⁶⁵ crystals receive ADC counts on the amplitudes of the photomultipliers, and uses information
¹³⁶⁶ encoded in the electronics to convert this sum to the transverse energy, E_T deposited in the
¹³⁶⁷ crystals. The EB TPG also encodes information about the distribution of energy, and thus the

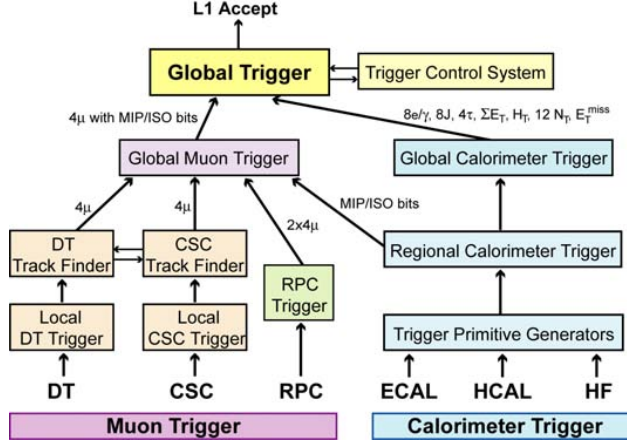
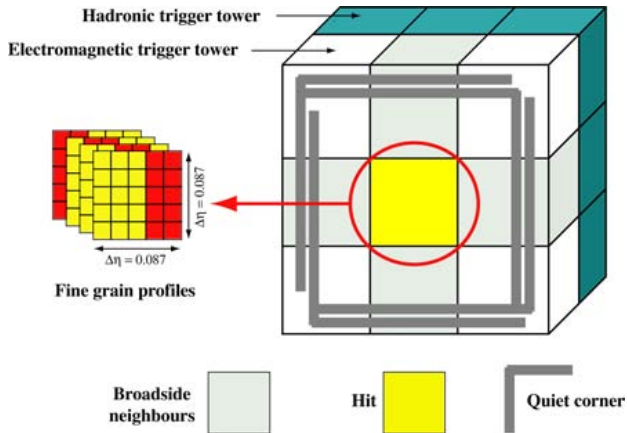


Figure 4.33: A block diagram of the L1 trigger [15]

shower shape in the 5×5 array, which is used to veto anomalous signals. In the HCAL, a trigger tower consists of one of the 16 azimuthal wedges, with segmentation $(\Delta\eta, \Delta\phi) = (0.087, 0.087)$, in the barrel and endcap. Similarly to the ECAL, front-end electronics digitize the signal from the HCAL HPDs, and convert the ADC counts into sums of transverse energy. These calorimeter TPGs are sent to a Regional Calorimeter Trigger (RCT) that is composed of a 4×4 array of trigger towers, with the exception of the HF, which is formed by a single trigger tower.

Figure 4.34: A schematic of the e/γ trigger algorithm [15].

The RCT determines electron and photon candidates from the calorimeter sums. The e/γ trigger searches for the highest energy trigger tower in the ECAL. Within that trigger tower, it checks that the EM shower is contained in a 2×5 array of crystals and that the ratio of ECAL to HCAL energies is less than 5%. It is considered an isolated electron if all eight of its nearest neighbors pass these requirements, and a corner of five neighbors has energy below a threshold requirement. It is considered a non-isolated electron if only the second highest E_T

1380 broadside neighbor trigger tower passes these criteria. Up to four isolated, and four non-isolated
1381 e/γ candidates per RCT are passed to the Global Calorimeter Trigger (GCT).

1382 The GCT determines jets, total transverse energy, missing transverse energy, jet counts, and
1383 H_T (scalar sum of transverse momentum), in addition to the highest rank isolated and non-
1384 isolated *egamma* candidates. Jets are found in a clustering algorithm that looks for large energy
1385 deposits in 2×12 cells of ϕ or η that span 40° and half the detector in each of the coordinates,
1386 respectively. Up to four jets, and four tau jets from the HCAL and four jets from the HF are
1387 forwarded to the Global Trigger (GT).

1388 The non-calorimeter based triggers are based on measurements of the DTs, CSCs, and RPCs
1389 in the muon drift chambers. The barrel DTs look for hit patterns among neighboring tubes in
1390 successive layers, and fits a track segment in the η and ϕ coordinates. The endcap CSCs provide
1391 3-dimensional track segments and are combined with the DTs to form tracks that are passed to
1392 the Global Muon Trigger (GMT). The RPCs provide an independent set of tracks and timing
1393 hits to the GMT. Each bunch crossing the GMTs receive up to four muon candidates in the
1394 barrel RPCs, four from the barrel DTs, four from the endcap RPCs, and four from the endcap
1395 CSCs. The GMT records the candidate's p_T , charge, η , and ϕ position, as well as a quality code
1396 related to the fit of the track to the hit positions of the detector. The GMT sends then sends
1397 these muon candidates to the GT.

1398 The Global Trigger can execute up to 128 trigger algorithms in parallel to analyze the p_T ,
1399 charge, η , and ϕ position, and associated quality codes for muons, electrons, photons, jets, and
1400 missing transverse energy. Most algorithms compare single object characteristics to thresholds
1401 to determine if they pass minimally interesting criteria. If any of the algorithms return a passing
1402 decision, the L1 trigger issues an accept statement that allows the data stored in buffers to be
1403 readout by the CMS Data Acquisition (DAQ) system.

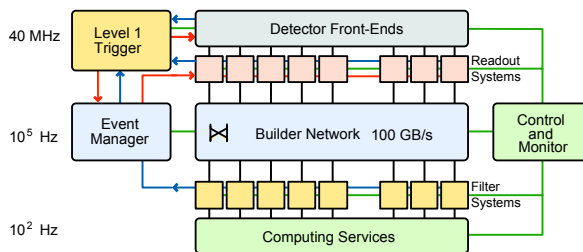


Figure 4.35: Layout of the CMS DAQ [15]

1404 The CMS DAQ collects information from 626 sub-detector Front End Drivers (FEDs), which
1405 extract the buffered information from the various front-end systems, upon the arrival of a L1
1406 trigger accept. An event builder algorithm assembles the fragments from the various sub-systems
1407 into a single coherent event, and transmits the information to the HLT computing farms. Figure
1408 4.35 shows a schematic of the DAQ system.

1409 The HLT computer farm performs the final reduction of data rate, from 100kHz from the
1410 L1 to 100Hz. The computer farm performs basic consistency checks to ensure the quality of
1411 the data, then performs calculations based on topology of the HLT path. Typically, a more
1412 sophisticated reconstruction of an object takes place, and kinematic cuts are applied to the
1413 object or in relationship to other objects in the event. Each HLT path forms its own data set,
1414 thus creating single muon, single electron, electron+jets, etc. type datasets. The unpacked
1415 detector information read by the DAQ is composed of ADC counts for each readout channel,
1416 TPGs, and the L1 decision. This is known as the RAW dataset. Reconstructed physics objects
1417 are stored RECO data tier, and finally an analysis object data (AOD) tier is created containing
1418 only information about the reconstructed objects without having to store detector information.
1419 This last format requires the least amount of data per event for storage, and contains the
1420 reconstructed physics objects, such as electrons, muons, jets, etc. which are be used to search
1421 for new physics phenomenon.

₁₄₂₂ **Chapter 5**

₁₄₂₃ **Particle Reconstruction at CMS**

₁₄₂₄ Charged and neutral hadrons in the form of jets, missing transverse energy (MET), photons,
₁₄₂₅ electrons, muons, and tau leptons are reconstructed at CMS using the particle-flow event-
₁₄₂₆ reconstruction algorithm [24]. The algorithm is based on a three-step process of identifying
₁₄₂₇ charged particle tracks using the muon chambers and silicon tracker, identifying clusters of en-
₁₄₂₈ ergy in the ECAL and HCAL, and linking the tracks to the calorimeter clusters. The calorimeter
₁₄₂₉ energy deposits were calibrated with test beam sources, data from cosmic rays and beam dumps,
₁₄₃₀ and finally from collision data. The algorithm constructs muons by fitting the tracks formed
₁₄₃₁ between the muon chambers, pixel and silicon trackers. Electrons have tracks from the pixel and
₁₄₃₂ silicon tracker matched to the ECAL, with a minimum energy deposited in the HCAL. Jets are
₁₄₃₃ formed from tracks, ECAL, and HCAL clusters falling within a conical angle. The identification
₁₄₃₄ of one, three, or larger odd number of tracks, and the majority of the energy contained in a small
₁₄₃₅ cone size, allows a jet to be tagged as a hadronically decaying tau lepton. Additional algorithms
₁₄₃₆ are also used to identify a jet as coming from the decay of a b-quark, primarily by looking for
₁₄₃₇ secondary vertices in the pixel and silicon tracker.

₁₄₃₈ **5.1 Iterative Tracking**

₁₄₃₉ Since approximately two-thirds of the energy of a jet is carried by charged hadrons, the tracker is
₁₄₄₀ the cornerstone of the particle-flow algorithm [24]. The path of a charged particle in a magnetic
₁₄₄₁ field follows a helical pattern, described by 5 parameters. The extraction of these requires
₁₄₄₂ three 3-dimensional measurements of the particle, or two 3-dimensional measurements and a
₁₄₄₃ constraint on the origin [135]. The pixel detector is ideal for this since each pixel provides a
₁₄₄₄ 3-dimensional measurement of the particle's location. Track reconstruction is the process of
₁₄₄₅ using hits in the pixel and silicon detector elements to estimate the momentum and trajectory of

1446 the charged particle responsible for the hit [135]. The tracking software at CMS is known as the
 1447 Combinatorial Track Finder (CTF), which is based on producing tracks over multiple iterations
 1448 of the reconstruction sequence, removing the tracks with the largest p_T closest to the interaction
 1449 region first, reducing the combinatorial complexity over each iteration.

1450 Each iteration begins by identifying a seed for the particle tracks, which is a minimum
 1451 combination of pixel or silicon tracker hits that is used as an initial estimate of the trajectory
 1452 of the particle [135]. Then, tracks are found by applying the Kalman filter [136]. This method
 1453 is based on applying a small Gaussian uncertainty to the location of the seed hits, fitting an
 1454 initial track to these hits, then looking for additional hits that fall within the error of the initial
 1455 estimate, deeper in the tracker. These hits are added to the fit with their own uncertainties,
 1456 and the fit is re-calculated, each time attempting to minimize the mean-square estimation of the
 1457 error. The 5 helical trajectory parameters are extracted, and tracks with poor fits are discarded.

1458 A total of six iterations are used, each with a different starting seed or kinematic requirement
 1459 on the p_T of the track, as well as the transverse and longitudinal distance from the reconstructed
 1460 vertex [136]. The first iteration is seeded by three hits in the pixel detector. The second, is
 1461 seeded by two hits in the pixel detector and a pixel vertex, which occurs when at least four pixel
 1462 tracks point back to a common origin. The third iteration is seeded once again by three hits in
 1463 the pixel detector, except with a looser minimum p_T cut. The fourth iteration uses seeds from
 1464 any three hits in the pixel detector or silicon tracker, with at least one hit coming from the pixel
 1465 detector. In the fifth iteration seeds are formed from the inner two rings of the TIB, TID, and
 1466 TEC. The final iteration begins with seeds from the first two rings of the TOB and the fifth ring
 1467 of the TEC.

1468 5.2 Calorimeter Clustering

1469 The clustering algorithm is used to detect the energy and direction of stable, neutral particles
 1470 such as photons and neutral hadrons [24]. It also separates the energy contributions from
 1471 the neutral and charged hadrons, and provides an additional energy measurement for charged
 1472 hadrons with very low or high p_T tracks, both cases that degrade the energy resolution. Finally,
 1473 the clustering algorithm properly accounts for bremsstrahlung energy losses from electrons. The
 1474 algorithm is performed independently for the ECAL barrel, ECAL endcaps, HCAL barrel, and
 1475 HCAL endcaps. In the HF, no clustering algorithms are used, as each cell is used as its own
 1476 cluster in an event.

1477 The clustering algorithm begins by identifying "cluster seeds", which are the highest p_T cells
 1478 above a defined energy threshold [24]. Then, "topological clusters" are formed by grouping

1479 adjacent cells together with energy above 80 MeV in the ECAL barrel, 300 MeV in the ECAL
1480 endcaps, and 800 MeV in the HCAL. As a new cell is added, the total cluster energy and
1481 position is updated until no new cells are able to be added. Each cluster seed thus gives rise
1482 to a "particle-flow cluster". Each of these clusters is used as a candidate to be associated with
1483 tracks during the third stage of the algorithm, the linking step.

1484 5.3 Calorimeter Energy Calibration

1485 One of the most critical steps in reconstructing particles is the calorimeter energy calibration,
1486 which is the conversion of calorimeter scintillator light and photodetector current to the energy
1487 deposited in the calorimeter by the particle traversing it. This is done by exposing the crystals
1488 to particles of a known energy, using large samples of cosmic ray muons, by measuring minimum-
1489 bias events assuming a ϕ symmetry, the of π^0 and η^0 meson resonances decaying into photons,
1490 and W and Z bosons into electrons.

1491 Before installation at P5, the ECAL and HCAL were pre-calibrated using a dedicated "test
1492 beam" of known energy. In 2006, the ECAL was exposed to an electron beam with energies
1493 between 15 and 250 GeV [137] at CERN. Additionally, intercalibrations between crystals were
1494 performed with 90 and 120 GeV beams. Also at CERN in 2006, the HCAL was calibrated, prior
1495 to installation, using a beam of 50 GeV pions [138].

1496 Once both calorimeters were installed, the detectors were calibrated with cosmic ray muon
1497 events in 2007 with the CMS magnet de-energized during the CRUZET (Cosmic RUn at ZEro
1498 Tesla) data taking campaign, and again with the CMS field on in 2008 during the CRAFT
1499 (Cosmic Run At Four Tesla) campaign. Shortly after the CRAFT campaign, the LHC delivered
1500 450 GeV proton beams to collimator targets upstream of the CMS detector, creating accelerated
1501 muons that were additionally used to calibrate the detector response. The ECAL endcap energy
1502 resolution was improved from 7.6% to 6.3%, and in the barrel, the intercalibrations from the test
1503 beam were validated at a 2% level of agreement [139]. The HCAL energy calibration resulted in
1504 5% energy resolution in the HB, 10% in the HE, 12% in the HF, and 5% in the HE[140].

1505 After an initial set of data collection three independent calibration methods are combined to
1506 determine the absolute energy scale and intercalibration coefficients for the crystals [22]. The first
1507 method uses a large amount of data collected from minimum-bias trigger events, events which
1508 are dominated by glancing collisions and QCD jet production. The processes that contribute
1509 to these events have final state particles symmetrically distributed in the ϕ coordinate. By
1510 grouping the crystals into rings of η , and the response of each crystal can be determined and
1511 modified such that it matches the average crystal response in that η ring, with the uncertainty on

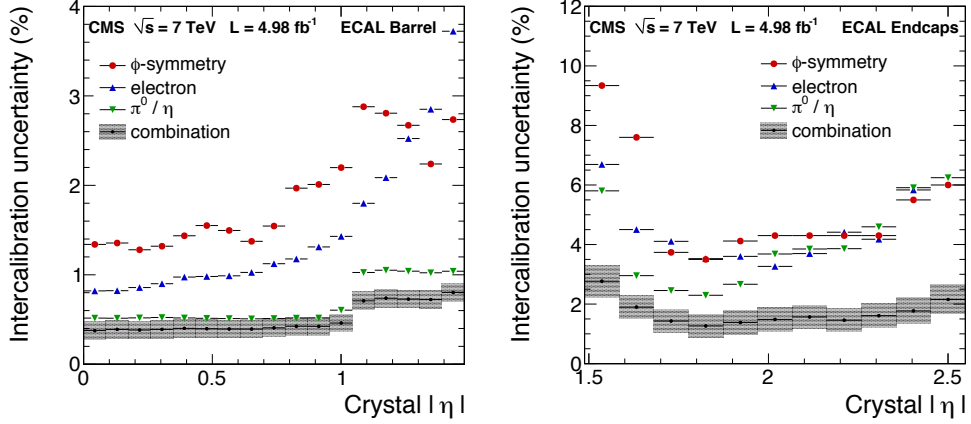


Figure 5.1: Results of the uncertainty on the ECAL intercalibration coefficients for the barrel (left) and endcaps (right) [22].

the average representing the uncertainty on the intercalibration coefficient. The second method involves reconstructing the resonances of the π^0 and η^0 mesons decaying to two photons and relying on the high-precision measurements from other experiments to determine the exact mass of the resonance. Events near the resonance of these two particles are once again divided into rings of η , and averaged over the ϕ coordinate. Decays of the Z boson to an electron pair are also used to determine the absolute scale (ADC counts/GeV) of the crystals, once again relying on the higher-precision measurements of previous experiments for the location of the mass peak. Finally, comparisons between the energy measured in the tracker and that measured in the ECAL are made from W and Z boson decays to electrons. Figure 5.1 shows the results of combining all three methods, to determine the uncertainty of the intercalibration coefficients.

The ECAL also has a strong dependence on the rate of instantaneous luminosity that the crystals are exposed to. It is therefore necessary to perform additional crystal calibrations as a function of time during a run of data collection. Blue and orange LED light, and blue laser light is fed through a network of optical fibers to each crystal. A known amount of light is injected and the crystal response is measured. Figure 5.2 shows a plot of the crystal response versus time. Rings of η are formed and crystals within the same η ring are used to calculate an average response, as is done in the intercalibration procedures described above.

The performance of the HCAL calibration to the 50 GeV pion beam is validated by comparing energy measurements in the tracker to energy deposits in the HCAL [141]. Since neutral hadrons contribute approximately 10% of the energy contained in a jet, it is necessary to recalibrate the measured energy in the HCAL using simulated events where the true hadronic energy is known. The equation for the total calorimeter energy is given by:

$$E_{\text{calib}} = a + b(E, \eta)E_{\text{ECAL}} + c(E, \eta)E_{\text{HCAL}} \quad (5.1)$$

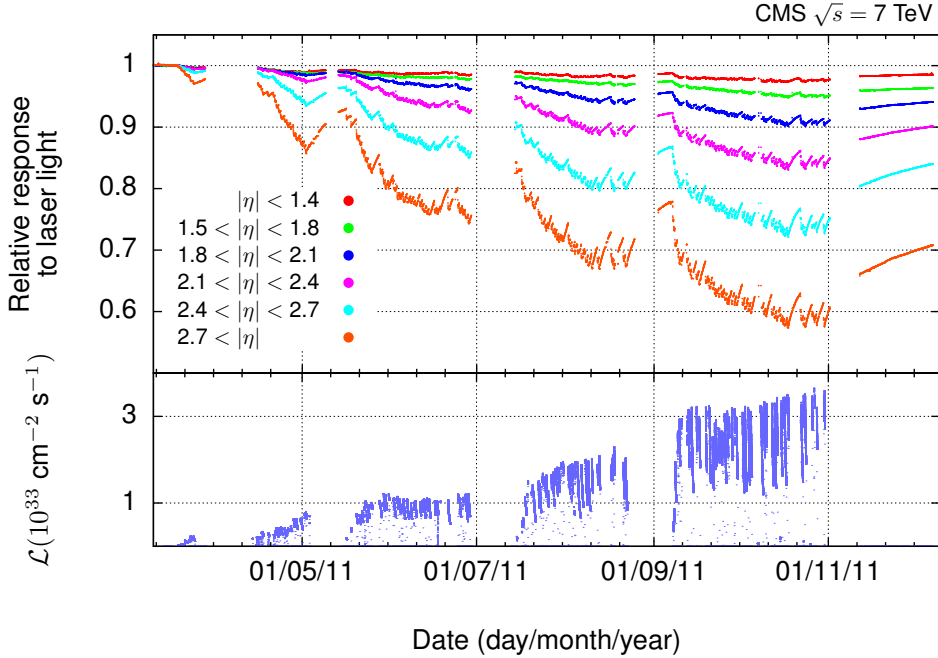


Figure 5.2: Instantaneous luminosity response to the crystals as measured by the laser and LED system. Additional crystal calibration constants are derived to normalize the crystal response over the range of collected data [23]

1534 The coefficients, a, b, and c are determined through a χ^2 -minimization procedure over each bin
 1535 of energy, minimizing the difference between the reconstructed and true energies and solving for
 1536 the parameters a, b, and c. Figure 5.3 shows the resulting HCAL energy resolution as a function
 1537 of energy, and the values of the coefficients a, b, and c.

1538 5.4 Linking

1539 Once clusters are formed in the ECAL and HCAL barrels and endcaps, they are associated with
 1540 nearby tracks in the pixel and silicon tracker in the step of the particle-flow algorithm known as
 1541 linking [24]. Single particles are formed out of the tracks and calorimeter clusters without double
 1542 counting contributions from different detectors, forming "blocks" of linked elements. Due to the
 1543 high granularity of each sub-detector, blocks of two to four elements are typical.

1544 The linking procedure between pixel and silicon strip tracks and the calorimeter deposits
 1545 occurs in three steps: extrapolating the track to the ECAL preshower (PS); then to the ECAL
 1546 to a depth corresponding to the maximum longitudinal shower profile; and finally to the HCAL
 1547 to a depth corresponding to one interaction length. A track is then linked to a cluster if it falls
 1548 within the cluster boundaries. One HCAL cluster may be associated to many tracks, but each
 1549 track can only be associated with a single cluster, determined as the track with the shortest

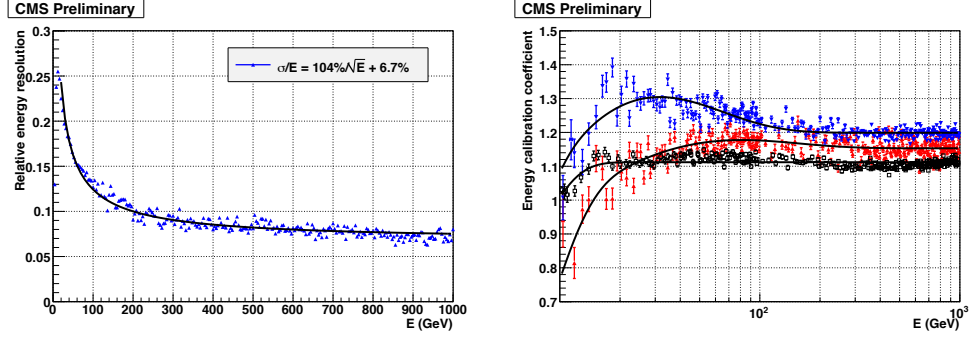


Figure 5.3: Results of using a χ^2 minimization procedure to estimate the neutral hadron energy contribution in the HCAL using simulated events[24]

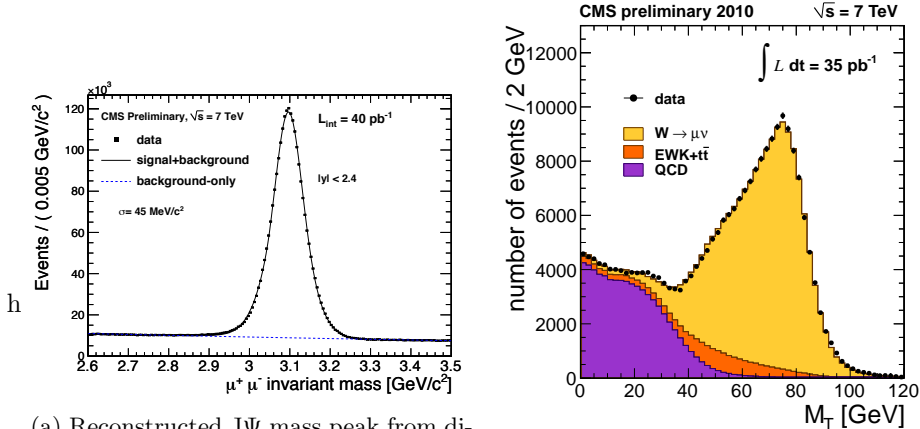
1550 distance to the center of the HCAL cluster in the case of many candidates. For the ECAL, one
 1551 track may be associated with many energy clusters, since they may have originated from hadronic
 1552 shower fluctuations, so links to tracks should be preserved to avoid double counting the hadron
 1553 energy. In order to account for the bremsstrahlung energy losses of electrons, tangent lines to
 1554 the tracks are linked to the ECAL. If this extrapolated, tangent track falls within the ECAL
 1555 cluster boundaries, it becomes a candidate for a bremsstrahlung photon from an electron. Since
 1556 the ECAL has a finer granularity than the HCAL, clusters of the ECAL are linked to HCAL
 1557 clusters if an ECAL cluster falls within the boundary of the HCAL cluster. Finally, linking
 1558 between the muon chambers and the inner tracker occurs via a χ^2 fit to a muon trajectory that
 1559 would traverse the entire detector.

1560 5.5 Physics Object Reconstruction

1561 Once tracks have been formed from the muon chambers, pixel, and silicon tracker detectors
 1562 and linked to clusters in the ECAL and HCAL, particles can be reconstructed. The process
 1563 begins by reconstructing muons, then electrons and photons, finishing with charged and neutral
 1564 hadrons. The charged and neutral hadrons are then clustered together to make jets, which
 1565 can be tagged as τ or b -jets. After each object is formed, the tracks and calorimeter energy
 1566 depositions associated with it are removed from the collection of blocks that are used to form
 1567 the particle-flow candidates, ensuring that no double counting of energy contributions is taking
 1568 place.

1569 5.5.1 Muon Reconstruction

1570 The reconstruction of physics objects in the particle-flow algorithm begins by identifying muons
 1571 [24]. The algorithm begins by identifying tracks in the pixel and silicon strip detectors that have



(a) Reconstructed J/ψ mass peak from di-muon events in 7 TeV data, used to commission low p_T muons reconstructed with the particle flow algorithm [142].

(b) Transverse mass peak of W boson events reconstructed from single muon events in 7 TeV data, used to commission high p_T muons reconstructed with the particle flow algorithm [142].

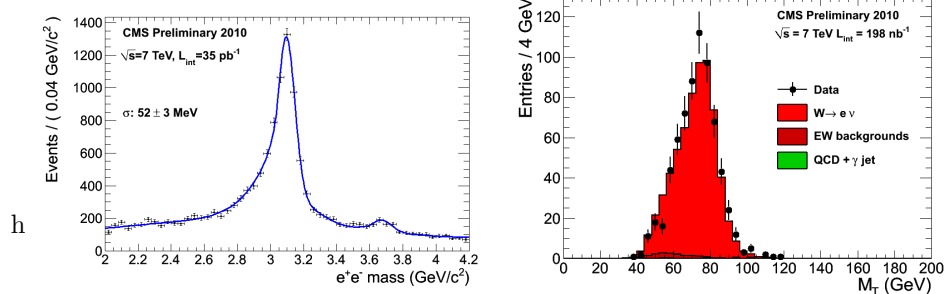
Figure 5.4: Muon validation plots for the particle-flow reconstruction

been linked to tracks in the muon chambers, and fit with a muon trajectory with a minimum χ^2 . Additionally, it is required that muon track that is fit with both muon chambers, pixel, and silicon tracker information is compatible, within 3 sigma, to a track fit with the pixel and silicon tracker information alone. When the "particle-flow" muon is removed from the collection of candidate blocks, 3 (0.5) $\text{GeV} \pm 100\%$ is removed from the HCAL (ECAL) cells that the muon traverses, based on studies from the CRAFT data run.

In 2010, 7 TeV data was collected [143] in order to commission the reconstruction of muons. The J/ψ resonance at 3.1 GeV provides a large number of low p_T di-muon pairs. Figure 5.4(a) shows the reconstructed J/ψ mass with 40 pb^{-1} of data. High p_T muons are commissioned by reconstructing the W boson mass. Figure 5.4(b) shows the results the first 35 pb^{-1} of 7 TeV data.

5.5.2 Electron Reconstruction

The next stage in particle-reconstruction is the identification of electrons [24]. Electrons leave hits in the tracker and deposits most of their energy into the ECAL, with the clustering widest in the ϕ direction due to bremsstrahlung. Electron tracks tend to be shorter and lose energy in the tracker due to bremsstrahlung, a highly non-linear process, that the Kalman fitter used in the track identification phase is not optimized for. These tracks are re-fit using the Gaussian Sum Filter (GSF) algorithm [144]. This algorithm accounts for the change in trajectory of the electron due to bremsstrahlung, extending the linking to ECAL clusters in the ϕ direction. Blocks that have GSF tracks linked to ECAL clusters, including clusters identified as bremsstrahlung



- (a) Reconstructed J/Ψ mass peak from di-electron events in 7 TeV data, used to commission low p_T electrons reconstructed with the particle flow algorithm [145].
- (b) Transverse mass peak of W boson events reconstructed from single electron events in 7 TeV data, used to commission high p_T electrons reconstructed with the particle flow algorithm [146]

Figure 5.5: Electron validation plots for the particle-flow reconstruction

1592 photons, and additionally linked to an HCAL cluster with a much smaller energy deposition
 1593 than in the ECAL are then identified as a "particle-flow electron".

1594 Similarly to the muons, the electron identification from the particle-flow algorithm was com-
 1595 misioned using 7 TeV data collected in 2010. Low p_T electrons were commissioned from the
 1596 J/Ψ mass peak, shown in figure 5.5(a) and high p_T electrons were commissioned from W boson
 1597 decays, shown in figure 5.5(b).

1598 5.5.3 Charged Hadron Reconstruction

1599 Charged hadrons are reconstructed next in the particle flow algorithm [24]. Tracks linked to
 1600 both ECAL and HCAL energy deposits give rise to "particle-flow charged hadrons" if calorimeter
 1601 energy is compatible to what is measured from the curvature of the tracks in the pixel and silicon
 1602 detector. A fit is then performed between all of the tracks and the HCAL energy clusters to
 1603 determine an optimally-measured momentum. In the case where there is only one track, this fit
 1604 reduces to a weighted average between the track and HCAL energy clusters.

1605 5.5.4 Photon and Neutral Hadron Reconstruction

1606 The next step in the algorithm is to identify ECAL and HCAL energy clusters that aren't linked
 1607 to tracks or clusters that are linked to tracks, but have a much larger energy measurement . In
 1608 the latter case, blocks are kept if the excess energy in the calorimeter clusters is larger than the
 1609 energy resolution of the calorimeter. In both cases, if the total energy excess in the HCAL is
 1610 larger than the energy measured in the ECAL, than a "particle-flow photon" is created using the
 1611 energy in the ECAL and the remaining HCAL energy forms a "particle-flow neutral hadron",
 1612 with calibrations performed in the manner described in section 5.3. In the case where the ECAL

energy is larger than the HCAL energy, both cluster energies form a particle-flow photon. This is justified by the observation that, in jets, the neutral component of the hadronic energy only deposits 3% of the total jet energy in the ECAL, compared to 25% of the jet energy from photons.

5.5.5 Jet Reconstruction

After the formation of photons, charged and neutral hadrons, and jets can be formed by clustering groups of these objects together based on their momentum weighted, spatial separation from one another. This clustering procedure is performed with the anti- k_T algorithm [25]. The momentum weighted spatial separation function between two particles, i and j , is defined as:

$$d_{ij} = \min\left(\frac{1}{p_{iT}^2}, \frac{1}{p_{jT}^2}\right) \frac{\Delta_{ij}^2}{R^2} \quad (5.2)$$

where $\Delta_{ij}^2 = (y_i - y_j)^2 + (\phi_i - \phi_j)^2$ and $y_{i,j}$ is the rapidity, and ϕ is the azimuthal angle in the CMS detector. R is the distance parameter, which is a user-defined quantity for the algorithm.

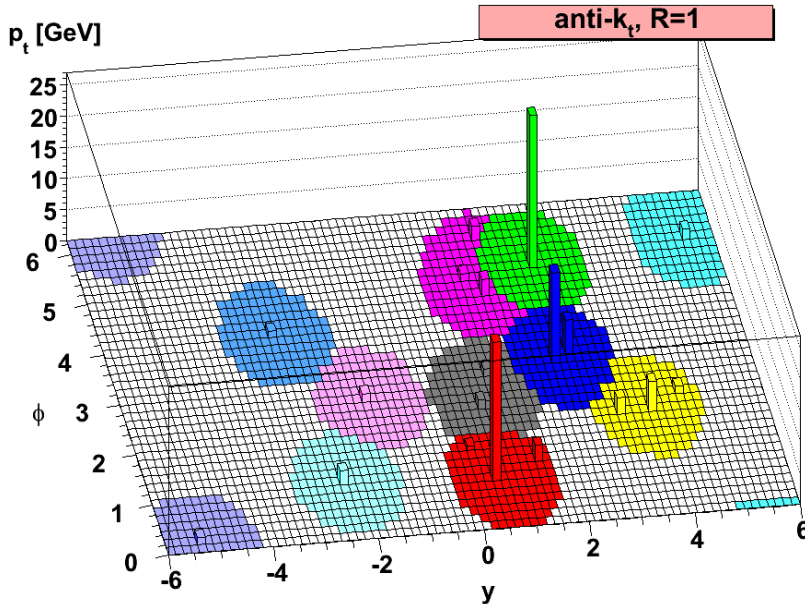


Figure 5.6: The anti- k_T jet clustering algorithm with distance parameter $R=1.0$ [25]

The algorithm proceeds by looping over all of the particle-flow candidate objects that have been formed and calculates the quantity d_{ij} , and combines the two objects with smallest value, into a single object. The process is repeated until the smallest value, d_{ij} has a value $d_{ij} > \frac{1}{p_{Ti}^2}$ for all remaining pairs. The parameter, d_{ij} , will be larger for two small p_T objects, when compared to a pair of equally spatially separated high p_T objects. Thus, softer particles will cluster around harder objects before clustering amongst themselves. If no hard particles are present within the distance parameter, then the object will accumulate soft particles in a circle of radius R . The

tendency is to produce circular jets, but in the case where a soft p_T cluster intersects with a hard p_T cluster, the $1/p_T^2$ weighting will tend to favor clustering around the harder p_T object. Figure 5.6 shows an example of the results of an anti-kt algorithm with distance parameter $R = 1.0$, in the azimuthal-rapidity coordinate system. An example of the preferential grouping around harder p_T objects can be seen at $\phi = 5, y = 2$.

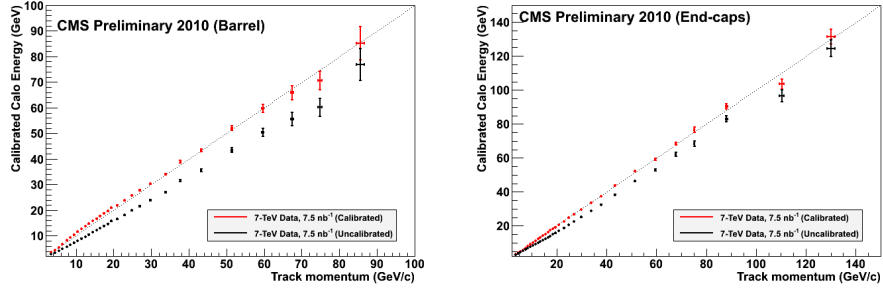


Figure 5.7: Commissioning of the particle-flow algorithm on jets, involved comparing the energy measured from charged hadron tracks, to energy measured in calorimeter clusters linked to the tracks [26].

In 2010, the particle-flow algorithm for jet reconstruction was commissioned with 7 TeV data [26]. The calibration procedure involved selecting charged hadrons from tracks in the pixel and silicon strip detector, and comparing the energy measured there to the energy measured in the calorimeter. After calibration, the measurements between tracker and calorimeter agree within error bars up to 100 GeV, as shown in figure 5.7.

1640 Hadronic Tau Reconstruction

Tau leptons are unstable particles which decay via the weak interaction. If the resulting W boson decays hadronically to two quarks, the tau lepton can be reconstructed by analyzing the resulting jets that are clustered by the anti-kt algorithm. Tau jets are characterized by the number of charged hadrons produced in the decay. Since charge must be conserved, this results in one charged hadron being produced $\sim 85\%$ of the time, known as a "one-pronged" decay, and three charged hadrons being produced $\sim 15\%$ of the time, known as a "three-pronged" decay. Thus, a tau jet is identified as a jet with only 1 or 3 tracks associated with the calorimeter cluster. Additionally, the jets from hadronic tau decays tend to have their energy more collimated than jets produced from quarks or gluons. Jets are clustered twice, using two different distance-parameters. The ratio of energies of the smaller to the larger of the distance parameter jets is used to determine how collimated a jet is. If the ratio is within a given threshold, determined by the analyst in terms of the reconstruction efficiency and fake rate, the jet is tagged as a hadronic tau jet.

1654 **b-Tagging**

1655 Jet that originate from b -quarks have unique characteristics that allow them to be distinguished
1656 from jets originating from other quarks or gluons. This identification process is known as b
1657 tagging. Several algorithms exist to identify b jets, since there are many kinematic variables
1658 that distinguish them from other jets. Due to the heavier nature of the b quark, b jets have
1659 a larger transverse momentum compared to lighter-flavor quarks. Since it belongs to the third
1660 quark generation, it is much more likely to find a non-prompt lepton embedded in the jet. Muons
1661 are especially useful to tag b jets since the information they leave in the tracker can be used to easily
1662 identify if it came from prompt decay or not.

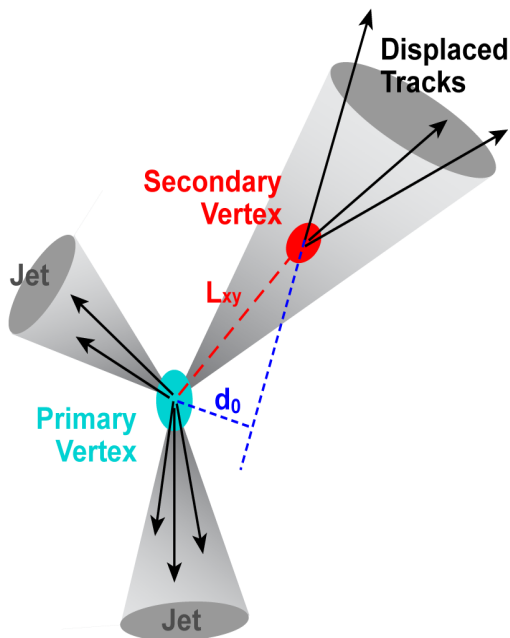


Figure 5.8: A b -meson will travel a distance L_{xy} before decaying and creating a secondary vertex. The impact parameter, d_0 measures the longitudinal displacement of the two vertices [27].

1663 The most important characteristic of the b quark is its relatively long lifetime compared to
1664 light-flavor quarks. The consequence is that a B -hadron will travel a very small, but observable
1665 distance within the tracker before it decays, forming a secondary vertex. The distance and
1666 uncertainty measured on the distance between the primary and secondary vertex is then used as
1667 discriminating variables to tag b -jets. Figure 5.8 shows a cartoon of a b jet creating a secondary
1668 vertex after traveling some distance from the primary vertex.

1669 **5.5.6 Missing Transverse Energy Reconstruction**

1670 CMS has a hermetic design to ensure that all particles produced in a collision would pass through
1671 the detector. Only long-lived, neutral particles avoid detection, such as neutrinos in the standard

1672 model. Many BSM theories, such as SUSY, are also characterized by stable, neutral particles.
1673 These particles can only be detected by measuring a momentum imbalance after measuring all
1674 of the particles in the event.

1675 The missing transverse energy (MET), \cancel{E}_T , is the vector sum of all of particle-flow candidates
1676 reconstructed in the event. It is defined as

$$\cancel{E}_T = \left| - \sum_{i=1}^{nPF} \vec{p}_{Ti} \right| \quad (5.3)$$

1677 where nPF is the number of particle-flow candidates in the event, and \vec{p}_{Ti} is the vector sum of
1678 their transverse momentum.

1679 The particle-flow algorithm for reconstructing MET was commissioned in 2010 with 7 TeV
1680 data [26]. Minimum-bias collisions and QCD multi-jet production are processes that produce no
1681 real MET. Therefore, a sample of these events were collected, allowing for the algorithm to be
1682 tuned and calibrated.

1683 Chapter 6

1684 Analysis I: The first 5.08 fb^{-1} of 1685 8 TeV data

1686 The search for $t\bar{t}H$ production begins by identifying pp collisions consistent with the production
1687 of a top-quark pair with additional b jets. Top quarks decay $\sim 100\%$ of the time to a bottom
1688 quark and a W boson, and the W boson can decay either into a charged lepton and a neutrino
1689 or into a pair of quarks. Since there are two W bosons in the event, the decays of the W
1690 bosons determine the specific top-pair signatures recorded in the detector. The decay of the two
1691 W bosons define the categorizations of $t\bar{t}$ -like events as either all-hadronic, in the case of zero
1692 charged leptons; semi-leptonic, in the case of one charged lepton; and di-leptonic in the case of
1693 two charged leptons. This analysis describes the Lepton+Jets (LJ) channel, where one of the W
1694 bosons has decayed to an electron or a muon and the corresponding neutrino, while the other
1695 W boson decays into two quarks. To compensate for the low production rate, the analysis is
1696 optimized to search for the Higgs boson decaying to a b -quark pair, since the branching ratio to
1697 b -quarks is highest for the mass range favored by the exclusion limits of LEP and the Tevatron,
1698 as well as preliminary results by CMS and ATLAS, for a Higgs boson mass of ~ 125 GeV.
1699 The final state is then $l\nu qqqbb$, where l refers to either an electron or a muon. In the case
1700 of an ideal reconstruction of the event, the LJ signal events contains six jets, four of which
1701 are b -tagged. However, to accommodate jets lost to detector acceptance and merging between
1702 separate partons, and the b -tagging efficiency, events with four or more jets and two or more b
1703 tags are included in the signal region.

1704 The largest background contribution is $t\bar{t}+\text{jets}$ production. This process can be decomposed
1705 in terms of the flavor of the extra jets produced in the event. For this analysis, the inclusive
1706 $t\bar{t}+\text{jets}$ process is broken into three sub-processes: $t\bar{t}+$ light flavor jets where one or more of

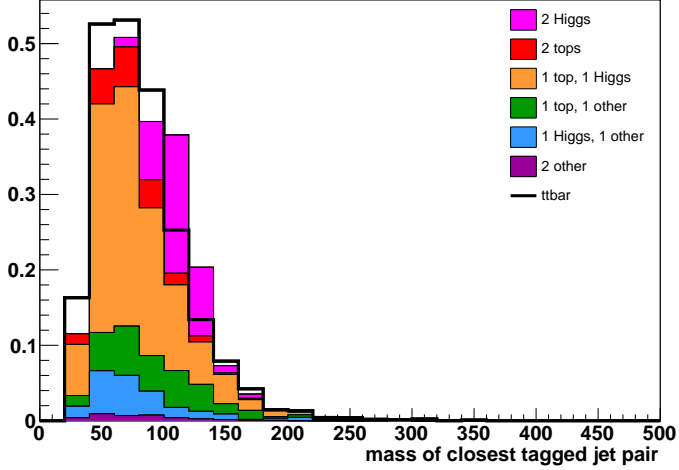


Figure 6.1: This figure shows the breakdown of jet-to-parton assignments for the two jets with the minimum ΔR separation in the event for events with greater or equal 4 b -tagged jets.

1707 the jets is mistagged, $t\bar{t} + c\bar{c}$ and $t\bar{t} + b\bar{b}$. Smaller background contributions come from $W+jets$,
1708 $Z+jets$, single top quark, diboson, and $t\bar{t} + W/Z$ production.

1709 In other Higgs searches involving the decay to two b -quarks, the most powerful discriminating
1710 variable is the invariant mass of the $b\bar{b}$ pair, which has a peak at the mass of the Higgs. However,
1711 for $t\bar{t}H$ production, with a final state of four b -quarks, the combinatorics of selecting the quarks
1712 coming from the Higgs, instead of the $t\bar{t}$ system, prevents the reconstruction of a clear resonant
1713 peak, as shown in figure 6.1. This results in an additional loss of mass resolution, or smearing,
1714 on the $b\bar{b}$ invariant mass spectrum.

1715 Although there is poor resolution on the Higgs boson resonance in the b -quark dijet mass
1716 spectrum, there are a number of kinematic variables that can be used to discriminate between
1717 the $t\bar{t}+jets$ background and the $t\bar{t}H$ signal. For example, the recoil of the Higgs off of the
1718 $t\bar{t}$ system, the decay products of the top quarks from the $t\bar{t}H$ signal will have, on average, a
1719 slightly larger component of momentum transverse to the beam-line. Additionally, the larger
1720 number of authentic b -jets in $t\bar{t}H$ events can be exploited through the likelihood value returned
1721 by a b -tagging algorithm for all of the jets in the event. By themselves, none of these variables
1722 provide a large degree of discriminating power to separate the $t\bar{t}H$ signal from the large, and
1723 kinematically-similar background. Therefore, the discriminating power of several variables is
1724 combined using a multivariate analysis technique (MVA), which is used to set upper limits on
1725 $t\bar{t}H$ production in the data set.

1726 The following sections will describe the analysis that was carried out on the first 5 fb^{-1} of
1727 data collected by the CMS detector at 8 TeV. This includes definitions of the simulated samples
1728 used to estimate the expected backgrounds in data, the event selection used to isolate the $t\bar{t}H$

1729 signal, the application of MVA techniques, evaluation of systematic uncertainties, and upper
1730 limit setting on the production rate of $t\bar{t}H$.

1731 6.1 Data and Simulated Samples

1732 pp collision data is collected by the CMS detector, as described in previous chapters. The
1733 signal and background signatures are estimated using Monte Carlo simulation techniques. The
1734 simulation involves the combination of the most current theoretical and empirical information
1735 about the interactions of the known particles. The simulation of an event is decomposed into
1736 a sequence of calculations and each signal and background process is calculated separately.
1737 Information about Monte Carlo event simulation techniques is taken from reference [147].

1738 The first stage of event simulation for a given signal or background process is to calculate
1739 the probability that some set of initial state particles with a certain momentum will create a
1740 final state of particles with a certain momentum. For example, in the case of the $t\bar{t}H$ signal, this
1741 is the probability that two protons traveling towards each other along the z-axis (beam-line),
1742 each with a given energy and momentum, will produce a top-quark pair and a Higgs boson,
1743 each with some momentum vector, \hat{p}_t , $\hat{p}_{\bar{t}}$, \hat{p}_H , which points into the hermetic CMS detector. As
1744 discussed in section 2.1, this probability is calculated by examining the Lagrangian of the theory
1745 describing the process and calculating its scattering amplitude, to some order in perturbation
1746 theory, using the Feynman rules derived from the Lagrangian. The scattering amplitude is a
1747 multi-dimensional probability function, which depends on the initial- and final-state momenta
1748 of the particles in the process. Thus, given some initial state momentum, p_i , it tells you the
1749 probability to produce a final state particle with momentum p_f . It is understandable that the
1750 scattering amplitude is often referred to as a matrix element, since given a vector of initial state
1751 particles with a certain momentum, the scattering amplitude would be a matrix, whose elements
1752 would give the probability of creating the vector of final state particles.

1753 Since protons are composite objects, when they collide, it is their quarks or gluons which
1754 are actually interacting. The momentum distribution of each of the valence quarks, the gluons,
1755 and the sea quarks, which account for quantum fluctuations that temporarily create all other
1756 quark flavors inside the proton, is described by a Parton Distribution Function (PDF). The PDF
1757 describes what fraction of the proton's momentum is distributed among each of its constituents.
1758 Due to the large strength of the QCD interactions that bind the quarks together, the PDF cannot
1759 be calculated perturbatively from QCD. It has been measured empirically, and is a composition
1760 of the results of several experiments over the past decades.

1761 Event generator algorithms are computer programs that, given a Lagrangian of particle

theory, will calculate the matrix element for a given process. Then, the generator is provided with values of the momenta of the initial state particles. For protons, this would be the beam energy of the LHC. To assign momentum values to the constituent quarks or gluons that actually participate in the interaction, random values are sampled from the probability distributions described by a PDF that is provided to the algorithm. Given a choice of momentum for the input particles, a value and direction of the momentum for each of the final state particles is sampled from the probability function provided by the calculated matrix element (ME). The process of randomly sampling a probability function, in order to conduct a calculation, is known as a Monte Carlo sampling technique.

In the case where final-state particles are quarks or gluons, also known as partons, an additional calculation is necessary to create the physical hadron states. First, the decay sequence of each parton is calculated until the decay products reach a user-defined value, known as the hadronization scale. This decay sequence is referred to as the parton shower (PS), since each parton creates a multitude, or a shower, of additional partons. Once the parton shower is calculated, each of the colored partons are transformed into color-singlet primary hadrons, which themselves decay, and form secondary hadrons. This process, known as hadronization, results in a collimated spray of hadrons, each with a component of momentum along the original parton's direction. These hadrons are clustered together and referred to as a hadron jet.

Once the hadronization is completed, the next stage of the event generation is to simulate the response of the CMS detector when this process occurs at the interaction point where the LHC beams are made to collide. The Geant 4 detector simulation framework is used to create a model of each and every detector element, electronic readout, and mechanical support structures that compose CMS [148]. Geant 4 also describes how energy is deposited into the different types of material as a particle passes through each detector element, simulating the response of each element to the presence of a particle in the detector. The digitization and signal acquisition of the electronics that read-out the detector elements is also simulated.

The final stage of the generation of an event is the reconstruction of the simulated detector signals into physics objects. This process is described in detail in the previous chapter. It proceeds with simulated, instead of real, detector signals.

The entire event simulation, reconstruction, and subsequent analysis is implemented in a software framework that is known as CMS Software (CMSSW).

6.1.1 Data Samples

The results presented here are based on the first 5.08 fb^{-1} of the 2012 CMS dataset. Data-sets are collected through HLT triggers and stored offline for analysis. Table 7.1 lists the datasets

1796 used for this analysis, which is composed of two runs of data collection triggered on the presence
1797 of one muon or electron in an event. The luminosities are quoted from a calculation performed
1798 with minimum-bias events measured with the HF detector and have been determined to have a
1799 2.2% uncertainty.

Dataset	Run Range	Integrated Luminosity
SingleMu, Run2012A, PromptReco	190645–193621	0.87 fb^{-1}
SingleMu, Run2012B, PromptReco	193834–196531	4.21 fb^{-1}
Total SingleMu	190645–196531	5.08 fb^{-1}
SingleElectron, Run2012A, PromptReco	190645–193621	0.87 pb^{-1}
SingleElectron, Run2012B, PromptReco	193834–196531	4.21 pb^{-1}
Total SingleElectron	190645–196531	5.08 fb^{-1}

Table 6.1: The datasets analyzed for this analysis.

1800 6.1.2 Signal Samples

1801 The $t\bar{t}H$ signal is modeled using the leading order Pythia Monte Carlo generator. Signal events
1802 were generated privately using the same conditions and configuration as the "Summer" MC
1803 campaign, which generated the background samples used in this analysis and is a central effort
1804 by a dedicated team of collaborators within the CMS experiment. The samples and associated
1805 cross sections used are listed in Table 7.2.

Mass	Dataset	Cross Sect.
$110 \text{ GeV}/c^2$	TTH, Inclusive Decays, $M_H = 110$, Pythia6	0.1887 pb
$115 \text{ GeV}/c^2$	TTH, Inclusive Decays, $M_H = 115$, Pythia6	0.1663 pb
$120 \text{ GeV}/c^2$	TTH, Inclusive Decays, $M_H = 120$, Pythia 6	0.1470 pb
$122.5 \text{ GeV}/c^2$	TTH, Inclusive Decays, $M_H = 122.5$, Pythia 6	0.1383 pb
$125 \text{ GeV}/c^2$	TTH, Inclusive Decays, $M_H = 125$, Pythia 6	0.1302 pb
$127.5 \text{ GeV}/c^2$	TTH, Inclusive Decays, $M_H = 127.5$, Pythia 6	0.1227 pb
$130 \text{ GeV}/c^2$	TTH, Inclusive Decays, $M_H = 130$, Pythia 6	0.1157 pb
$135 \text{ GeV}/c^2$	TTH, Inclusive Decays, $M_H = 135$, Pythia 6	0.1031 pb
$140 \text{ GeV}/c^2$	TTH, Inclusive Decays, $M_H = 140$, Pythia 6	0.09207 pb

Table 6.2: List of signal MC datasets and cross sections used to determine the SM expectation.

1806 6.1.3 Background Samples

1807 In order to estimate the rate and kinematic behavior of the backgrounds, this analysis primarily
1808 uses Monte Carlo (MC) samples from the "Summer12" MC campaign, based on leading order
1809 event generators. Most of the samples are generated either with the Madgraph tree-level matrix
1810 element generator matched to Pythia for the parton shower, or with the NLO generator Powheg
1811 combined with Pythia. These samples are reconstructed with the same CMSSW version as the
1812 data samples listed above. Table 7.3 lists the background MC samples and associated cross
1813 sections.

Sample	Dataset	Cross Sect.
$t\bar{t}$ +jets	TTJets, Madgraph	225.197 pb
$t\bar{t} + W$	TTWJets, Madgraph	0.249 pb
$t\bar{t} + Z$	TTZJets, Madgraph	0.208 pb
W +jets	WJets to Leptons, Madgraph	36257.2 pb
$Z/\gamma^* + \text{jets}$ $M_{\ell\ell} > 50 \text{ GeV}/c^2$ $10 \text{ GeV}/c^2 < M_{\ell\ell} < 50 \text{ GeV}/c^2$	DYJets to Leptons $M_{\ell\ell} > 50$, Madgraph DYJets to Leptons $10 < M_{\ell\ell} < 50$, Madgraph	3503.17 pb 860 pb
Single t s -channel t -channel tW	T, s channel, Powheg T, t channel, Powheg T, tW channel, Powheg	3.79 pb 56.4 pb 11.1 pb
Single \bar{t} s channel t channel tW	\bar{T} , s channel, Powheg \bar{T} , t channel, Powheg \bar{T} , tW channel, Powheg	1.76 pb 30.7 pb 11.1 pb
WW	WW, Pythia6	54.8 pb
WZ	WZ, Pythia6	32.3 pb
ZZ	ZZ, Pythia6	7.7 pb

Table 6.3: List of background MC datasets and cross sections used for normalization.

1814 6.1.4 MC pileup reweighting

1815 During 2012 data collection, the LHC provided increasingly large instantaneous luminosities to
 1816 the CMS experiment. Consequently, the average number of overlapping events reconstructed
 1817 in single detector readout window also increased. When these overlapping events, known as
 1818 pileup events, occur within the same bunch crossing, this is referred to as "in-time" pileup.
 1819 Alternatively, "out-of-time" pileup, comes from energy deposits in the detector from previous
 1820 bunch crossings and from very early arrivals of particles from the forthcoming bunch crossing.
 1821 Pileup events can affect many aspects of the reconstruction of a more interesting event, such
 1822 as the degradation of lepton isolation and jet energy resolution. The simulated samples used in
 1823 the analysis must also have the same distribution of pileup events as what was measured in the
 1824 data.

1825 During the generation of the simulated samples used in the analysis, the average amount of
 1826 expected pileup was unknown. Events were thus simulated with a conservatively large estimate
 1827 of the pileup distribution, so that if the measured data revealed a smaller average value, the
 1828 simulation could be reweighted to match the data. For the simulation, the number of interactions
 1829 is a user-defined value added to every generated event. For the data, the number of pileup
 1830 interactions for each unit of time depends on the instantaneous luminosity for each bunch pair
 1831 and the total inelastic cross section, $\sigma_{inelastic}$, of the proton. The value of $\sigma_{inelastic} = 69.4 \text{ mb}$
 1832 was found to describe the data well. To estimate the effect of the systematic uncertainty of this
 1833 choice, the value was varied by $\pm 7\%$.

1834 To gauge the accuracy of the calibration of the pileup distribution used in the simulated
 1835 samples, a comparison of the number of reconstructed vertices between data and the simulated
 1836 $t\bar{t}$ MC sample is shown in figure 7.1. The unweighted MC distribution is shown in blue, the

1837 reweighted distribution in red, and the measured data in black points. After reweighting, there
1838 is a good level of agreement between the data and MC distributions.

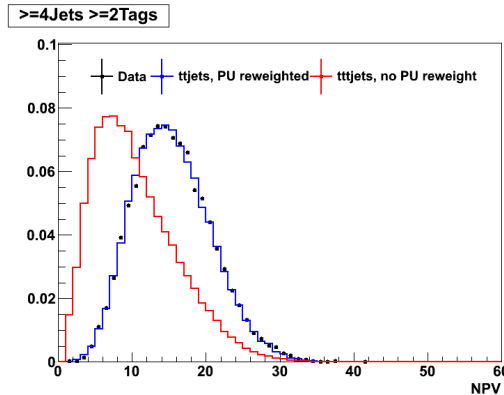


Figure 6.2: Comparison of number of reconstructed vertices for data (black) and the $t\bar{t}$ MC sample before (blue) and after (red) pileup reweighting. After pileup reweighting, the MC matches the data well.

1839 6.1.5 Additional Pileup Corrections

1840 Studies comparing the Monte Carlo simulations to observed data revealed that the jet p_T spectra
1841 was not well modeled. Many sources of this discrepancy were investigated, but the clearest
1842 correlations arises when the 8 TeV data events are divided into three categories according to
1843 their amount of pileup:

- 1844 • Low PU, number of primary vertices ≤ 10
- 1845 • Medium PU, number of primary vertices from 11 to 15
- 1846 • High PU, number of primary vertices ≥ 16

1847 The modeling of jet p_T was worse for events with a larger number of pileup events overlapping
1848 in the detector. The same effect was present for the majority of the jets in the event, evidenced
1849 by the discrepancy in the H_T distribution, shown in figure 6.3, where H_T is defined as the scalar
1850 sum of the transverse momentum for reconstructed jets in the event:

$$H_T = \sum_i^{jets} p_T^i \quad (6.1)$$

1851 The effect makes the data have a softer p_T spectrum than the simulations. The same effect
1852 was observed in 7 TeV data as well. It was present even after employing several sophisticated
1853 reconstruction techniques designed to mitigate pileup effects. These techniques included the
1854 removal of charged hadrons in the particle-flow algorithm, not associated with the primary

1855 vertex and re-weighting the simulated samples to match the pileup distribution measured in the
 1856 data.

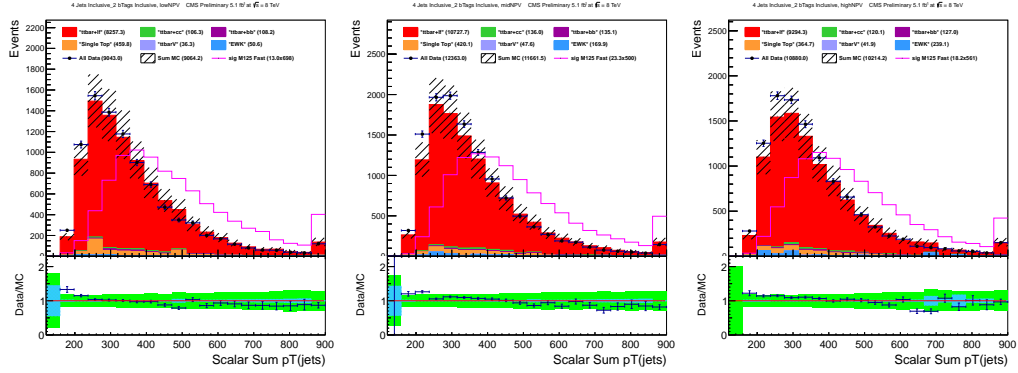


Figure 6.3: H_T distribution for 8 TeV lepton plus jet events with ≥ 4 jets and ≥ 2 tags shown for different amounts of pileup. The left-hand plot shows low pileup, the middle plot shows medium pileup, and the right-hand plot shows high pileup.

1857 Although the exact underlying cause of the jet mis-modeling effect was not able to be iden-
 1858 tified, the magnitude of the effect seemed to be related to the number of pileup events. As
 1859 such, an additional correction factor is needed to account for the remaining difference in pileup
 1860 effects between data and Monte Carlo. The correction factor was calculated from data that was
 1861 dominated by background events, with a single lepton, ≥ 4 jets, and ≥ 2 tags. The expected
 1862 signal-to-background ratio in this sample is 0.002, which is low enough that the correction factor
 1863 will not be biased by signal events. The correction factor is based on the H_T distribution for
 1864 data and Monte Carlo for Low pileup (PU), Medium PU, and High PU events. The correction
 1865 factor is the bin-by-bin ratio of the data and the Monte Carlo H_T distributions in each PU
 1866 category. By preparing a separate correction factor for each PU category smaller adjustments
 1867 were made to well-modeled Low PU events and larger adjustments to the poorly modeled High
 1868 PU events. H_T shows the same mis-modeling as each of the jet p_T s and it effects all of the jet
 1869 p_T s. This makes it a natural choice for a correction factor.

1870 In order to evaluate the systematic shape uncertainty introduced by the correction factor,
 1871 the uncorrected simulated distributions are used as -1σ systematic uncertainty and the $+1\sigma$
 1872 uncertainty is determined by doubling the correction factor. The factor of two for the $+1\sigma$
 1873 variation is motivated by the desire to provide a large enough systematic uncertainty to cover
 1874 any possible over-correction of the simulations. This is a reasonable choice because it creates a
 1875 deviation that is the same size as the original observed difference between data and simulations.

1876 The correction factor and uncertainty improved the agreement between data and Monte
 1877 Carlo. Figure 6.4 compares the H_T distributions before and after reweighting. The data-to-MC
 1878 ratio plots are the clearest indicators of the improvement from the correction factor. Before the

1879 correction, the H_T ratio plot forms a line with a slope. After the correction the slope is gone.

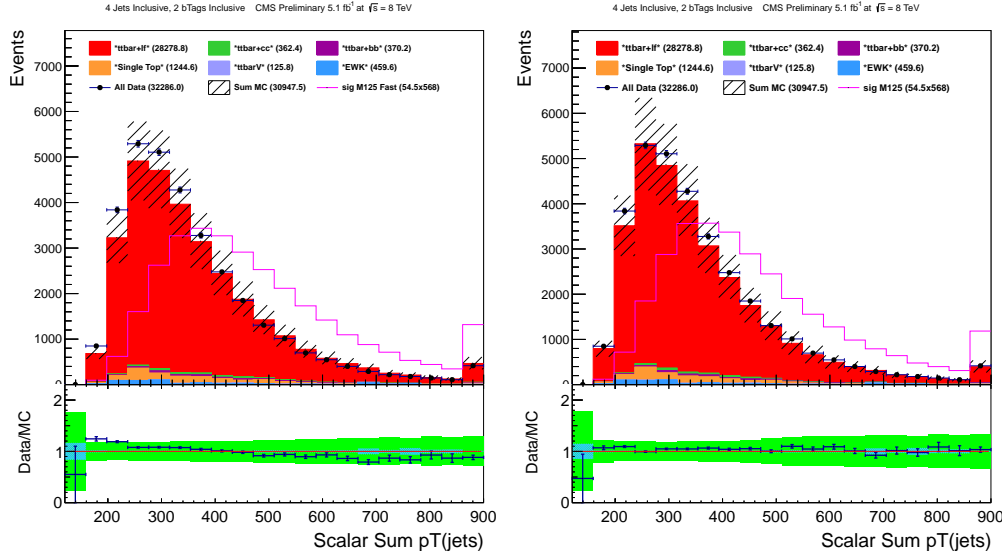


Figure 6.4: H_T distribution for 8 TeV lepton plus jet events with ≥ 4 jets and ≥ 2 tags. The left-hand plot shows the distribution before correction. The right-hand plot shows the distribution after correction. Note that the ratio in the right-hand plot is flatter than the left-hand plot.

1880 6.2 Event Selection

1881 This section defines the common physics objects and event selection requirements. Leptons are
 1882 classified into two categories, tight and loose, defined for muons in section 6.2.3 and for electrons
 1883 in 6.2.4. For this analysis, exactly one tight muon or exactly one tight electron is required and
 1884 events with any additional loose leptons are rejected.

1885 6.2.1 Event cleaning

1886 For data and MC events, certain cuts are applied to remove events that are either non-physical
 1887 or that come from non-collision events, such as instrumental noise or beam backgrounds. In the
 1888 data, every event is required to pass the following filters:

- 1889 • CSC tight beam halo filter - Secondary particles are produced in showers which are ini-
 1890 tiated by collisions of the beam with residual gas inside the LHC vacuum chamber or by
 1891 interactions of the particles with a large transverse emmitance with limiting apertures.
- 1892 • HBHE noise filter with isolated noise rejection - this filters spurious signals from the HCAL
 1893 barrel and endcap sub-detectors which are not associated with particles measured in a
 1894 collision event.

- 1895 • HCAL laser filter - ensures that data is not taken simultaneously with the laser calibration
1896 system
- 1897 • ECAL dead cell trigger primitive (TP) filter - removes dead or noisy ECAL cells from
1898 being used in the reconstruction, these compose < 1% of the total crystals in the ECAL
- 1899 • Tracking failure - designed to catch events with too-few tracks
- 1900 • Noisy SCs in EE - new filter from the ECAL Detector Performance Group (PDG), and
1901 validated by the MET Physics Object Group (POG)

1902 which are described in [149].

1903 Additionally, beam-scraping events are filtered based on the fraction of good tracks. At least
1904 25% of tracks are required to be of high purity. Finally, every data event must contain at least
1905 one primary vertex (PV) that passes the following selection:

- 1906 • The number of degrees of freedom used to find the PV must be larger than 4,
- 1907 • The absolute value of the z -coordinate of the PV must be smaller than 24 cm,
- 1908 • The absolute value of the ρ -coordinate of the PV must be smaller than 2 cm,
- 1909 • The PV must not be identified as fake.

1910 6.2.2 Trigger

1911 Each data and MC event is required to pass passes one of the triggers in Table 6.4, which are a
1912 subset of the total number of SingleMu and SingleEle HLT triggers available. Muon+jet events
1913 must pass the SingleMu trigger, while electron+jet events must pass the SingleEle trigger.

Dataset	Trigger Name
SingleMu	HLT_IsoMu24_eta2p1_v*
SingleEle	HLT_Ele27_WP80_v*

Table 6.4: List of lepton+jets triggers

1914 6.2.3 Muon Selection

1915 In this analysis, muons are selected from the set of "particle-flow' muon" objects that have been
1916 reconstructed in the event. Muons are classified into two categories: tight and loose, according
1917 to the quality of their reconstruction. This is ensured by applying the selection cuts shown in
1918 Table 6.5. The cuts are defined as follows:

- 1919 • p_T - the component of the momentum transverse to the beam-line.

- 1920 • PFRelIso - this is the quantity known as relative isolation, computed by the particle flow
1921 algorithm. It is a ratio of the energy deposits remaining in the calorimeter and tracker,
1922 after the contribution from the muon has been removed, in a cone size $\Delta R = 0.3$, around
1923 the muon track.
- 1924 • $|\eta|$ - the absolute value of the pseudorapidity of the muon
- 1925 • ID - This refers to whether the muon was reconstructed with a χ^2 fit to the tracks from
1926 the tracker only (tracker muon), the tracker and the muon chambers (global muon), or if
1927 the particle was reconstructed from the particle-flow algorithm (PFmuon)
- 1928 • $N_{layers}(\text{tracker})$ - the number of layers in the tracker with hits used in the muon track
1929 reconstruction
- 1930 • X^2 of track fit - the reduced χ^2 (raw χ^2 /Number of Degrees of Freedom in the fit), typically
1931 a value of 1 indicates the fit describes the data well
- 1932 • $N_{layers}(\text{pixel})$ - the number of hit-containing layers in the inner pixel detector used in the
1933 muon track reconstruction
- 1934 • $N_{segments}(\mu)$ - the number of segments in the muon chambers used to reconstruct the
1935 muon tracks
- 1936 • $|d_0(\text{BS})|$ - the absolute value of the transverse distance of the extrapolated muon track to
1937 the primary vertex, as calculated from the beam spot (BS)
- 1938 • $|d_Z(\text{BS})|$ - the absolute value of the longitudinal distance of the extrapolated muon track
1939 to the primary vertex

Cuts	Tight μ	Loose μ
p_T	$>30\text{ GeV}/c$	$>10\text{ GeV}/c$
PFRelIso(0.4)	0.12	<0.2
$ \eta $	<2.1	<2.5
ID	Global Muon	Global Muon or Tracker Muon
ID	PFMuon	PFmuon
$N_{layers}(\text{tracker})$	>5	
X^2 of track fit	<10	
$N_{layers}(\text{pixel})$	>0	
$N_{segments}(\mu)$	>1	
$ d_0(\text{BS}) $	<0.2 cm	
$ d_Z(\text{BS}) $	<0.5 cm	

Table 6.5: Tight and loose muon definition

1940 6.2.4 Electron Selection

- 1941 Electrons are selected from the set of "particle-flow electron" objects reconstructed in the event.
1942 Similarly to muons, electrons are classified into two categories: tight and loose, according to the

1943 quality of their reconstruction. The selection cuts are shown in the Table 6.6. The definitions
 1944 are identical to the ones provided in section 6.2.3. Additional variables not described are:

- 1945 • E_T - the transverse energy of the electron, which due to its relatively light mass, is ap-
 1946 proximately equal to its p_T
- 1947 • ID - electron ID is passed on a multivariate analysis (MVA) technique, which provides a
 1948 discriminant value to separate fake from real electrons, and is trained with events that are
 1949 required to pass a HLT trigger (mvaTrigV0), or not (mvaNonTrigV0). The "passConver-
 1950 sionVeto" ID ensures that the electron has not been reconstructed from a photon which
 1951 has converted to an electron positron pair

Cuts	Tight e	Loose e
E_T	$>30 \text{ GeV}/c^2$	$>15 \text{ GeV}/c^2$
PFRelIso(0.3)	<0.1	<0.2
$ \eta $	<2.5	<2.5
ID	MVA ID("mvaTrigV0") >0.0	MVA ID("mvaNonTrigV0") >0.0
ID	passConversionVeto	passConversionVeto
$ d0(BS) $	$<0.02 \text{ cm}$	
$ dZ(PV) $	$<1 \text{ cm}$	

Table 6.6: Tight and loose muon definition

1952 6.2.5 Lepton selection and trigger efficiencies

1953 The cumulative reconstruction efficiency of ID+isolation+trigger has been calculated from data,
 1954 as a function of p_T and η , as shown in figure 6.5 for electrons and muons. In order to reproduce
 1955 the same response in the simulations as found in data, an event-by-event scale factor
 1956 is applied to correct for this difference in efficiency.

1957 The efficiency in data was measured by selecting events with two tight muons, or two tight
 1958 electrons with an invariant mass in a range between 70 and 130 GeV. This is centered on the
 1959 Z -boson resonance, and ensures that the selected leptons are authentic. The two leptons are
 1960 additionally required to have opposite charge, which is measured by the direction of the curvature
 1961 of their tracks in the magnetic field. A "tag" lepton is selected if has $p_T > 30 \text{ GeV}$, and passes
 1962 the appropriate muon or electron trigger. The second lepton, the "probe" lepton, since selected
 1963 as a pair coming from a Z boson, should be identical to the tag lepton, and thus should be
 1964 identically reconstructed. The efficiency is then the ratio of the number events where both tag
 1965 and probe leptons pass the p_T and trigger requirements over the number of events where only
 1966 the tag lepton passes the p_T and trigger requirements. This study is repeated in bins of p_T and
 1967 η to remove any kinematic dependence on lepton efficiency.

1968 The combined ID, isolation, and trigger scale factor uncertainty is evaluated by looking at
 1969 the variation of the scale factor as a function of parameters besides p_T and η , such as pileup and

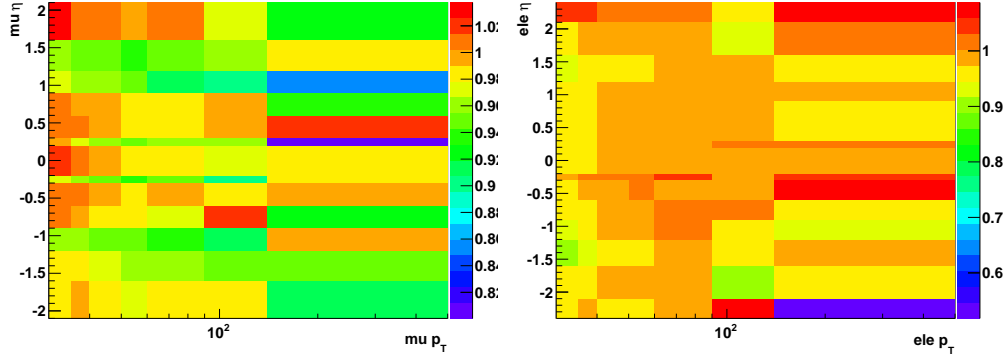


Figure 6.5: Muon and electron ID, isolation selection and trigger efficiency scale factors in bins of p_T and η .

¹⁹⁷⁰ b -tag scale factor reweighting (described below). A flat uncertainty of 4% covers the variations
¹⁹⁷¹ that are observed, and is thus adopted as a conservative estimate of the uncertainty on the
¹⁹⁷² combined lepton reconstruction efficiency.

¹⁹⁷³ 6.2.6 Jet selection

¹⁹⁷⁴ As described in the previous chapter, jets are reconstructed with the anti-kt clustering algo-
¹⁹⁷⁵ rithm [25], with a distance parameter of 0.5, starting from the set of objects reconstructed
¹⁹⁷⁶ by the particle flow algorithm [24]. Non-isolated leptons, not associated with the decay of a
¹⁹⁷⁷ W boson, are allowed to be clustered into the jets. The selection cuts defining our jets can be
¹⁹⁷⁸ found in Table 6.7. The cuts use the following variables to ensure the reconstruction of authentic
¹⁹⁷⁹ hadronic jets:

- ¹⁹⁸⁰ • p_T - component of the momentum transverse to the beam-line
- ¹⁹⁸¹ • η - the pseudorapidity of the reconstructed jet
- ¹⁹⁸² • CEF - Charged Electromagnetic Fraction: the ratio of charged particles to the total number
¹⁹⁸³ of particles in the jet
- ¹⁹⁸⁴ • NHF - Neutral Hadron Fraction: the ratio of neutral particles to the total number of
¹⁹⁸⁵ particles in the jet
- ¹⁹⁸⁶ • NEF - Neutral Electromagnetic Fraction: the ratio of photons to the total number of
¹⁹⁸⁷ particles in the jet
- ¹⁹⁸⁸ • CHF - Charged Hadron Fraction: the ratio of charged hadrons to the total number of
¹⁹⁸⁹ particles in the jet
- ¹⁹⁹⁰ • NCH - Number of Charged Hadrons: raw charged hadron multiplicity

- 1991 • $N_{\text{constituents}}$ - Number of constituents, which can be charged and neutral hadrons, as well
 1992 as non-prompt photons and leptons.

Cuts	Jet
p_T	$>30 \text{ GeV}/c$
$ \eta $	<2.4
CEF, NHF, NEF	<0.99
CHF, NCH	>0
$N_{\text{constituents}}$	>1

Table 6.7: Jet definition

1993 Additional correction factors are required such that the measured energy of the jet correctly
 1994 reproduces the energy of the initial parton. This is done in four stages. The L1 Charged
 1995 Hadron Subtraction (CHS) correction, is implemented in the particle-flow algorithm, and involves
 1996 subtracting the energy contributions from charged hadrons that are not associated with the jet
 1997 from the energy cluster. The next stage, L2 correction is a relative correction to make the
 1998 measured jet response flat in η . The third stage, L3, is an absolute correction to the measured
 1999 p_T of a jet in order to match the simulated jet p_T created using generator-level input and a similar
 2000 jet-clustering algorithm. The L2 and L3 corrections are calculated using Monte Carlo, and thus
 2001 an fourth correction factor, the L2L3 residual correction is applied that fixes the discrepancies
 2002 between Monte Carlo and data. The correction factors are described in reference [150], and are
 2003 derived from 2011 7 TeV data, with a selection of dijet events near the Z -boson mass peak. A
 2004 "tag-and-probe" procedure similar to the lepton scale factors is applied to jets to determine the
 2005 kinematic dependence (p_T and η) of the detector in both simulations and data. Additionally, a
 2006 scale factor is needed to adjust for the difference in jet energy resolution as measured in data
 2007 and predicted in simulation. Table 6.8 gives the scale factors, and uncertainties, as derived from
 2008 dijet events [150] as a function of η only, since no significant p_T dependence was observed.

2009 6.2.7 b -tagging selection

2010 The algorithm used to perform b -tagging in this analysis is the combined secondary vertex (CSV)
 2011 algorithm [151]. It relies on the superior ability of the inner tracker to reconstruct secondary

$ \eta $	Data/MC Ratio (factor +stat. +syst.- syst.)
0.00.5	$1.052 \pm 0.012 + 0.062 - 0.061$
0.51.1	$1.057 \pm 0.012 + 0.056 - 0.055$
1.11.7	$1.096 \pm 0.017 + 0.063 - 0.062$
1.72.3	$1.134 \pm 0.035 + 0.087 - 0.085$
2.35.0	$1.288 \pm 0.127 + 0.155 - 0.153$

Table 6.8: Jet Energy Resolution (JER) scale factors

2012 vertices, which are the characteristic signature of B -hadron decays. Tracks are selected if they
2013 meet the following requirements:

- 2014 • At least 8 hits in the pixel and silicon tracker, with at least 2 hits in the pixel detector
- 2015 • tracks must have $p_T > 1\text{ GeV}$
- 2016 • χ^2/NDF of the fitted track < 10
- 2017 • $|d_0|$ - transverse impact parameter $< 2\text{ mm}$, since b -quarks will on average travel 0.45 mm
- 2018 in the detector before decaying

2019 Additionally, the following cuts are required:

- 2020 • The transverse distance between the primary and secondary vertices, L_T , is between 100
2021 μm and 2.5 cm
- 2022 • The ratio of L_T and the uncertainty on its measurement, $L_T/\sigma_{L_T} > 3$
- 2023 • The invariant mass formed by adding the four-vectors of all the tracks forming the sec-
2024 ondary vertex $< 6.5\text{ GeV}$
- 2025 • The invariant mass falls outside a window near 50 MeV, corresponding to the K_S^0 resonance

2026 Secondary vertices are decomposed into three categories. If a secondary vertex is found meeting
2027 the above criteria, it is a "reco vertex". If no secondary vertex is found meeting all the above
2028 criteria, the event can be classified as a "pseudo vertex" if more than two tracks have a signed
2029 transverse impact parameter significance, relative to the primary vertex, greater than 2. "No
2030 vertex" is found if neither of the prior two classification criteria can be met.

2031 For each of the vertex categories, a set of variables is used to create a single discriminating
2032 variable, using a likelihood ratio technique. The following input variables are used:

- 2033 • The invariant mass of the charged particles associated with the secondary vertex
- 2034 • The multiplicity of charged tracks associated with the primary vertex
- 2035 • The distance between the primary and secondary vertex in the transverse plane, divided
2036 by its error (only used in reco vertex category)
- 2037 • The pseudorapidities of the charged particle tracks associated with the secondary vertices
- 2038 • The track impact parameter significance of the highest p_T track with invariant mass larger
2039 than the charm quark threshold, 1.5 GeV.

2040 The likelihood function is split to separate between the charm and light-flavor backgrounds and
 2041 is defined as:

$$\mathcal{L}^{b,c,q} = f^{b,c,q}(\alpha) \times \prod_i f_{\alpha}^{b,c,q}(x_i) \quad (6.2)$$

2042 where $\alpha = 1,2,3$, denotes the different vertex categories, x_i are the individual variables, q stands
 2043 for the light flavor quarks, while b and c stand for the bottom and charm quarks respectively.
 2044 $f^{b,c,q}(\alpha)$ is the probability for a quark flavor b , c , or q , to fall into category α . $f_{\alpha}^{b,c,q}(x_i)$ is the
 2045 probability density function of the variable x_i in category α for quark flavor b , c , or q . The
 2046 combined discriminant is defined as

$$d = f_{BG}(c) \times \frac{\mathcal{L}^b}{\mathcal{L}^c + \mathcal{L}^b} + f_{BG}(q) \times \frac{\mathcal{L}^b}{\mathcal{L}^q + \mathcal{L}^b} \quad (6.3)$$

2047 where $f_{BG}(c)$, and $f_{BG}(q)$ are the a-priori probabilities for the content of charm and light flavor
 2048 quarks in non- b jets.

2049 A jet is considered b -tagged if the CSV discriminant is greater than 0.679, which is the
 2050 medium working point defined by the BTag Physics Object Group (POG) [152], defined in order
 2051 to produce a light-flavor mistag rate at $\sim 1\%$, with the reconstruction efficiency for real b jets
 2052 at $\sim 70\%$.

2053 Additionally, it is necessary to account for differences in the measured efficiency for b -tagging
 2054 jets between data and simulation [153]. An event weight scale factor is used to correct the MC
 2055 b -tagging efficiency ($SF_{tag} = \epsilon_{tag}^{data}/\epsilon_{tag}^{MC}$). The scale factor is measured for three different cuts,
 2056 or working points, on the CSV discriminant value, and it is binned in terms of the p_T and η and
 2057 flavor of the jet.

2058 In addition to providing jet flavor identification for event classification, the discriminant value
 2059 of the algorithm will be used to separate between $t\bar{t}H$ signal and $t\bar{t}+jets$ background. Therefore,
 2060 a correction value for the efficiency difference between data and MC over the whole range of
 2061 discriminator values is needed, not just for three working points. This procedure was developed
 2062 in the context of the search for the standard model Higgs boson produced in association with a
 2063 W or Z boson, with the Higgs decaying to bottom quarks [154].

2064 For each of the three operating points and for each of the data/MC SFs, an equivalent cut
 2065 on the CSV value is determined, CSV_{equiv} , such that

$$\epsilon_{CSV>CSV_{orig}}^{data} = SF_{CSV>CSV_{orig}} \cdot \epsilon_{CSV>CSV_{orig}}^{MC} = \epsilon_{CSV>CSV_{equiv}}^{MC} \quad (6.4)$$

2066 where the SFs are measured in data and the MC efficiency measurements are calculated for each
 2067 sample.

In order to correct or "reshape" the CSV discriminator output values, a function is applied to the MC to produce a corrected CSV value: $CSV_{\text{corr}} = f(CSV_{\text{orig}})$. Given that there are three b -tag efficiency measurements, there are three pairs of (CSV_{orig} , CSV_{equiv}). The reshaping function must satisfy $f(CSV_{\text{equiv}}) = CSV_{\text{orig}}$ for each of the operating points and for the upper and lower values of the CSV discriminant to make sure those values do not change (e.g., $CSV = 0.0$ and $CSV = 1.0$). The whole range of CSV discriminant values is found by linearly interpolating between these five points (the three working points, and upper and lower limit of the discriminate range).

6.2.8 Lepton + Jets Selection

The final Lepton+Jets (LJ) selection is carried out by requiring that events have exactly one tight lepton (e or μ), and at least four jets. Events with any additional loose or tight leptons are vetoed so this analysis can later be combined with a diLepton final state, without double counting events. Additionally, each event must have at least three jets with $p_T > 40\text{ GeV}/c$.

Events are further categorized by the reconstructed jet, and b -tagged jet multiplicities as follows:

- ≥ 6 jets, $=2$ b -tags: At least 6 jets, 2 of which are b -tagged
- $=4$ jets, $=3$ b -tags: Exactly 4 jets, 3 of which are b -tagged
- $=5$ jets, $=3$ b -tags: Exactly 5 jets, 3 of which are b -tagged
- ≥ 6 jets, $=3$ b -tags: At least 6 jets, 3 of which are b -tagged
- $=4$ jets, $=4$ b -tags: Exactly 4 jets, 4 of which are b -tagged
- $=5$ jets, $=4$ b -tags: Exactly 5 jets, 4 of which are b -tagged
- ≥ 6 jets, ≥ 4 b -tags: At least 6 jets, with at least 4 of which are b -tagged

Events with either 4 or 5 jets, where 2 of those jets are b -tagged, make up two categories, which are used only as a control region to validate comparisons between collected data and simulations. The number of $t\bar{t}H$ events increases with the number of jets and tags because the largest branching fraction is H to $b\bar{b}$. Data to Monte Carlo comparisons of the jet and b -tag multiplicities are shown in figure 6.6. The event yields for the μ +jets and e +jets channels are shown in tables 6.11 and 6.10 respectively.

Table 6.9: Expected event yields in 5 fb^{-1} for signal and backgrounds in the $\mu+\text{jets}$ channel.

	≥ 6 jets 2 tags	4 jets 3 tags	5 jets 3 tags	≥ 6 jets 3 tags	≥ 6 jets 4 tags	4 jets 4 tags	5 jets ≥ 4 tags	≥ 6 jets ≥ 4 tags
$t\bar{t}H(125)$	6.1 ± 1.1	2.1 ± 1.9	3.2 ± 2.7	3.6 ± 3.3	0.3 ± 0.3	0.8 ± 0.9	1.3 ± 1.4	
$t\bar{t}+\text{lf}$	1750 ± 480	680 ± 150	460 ± 110	270 ± 84	9.5 ± 3.2	13.0 ± 4.2	20.6 ± 7.8	
$t\bar{t}+b\bar{b}$	34 ± 19	21 ± 12	24 ± 14	17.3 ± 10.0	1.5 ± 1.1	5.1 ± 3.2	8.6 ± 5.6	
$t\bar{t}+c\bar{c}$	29.5 ± 8.7	10.0 ± 2.9	13.2 ± 3.9	11.1 ± 3.5	0.2 ± 0.2	0.2 ± 0.1	1.1 ± 0.8	
$t\bar{t}V$	18.7 ± 3.9	2.3 ± 0.6	3.3 ± 0.8	4.1 ± 1.1	0.1 ± 0.0	0.4 ± 0.2	0.8 ± 0.2	
Single t	42.6 ± 9.8	25.8 ± 6.0	14.3 ± 3.8	4.3 ± 1.3	0.2 ± 0.3	1.6 ± 1.8	0.7 ± 0.5	
V+jets	39 ± 32	1.0 ± 0.9	0.0 ± 0.0	0.0 ± 0.0	0.0 ± 0.0	0.0 ± 0.0	0.0 ± 0.0	
Diboson	0.6 ± 0.2	0.9 ± 0.4	0.3 ± 0.1	0.1 ± 0.1	0.0 ± 0.0	0.0 ± 0.0	0.0 ± 0.0	
Total bkg	1910 ± 500	740 ± 160	520 ± 120	307 ± 90	11.4 ± 3.8	20.3 ± 6.1	32 ± 11	
Data	1780	861	585	362	15	32	37	

Table 6.10: Expected event yields in 5 fb^{-1} for signal and backgrounds in the $e+\text{jets}$ channel.

	≥ 6 jets 2 tags	4 jets 3 tags	5 jets 3 tags	≥ 6 jets 3 tags	≥ 6 jets 4 tags	4 jets 4 tags	5 jets ≥ 4 tags	≥ 6 jets ≥ 4 tags
$t\bar{t}H(125)$	5.6 ± 1.0	1.8 ± 1.2	2.9 ± 1.8	3.2 ± 2.1	0.3 ± 0.2	0.7 ± 0.6	1.2 ± 1.0	
$t\bar{t}+\text{lf}$	1720 ± 470	640 ± 140	410 ± 94	293 ± 85	8.6 ± 2.9	14.5 ± 5.2	20.7 ± 7.8	
$t\bar{t}+b\bar{b}$	27 ± 15	14.3 ± 7.9	19 ± 11	18 ± 10	1.0 ± 1.0	3.3 ± 2.6	6.7 ± 4.3	
$t\bar{t}+c\bar{c}$	32.8 ± 9.4	9.6 ± 2.9	11.8 ± 3.5	14.8 ± 4.8	0.4 ± 0.3	0.6 ± 0.6	2.6 ± 1.4	
$t\bar{t}V$	17.0 ± 3.6	2.1 ± 0.6	2.8 ± 0.7	4.5 ± 1.1	0.0 ± 0.0	0.3 ± 0.1	0.6 ± 0.2	
Single t	35.9 ± 8.9	30.5 ± 6.4	11.3 ± 3.4	6.0 ± 2.0	0.1 ± 0.3	1.4 ± 1.2	0.4 ± 0.4	
V+jets	14 ± 14	4.8 ± 5.8	0.8 ± 0.9	0.0 ± 0.0	0.0 ± 0.0	0.0 ± 0.0	0.0 ± 0.0	
Diboson	0.7 ± 0.3	1.0 ± 0.3	0.2 ± 0.1	0.1 ± 0.0	0.0 ± 0.0	0.0 ± 0.0	0.0 ± 0.0	
Total bkg	1850 ± 490	700 ± 150	460 ± 110	336 ± 93	10.1 ± 3.2	20.2 ± 6.6	31 ± 11	
Data	1723	785	531	324	13	24	37	

Table 6.11: Expected event yields in 5 fb^{-1} for signal and backgrounds in the $\mu+\text{jets}$ channel.

	≥ 6 jets 2 tags	4 jets 3 tags	5 jets 3 tags	≥ 6 jets 3 tags	4 jets ≥ 4 tags	5 jets ≥ 4 tags	≥ 6 jets ≥ 4 tags
$t\bar{t}H(125)$	11.7 ± 1.9	3.9 ± 1.9	6.1 ± 3.1	6.9 ± 3.5	0.6 ± 0.3	1.5 ± 0.8	2.5 ± 1.3
$t\bar{t}\ell\bar{\nu}$	3460 ± 940	1320 ± 280	870 ± 210	570 ± 170	18.0 ± 5.1	27.6 ± 8.6	41 ± 15
$t\bar{t} + b\bar{b}$	61 ± 34	35 ± 19	43 ± 24	35 ± 20	2.5 ± 1.7	8.4 ± 5.4	15.4 ± 9.4
$t\bar{t} + c\bar{c}$	62 ± 17	19.6 ± 5.2	25.0 ± 6.9	25.9 ± 7.7	0.6 ± 0.4	0.8 ± 0.9	3.7 ± 1.8
$t\bar{t}V$	35.7 ± 7.5	4.5 ± 1.1	6.1 ± 1.4	8.6 ± 2.1	0.1 ± 0.1	0.7 ± 0.2	1.5 ± 0.4
Single t	79 ± 18	56 ± 11	25.6 ± 6.3	10.3 ± 2.9	0.3 ± 0.6	3.1 ± 2.2	1.0 ± 0.6
$V+\text{jets}$	53 ± 40	5.9 ± 5.9	0.8 ± 0.9	0.0 ± 0.0	0.0 ± 0.0	0.0 ± 0.0	0.0 ± 0.0
Diboson	1.2 ± 0.4	1.8 ± 0.6	0.5 ± 0.2	0.2 ± 0.1	0.0 ± 0.0	0.0 ± 0.0	0.0 ± 0.0
Total bkg	3760 ± 980	1440 ± 300	970 ± 230	650 ± 190	21.5 ± 6.1	41 ± 12	63 ± 21
Data	3503	1646	1116	686	28	56	74

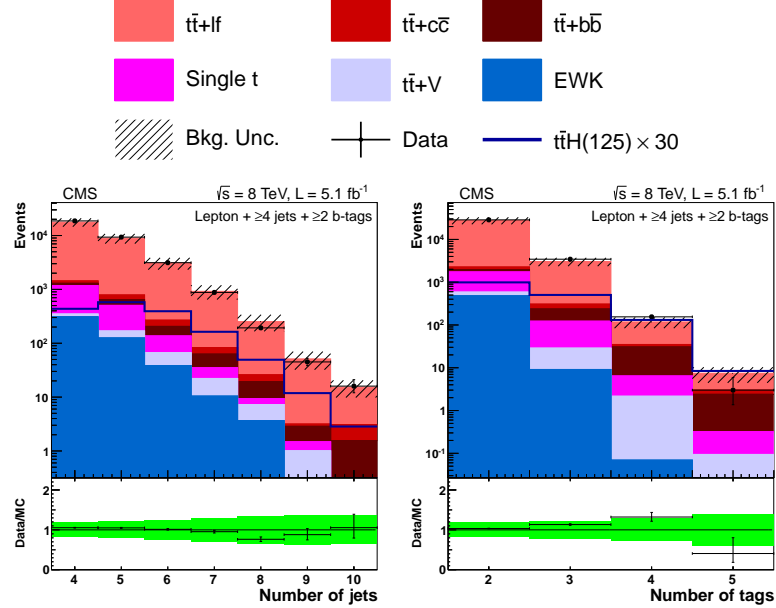


Figure 6.6: Number of jets (left) and number of b-tagged jets (right) in data and simulation for events with ≥ 4 jets + ≥ 2 b-tags in the lepton+jets channel at 8 TeV. The background is normalized to the SM expectation; the uncertainty band (shown as a hatched band in the stack plot and a green band in the ratio plot) includes statistical and systematic uncertainties that affect both the rate and shape of the background distributions. The $t\bar{t}H$ signal ($m_H = 125 \text{ GeV}/c^2$) is normalized to $30 \times$ SM expectation.

2096 6.3 Multivariate Analysis

2097 As discussed in the chapter introduction, no single variable offers sufficient discriminating power,
 2098 to separate the $t\bar{t}H$ signal from the $t\bar{t} + \text{jets}$ background. Instead, the combined power of several
 2099 input variables is utilized through a multivariate analysis (MVA) technique. For this analysis, the
 2100 MVA algorithm chosen from the sub-class of artificial neural network (ANN) algorithms, known
 2101 as multi-layer perceptrons (MLPs). The specific algorithm is the Clermont-Ferrand Multi-Layer
 2102 Perceptron Artificial Neural Network (CFMlpANN). It was first developed at the Universitye
 2103 Blaise Pascal in Clermont-Ferrand, for the ALEPH experiment at the LEP collider to search for
 2104 the Standard Model Higgs and has also been utilized by the BABAR experiment to search for
 2105 rare B meson decays [155]. It has been implemented in the ROOT TMVA framework, available
 2106 in all CMSSW releases. A CFMlpANN is trained for each jet-tag category listed in section 6.2.8.
 2107 A total of 10 input variables is used in each category, with the exception of the ≥ 6 jets, ≥ 4
 2108 b tags category, where the full reconstruction of the $t\bar{t}H$ system is possible, features an additional
 2109 variable that is the invariant mass of the di-jet system of b -jets selected by a χ^2 minimization
 2110 algorithm.

6.3.1 Artificial Neural Network Overview

An artificial neural network (ANN), most generally speaking, is any collection of interconnected, simulated "neurons" which produce a certain response to a set of input variables [155]. A simulated neuron is some independent function which takes several input variables, performs a mathematical operation, and passes the result to one or more other neurons. In the most general case, a set of n input variables, connected to a single output, will produce on the order of n^2 connections. For case of using the network to discriminate between signal from background (a yes or no answer on whether an event is signal-like), the ANN is mapping an n -dimensional space onto a one-dimensional space.

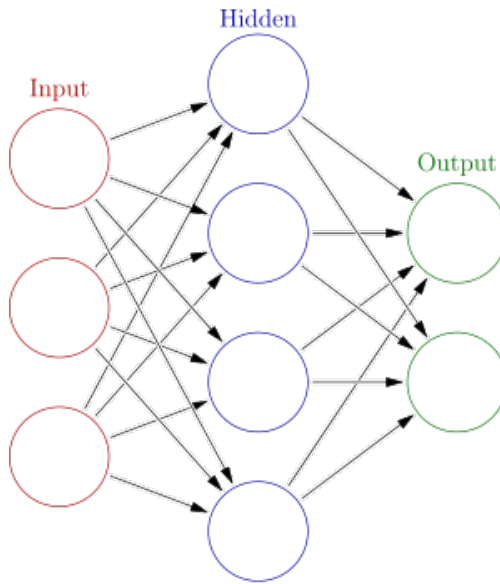


Figure 6.7: A simple example of a MLP type ANN, with one layer of input neurons that make connections to a hidden layer, which is connected to the output layer [28]

The multi-layer perceptron (MLP) is a specific type of arrangement of neurons. Any number of neurons are arranged into a single layer, and connections to other neurons are only made if they are arranged in a successive layer [155]. This is known as feed-forward network, and a simple example with one input layer, one hidden layer, and one output layer is shown in figure 6.7. This limits the complexity of the connections formed by the neurons and allows for simplified calculations.

This analysis uses an architecture that consists of two hidden layers, with N and $N - 1$ variables respectively, where N is the number of input variables for the given jet/tag category. An example diagram is shown in figure 6.8. The output of the CFMlpANN algorithm is one-dimensional discriminant with range from 0 to 1, for background-like and signal-like events. Each neuron response is based on an activation function $A(\alpha)$, and a synapse response, α .

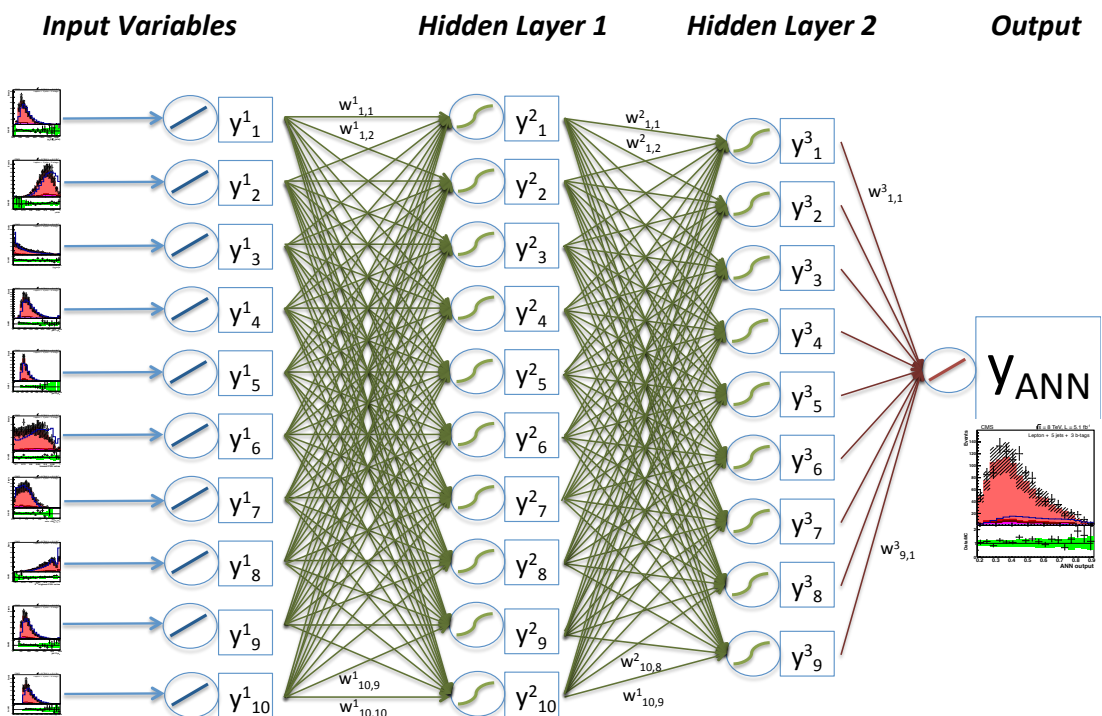


Figure 6.8: The CFMlpANN architecture used in this analysis features two hidden layers, and 10 input variables for each jet/tag category (11 variables for the ≥ 6 jets, $\geq 4b$ -tags category)

2131 In this case, a sigmoid function is used as the activation function:

$$A(\alpha) = \frac{1}{1 + e^{-x}} \quad (6.5)$$

2132 and the synapse response is a simple weighted sum:

$$\alpha = w_{0j}^{(l)} + \sum_{i=1}^n y_i^{(l)} w_{ij}^{(l)} \quad (6.6)$$

2133 The entire CFMlpANN response is then

$$y_{ANN} = \sum_{k=1}^{n-1} y_k^{(3)} w_{k1}^{(3)} = \sum_{k=1}^{n-1} A \left(\sum_{j=1}^n y_j^{(2)} w_{jk}^{(2)} \right) w_{k1}^{(3)} = \sum_{k=1}^{n-1} A \left(\sum_{j=1}^n A \left(\sum_{i=1}^n x_i w_{ij}^{(1)} \right) w_{jk}^{(2)} \right) w_{k1}^{(3)} \quad (6.7)$$

2134 where n is the number of input variables for that jet tag category and A is the sigmoid function
2135 described in equation 6.5.

2136 The CFMlpANN is trained with $t\bar{t}H$ signal events and inclusive $t\bar{t} + jets$ background events
2137 in order to optimize the weights $w_{ij}^{(l)}$ that are used for each neuron connection such that the
2138 output, y_{ANN} is closest to 1 for signal-like events, and closest to 0 for background-like events.
2139 This process involves sending the CFMlpANN an event from a known source (either signal or
2140 background), calculating the response, y_{ANN} , and computing an error function associated with
2141 the answer, given by:

$$E(x_1, \dots, x_N | w) = \sum_{a=1}^N E_a(x_a | w) = \sum_{a=1}^N \frac{1}{2} (y_{ANN} - \hat{y}_a) \quad (6.8)$$

2142 where \hat{y}_a is the correct response (either 0 or 1), knowing that the event was either signal or
2143 background, and N is the number of events used to train the CFMlpANN. The optimized set
2144 of weights is the set that minimizes this error function. This is done by the method of steepest
2145 descent, where a random set of weights is moved a small distance in the direction that gives the
2146 largest change in minimizing the error function.

$$w^{t+1} = w^t - \eta \nabla_w E \quad (6.9)$$

2147 where ∇_w is the direction that reduces the error function the most, and η is a parameter that
2148 determines how large of an adjustment is made. After the weights are adjusted, the CFMlpANN
2149 makes another iteration over the training events, re-calculating the CFMlpANN output for each
2150 event and the error function. For this analysis a total of 2000 iterations were used to train the
2151 CFMlpANN.

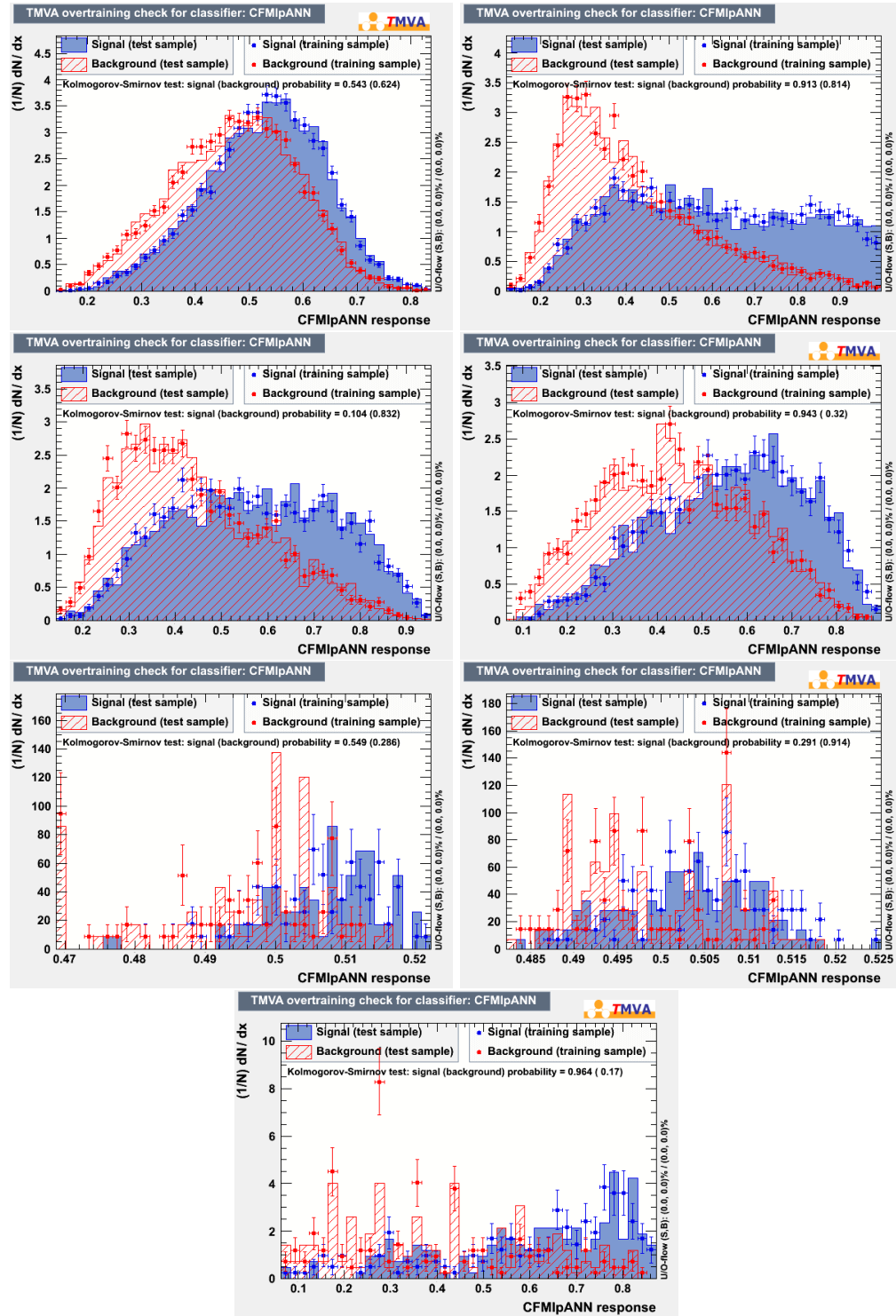


Figure 6.9: Comparisons of the testing and training samples used to optimize the CFMlpANN weights for each jet/tag category

It is possible to bias the CFMlpANN response by overtraining it. This is the case where the weights are over-adjusted to correctly classify events in the training sample. If overtrained, small fluctuations in the input variable distributions of authentic signal events can lead to incorrect classification of the signal events when the CFMlpANN attempts to classify the data. To avoid this, half of the simulated events for $t\bar{t}H$ signal and $t\bar{t}+jets$ background are used during training. After training, the other half are used to test the response of the algorithm. If properly trained, the testing and training samples should have identical CFMlpANN responses. The figure of merit used to assess this is the Kolomogrov-Smirnoff test, which computes the probability that two distributions have been sampled from the same underlying probability distribution. The results of the training and testing for each of the jet/tag categories is shown in figure 6.9. No signs of overtraining are observed.

6.3.2 MVA Input Variables, Data to Monte Carlo Comparisons

As mentioned in the previous section, each jet/tag category has been trained with its own CFMlpANN. Each category uses ten input variables, except for the $\geq 6j$, $\geq 4t$ category, which uses eleven. A total of 24 unique input variables are used in the 7 different jet/tag categories and are listed in table 6.12. The most discriminating variable for each category is denoted by a \star . The inputs are selected from a ranked list based on initial separation between signal and background. The separation of the individual variables is evaluated using a separation benchmark $\langle S^2 \rangle$ [155] defined as follows:

$$\langle S^2 \rangle = \frac{1}{2} \int \frac{(\hat{y}_S(y) - \hat{y}_B(y))^2}{\hat{y}_S(y) + \hat{y}_B(y)} dy, \quad (6.10)$$

where y is the input variable, and \hat{y}_S and \hat{y}_B are the signal and background probability density functions for that input variable in the signal and background samples, respectively. The maximum number of input variables used in each category is limited by the statistics in the simulated samples used for the CFMlpANN training. The number of variables per category is determined by reducing the number of variables until the minimum number of variables needed to maintain roughly the same ANN performance is reached. In this case, 10 input variables yields stable and approximately identical performance to using 15, while using 5 variables degraded discrimination power significantly.

The input variables used in the CFMlpANN can be broken down into several classes. The first is related to jet, and multi-object kinematics. The b -jets produced by the Higgs boson tend to have a harder p_T spectrum compared to b -jets produced from gluon radiation. Additionally, the recoil of the Higgs off of the top-system produces small differences in the p_T and invariant

Table 6.12: The ANN inputs for the nine jet-tag categories in the 8 TeV $t\bar{t}H$ analysis in the lepton+jets and dilepton channels. The choice of inputs is optimized for each category. Definitions of the variables are given in the text. The best input variable for each jet-tag category is denoted by \star .

Jets Tags	Lepton+Jets						
	≥ 6 2	4 3	5 3	≥ 6 3	4 4	5 ≥ 4	≥ 6 ≥ 4
Jet 1 p_T		✓	✓		✓		
Jet 2 p_T		✓	✓				
Jet 3 p_T	✓	✓	✓			✓	
Jet 4 p_T	✓	✓	✓			✓	
$p_T(\ell, E_T^{\text{miss}}, \text{jets})$		★		✓	✓	✓	
$M(\ell, E_T^{\text{miss}}, \text{jets})$	✓	✓		✓	✓		✓
Average $M((j_m^{\text{untag}}, j_n^{\text{untag}}))$	✓			✓			
$M((j_m^{\text{tag}}, j_n^{\text{tag}})_{\text{closest}})$							✓
$M((j_m^{\text{tag}}, j_n^{\text{tag}})_{\text{best}})$							✓
Average $\Delta R(j_m^{\text{tag}}, j_n^{\text{tag}})$				✓	✓	✓	✓
Minimum $\Delta R(j_m^{\text{tag}}, j_n^{\text{tag}})$			✓				
$\Delta R(\ell, j_{\text{closest}})$						✓	✓
Sphericity	✓			✓			✓
Aplanarity	✓				✓		
H_0	✓						
H_1	✓				✓		
H_2				✓			✓
H_3	★			✓			✓
μ^{CSV}	✓	✓	★	★	★	★	★
$(\sigma_n^{\text{CSV}})^2$	✓	✓	✓	✓	✓	✓	
Highest CSV value						✓	
2 nd -highest CSV value	✓	✓	✓	✓	✓	✓	✓
Lowest CSV value	✓	✓	✓	✓	✓	✓	✓

mass of the reconstructed $t\bar{t} + jets$ system.

- Jet 1 p_T - the highest value of transverse jet momentum in the event
- Jet 2 p_T - the second highest value of transverse jet momentum in the event
- Jet 3 p_T - the third highest value of transverse jet momentum in the event
- Jet 4 p_T - the fourth highest value of transverse jet momentum in the event
- $p_T(\ell, E_T^{\text{miss}}, \text{jets})$ - the transverse momentum of the four-vector formed by summing the four-vectors of the lepton, MET, and all selected jets in the event
- $M(\ell, E_T^{\text{miss}}, \text{jets})$ - the invariant mass of the four-vector formed by summing the four-vectors of the lepton, MET, and all selected jets in the event
- Average $M((j_m^{\text{untag}}, j_n^{\text{untag}}))$ - the average di-Jet mass formed by all combinations of jets that have not been b -tagged in the event
- $M((j_m^{\text{tag}}, j_n^{\text{tag}})_{\text{closest}})$ - the invariant di-Jet mass of the two b -tagged jets that are closest to one another in the detector

- $M((j_m^{\text{tag}}, j_n^{\text{tag}})_{\text{best}})$ - the invariant mass constructed from the two tagged jets least likely to be a part of the $t\bar{t}$ system as determined by a minimum χ^2 search among all the jet, lepton, and E_T^{miss} combinations in the event, using the W boson and top masses as kinematic constraints.

The next class of input variables describe the angular relationship between reconstructed objects in the event. These are event shape variables. Production of a relatively massive object, in addition to top quarks, such as the Higgs, tends to make $t\bar{t}H$ events more spherically distributed in the detected, while the background events are more collimated. Variables in this class include angular correlations, like the opening angle between the tagged jets

- Average $\Delta R(j_m^{\text{tag}}, j_n^{\text{tag}})$ - the average ΔR spatial separation between all combinations of b -tagged jets in the event
- Minimum $\Delta R(j_m^{\text{tag}}, j_n^{\text{tag}})$ - the smallest value of ΔR measured between a pair of b -tagged jets
- $\Delta R(\ell, j_{\text{closest}})$ - the ΔR spatial separation of the lepton and the closest reconstructed jet
- Sphericity - Event shape variable equal to $\frac{3}{2}(\lambda_2 + \lambda_3)$, where λ_2 and λ_3 are the second and third eigenvalues of the sphericity tensor as described in [156]
- Aplanarity - Event shape variable equal to $\frac{3}{2}(\lambda_3)$, where λ_3 is the third eigenvalue of the sphericity tensor as described in
- H_0 - the zeroth Fox-Wolfram moment [157]
- H_1 - the first Fox-Wolfram moment
- H_2 - the second Fox-Wolfram moment
- H_3 - the third Fox-Wolfram moment

where $\Delta R = \sqrt{\Delta\eta^2 + \Delta\phi^2}$. The sphericity tensor is given by the equation:

$$S^{a,b} = \frac{\sum_i p_i^a p_i^b}{\sum_i |\hat{p}_i|^2} \quad (6.11)$$

where $a, b = x, y, z$ coordinates. This tensor is diagonalized, and solved for its eigenvalues, which are used to compute the sphericity and aplanarity variables. The Fox-Wolfram moments are defined are momentum weighted spherical harmonics, defined as:

$$H_\ell = \sum_{i,j=1}^{N_{\text{jets}}} \frac{|\hat{p}_i||\hat{p}_j|}{|\hat{p}|_{\text{tot}}^2} P_\ell(\cos \Omega_{ij}) \quad (6.12)$$

2222 where $P_\ell(\cos \Omega_{ij})$ is the ℓ^{th} spherical harmonic, with polar angle calculated between jets i and j.

2223 The final class of variables is based on the discriminant output from the b-tagging algorithm.

2224 For many of the categories, the average b -tag discriminant of all of the jets in the event tends
 2225 to be the most powerful single variable. This is due to the high multiplicity of authentic b -jets
 2226 in a $t\bar{t}H$ event. Additionally, since the b -quarks are coming from high mass sources, such as the
 2227 top-quark and the Higgs boson, they will, on average, have a higher momentum in the transverse
 2228 plane than b -jets originating from gluon radiation, as in $t\bar{t} + b\bar{b}$ events. This allows for this high
 2229 transverse momentum b -jets to travel a further distance inside the detector before decaying,
 2230 making the significance of impact parameter of the secondary vertex much higher, increasing
 2231 the probability it will be tagged as a b -jet by the CSV algorithm. Thus, variables related to the
 2232 value b -tagging discriminant provide the greatest signal extraction power.

2233 • μ^{CSV} - the average value of the output of the CSV algorithm for all b -tagged jets in the
 2234 event.

2235 • $(\sigma_n^{\text{CSV}})^2$ - the variance of the average value of the output of the CSV algorithm for all
 2236 b -tagged jets in the event.

2237 • Highest CSV value - the highest value of the CSV discriminant for any b -tagged jet in the
 2238 event

2239 • 2^{nd} -highest CSV value - the second highest value of the CSV discriminant for any b -tagged
 2240 jet in the event

2241 • Lowest CSV value - the lowest value of the CSV discriminant for any b -tagged jet in the
 2242 event

2243 The modeling of the input variables is compared against data for each of the jet/tag diagrams
 2244 in the the following figures:

2245 • ≥ 6 jets, $\equiv 2$ b -tags: Figure 6.10, and Figure 6.11

2246 • $\equiv 4$ jets, $\equiv 3$ b -tags: Figure 6.12, and Figure 6.13

2247 • $\equiv 5$ jets, $\equiv 3$ b -tags: Figure 6.14, and Figure 6.15

2248 • ≥ 6 jets, $\equiv 3$ b -tags: Figure 6.16, and Figure 6.17

2249 • $\equiv 4$ jets, $\equiv 4$ b -tags: Figure 6.18, and Figure 6.19

2250 • $\equiv 5$ jets, $\equiv 4$ b -tags: Figure 6.20, and Figure 6.21

2251 • ≥ 6 jets, ≥ 4 b -tags: Figure 6.22, and Figure 6.23

2252 Below each histogram is a ratio of the yields for data over the simulated sample prediction. The
2253 green band is the total uncertainty estimated for the simulation, and the error bars on the points
2254 are determined by the statistical error on the data collected.

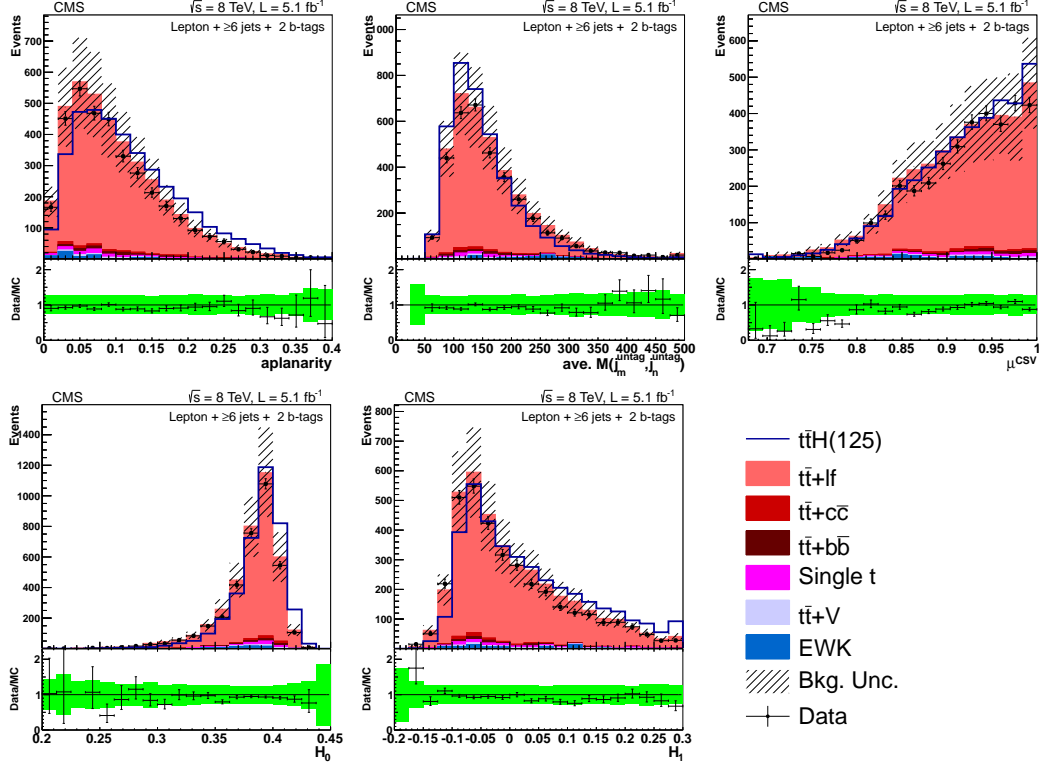


Figure 6.10: Lepton + jets data/MC comparison for the ≥ 6 jets + 2 tag category. The uncertainty band includes statistical and systematic uncertainties that affect both the rate and shape of the background distributions.

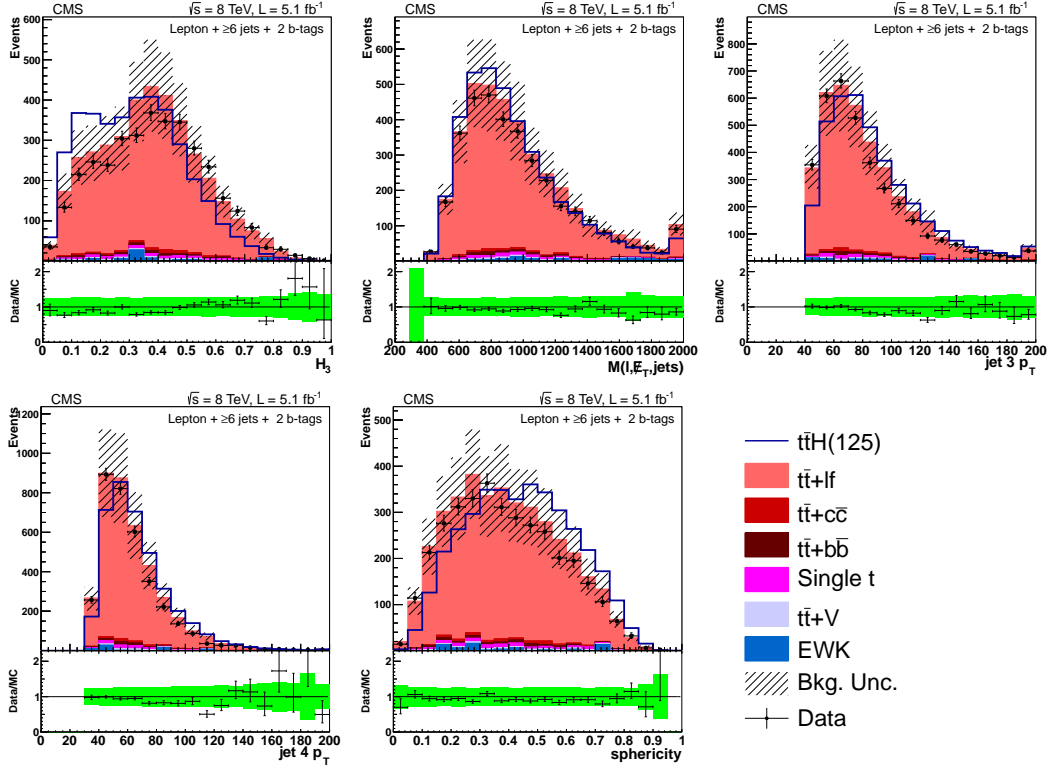


Figure 6.11: Lepton + jets data/MC comparison for the ≥ 6 jets + 2 tag category. The uncertainty band includes statistical and systematic uncertainties that affect both the rate and shape of the background distributions.

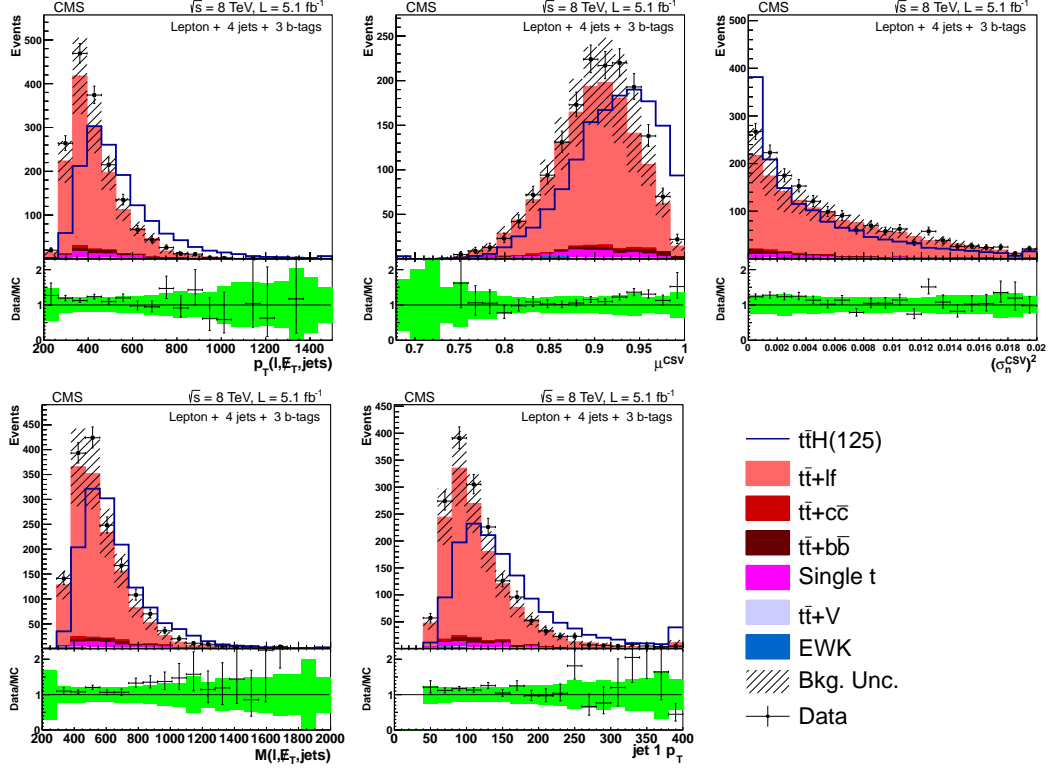


Figure 6.12: Lepton + jets data/MC comparison for the 4 jets + 3 tag category. The uncertainty band includes statistical and systematic uncertainties that affect both the rate and shape of the background distributions.

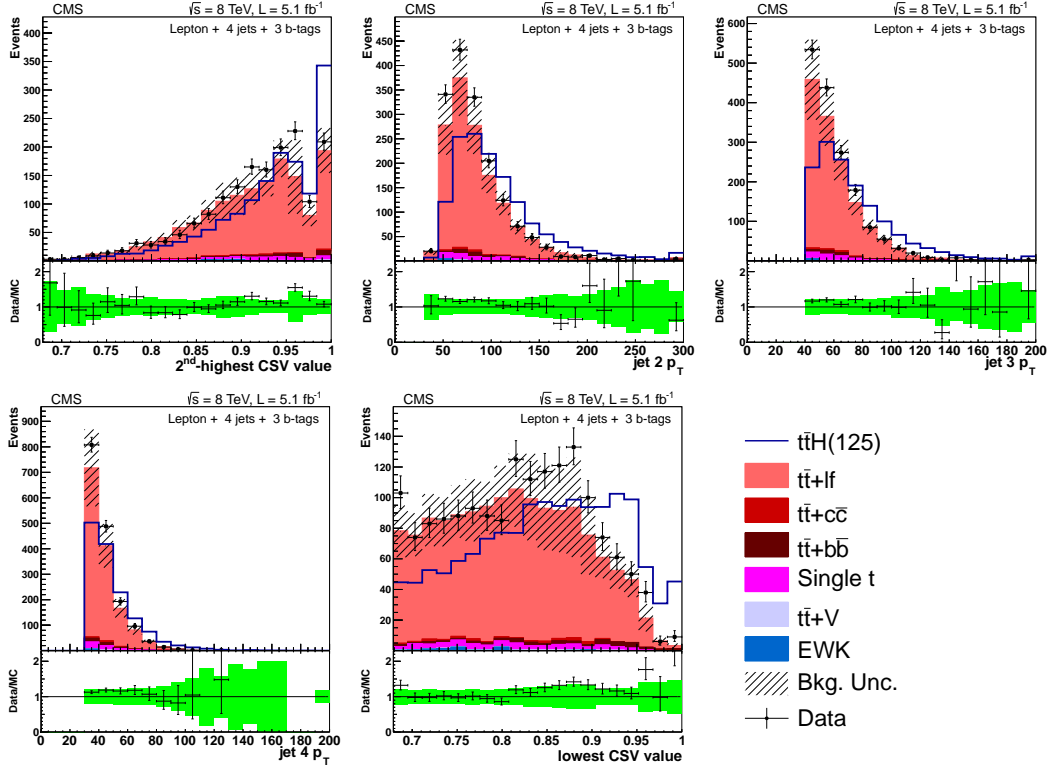


Figure 6.13: Lepton + jets data/MC comparison for the 4 jets + 3 tag category. The uncertainty band includes statistical and systematic uncertainties that affect both the rate and shape of the background distributions.

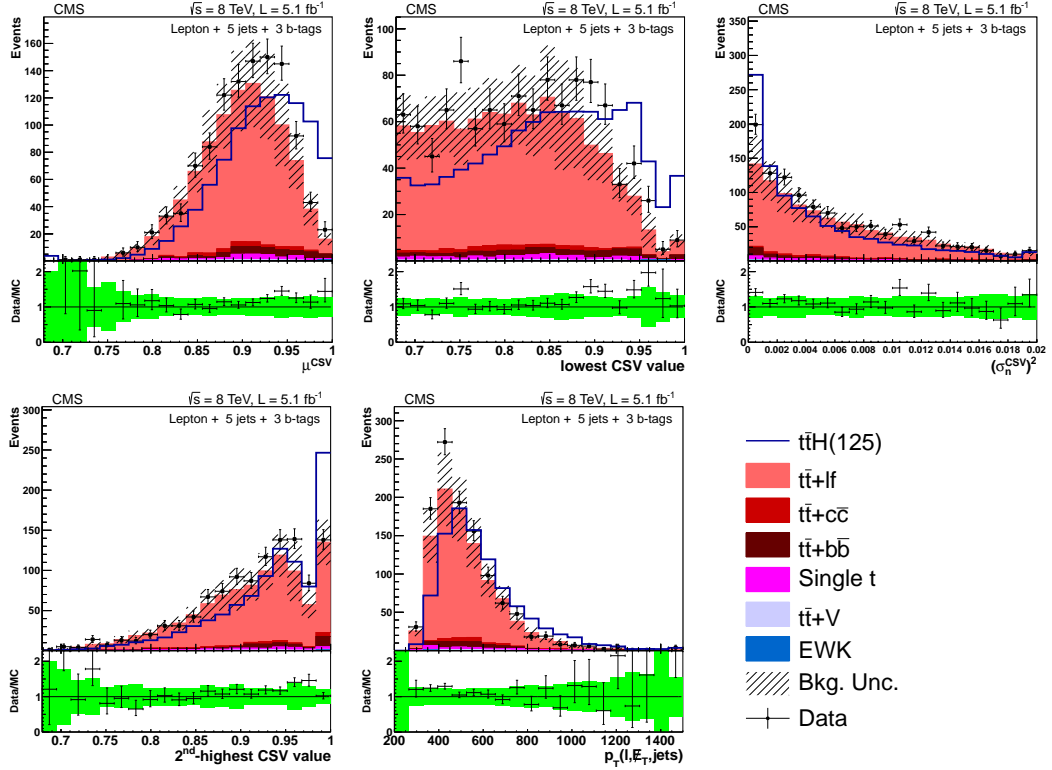


Figure 6.14: Distributions of the five ANN input variables with rankings 1 through 5, in terms of separation, for the 5 jets + 3 b-tags category of the lepton+jets channel at 8 TeV. Definitions of the variables are given in the text. The background is normalized to the SM expectation; the uncertainty band (shown as a hatched band in the stack plot and a green band in the ratio plot) includes statistical and systematic uncertainties that affect both the rate and shape of the background distributions. The $t\bar{t}H$ signal ($m_H = 125 \text{ GeV}/c^2$) is normalized to the total background yield, for easier comparison of the shapes.

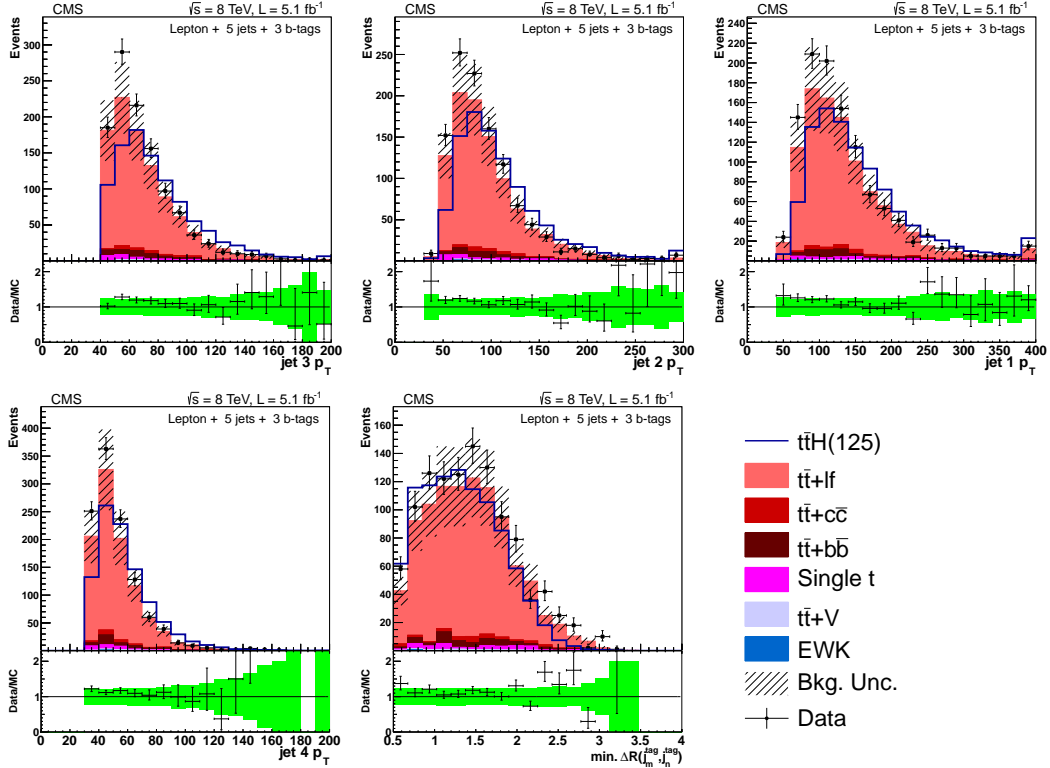


Figure 6.15: Distributions of the five ANN input variables with rankings 6 through 10, in terms of separation, for the 5 jets + 3 b-tags category of the lepton+jets channel at 8 TeV. Definitions of the variables are given in the text. The background is normalized to the SM expectation; the uncertainty band (shown as a hatched band in the stack plot and a green band in the ratio plot) includes statistical and systematic uncertainties that affect both the rate and shape of the background distributions. The $t\bar{t}H$ signal ($m_H = 125 \text{ GeV}/c^2$) is normalized to the total background yield, for easier comparison of the shapes.

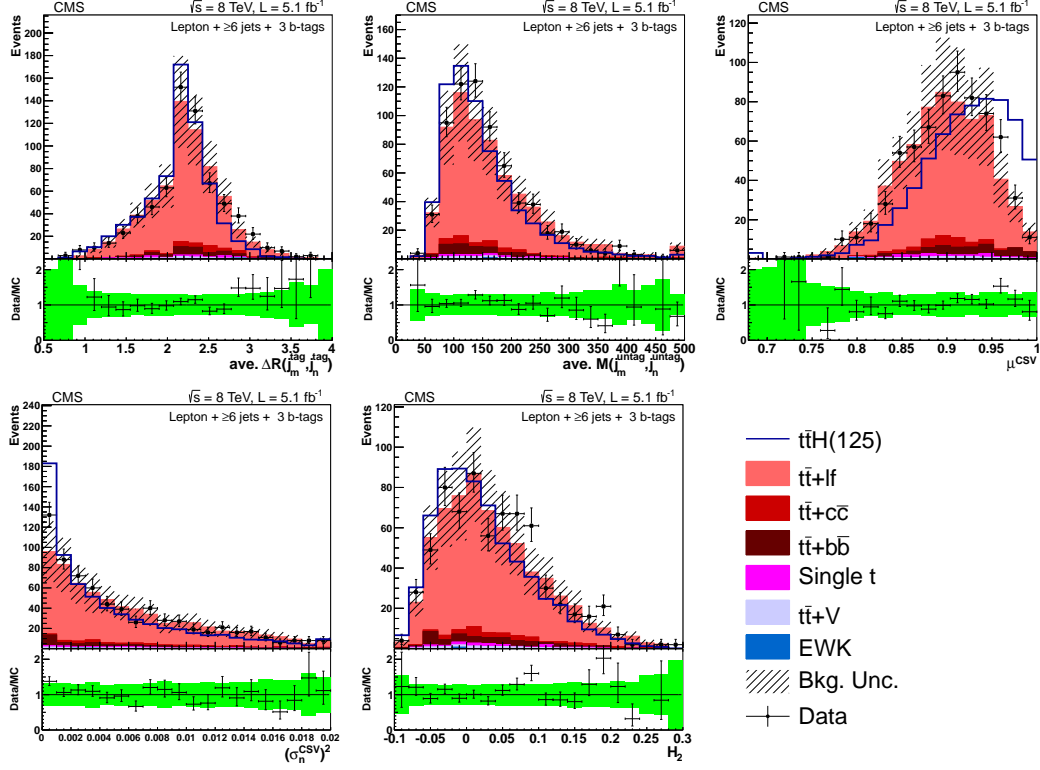


Figure 6.16: Lepton + jets data/MC comparison for the ≥ 6 jets + 3 tag category. The uncertainty band includes statistical and systematic uncertainties that affect both the rate and shape of the background distributions.

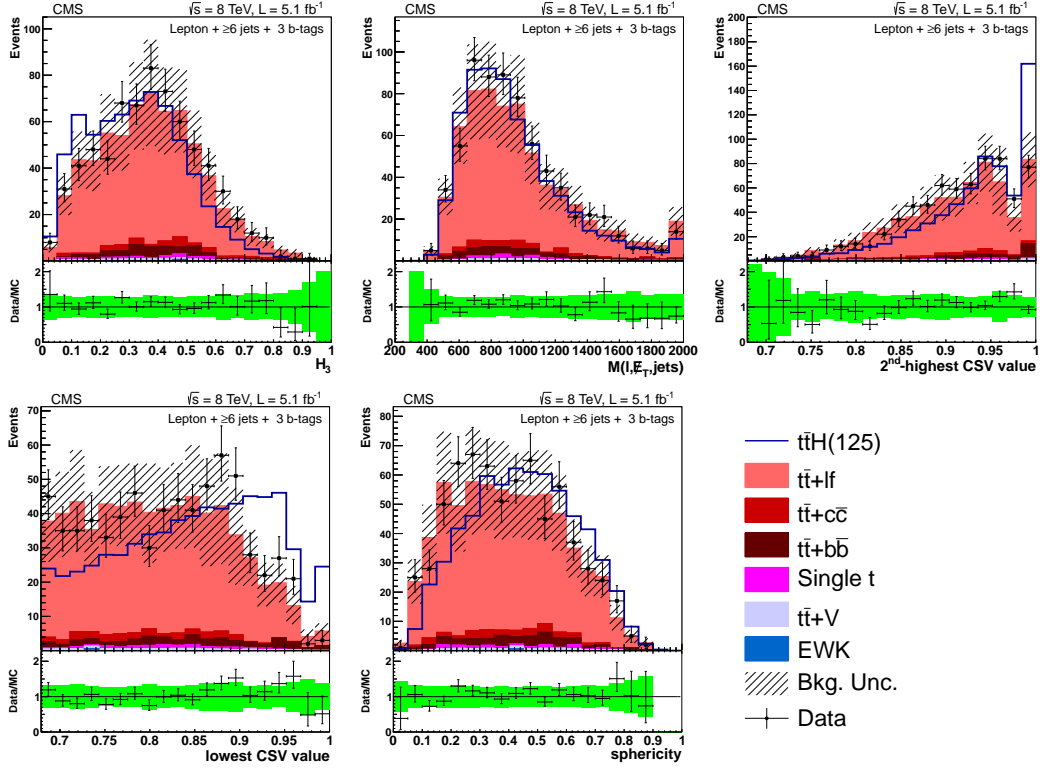


Figure 6.17: Lepton + jets data/MC comparison for the ≥ 6 jets + 3 tag category. The uncertainty band includes statistical and systematic uncertainties that affect both the rate and shape of the background distributions.

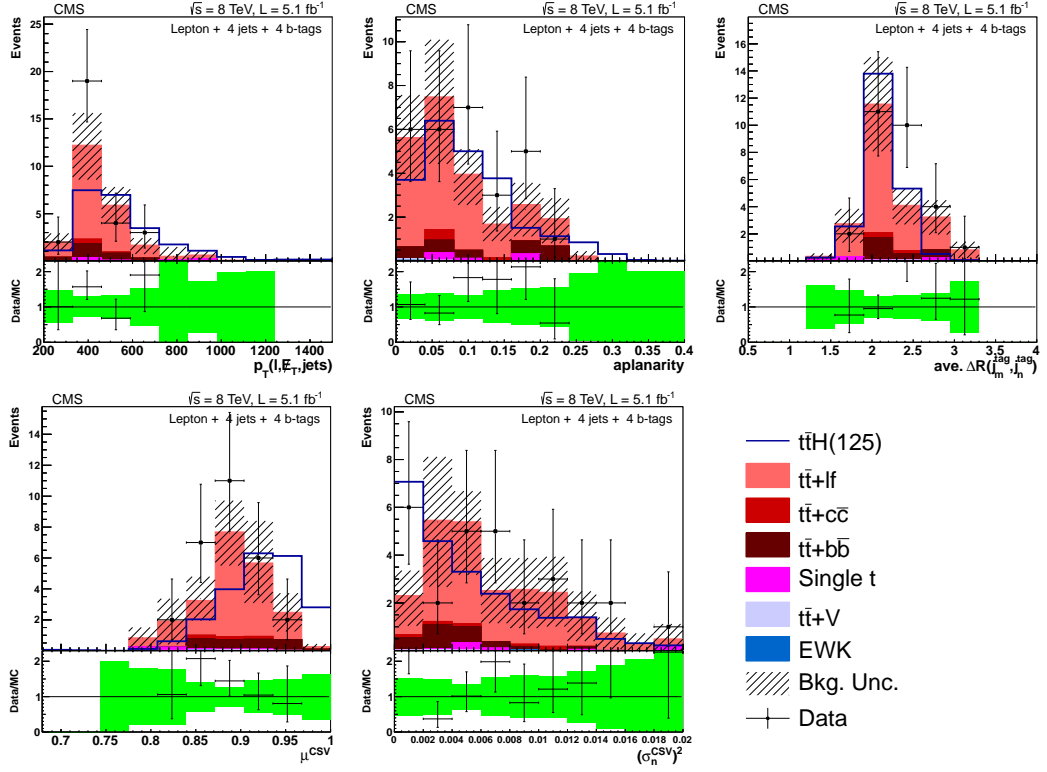


Figure 6.18: Lepton + jets data/MC comparison for the 4 jets + 4 tag category. The uncertainty band includes statistical and systematic uncertainties that affect both the rate and shape of the background distributions.

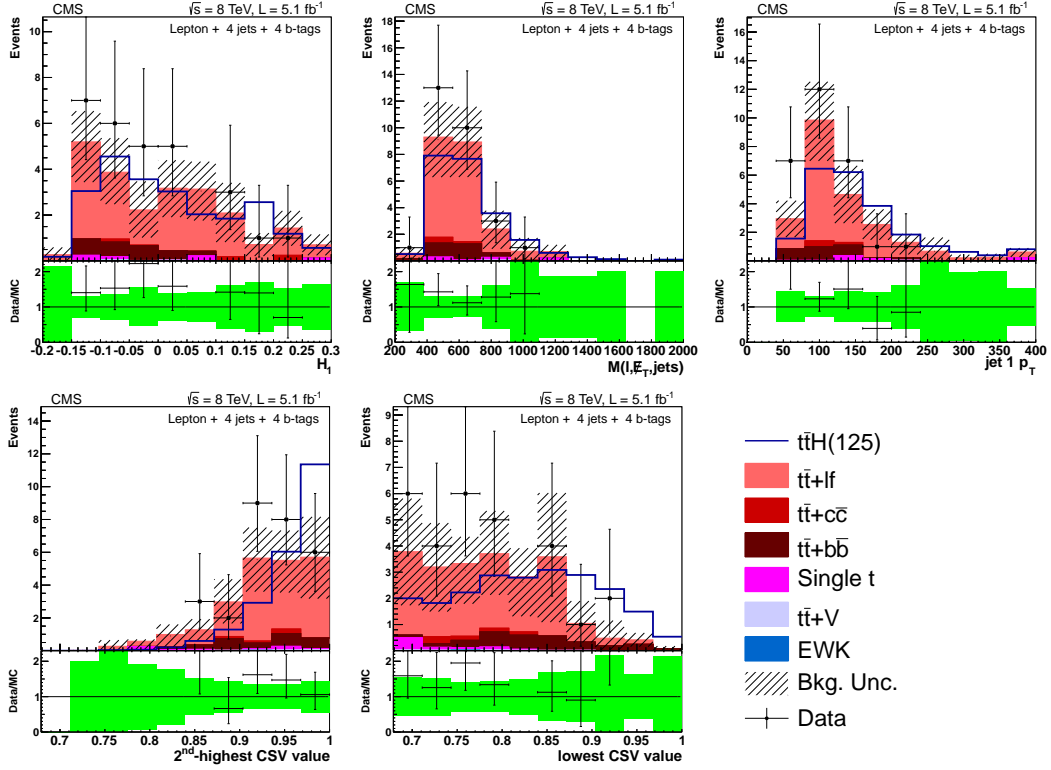


Figure 6.19: Lepton + jets data/MC comparison for the 4 jets + 4 tag category. The uncertainty band includes statistical and systematic uncertainties that affect both the rate and shape of the background distributions.

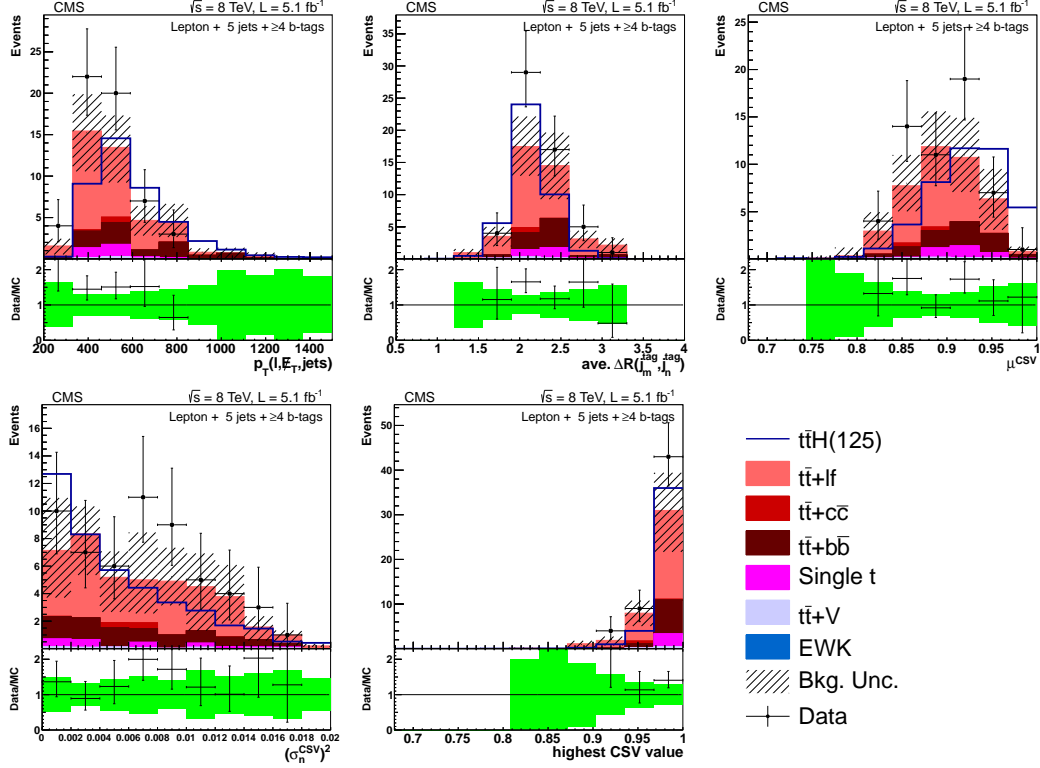


Figure 6.20: Lepton + jets data/MC comparison for the 5 jets + 4 tag category. The uncertainty band includes statistical and systematic uncertainties that affect both the rate and shape of the background distributions.

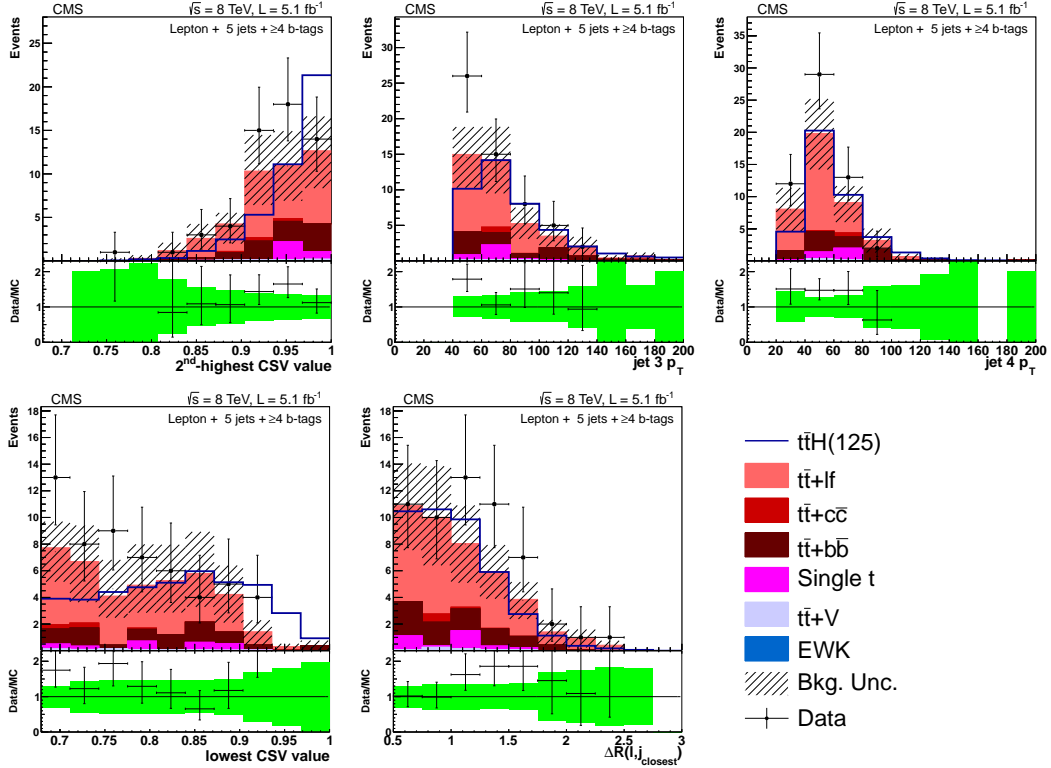


Figure 6.21: Lepton + jets data/MC comparison for the 5 jets + 4 tag category. The uncertainty band includes statistical and systematic uncertainties that affect both the rate and shape of the background distributions.

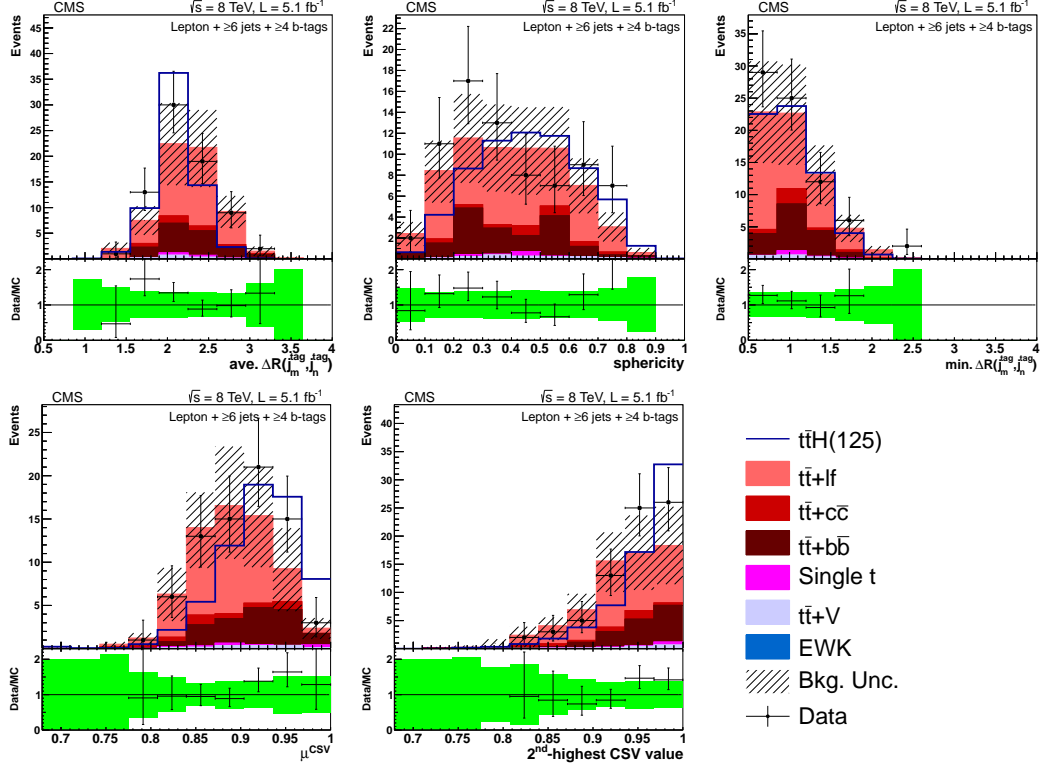


Figure 6.22: Lepton + jets data/MC comparison for the ≥ 6 jets + ≥ 4 tag category. The uncertainty band includes statistical and systematic uncertainties that affect both the rate and shape of the background distributions.

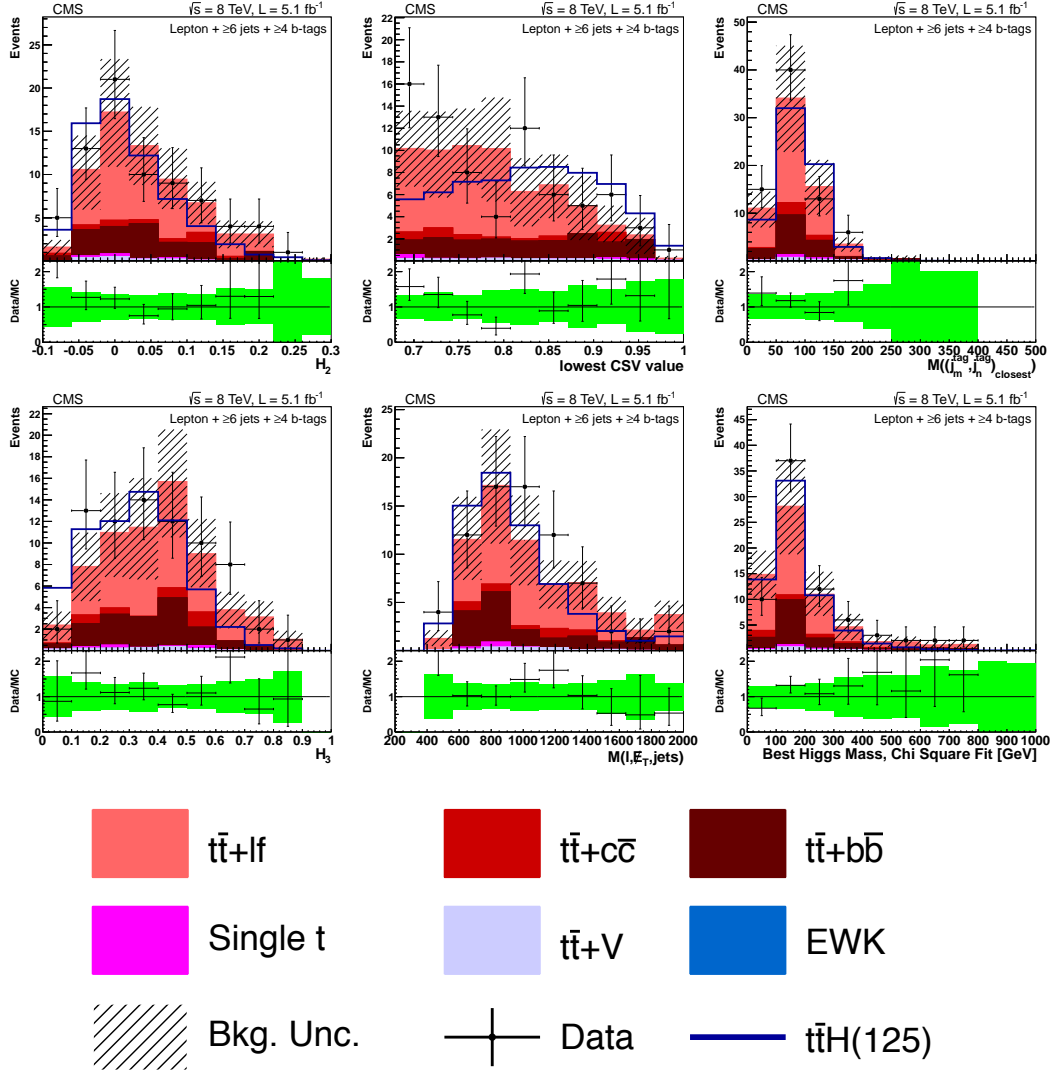


Figure 6.23: Lepton + jets data/MC comparison for the ≥ 6 jets + 4 tag category. The uncertainty band includes statistical and systematic uncertainties that affect both the rate and shape of the background distributions.

2255 6.3.3 MVA Output, Data to Monte Carlo Comparisons

2256 Data to Monte Carlo comparisons for the CFMlpANN output can be seen on figure 6.24. In
 2257 the plots, the signal shape has been multiplied by a factor of 30 in order to make its shape
 2258 visible, and in order to gauge a scale of the expected size of signal to background in each jet/tag
 2259 category.

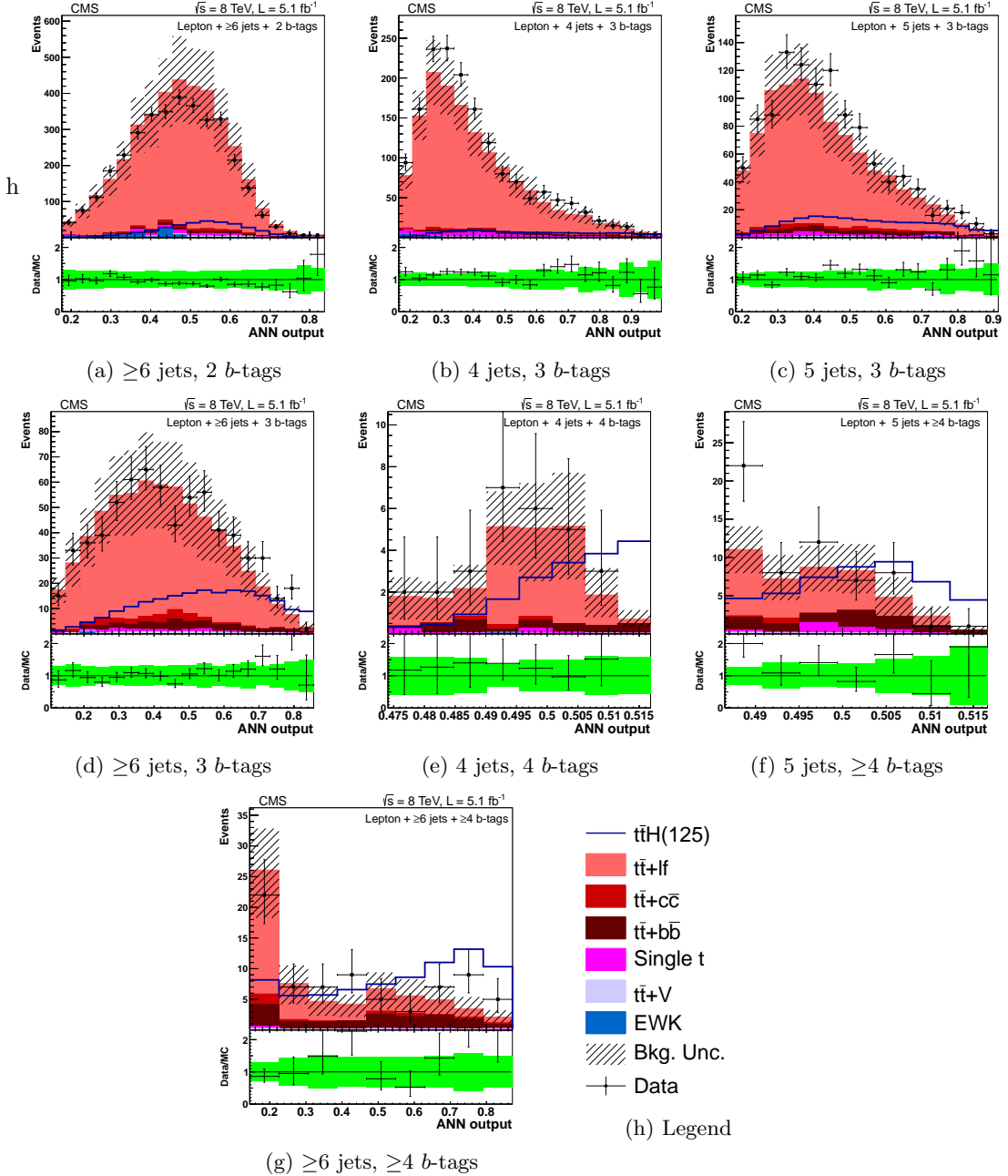


Figure 6.24: The distributions of the CFMlpANN output for lepton+jets events at 8 TeV in the various analysis categories. Background-like events have a low CFMlpANN output value. Signal-like events have a high CFMlpANN output value. The background is normalized to the SM expectation; the uncertainty (shown as a hatched band in the stack plot and a green band in the ratio plot) includes statistical and systematic uncertainties that affect both the rate and shape of the background distributions. The $t\bar{t}H$ signal ($m_H = 125 \text{ GeV}/c^2$) is normalized to $30 \times$ SM expectation.

2260 6.4 Systematic Uncertainties

2261 There are three types of systematic effects considered in this analysis: those that affect only the
 2262 rates of signal or background processes, those that affect only the shapes of the CFMlpANN
 2263 discriminants for signal or background processes, and those that affect both the rate and the
 2264 shape. In the last case, the rate and shape effects are treated simultaneously so that they are
 2265 considered completely correlated. Unless otherwise noted, all of the uncertainties listed here
 2266 apply equally to signal and background and are treated as 100% correlated between the two.
 2267 Below is a list of systematic effects considered for this analysis:

Table 6.13: Summary of the systematic uncertainties considered on the inputs to the limit calculation. Except where noted, each row in this table will be treated as a single, independent nuisance parameter.

Source	Rate Uncertainty	Shape	Remarks
Luminosity (8 TeV)	2.2%	No	All signal and backgrounds
Lepton ID/Trig	4%	No	All signal and backgrounds
Pileup	1%	No	All signal and backgrounds
Additional Pileup Corr.	–	Yes	All signal and backgrounds
Jet Energy Resolution	1.5%	No	All signal and backgrounds
Jet Energy Scale	0-60%	Yes	All signal and backgrounds
b-Tag SF (b/c)	0-33.6%	Yes	All signal and backgrounds
b-Tag SF (mistag)	0-23.5%	Yes	All signal and backgrounds
MC Statistics	–	Yes	All backgrounds
PDF (gg)	9%	No	For gg initiated processes ($t\bar{t}$, $t\bar{t}Z$, $t\bar{t}H$)
PDF ($q\bar{q}$)	4.2-7%	No	For $q\bar{q}$ initiated processes ($t\bar{t}W$, W , Z).
PDF (qg)	4.6%	No	For qg initiated processes (single top)
QCD Scale ($t\bar{t}H$)	15%	No	For NLO $t\bar{t}H$ prediction
QCD Scale ($t\bar{t}$)	2-12%	No	For NLO $t\bar{t}$ and single top predictions
QCD Scale (V)	1.2-1.3%	No	For NNLO W and Z prediction
QCD Scale (VV)	3.5%	No	For NLO diboson prediction
Madgraph Scale ($t\bar{t}$)	0-20%	Yes	$t\bar{t}$ + jets/ bb / $c\bar{c}$ uncorrelated. Varies by jet bin.
Madgraph Scale (V)	20-60%	No	Varies by jet bin.
$t\bar{t} + bb$	50%	No	Only $t\bar{t} + bb$.

2268 **Jet Energy Scale (JES):** The Jet Energy Scale systematic is based on the uncertainty on the
 2269 L1, L2, L3, and L2L3 residual corrections to the reconstructed jet energy, as described
 2270 in section 6.2.6. To evaluate the effect on the CFMlpANN output, the jet energy scale is
 2271 shifted by one standard deviation up and down using the standard JetMET procedure [158].
 2272 For each variation, the jet energies are recalculated, allowing for new jets to pass the
 2273 selection where once they failed, or fail the selection where once they passed, resulting
 2274 in a migration of events across jet/tag categories. Finally, the CFMlpANN response is
 2275 recalculated, and the effect for signal and the $t\bar{t} + jets$ background is shown in figure 6.25.

Jet Energy Resolution (JER): The jet p_T resolution in MC differs from that observed in
 data by approximately 10% in a η dependent way, as described in table 6.8, as per the
 recommendations of the JetMET group [159]. The value of the jet p_T is adjusted according

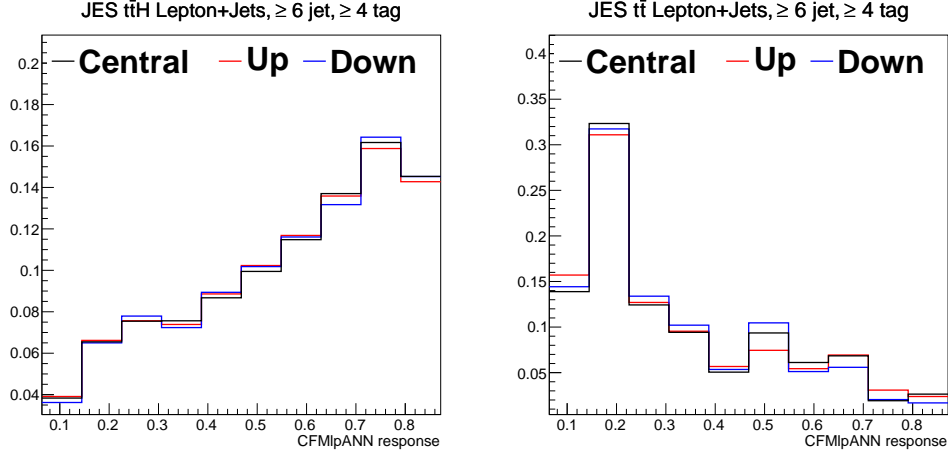


Figure 6.25: Comparison of the MVA discriminator for JES shift upwards (red) and downwards (blue) relative to the nominal (black) shape for the $t\bar{t}H(120)$ signal (left) and the main background sample $t\bar{t}$ + light flavor (right). The plots shown are from the ≥ 6 jet ≥ 4 tag category in the lepton+jets channel. All plots are normalized to unit area.

JES systematic yield change			
sys	shift	lepton+jets	
		$t\bar{t}H(120)$	$t\bar{t}$
JES	up	+8.6%	+12.1%
	down	-8.4%	-7.3%

Table 6.14: Relative yield change due to JES shift up/down for the ≥ 6 jets + ≥ 4 tags category in the lepton+jets channel.

to the formula:

$$p'_T = \max [0, p_T^{gen} + c(p_T^{reco} - p_T^{gen})] \quad (6.13)$$

2276 The correction factor c is taken from table 6.8. To assess the effect of the systematic
 2277 uncertainty on the JER, the value of c is shifted up and down by standard deviation, the
 2278 JER correction is applied to the jets using this new c value, and the event rates and ANN
 2279 shapes are recalculated. The effect of the JER on the shape variation is negligible, so it is
 2280 treated as a rate-only effect in limit setting.

2281 **b-tag Scale Factor:** The uncertainty in the b -tagging scale factor is assessed according to the
 2282 prescriptions developed by the BTag POG [160]. Each per-jet b -tag scale factor is shifted
 2283 up or down by its uncertainty, and the new CSV output value corresponding to that
 2284 uncertainty is recalculated. This new CSV value is used to determine both the number of
 2285 tags associated with that systematic and the new shape of variables that use the CSV
 2286 output, such as the average CSV value for b -tagged jets. This uncertainty effects both rate
 2287 and shape estimates. The effects of the b -tag scale factors on the ANN shape and event
 2288 yields are summarized in Fig. 6.26 and Table 6.15 respectively.

2289 **Lepton ID and Trigger Scale Factors:** As discussed previously, an uncertainty of 4% covers

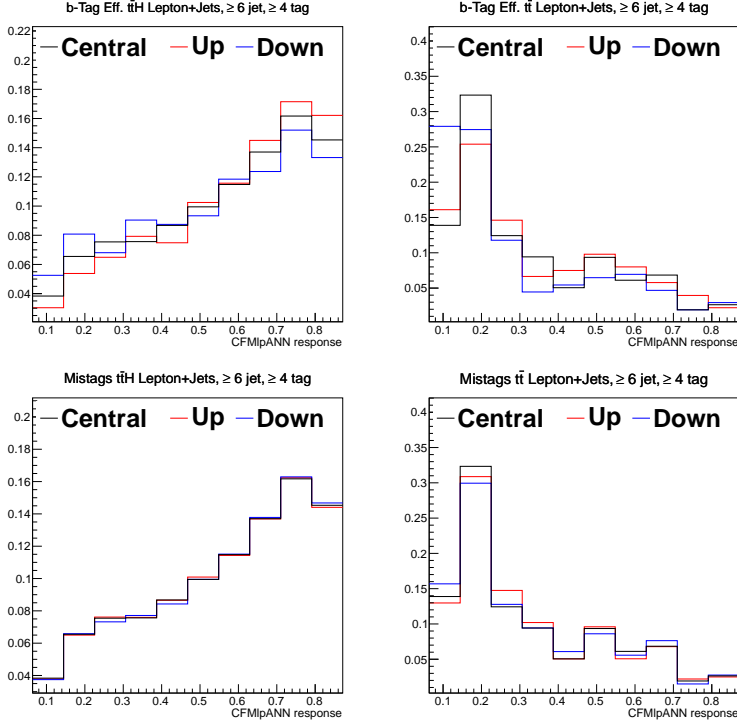


Figure 6.26: Comparison of the MVA discriminator for b -tag scale factor shift upwards (red) and downwards (blue) relative to the nominal (black) shape for the $t\bar{t}H(120)$ signal (left) and the main background sample $t\bar{t} + \text{light flavor}$ (right). The plots are from the ≥ 6 jets + ≥ 4 tags category in the lepton+jets channel. All plots are normalized to unit area.

b -tag systematic yield change			
		lepton+jets	
sys	shift	$t\bar{t}H(120)$	$t\bar{t}$
heavy flavor SF	up	+14.9%	+23.7%
	down	-15.3%	-16.0%
light flavor SF	up	+0.7%	+5.7%
	down	-1.1%	-4.2%

Table 6.15: Relative yield change due to b -tag scale factor shift up/down for the ≥ 6 jets + ≥ 4 tags category in the lepton+jets channel.

2290 variations of the combined trigger, ID, and isolation scale factor.

2291 **Pileup Reweighting:** The uncertainty on the pileup reweighting comes from changing the
 2292 minimum bias cross section used to calculate the pileup reweighting by $\pm 7\%$ from the
 2293 default value of 69.4 mb. The pileup reweighting is calculated using the shifted cross
 2294 sections and the new weights are applied to determine the uncertainty on both the rate
 2295 and shapes. Since the effect of the pileup on the shape variation is negligible, the effects
 2296 of pileup are accounted through a rate-only uncertainty for the limit calculations.

2297 **Additional Pileup Correction** The uncertainty associated with the additional pileup correc-
 2298 tion, described in section 6.1.5, is applied as a pure shape uncertainty to all processes.
 2299 Fig. 6.27 shows the effects of the additional pileup correct uncertainty on the CFMlpANN
 2300 shape.

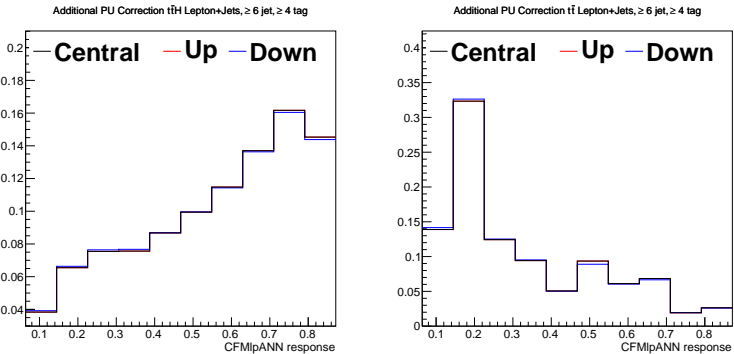


Figure 6.27: Comparison of the MVA discriminator for additional PU correction systematic upwards (red) and downwards (blue) relative to the nominal (black) shape for the $t\bar{t}H(120)$ signal (left) and the main background sample $t\bar{t} + \text{light flavor}$ (right). The plots are from the ≥ 6 jets + ≥ 4 tags category in the lepton+jets channel. All plots are normalized to unit area.

2301 **Cross Sections:** The expectation for signal and background yields are derived from theoretical
 2302 predictions of at least NLO accuracy. Uncertainties affecting these normalizations are
 2303 summarized in table 6.16. Where appropriate, factors contributing to these uncertainties
 2304 that are common to multiple processes are treated as 100% correlated. Note that for the
 2305 $t\bar{t}+\text{jets}$ (including $t\bar{t} + b\bar{b}$ and $t\bar{t} + c\bar{c}$ processes, as well as the $V+\text{jets}$ processes, there
 2306 is an additional uncertainty coming from the scale choice in Madgraph that effects these
 2307 channels in a jet-bin specific way. This uncertainty is not included in the table 6.16, but
 2308 is detailed in the next point.

2309 **Luminosity:** The uncertainty on the luminosity estimate is 2.2%. This affects all rates.

2310 **Madgraph Q^2 Uncertainty:** Although that backgrounds are normalized using NLO accurate
 2311 theoretical calculations, these are only applicable to inclusive distributions. To extrap-

Process	pdf			QCD Scale			
	gg	qb	qg	$t\bar{t}$	V	VV	$t\bar{t}H$
$t\bar{t}H$	9%						12.5%
$t\bar{t}+\text{jets}$	9%			12%			
$t\bar{t} + W$		7%		15%			
$t\bar{t} + Z$	9%			15%			
Single top			4.6%	2%			
$W+\text{jets}$		4.8%			1.3%		
$Z+\text{jets}$		4.2%			1.2%		
Dibosons						3.5%	

Table 6.16: Cross section uncertainties used for the limit settings. Each column in the table is an independent source of uncertainty, except for the last column which represents uncertainties uncorrelated with any others. Uncertainties in the same column for two different processes (different rows) are completely correlated.

2312 olate these inclusive predictions to exclusive rates in particular jet bins requires the use
 2313 of a Monte Carlo sample. The MADGRAPH generator is used at the matrix element level
 2314 and includes tree-level calculations for processes with multiple additional jets, matched
 2315 to the PYTHIA parton shower to model additional soft and collinear radiation. Since the
 2316 MADGRAPH + PYTHIA is tree-level, the choice of the renormalization and factorizations
 2317 scales in this calculation has a significant impact. To include the effects of this uncertainty,
 2318 the factorization and renormalization scales are varied by a factor of two. The ideal way
 2319 to study this effect would be to generate dedicated samples with the varied scale choice,
 2320 however the required statistics to get a precise determination of the systematic effect is
 2321 computationally prohibitive. Therefore, as an alternative, we reweight the samples, divid-
 2322 ing by the appropriate power of α_s and the *pdf* values at the original scale, and multiplying
 2323 by the values at the new scale choice. This reweighting procedure is supported by the CMS
 2324 Monte Carlo Generators group, and has been validated against dedicated scale-varied sam-
 2325 ples and has been shown to produce consistent results [161]. This reweighting procedure
 2326 provides both a rate and a shape uncertainty, separately for $t\bar{t}$ +light flavor, $t\bar{t} + c\bar{c}$, and
 2327 $t\bar{t} + b\bar{b}$ components of the $t\bar{t}$ sample. Figure 6.28 shows the shape and rate variations for
 2328 selected event categories. To prevent the strength of the $t\bar{t}$ +jets constraint from over-
 2329 constraining the $t\bar{t} + b\bar{b}$ and $t\bar{t} + c\bar{c}$ components, we allow the Madgraph scale to vary
 2330 independently for these three components.

2331 **MC Statistics Uncertainty:** To account for the effect of limited MC statistics in the analysis,
 2332 a method described by Barlow and Beeston, is used to select regions of the CFMlpANN
 2333 output that should have additional nuisance parameters applied [162, 163]. For the CFMl-
 2334 pANN shapes of every MC process in all different categories, each bin is allowed to float
 2335 within statistic uncertainty and a corresponding nuisance parameter is added. To make

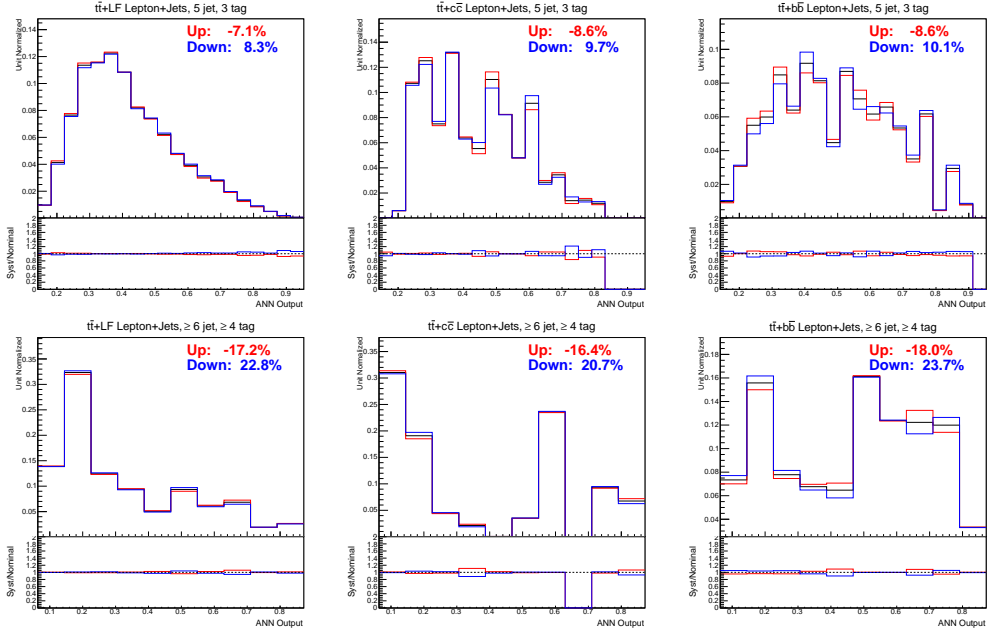


Figure 6.28: The rate and shape variations for selected categories due to the Q^2 uncertainty.

the limit computation more efficient and stable, bins are removed as nuisance parameters if the MC statistics uncertainty is negligible compared to the data statistics uncertainty or where there is no appreciable contribution from signal. In total, there are 60 nuisance parameters used to describe the MC statistics for this analysis. Tests show that the effect of neglecting bins as described above is smaller than 5%.

Additional $t\bar{t} + b\bar{b}$ Rate Uncertainty: $t\bar{t} + b\bar{b}$ background is very similar to our signal, the uncertainty on its rate and shape will have a big impact on our search. Due to the lack of more accurate next leading order(NLO) theoretical predication for this process, we obtained this background and assessed its uncertainty based on the inclusive 8 TeV $t\bar{t}$ sample. Since the inclusive $t\bar{t}$ sample is generated with Madgraph + Pythia, we need to apply a K-factor to the Madgraph cross section. According to calculations done in [164], the K-factor from leading order(LO) to NLO ranges between 1.2 and 1.8, depending on the scale choice. To be conservative, an extra 50% rate uncertainty is assigned to $t\bar{t} + b\bar{b}$ which corresponds to a K-factor of 1.7 for $\sigma_{NLO}/\sigma_{Madgraph}$. Studies also showed consistently that $t\bar{t} + b\bar{b}$ rate is correct to within factor of 2 in control regions dominated by $t\bar{t}$ +light flavor statistics. The extra 50% rate uncertainty should possibly include additional uncertainty beyond the 20% from Q^2 scale to account for the differences between NLO and Madgraph.

In order to validate this assessment further, a dedicated CFMlpANN was trained to separate $t\bar{t} + b\bar{b}$ from the $t\bar{t} + jets$ background. In order to have sufficient statistics, two jet/tag categories are used: 5jets, $\geq 3b$ -tags, and ≥ 6 jets, $\geq 3b$ -tags. The nominal $t\bar{t} + b\bar{b}$ cross section

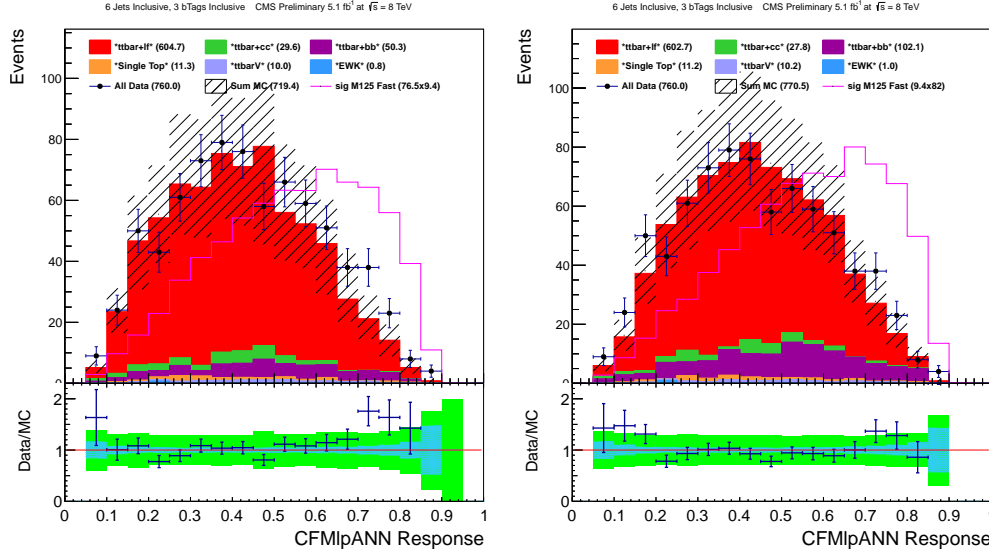


Figure 6.29: A dedicated CFMlpANN trained to isolate $t\bar{t} + b\bar{b}$ from $t\bar{t} + jets$. The left plot shows is for the case of nominal $t\bar{t} + b\bar{b}$ cross-section, the right plot shows the case for $x2 t\bar{t} + b\bar{b}$ cross-section. The left-most region of both plots is the most sensitive to the $t\bar{t} + b\bar{b}$ normalization, and shows no significant improvement in data to MC agreement, justifying the reasoning that an uncertainty larger than 50% is needed.

2356 was doubled, in an attempt to observe an improvement in the range of the discriminant
 2357 that was enriched in $t\bar{t} + b\bar{b}$. However, as figure 6.29 shows, no significant improvement
 2358 was seen, justifying the reasoning that an uncertainty much larger than 50% is needed.

2359 6.5 Statistical Methods

2360 In the lack of an observation of any deviation from SM predictions, upper limits are set on the
 2361 Higgs boson production cross section, with respect to the SM expectation, $\sigma^{95\%}/\sigma^{SM}$. Although
 2362 the analysis has been optimized for Higgs decays to b -quarks, there is still acceptance from WW
 2363 and ZZ decays. As such, limits on the inclusive decay of the Higgs boson are set. The statistical
 2364 method used to report results is the modified frequentist approach, also known as CL_s .

2365 For the CL_s method, the likelihood function $\mathcal{L}(\text{data}|\mu, \theta)$ is defined as

$$\mathcal{L}(\text{data}|\mu, \theta) = \text{Poisson}(\text{data}|\mu \cdot s(\theta) + b(\theta)) \cdot p(\tilde{\theta}|\theta) \quad (6.14)$$

$$= \prod_i \frac{(\mu s_i + b_i)^{n_i}}{n_i!} e^{-(\mu s_i + b_i)} \cdot p(\tilde{\theta}|\theta) \quad (6.15)$$

2366 where μ is the signal strength modifier which is often reported in the upper limit results as the
 2367 ratio of the cross-section upper limit over the standard model cross-section and θ represents a
 2368 full set of nuisance parameters that are used to incorporate systematic uncertainties [165]. The

2369 Probability Distribution Function (*pdf*) of the nuisance parameter $p(\tilde{\theta}|\theta)$, where $\tilde{\theta}$ is the default
 2370 value, reflects the degree of confidence in what the true value of θ is. For rate uncertainties, this
 2371 is parameterized by a log-normal distribution given by:

$$\rho(\theta) = \frac{1}{\sqrt{2\pi} \ln \kappa} \exp \left(-\frac{(\ln(\theta/\tilde{\theta}))^2}{2\ln(\kappa)^2} \right) \frac{1}{\theta} \quad (6.16)$$

2372 where κ is the parameter used to determine the width of the uncertainty, and $\tilde{\theta}$ is the nominal
 2373 value of the distribution. Shape uncertainties can be taken into account by "vertical morphing"
 2374 [166]. For each shape uncertainty, two additional histograms of the CFMlpANN output
 2375 are needed, with $\pm 1\sigma$ variations of the systematic uncertainty in question. When building the
 2376 likelihood, the systematic is associated to a nuisance parameter taken from a unit gaussian dis-
 2377 tribution, which is used to parameterize a quadratic interpolation for shifts below the 1σ value
 2378 of a given bin, and linear interpolation for values beyond.

2379 To compare the compatibility of the data with the *background – only* ($\mu = 0$) and *signal +*
 2380 *background* hypotheses, where the signal is allowed to be scaled by some factor μ , the test
 2381 statistic \tilde{q}_μ is constructed based on the profile likelihood ratio:

$$\tilde{q}_\mu = -2 \ln \frac{\mathcal{L}(\text{data}|\mu, \hat{\theta}_\mu)}{\mathcal{L}(\text{data}|\hat{\mu}, \hat{\theta})} \quad , 0 \leq \hat{\mu} \leq \mu \quad (6.17)$$

2382 where $\hat{\theta}_\mu$ refers to the conditional maximum likelihood estimator of θ , given the signal strength
 2383 parameter μ and data. The pair of parameter estimators $\hat{\mu}$ and $\hat{\theta}$ correspond to the global
 2384 maximum of the likelihood.

2385 To perform the full CL_S technique, *pdf's* of the results of the *background – only*, $f(\tilde{q}_\mu|\mu, \hat{\theta}_\mu^{obs})$,
 2386 and *signal + background*, $f(\tilde{q}_\mu|0, \hat{\theta}_\mu^{obs})$ test statistics are formed by creating *psuedo – datasets*
 2387 of the signal and background CFMlpANN distributions, with the values of $\hat{\theta}_0^{obs}$ and $\hat{\theta}_\mu^{obs}$ fixed,
 2388 but allowing the shapes and normalizations of the CFMlpANN distributions to vary within
 2389 the constraints of the nuisance parameter shapes. Once the *pdfs* for each of the test statistics
 2390 are constructed, the *p*-value associated with each hypothesis, p_μ and p_0 , are evaluated by the
 2391 following integrals:

$$p_\mu = P(\tilde{q}_\mu \geq \tilde{q}_\mu^{obs} | \text{signal + background}) = \int_{\tilde{q}_\mu^{obs}}^{\inf} f(\tilde{q}_\mu|\mu, \hat{\theta}_\mu^{obs}) d\tilde{q}_\mu \quad (6.18)$$

2392 for the *signal + background* hypothesis, and

$$1 - p_0 = P(\tilde{q}_\mu \geq \tilde{q}_\mu^{obs} | \text{background – only}) = \int_{\tilde{q}_0^{obs}}^{\inf} f(\tilde{q}_\mu|0, \hat{\theta}_0^{obs}) d\tilde{q}_\mu \quad (6.19)$$

2393 for the *background – only* hypothesis. $CL_s(\mu)$ is calculated as a ratio of these p -values:

$$CL_s(\mu) = \frac{p_\mu}{1 - p_0} \quad (6.20)$$

2394 To quote the 95% upper limit on μ , $\mu^{95\% CL}$, the value of μ is adjusted until $CL_s = 0.05$.

2395 The frequentist CL_s approach uses a large number of pseudo-experiments to extract the
2396 limit results. The "asymptotic" approach makes an analytic approximation of the full CL_s
2397 technique and therefore avoids throwing pseudo-experiments [167]. The *pdfs*, $f(\tilde{q}_\mu|\mu, \hat{\theta}_\mu^{obs})$, and
2398 $f(\tilde{q}_\mu|0, \hat{\theta}_\mu^{obs})$ are approximated as a falling exponential below $q_{\mu,A}$, and a Gaussian above, where
2399 $q_{\mu,A}$ is the test statistic of the Asimov dataset, the background only hypothesis with nominal
2400 nuisance value parameters. The asymptotic approach is used for optimization and the results of
2401 this analysis. For the limits set from the combined Lepton+Jets and di-Lepton channels, using
2402 both 7 and 8 TeV data, the results are calculated using the full CL_s treatment. Comparisons
2403 have shown that limits obtained with the two techniques agree at the 10% level.

2404 In the limit calculation, the backgrounds are decomposed into the following distinct cate-
2405 gories: $t\bar{t}$ +jets, $t\bar{t} + b\bar{b}$, $t\bar{t} + c\bar{c}$, single top (*s*-channel, *t*-channel, and *tW*-channel combined),
2406 W +jets, Z +jets, $t\bar{t} + W$, $t\bar{t} + Z$, and dibosons (WW , WZ , and ZZ combined). The rates and
2407 shapes of these background processes, as well as the signal are allowed to vary according to a set
2408 of nuisance parameters, and the values of these nuisance parameters are constrained according
2409 to the uncertainties summarized in Table 7.13. Except where noted below, each row in that table
2410 represents a single nuisance parameter, completely correlated across all categories and processes
2411 to which it applies. The exceptions to this approach are as follows:

- 2412 • In the case of the Madgraph Q^2 uncertainty, there are separate nuisance parameters for
2413 each of the three components of the $t\bar{t}$ background (+jets, + $b\bar{b}$, and + $c\bar{c}$). Furthermore, for
2414 the $t\bar{t}$ +jets component, the uncertainty is actually broken into three nuisance parameters
2415 for the contributions coming from diagrams with zero extra partons, one extra parton, or
2416 at least two extra partons.
- 2417 • For the *b*-tagging efficiency and mistag rate uncertainties, the rate and shape components
2418 are described by separate, independent nuisance parameters. Furthermore, each event
2419 selection category has its own, independent nuisance parameter. This is to prevent the
2420 high statistics background rich regions from over-constraining the shape uncertainties in
2421 the lower statistics, more signal rich regions.

2422 For systematic effects such as the jet energy scale or the rate component of the *b*-tagging
2423 scale factor that may cause migration between event categories, care has been taken to correlate
2424 properly the different categories so that, for example, increasing the jet energy scale will cause

the appropriate increases and decreases in the yields in various categories. The binning of the CFMlpANN output is chosen to minimize the impact of MC statistics and, as described in section 6.4 the MC statistics for bins where the MC statistical uncertainty causes a significant impact are accounted for.

6.6 Results and Conclusions

The variable used for signal extraction is the shape of the MVA output discriminator distribution. The fit of the simulated samples to the measured data will test for the presence of signal and, in its absence, it will set upper limits on the Higgs boson cross section. Besides the MVA discriminator shapes for data, background and signal, inputs to the "Higgs Combination" package also include the number of events passing our selection for each of the above processes. Various systematic uncertainties described in section 6.4 have all been taken into account in our limit calculation. The Higgs mass points we set limits for are: 110, 115, 120, 125, 130, 135 and 140 GeV/c^2 . The upper limits are shown in Tab. 6.17 and Fig. 6.30.

Higgs Mass	Observed	Median	Expected 68% C.L. Range	95% C.L. Range
110 GeV/c^2	5.9	3.1	[2.1,4.6]	[1.6,6.8]
115 GeV/c^2	7.2	3.9	[2.7,5.7]	[2.0,8.1]
120 GeV/c^2	8.8	4.8	[3.4,6.9]	[2.5,9.7]
125 GeV/c^2	9.5	5.4	[3.8,7.9]	[2.8,11.1]
130 GeV/c^2	11.4	6.6	[4.6,9.6]	[3.4,13.7]
135 GeV/c^2	15.0	8.9	[6.3,12.8]	[4.7,18.1]
140 GeV/c^2	17.0	11.0	[7.7,15.9]	[5.7,22.5]

Table 6.17: Expected and observed upper limits for SM Higgs for lepton + jets channel using the first 5.1 fb^{-1} of the 2012 dataset. These limits were extracted using the asymptotic method.

For this first 5.1 fb^{-1} of data collected by the CMS detector, the first search for the Standard Model Higgs boson produced in association with top-quark pairs. Although there have been no observed signs of Higgs production in association with top quarks, upper limits are set on the production cross-section, using the statistical methods described above. If this data set was repeatedly collected, allowing for statistical fluctuations, it should be expected that, for a Standard Model Higgs boson, with mass, $m_H = 125 \text{ GeV}$, that 95% of the results would fail to observe the $t\bar{t}H$ signal unless its cross-section was modified by a factor of 9.5. From simulations alone, this expected factor is 5.4, a difference of less than 2σ from the observed data.

The results of this analysis were combined with previous results in this channel from 7 TeV data and with a di-lepton final state channel and published in the Journal of High Energy Physics (JHEP) in May of 2013 [168]. The combined analytical power of all of the channels allowed for an upper limit of 5.8 times the predicted Standard Model cross section. This is less than 1σ

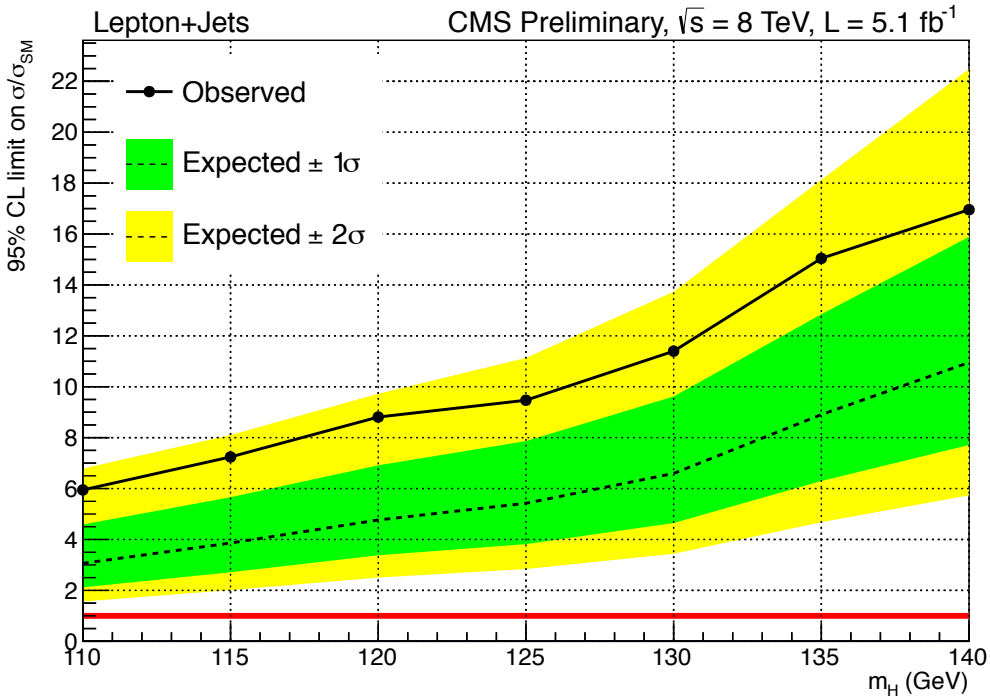


Figure 6.30: The expected and observed 95% CL upper limits on the signal strength parameter $\mu = \sigma/\sigma_{SM}$ for the lepton+jets channel using the 2012 dataset. These limits were extracted using the asymptotic method.

away from the expected factor of 5.2 from simulations alone.

The technique of using a simultaneous fit of the signal and background simulations across each of the jet/tag categories was developed in the 7 TeV analysis. My specific contributions included the creation of software to identify physics objects with variables and selections optimized for the 8 TeV dataset. The validation of the selection was achieved by synchronization with a $t\bar{t}$ cross-section analysis, careful inspection of the calibration factors used, and the evaluation of the simulations against data in the lower jet and tag multiplicity categories (to avoid signal bias). Additionally, I was responsible for the training, testing, and validation of the CFMlpANN algorithm used in this analysis. Finally, I performed limit calculations and evaluated normalization and pull distributions using the asymptotic limit setting method to validate the performance of the limit setting technique.

2461 **Chapter 7**

2462 **Analysis II: The Complete 19.5**
2463 **fb^{-1} of 8 TeV data**

2464 The CMS experiment recorded 19.5 fb^{-1} of data in the complete 8 TeV run during 2012.
2465 The previous analysis was updated with the full dataset. A similar lepton and jet selection
2466 is used, with the same classification scheme for events, based on the reconstructed jet and b -
2467 tag multiplicity. New signal and background simulations were generated to account for the
2468 increased dataset, requiring new calibration factors for the pileup, lepton and jet reconstruction,
2469 and b -tagging efficiency. Additionally, a new type of multivariate analysis (MVA) technique was
2470 employed, in place of the Clermont-Ferrand Multi-Layer Perceptron Artificial Neural Network
2471 (CFMlpANN), a Boosted Decision Tree (BDT) is used for signal extraction and limit setting. The
2472 number of input variables that were investigated for use in each jet/tag category, was expanded,
2473 and some new variables were found to offer slightly more discriminating power. The discriminant
2474 of a specialized BDT, trained to separate $t\bar{t} + b\bar{b}$ from $t\bar{t}H$, was added as an input variable to
2475 the BDT trained in the 5 jet, ≥ 4 b -tag; ≥ 6 jet, 3 b -tag; and ≥ 6 jet, ≥ 4 b -tag categories.

2476 **7.1 Data and Simulated Samples**

2477 As described in the earlier chapters, data is collected through an HLT trigger path and stored
2478 offline for analysis later. Simulated samples are generated with the latest theoretical and empir-
2479 ical inputs for the proton PDF, standard model cross sections, and hadronic showering. These
2480 events are processed with a simulation of the detector environment, and the subsequent elec-
2481 tronic response of each of its elements. Finally, physics objects, such as electrons, and muons
2482 are reconstructed with the particle-flow algorithm described in a previous chapter.

²⁴⁸³ 7.1.1 Data Samples

²⁴⁸⁴ The results presented here are based on the full $\sim 19.5 \text{ fb}^{-1}$ of the 2012 CMS dataset. Table 7.1
²⁴⁸⁵ lists the datasets used for this analysis, based on single muon and single electron triggers used to
²⁴⁸⁶ collect the data. Luminosities are quoted from the HF luminosity calculation and have a 2.2%
²⁴⁸⁷ uncertainty.

Dataset	Run Range	Integrated Luminosity
SingleMu, Run2012A	190456–193621	0.81 fb^{-1}
SingleMu, Run2012A	190782–190949	0.08 fb^{-1}
SingleMu, Run2012B	193834–196531	4.40 fb^{-1}
SingleMu, Run2012C	198022–198523	0.50 fb^{-1}
SingleMu, Run2012C	198941–203746	6.39 fb^{-1}
SingleMu, Run2012D	203768–208686	7.27 fb^{-1}
Total SingleMu	190645–208686	19.5 fb^{-1}
SingleElectron, Run2012A	190456–193621	0.81 fb^{-1}
SingleElectron, Run2012A	190782–190949	0.08 fb^{-1}
SingleElectron, Run2012B	193834–196531	4.40 fb^{-1}
SingleElectron, Run2012C	198022–198523	0.50 fb^{-1}
SingleElectron, Run2012C	198941–203746	6.40 fb^{-1}
SingleElectron, Run2012D	203768–208686	7.27 fb^{-1}
Total SingleElectron	190645–208686	19.5 fb^{-1}

Table 7.1: The datasets analyzed for this analysis.

²⁴⁸⁸ 7.1.2 Signal Samples

²⁴⁸⁹ The $t\bar{t}H$ signal is modeled using the PYTHIA Monte Carlo generator. The samples and associated
²⁴⁹⁰ cross sections used are listed in Table 7.2.

Mass	Higgs Decay	Dataset	Cross Sect.
$110 \text{ GeV}/c^2$	$H \rightarrow \text{all}$	TTH, Inclusive Decays $M_H = 110$, Pythia6	0.1887 pb
$115 \text{ GeV}/c^2$	$H \rightarrow \text{all}$	TTH, Inclusive Decays $M_H = 115$, Pythia6	0.1663 pb
$120 \text{ GeV}/c^2$	$H \rightarrow \text{all}$	TTH, Inclusive Decays $M_H = 120$, Pythia6	0.1470 pb
$122.5 \text{ GeV}/c^2$	$H \rightarrow \text{all}$	TTH, Inclusive Decays $M_H = 122.5$, Pythia6	0.1383 pb
$125 \text{ GeV}/c^2$	$H \rightarrow \text{all}$	TTH, Inclusive Decays $M_H = 125$, Pythia6	0.1302 pb
$127.5 \text{ GeV}/c^2$	$H \rightarrow \text{all}$	TTH, Inclusive Decays $M_H = 127.5$, Pythia6	0.1227 pb
$130 \text{ GeV}/c^2$	$H \rightarrow \text{all}$	TTH, Inclusive Decays $M_H = 130$, Pythia6	0.1157 pb
$135 \text{ GeV}/c^2$	$H \rightarrow \text{all}$	TTH, Inclusive Decays $M_H = 135$, Pythia6	0.1031 pb
$140 \text{ GeV}/c^2$	$H \rightarrow \text{all}$	TTH, Inclusive Decays $M_H = 140$, Pythia6	0.09207 pb

Table 7.2: List of signal MC datasets and cross sections used to determine the SM expectation.

²⁴⁹¹ 7.1.3 Background Samples

²⁴⁹² To model the backgrounds, this analysis primarily uses Monte Carlo (MC) samples from the
²⁴⁹³ "Summer12" MC campaign, discussed in the previous chapter. Most of the samples are generated
²⁴⁹⁴ either with the MADGRAPH tree-level matrix element generator matched to PYTHIA for the
²⁴⁹⁵ parton shower, or with the NLO generator POWHEG combined with PYTHIA. These samples are
²⁴⁹⁶ reconstructed with the same CMSSW version as the data samples listed above. Similarly to the
²⁴⁹⁷ previous analysis, the pileup distribution in all MC samples is reweighted, using the procedure

2498 listed below so that the MC pileup distribution matches the one expected for data. Table 7.3
 2499 lists the background MC samples and associated cross sections.

2500 For this analysis, the $t\bar{t} + jets$ background, is decomposed into four components. The $t\bar{t} + b\bar{b}$,
 2501 background is separated into two classes: $t\bar{t} + b\bar{b}$ events in which both b-quarks are well separated
 2502 and energetic enough to be reconstructed, and events in which either the two b-quarks are so
 2503 close together they merge into the same jet or one of the b-quarks is too soft or forward to be
 2504 reconstructed as a jet. The latter contribution is referred to as $t\bar{t} + b$.

Sample	Dataset	Cross Sect.
$t\bar{t} + jets$		
$t\bar{t} \rightarrow all$	TTJets, Inclusive Decays, Madgraph	245.8 pb
$t\bar{t} \rightarrow jets$	TTJets, Hadronic Decays, Madgraph	112.33 pb
$t\bar{t} \rightarrow \ell\nu + 4 jets$	TTJets, Semileptonic Decays, Madgraph	107.66 pb
$t\bar{t} \rightarrow \ell\nu\ell\nu + 2 jets$	TTJets, Fully Leptonic Decays, Madgraph	25.81 pb
$t\bar{t} + W$	TTWJets, Madgraph	0.249 pb
$t\bar{t} + Z$	TTZJets, Madgraph	0.208 pb
$W + jets$	WJets to Leptons, Madgraph	36257.2 pb
$W + 1 jet$	W+1Jet to Leptons, Madgraph	6440.4 pb
$W + 2 jets$	W+2Jets to Leptons, Madgraph	2087.2 pb
$W + 3 jets$	W+3Jets to Leptons, Madgraph	619.0 pb
$W + 4 jets$	W+4Jets to Leptons, Madgraph	255.2 pb
$Z/\gamma^* + jets$		
$10 \text{ GeV}/c^2 < M_{\ell\ell} < 50 \text{ GeV}/c^2$	DYJets to Leptons, $10 < M_{\ell\ell} < 50 \text{ GeV}$, Madgraph	14702 pb
$M_{\ell\ell} > 50 \text{ GeV}/c^2$	DYJets to Leptons, $M_{\ell\ell} > 50 \text{ GeV}$, Madgraph	3505.7 pb
$Z/\gamma^* + 1 jet$	DY+1Jet to Leptons, $M_{\ell\ell} > 50 \text{ GeV}$, Madgraph	666.7 pb
$Z/\gamma^* + 2 jets$	DY+2Jets to Leptons, $M_{\ell\ell} > 50 \text{ GeV}$, Madgraph	215.1 pb
$Z/\gamma^* + 3 jets$	DY+3Jets to Leptons, $M_{\ell\ell} > 50 \text{ GeV}$, Madgraph	66.07 pb
$Z/\gamma^* + 4 jets$	DY+4Jets to Leptons, $M_{\ell\ell} > 50 \text{ GeV}$, Madgraph	27.38 pb
Single t		
$s\text{-channel}$	T, s-channel, Powheg	3.79 pb
$t\text{-channel}$	T, t-channel, Powheg	56.4 pb
tW	T, tW-channel, Powheg	11.1 pb
Single \bar{t}		
$s\text{-channel}$	\bar{T} , s-channel, Powheg	1.76 pb
$t\text{-channel}$	\bar{T} , t-channel, Powheg	30.7 pb
tW	\bar{T} , tW-channel, Powheg	11.1 pb
WW	WW, Pythia6	54.8 pb
WZ	WZ, Pythia6	32.3 pb
ZZ	ZZ, Pythia6	7.7 pb

Table 7.3: List of background MC datasets and cross sections used for normalization.

2505 7.1.4 MC pileup reweighting

2506 As discussed in section 6.1.4, the large instantaneous luminosities provided by the LHC result in
 2507 the overlap of multiple proton-proton collisions during a single read-out window. These "pileup
 2508 events" affect many aspects of the reconstruction, including lepton isolation and jet energy
 2509 resolution, thus the simulated samples must accurately reproduce these effects.

2510 As with the last analysis, for the simulation, it is known how many additional interactions
 2511 were added to every generated event. For the data, the number of pileup interactions for each unit
 2512 of time depends on the instantaneous luminosity for each bunch pair and the total inelastic cross
 2513 section, $\sigma_{inelastic}$. Empirically, it was found that $\sigma_{inelastic} = 69.4 \text{ mb}$ described the data well.

2514 Changing of this value by $\pm 7\%$ are used for the $\pm 1\sigma$ variations for the associated systematic
2515 uncertainty. Figure 7.1 shows the number of reconstructed vertices for data and for the $t\bar{t}$
2516 MC sample, both before and after pileup reweighting. After reweighting, the data and MC
2517 distributions agree very well, indicating that the pileup reweighting is working as expected.

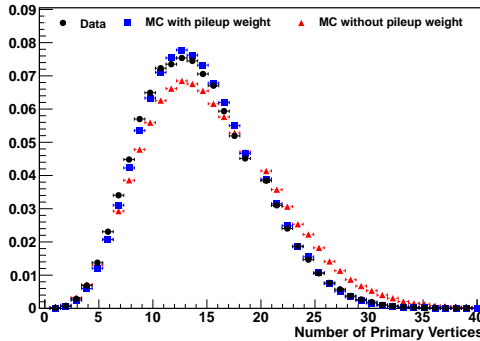


Figure 7.1: Comparison of number of reconstructed vertices for data (black) and the sum of all background MC samples before (red) and after (blue) pileup reweighting. After pileup reweighting, the MC matches the data well.

2518 7.1.5 Top p_T Reweighting

2519 It has been observed that the spectra of leptons and jets produced from top quark decays have
2520 softer p_T distribution than are predicted by the Monte Carlo. Investigations have shown that the
2521 p_T spectra of leptons and jets is softer than data and have traced this expected to the top quark
2522 p_T distribution [169, 170]. Measurements of the differential cross section for top pair production
2523 as a function of the top quark p_T , have allowed for the creation of correction factors for this effect.
2524 These predictions of the $t\bar{t}$ + jets Monte Carlo are also more consistent with calculations done at
2525 approximate NNLO accuracy. This correction factor replaces the additional pileup reweighting
2526 factor based on the H_T distribution, binned by number of reconstructed vertices.

2527 The scale factor used to correct the Madgraph top quark p_T distributions are shown in figure
2528 7.2. The associated uncertainty is a band shown in green, and corresponds to no correction
2529 factor for the down variation, and a doubling of the correction factor for the up variation. The
2530 scale factors are taken from a polynomial of the form:

$$SF = 1.18246 + 2.10061 \times 10^{-6} p_T (p_T - 2 \times 463.312)$$

2531 For $p_T > 463.312 \text{ GeV}/c$, a constant scale factor of 0.732 is used.

2532 The top p_T scale factor improves the agreement between data and Monte Carlo. Figure 7.3

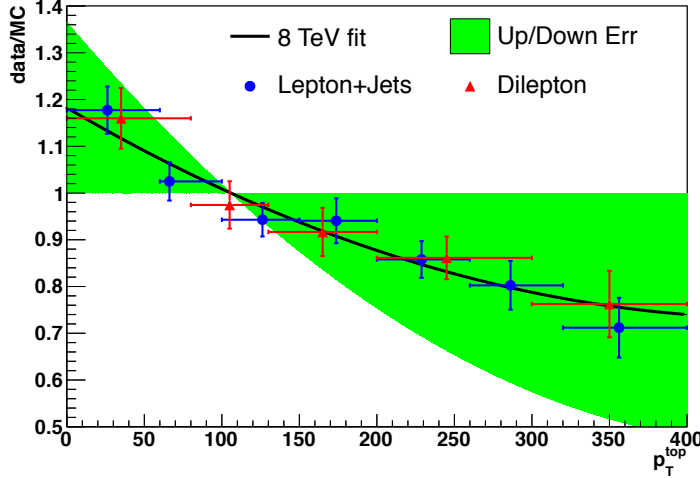


Figure 7.2: The scale factors from top differential cross section group, the fitting as well as the $\pm 1\sigma$ variations.

2533 compares the leading jet p_T distributions before and after reweighting. Before the correction,
2534 the leading jet p_T ratio plot forms a line with a slope, which is removed after the correction.

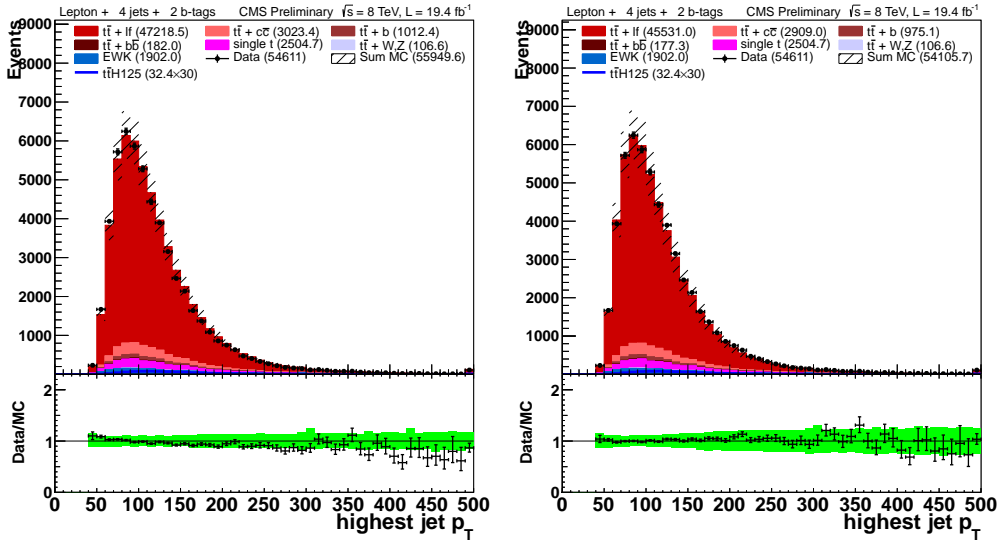


Figure 7.3: Leading jet p_T distribution for 8 TeV lepton plus jet events with ≥ 4 jets and ≥ 2 tags. The left-hand plot shows the distribution before top p_T reweighting. The right-hand plot shows the distribution after top p_T reweighting. Note that the ratio in the right-hand plot is flatter than the left-hand plot.

2535 7.2 Event Selection

2536 This section defines the common physics objects and event selection requirements. Events are
2537 required to pass quality filters, ensuring optimal operation of electronics and reconstruction, as

described in section 6.2.1. The same lepton selection is used that was employed in the previous analysis, with events being selected by triggers described in section ???. Leptons are classified into two categories, tight and loose, defined for muons in section 6.2.3 and for electrons in 6.2.4. For this analysis, exactly one tight muon or exactly one tight electron is required and events with any additional loose leptons are rejected. Lepton reconstruction efficiency scale factors are discussed in 6.2.5. The selection for jets is also the same, with the same procedure for correcting the energy as in section 6.2.6. The only significant change to the event selection comes from the b -tag scale factors used to calibrate the differences between efficiency in data and simulation for the CSV algorithm.

7.2.1 b -tag discriminant reweighting

As described in section 6.2.7, the algorithm used to tag jets as coming from a b -quark, is the Combined Secondary Vertex (CSV) algorithm. Differences have been observed in the measured efficiency for b -tagging jets between data and simulation [153]. To account for these efficiency differences, a scale factor to correct the MC b -tagging efficiency. Moreover, we found that the CSV distribution of MC doesn't match that of data, there making it necessary to correct the shape of the discriminant distribution as well.

A b -tag CSV reweighting method has been developed to address not only the difference in efficiency, but the difference in the shape of the discriminant distribution as well [171]. The method is based on a "tag and probe" approach. Events with two leptons, and exactly two jets are initially selected. One jet is required to pass a "tight" working point, characterized by a CSV value with $\sim 90\%$ efficiency and $\leq 1\%$ mistag rate. Then, the other jet is required to pass the analysis working point to assess the efficiency there. The results are binned by p_T , η , jet flavor and CSV value.

For MC the truth is available to assess the efficiency. For data, the full 8 TeV DoubleMu, DoubleElectron and MuEG datasets taken in 2012 are used. The scale factors for heavy flavor jets were derived in the dilepton channel, using a $t\bar{t}$ enriched control sample dominated by events which have two b flavor jets from the top pair decay. The scale factors for light flavor jets in the dilepton channel, using a control sample dominated by $Z+\text{jets}$ events where there are two light flavor jets. The scale factors for light flavor jets will account for the mis-tag efficiency discrepancy between data and MC. For events with one jet passing the tag requirements, the CSV distribution for the probe jet in given p_t and η bins. The total MC yields are normalized to the data yields. In order to account for heavy or light flavor contamination, the MC is divided into samples of heavy flavor and light flavor components and then non-relevant part from data is subtracted. The scale factor is then given by the ratio of subtracted data CSV distribution

2572 and the relevant MC CSV distribution, as shown below:

$$SF(CSV, p_t, \eta) = \frac{Data - MC_A}{MC_B} \quad (7.1)$$

2573 where A, B = heavy flavor component or light flavor component.

2574 Unlike the last analysis, where scale factors were applied to adjust the value of the CSV
2575 distribution, correction factor for this analysis is an event-by-event weight. If the jet is a b flavor
2576 jet, a heavy flavor scale factor is assigned to it; if it is a c flavor jet, a flat scale factor of 1.0 is
2577 applied, with the same uncertainty as a b flavor jet would receive; otherwise, if it is a light flavor
2578 jet, a light flavor scale factor is assigned. The total scale factor for the event is the product of
2579 all the scale factors of the jets:

$$SF_{total} = \prod_i^{N_{jets}} SF_{jet_i} = SF_{jet_1} \cdot SF_{jet_2} \cdot \dots \quad (7.2)$$

2580 7.2.2 Lepton + Jets Selection

2581 As with the previous analysis, the final selection requires events have exactly one tight lepton
2582 (e or μ), and at least four jets. Events with any additional loose or tight leptons are vetoed so
2583 this analysis can later be combined with a diLepton final state, without double counting events.
2584 Additionally, each event must have at least three jets with $p_T > 40$ GeV/c.

2585 As before, events are further categorized by the reconstructed jet, and b -tagged jet multiplicities:

- 2587 • ≥ 6 jets, $= 2$ b -tags: At least 6 jets, 2 of which are b -tagged
- 2588 • $= 4$ jets, $= 3$ b -tags: Exactly 4 jets, 3 of which are b -tagged
- 2589 • $= 5$ jets, $= 3$ b -tags: Exactly 5 jets, 3 of which are b -tagged
- 2590 • ≥ 6 jets, $= 3$ b -tags: At least 6 jets, 3 of which are b -tagged
- 2591 • $= 4$ jets, $= 4$ b -tags: Exactly 4 jets, 4 of which are b -tagged
- 2592 • $= 5$ jets, $= 4$ b -tags: Exactly 5 jets, 4 of which are b -tagged
- 2593 • ≥ 6 jets, ≥ 4 b -tags: At least 6 jets, with at least 4 of which are b -tagged

2594 Table 7.4 gives the event yield for MC backgrounds, both the total and each contribution,
2595 the expected event yield for signal $t\bar{t}H$ ($m_H = 125$ GeV/c 2), and the data observed in each
2596 category. Figure 7.4 shows the data/MC comparison for the number of jets and the number of
2597 tagged jets distributions for events with one lepton (e or μ), ≥ 4 jets and ≥ 2 b -tags, it also
2598 includes a plot showing the event yields for data and each MC background in each category.

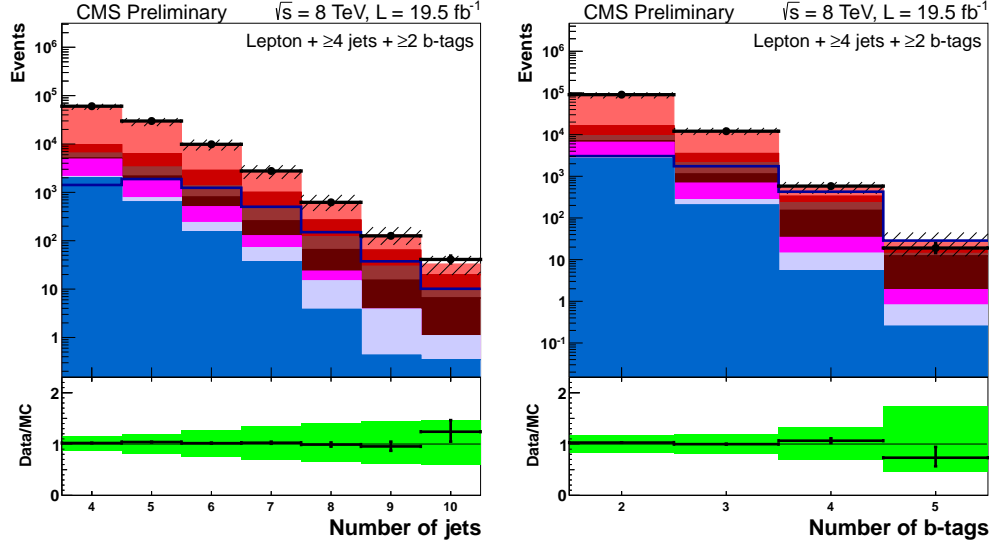


Figure 7.4: Comparison of yields for the different categories (top), number of jets (bottom left), and number of tagged jets (bottom right) in data and Monte Carlo for events with one lepton μ or e , ≥ 4 jets and ≥ 2 tags.

	≥ 6 jets 2 tags	4 jets 3 tags	5 jets 3 tags	≥ 6 jets 3 tags	4 jets 4 tags	5 jets ≥ 4 tags	≥ 6 jets ≥ 4 tags
$t\bar{t}H(125)$	33.4 ± 8.1	14.0 ± 3.0	21.1 ± 4.5	23.1 ± 5.5	1.8 ± 0.5	5.2 ± 1.4	8.3 ± 2.3
$t\bar{t}+lf$	7650 ± 2000	4710 ± 820	2610 ± 530	1260 ± 340	74 ± 30	79 ± 34	71 ± 36
$t\bar{t} + b$	530 ± 300	350 ± 190	360 ± 200	280 ± 160	21 ± 12	29 ± 17	33 ± 20
$t\bar{t} + b\bar{b}$	220 ± 120	99 ± 52	158 ± 85	200 ± 110	13.1 ± 7.3	38 ± 21	78 ± 47
$t\bar{t} + c\bar{c}$	1710 ± 1110	440 ± 230	520 ± 290	470 ± 280	19 ± 11	32 ± 18	52 ± 31
$t\bar{t}V$	99 ± 27	16.2 ± 3.8	23.9 ± 5.7	28.8 ± 7.4	1.1 ± 0.4	2.5 ± 0.7	5.8 ± 1.8
Single t	264 ± 54	235 ± 41	116 ± 22	55 ± 14	3.4 ± 1.6	10.3 ± 5.3	7.3 ± 3.1
$V+jets$	160 ± 110	122 ± 95	44 ± 38	29 ± 27	2.1 ± 2.4	1.9 ± 1.7	1.2 ± 1.3
Diboson	5.9 ± 1.6	6.3 ± 1.4	2.4 ± 0.7	1.0 ± 0.4	0.3 ± 0.2	0.1 ± 0.1	0.2 ± 0.1
Total bkg	10630 ± 2790	5970 ± 1060	3830 ± 790	2310 ± 620	133 ± 44	193 ± 62	249 ± 90
Data	10724	5667	3983	2426	122	219	260

Table 7.4: Observed data event yields, expected event yields in 19.5 fb^{-1} for signal and backgrounds in the lepton+jets channel.

2599 7.3 Multivariate Analysis

2600 The MVA technique used to analyze the full 8 TeV dataset is a Boosted Decision Tree (BDT).
 2601 Each jet/tag category is trained with half of the simulated $t\bar{t}H$ events for signal, and half of
 2602 the simulated $t\bar{t} + jets$ events as background. The top 10 variables, ranked with the separation
 2603 figure of merit given in equation 6.10, are used as input variables. The BDT distribution of the
 2604 discriminant is then used for signal extraction and limit setting.

2605 7.3.1 Boosted Decision Tree Overview

2606 A Boosted Decision Tree (BDT) is a code structure that makes a sequence of binary decisions
 2607 to classify events as either signal-like or background-like [155]. For this analysis, the BDT uses

2608 10 input variables for each jet/tag category. The BDT looks at the distribution of events for
 2609 signal and background, with 40 bins with a maximum and minimum value determined by the
 2610 the largest and smallest values respectively for either the signal or the background. Out of these
 2611 10 variables, the BDT selects the variable which maximizes the Ginni Index, which is given by
 2612 the equation:

$$GiniIndex = p \times (1 - p) \quad (7.3)$$

2613 where the purity, $p = s/b$, is the ratio of the integral number of signal, s , events and background,
 2614 b , events above or below the cut value chosen by the BDT. This effectively tries to find a cut on a
 2615 variable that maximizes the amount signal in sample afterwards, creating a background-like set
 2616 of events, and a signal-like set of events. After the first cut is chosen, the distributions for each
 2617 of the variables above and below the cut value are re-examined. A second cut on a variable,
 2618 at a point that maximizes the Ginni Index is found, for each of the signal and background-like
 2619 regions formed by the first cut. This process continues for a user-defined number of cuts. Since
 2620 the input events are known to be singal-like or background-like, the purity of the final region
 2621 that an event is classified as is used as the output for this set of decisions, known as a decision
 2622 tree. Figure 7.5 shows a diagram of the general process.

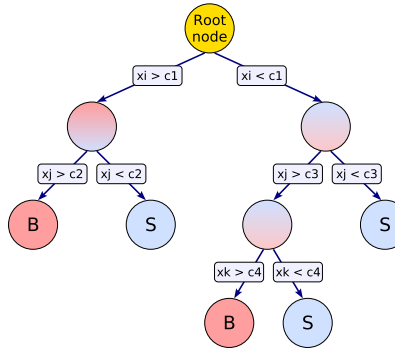


Figure 7.5: Example of a decision tree, which chooses a set of variables to cut on, in order to produce a region of events with high signal purity

2623 The BDT in this analysis uses 5 cuts for a single tree. The reason for using a small number, is
 2624 that the BDT employs a process known as "boosting" to enhance its discriminating power.

2625 Boosting is the process of using multiple, or a forest, of individual decision trees to cast
 2626 a majority vote for the decision to classify the event as signal-like or background-like [155].
 2627 Events from the training sample, which were misclassified, are given a larger weight, making
 2628 their contribution to the distributions of the input variable more prominent, making it more
 2629 likely for the next decision tree to classify the event correctly. The final discriminant, $F(\hat{x}, P)$,

2630 of the forest of decision trees is given by:

$$F(\hat{x}, P) = \sum_{m=0}^M \beta_m f(x; a_m); \quad P \in (\beta_m; a_m)_0^M \quad (7.4)$$

2631 where P is the set of parameter, whose values are optimized to create an optimized classification
2632 decision. For M trees in the forest, β_m is the weight for the output of a single decision tree,
2633 $f(x; a_m)$, which is the purity, s/b of the final region of the tree an individual event is classified
2634 into. The set of input variables for a single decision tree, m , is denoted by a_m .

2635 This analysis uses the "Gradient" method of boosting [155]. After the first tree is has been
2636 built, the "loss function", $L(F, y)$, is calculated with the function:

$$L(F, y) = \ln \left(1 + e^{-2F(\hat{x})y} \right) \quad (7.5)$$

2637 where y is the true value of the classification of the event (1 for signal, 0 for background).
2638 This function has a minimum value when all of the events have been classified correctly. The
2639 loss function is then minimized by varying the set of parameters, $P \in (\beta_m; a_m)_0^M$, using the
2640 steepest-descent method. A random selection of events are reweighted, and the loss-function is
2641 re-calculated. The error rate of classifying events for the previous tree is used to calculate the
2642 new weight, α , of events for the next tree:

$$\alpha = \frac{1 - err}{err} \quad (7.6)$$

2643 where err is the error rate. After events are re-weighted, a new decision tree is created and the
2644 process is repeated, iteratively minimizing the loss function until a desired set of decision trees
2645 are created. This analysis uses a forest of 100 decision trees to separate the $t\bar{t}H$ signal from the
2646 $t\bar{t} + \text{jets}$ background.

2647 Overtraining was checked in a similar procedure that was used in the last analysis. Half the
2648 events for the signal and background samples are used to train the BDT, the other half are used
2649 to test it. The response to the BDT is calculated for both the testing and training sample, and
2650 the Kolomogrov-Smirnoff statistic is used as a figure of merit to judge the compatibility of the
2651 two samples. As seen in figure 7.6, there are no significant deviations between the testing and
2652 training samples, implying that no overtraining has occurred.

2653 7.3.2 MVA Input Variables, Data to Monte Carlo Comparisons

2654 The set of 10 input variables for each jet/tag category were chosen through their ranking using
2655 the separation figure of merit given in equation 6.10. The categories most sensitive to signal, 5

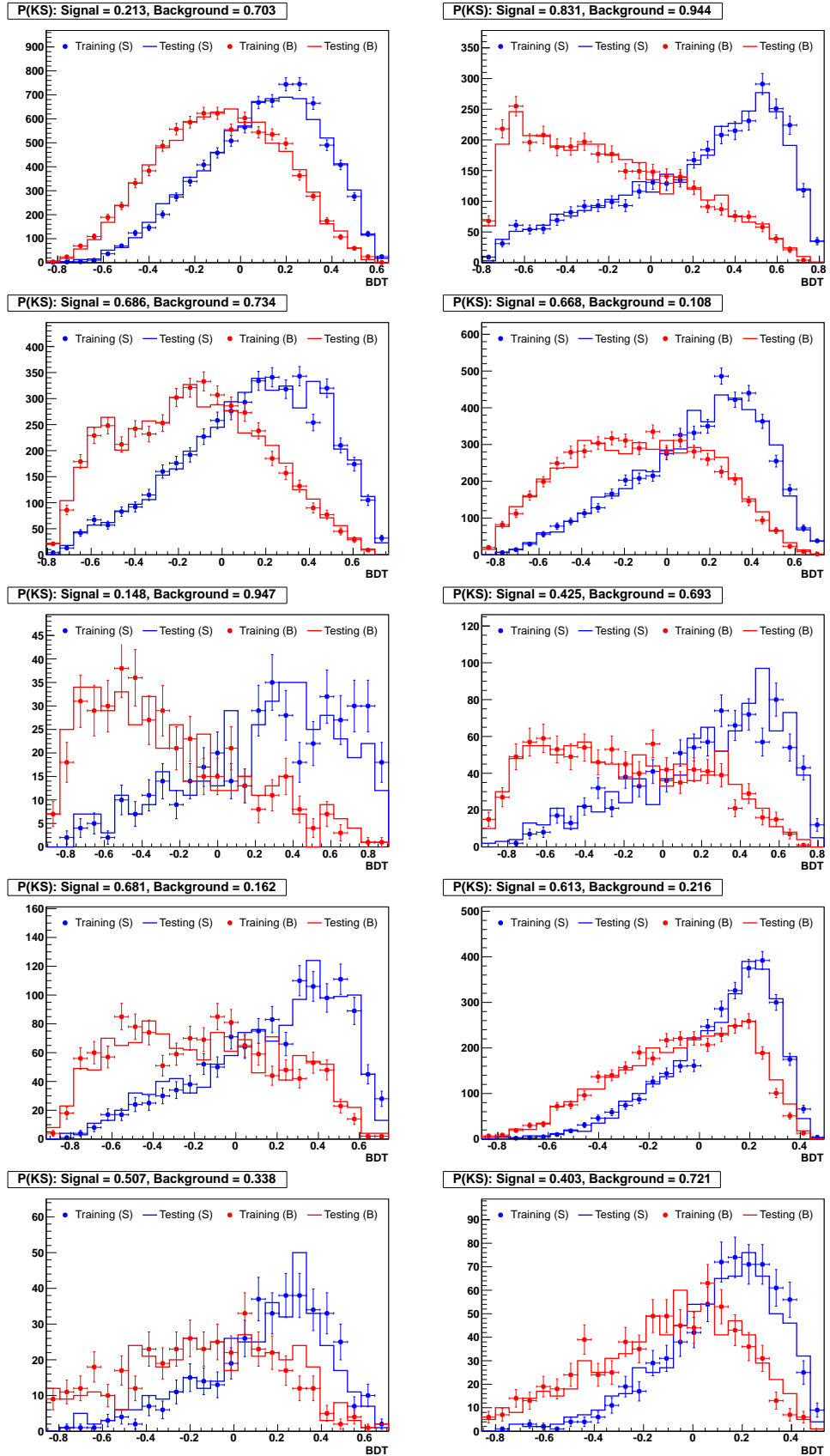


Figure 7.6: Comparisons of the testing and training samples used to optimize the BDT weights for each jet/tag category

2656 jets, ≥ 4 b -tags; ≥ 6 jets, ≥ 3 b -tags; and ≥ 6 jets, ≥ 4 b -tags all include a variable, which is the
2657 output discriminant of a dedicated BDT trained to separate $t\bar{t}H$ signal from $t\bar{t} + b\bar{b}$ background.

2658 Table 7.5 gives a description of each of the input variables used. Table 7.6 describes which
2659 variables are used in each jet/tag category, and table 7.7 lists the variables used in the dedicated
2660 $t\bar{t}H$, $t\bar{t} + b\bar{b}$ BDT.

Table 7.5: Event variables used in dilepton and lepton+jets BDT training and their descriptions.

abs $\Delta\eta$ (leptonic top, bb)	Delta-R between the leptonic top reconstructed by the best Higgs mass algorithm and the b -jet pair chosen by the algorithm
abs $\Delta\eta$ (hadronic top, bb)	Delta-R between the hadronic top reconstructed by the best Higgs mass algorithm and the b -jet pair chosen by the algorithm
aplanarity	Event shape variable equal to $\frac{3}{2}(\lambda_3)$, where λ_3 is the third eigenvalue of the sphericity tensor as described in [?].
ave CSV (tags/non-tags)	Average b -tag discriminant value for b -tagged/non- b -tagged jets
ave ΔR (tag,tag)	Average ΔR between b -tagged jets
best Higgs mass	A minimum-chi-squared fit to event kinematics is used to select two b -tagged jets as top-decay products. Of the remaining b -tags, the invariant mass of the two with highest E_t is saved.
best $\Delta R(b,b)$	The ΔR between the two b -jets chosen by the best Higgs mass algorithm
closest tagged dijet mass	The invariant mass of the two b -tagged jets that are closest in ΔR
dev from ave CSV (tags)	The square of the difference between the b -tag discriminant value of a given b -tagged jet and the average b -tag discriminant value among b -tagged jets, summed over all b -tagged jets
highest CSV (tags)	Highest b -tag discriminant value among b -tagged jets
H_0, H_1, H_2, H_3	The first few Fox-Wolfram moments [?] (event shape variables)
HT	Scalar sum of transverse momentum for all jets with $p_T > 30 \text{ GeV}/c$
$\sum p_T(\text{jets,leptons,MET})$	The sum of the p_T of all jets, leptons, and MET
$\sum p_T(\text{jets,leptons})$	The sum of the p_T of all jets, leptons
jet 1, 2, 3, 4 p_T	The transverse momentum of a given jet, where the jet numbers correspond to rank by p_T
lowest CSV (tags)	Lowest b -tag discriminant value among b -tagged jets
mass(lepton,jet,MET)	The invariant mass of the 4-vector sum of all jets, leptons, and MET
mass(lepton,closest tag)	The invariant mass of the lepton and the closest b -tagged jet in ΔR
max $\Delta\eta$ (jet, ave jet η)	max difference between jet eta and avg delta eta between jets
max $\Delta\eta$ (tag, ave jet η)	max difference between tag eta and avg delta eta between jets
max $\Delta\eta$ (tag, ave tag η)	max difference between tag eta and avg delta eta between tags
median inv. mass (tag pairs)	median invariant mass of all combinations of b -tag pairs
M3	The invariant mass of the 3-jet system with the largest transverse momentum.
MHT	Vector sum of transverse momentum for all jets with $p_T > 30 \text{ GeV}/c$
MET	Missing transverse energy
min $\Delta R(\text{lepton,jet})$	The ΔR between the lepton and the closest jet (LJ channel)
min $\Delta R(\text{tag,tag})$	The ΔR between the two closest b -tagged jets
min $\Delta R(\text{jet,jet})$	The ΔR between the two closest jets
$\sqrt{\Delta\eta(t^{lep},bb) \times \Delta\eta(t^{had},bb)}$	square root of the product of abs $\Delta\eta$ (leptonic top, bb) and abs $\Delta\eta$ (hadronic top, bb)
second-highest CSV (tags)	Second-highest b -tag discriminant value among b -tagged jets
sphericity	Event shape variable equal to $\frac{3}{2}(\lambda_2 + \lambda_3)$, where λ_2 and λ_3 are the second and third eigenvalues of the sphericity tensor as described in [?].
$(\Sigma \text{ jet } p_T)/(\Sigma \text{ jet E})$	The ratio of the sum of the transverse momentum of all jets and the sum of the energy of all jets
tagged dijet mass closest to 125 $ttbb/t\bar{t}H$ BDT	The invariant mass of the b -tagged pair closest to $125 \text{ GeV}/c^2$ BDT used to discriminate between $ttbb$ and $t\bar{t}H$ in the LJ ≥ 6 jets, ≥ 4 tags, ≥ 6 jets + 3 tags, and 5 jets + ≥ 4 tags categories. See text for description and table 7.7 for list of variables.

2661 The modeling of the input variables is compared against data for each of the jet/tag diagrams
2662 in the the following figures:

2663 • ≥ 6 jets, $=2$ b -tags: Figure 7.7

2664 • $=4$ jets, $=3$ b -tags: Figure 7.8

2665 • $=5$ jets, $=3$ b -tags: Figure 7.9

4 jets, 3 tags	4 jets, 4 tags	
jet 1 p_T jet 2 p_T jet 3 p_T jet 4 p_T M3 $\sum p_T(\text{jets,lepton,MET})$ HT lowest CSV (tags) MHT MET	jet 1 p_T jet 2 p_T jet 4 p_T HT $\sum p_T(\text{jets,lepton,MET})$ M3 ave CSV (tags) second-highest CSV (tags) third-highest CSV (tags) lowest CSV (tags)	
5 jets, 3 tags	5 jets, ≥ 4 tags	
jet 1 p_T jet 2 p_T jet 3 p_T jet 4 p_T $\sum p_T(\text{jets,lepton,MET})$ $(\Sigma \text{jet } p_T)/(\Sigma \text{jet E})$ HT ave CSV (tags) third-highest CSV (tags) fourth-highest CSV (jets)	max $\Delta\eta$ (tag, ave jet η) $\sum p_T(\text{jets,lepton,MET})$ $(\Sigma \text{jet } p_T)/(\Sigma \text{jet E})$ ave $\Delta R(\text{tag,tag})$ ave CSV (tags) dev from ave CSV (tags) second-highest CSV (tags) third-highest CSV (tags) lowest CSV (tags) ttbb/ttH BDT	
≥ 6 jets, 2 tags	≥ 6 jets, 3 tags	
$\sum p_T(\text{jets,lepton,MET})$ HT mass(lepton,closest tag) max $\Delta\eta$ (jet, ave jet η) min $\Delta R(\text{lepton,jet})$ H_2 sphericity $(\Sigma \text{jet } p_T)/(\Sigma \text{jet E})$ third-highest CSV (jets) fourth-highest CSV (jets)	H_0 sphericity $(\Sigma \text{jet } p_T)/(\Sigma \text{jet E})$ max $\Delta\eta$ (jet, ave jet η) $\sum p_T(\text{jets,lepton,MET})$ ave CSV (tags) second-highest CSV (tags) third-highest CSV (tags) fourth-highest CSV (jets) ttbb/ttH BDT	$(\Sigma \text{jet } p_T)/(\Sigma \text{jet E})$ ave $\Delta R(\text{tag,tag})$ product($\Delta\eta(\text{leptonic top, bb}), \Delta\eta(\text{hadronic top, bb})$) closest tag mass max $\Delta\eta$ (tag, ave tag η) ave CSV (tags) third-highest CSV (tags) fourth-highest CSV (tags) best Higgs mass ttbb/ttH BDT

Table 7.6: BDT input variable assignments for the lepton+jets categories.

5 jets, ≥ 4 tags	≥ 6 jets, 3 tags	≥ 6 jets, ≥ 4 tags
ave $\Delta R(\text{tag,tag})$ max $\Delta\eta$ (tag, ave tag η) $(\Sigma \text{jet } p_T)/(\Sigma \text{jet E})$ tagged dijet mass closest to 125 H_1 H_3 $\sum p_T(\text{jets,lepton,MET})$ fourth-highest CSV (tags) aplanarity MET	tagged dijet mass closest to 125 $(\Sigma \text{jet } p_T)/(\Sigma \text{jet E})$ $\sqrt{\Delta\eta(t^{lep}, bb) \times \Delta\eta(t^{had}, bb)}$ H_1 H_3 M3 max $\Delta\eta$ (tag, ave tag η) max $\Delta\eta$ (tag, ave jet η) max $\Delta\eta$ (jet, ave jet η) abs $\Delta\eta$ (hadronic top, bb) abs $\Delta\eta$ (leptonic top, bb) sphericity aplanarity min $\Delta R(\text{tag,tag})$ jet 3 p_T	H_3 ave $\Delta R(\text{tag,tag})$ closest tagged dijet mass sphericity max $\Delta\eta$ (tag, ave jet η) max $\Delta\eta$ (tag, ave tag η) mass(lepton,jet,MET) $(\Sigma \text{jet } p_T)/(\Sigma \text{jet E})$ abs $\Delta\eta$ (leptonic top, bb) abs $\Delta\eta$ (hadronic top, bb) $\sqrt{\Delta\eta(t^{lep}, bb) \times \Delta\eta(t^{had}, bb)}$ ave CSV (tags) best $\Delta R(b,b)$ best Higgs mass median inv. mass (tag pairs)

Table 7.7: List of variables used as inputs in each of the ttbb/ttH BDTs. See table 7.5 for definitions.

- ≥ 6 jets, $=3$ b -tags: Figure 7.10, and Figure 7.11

- $=4$ jets, $=4$ b -tags: Figure 7.12

- $=5$ jets, $=4$ b -tags: Figure 7.13, and Figure 7.14

- ≥ 6 jets, ≥ 4 b -tags: Figure 7.15, and Figure 7.16

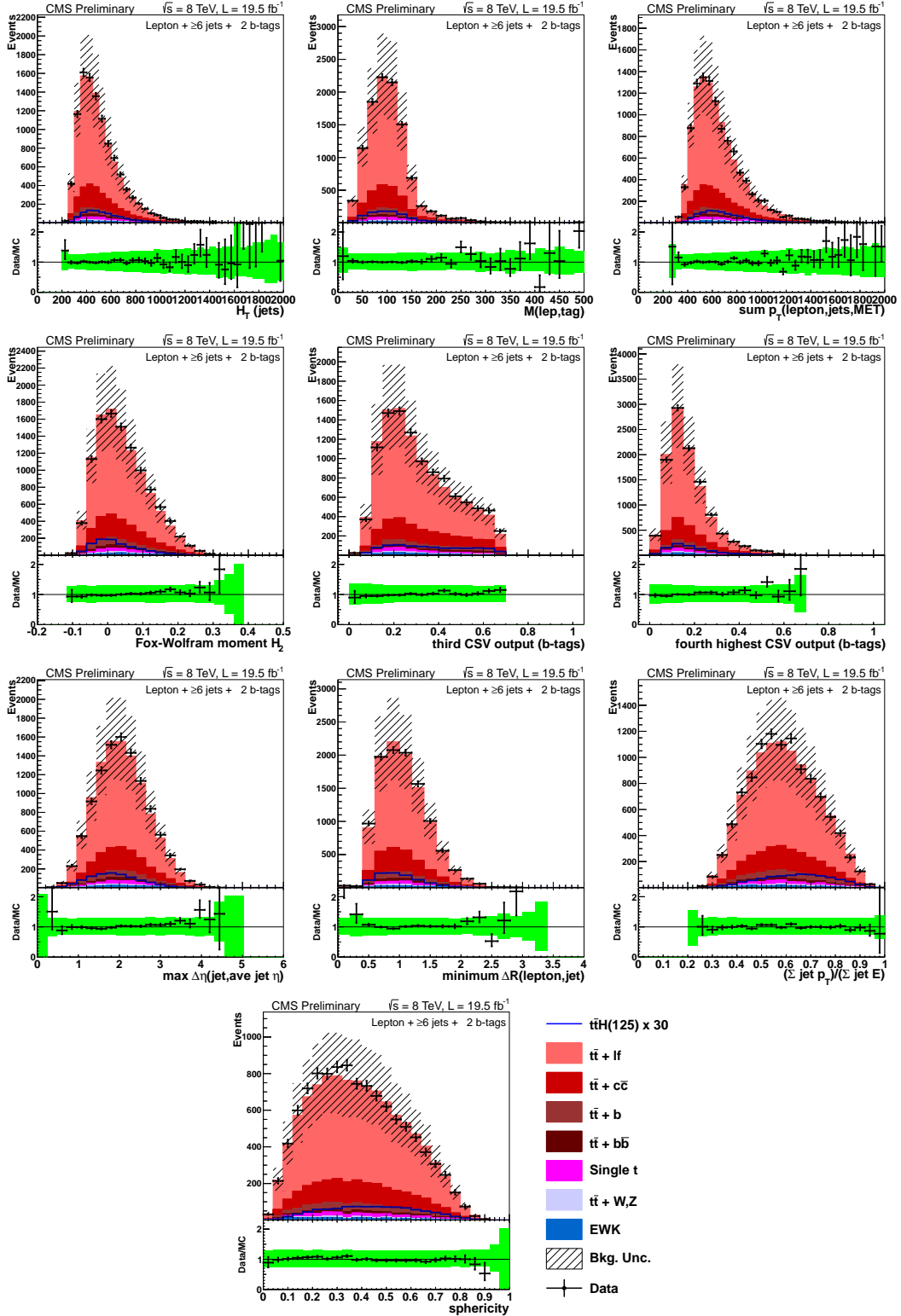


Figure 7.7: Data/MC comparisons for events with one lepton and ≥ 6 jets + 2 b-tags. The uncertainty band includes statistical and systematic uncertainties that affect both the rate and shape of the background distributions.

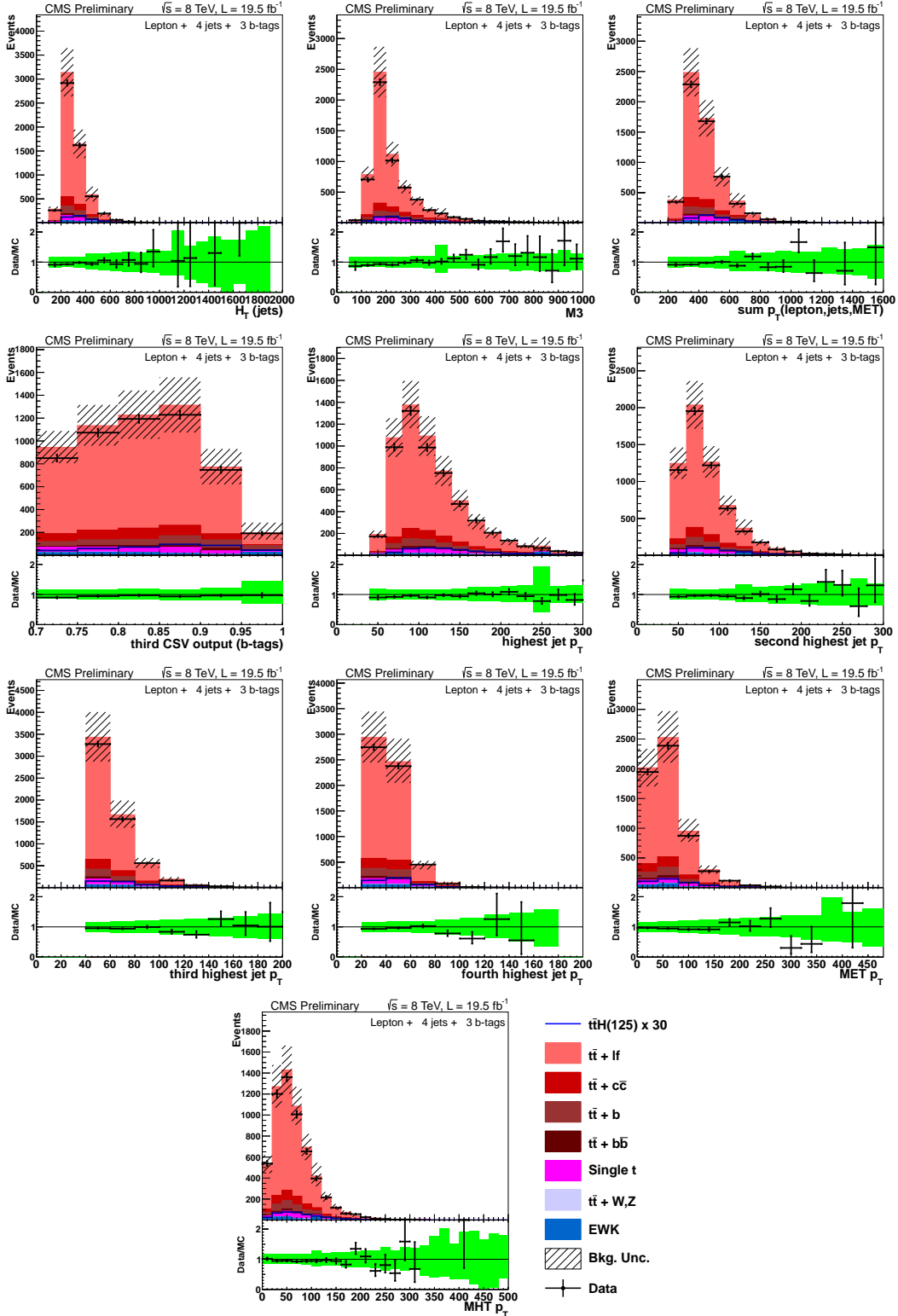


Figure 7.8: Data/MC comparisons for events with one lepton and 4 jets + 3 b-tags. The uncertainty band includes statistical and systematic uncertainties that affect both the rate and shape of the background distributions.

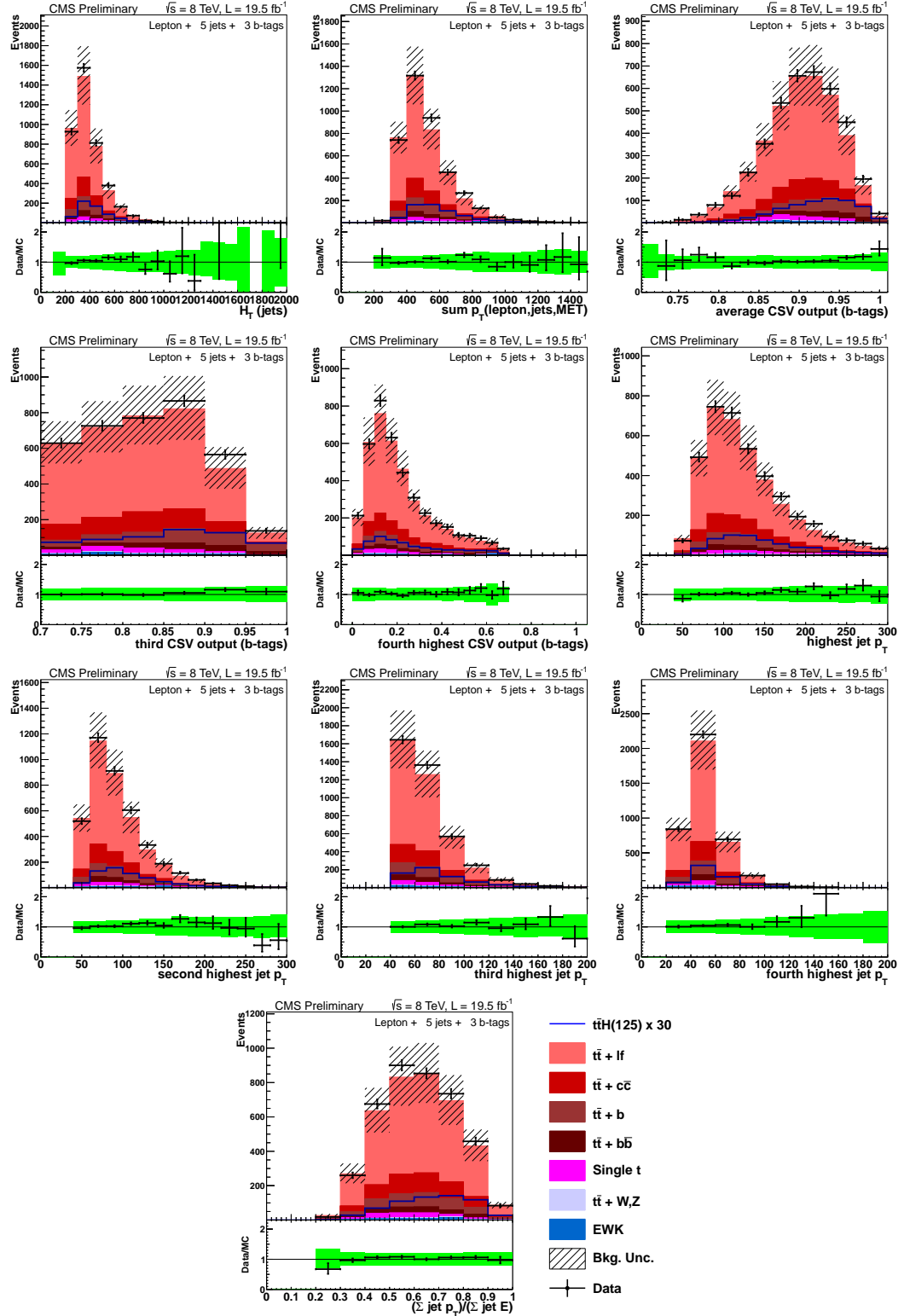


Figure 7.9: Data/MC comparisons for events with one lepton and 5 jets + 3 b-tags. The uncertainty band includes statistical and systematic uncertainties that affect both the rate and shape of the background distributions.

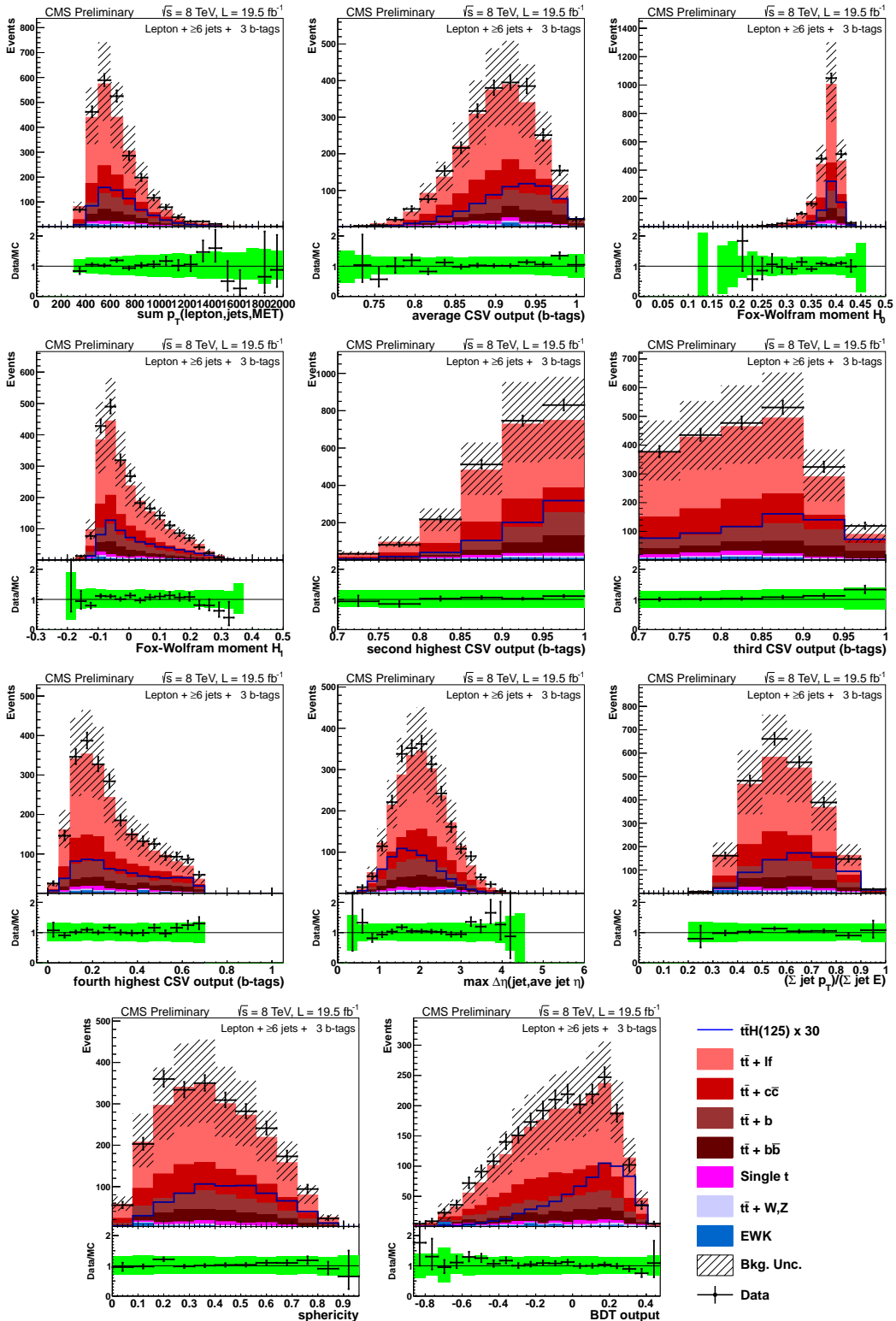


Figure 7.10: Data/MC comparisons for events with one lepton and ≥ 6 jets + 3 b-tags. The uncertainty band includes statistical and systematic uncertainties that affect both the rate and shape of the background distributions.

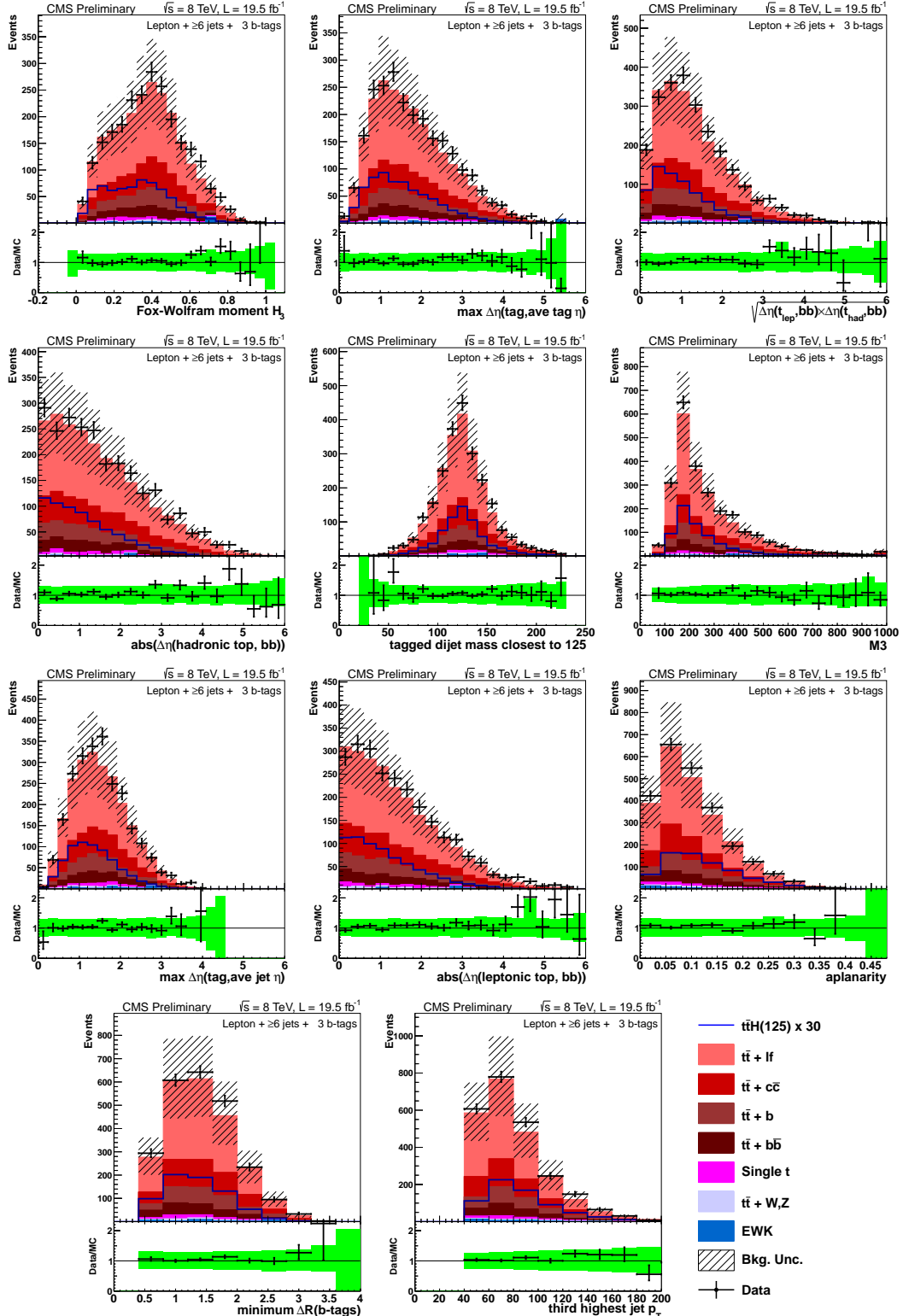


Figure 7.11: Data/MC comparisons for events with one lepton and ≥ 6 jets + 3 b-tags. The uncertainty band includes statistical and systematic uncertainties that affect both the rate and shape of the background distributions.

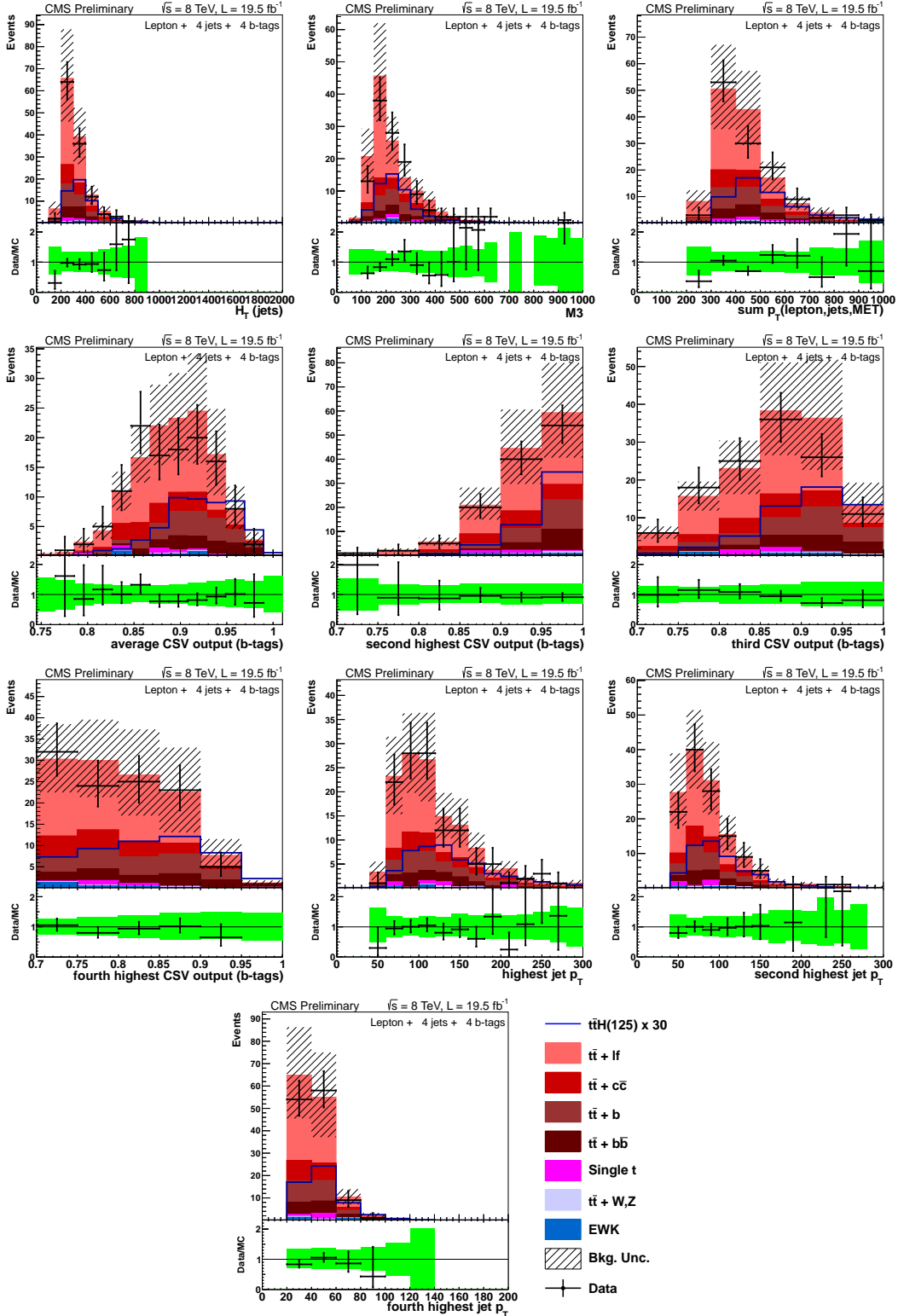


Figure 7.12: Data/MC comparisons for events with one lepton and 4 jets + 4 b-tags. The uncertainty band includes statistical and systematic uncertainties that affect both the rate and shape of the background distributions.

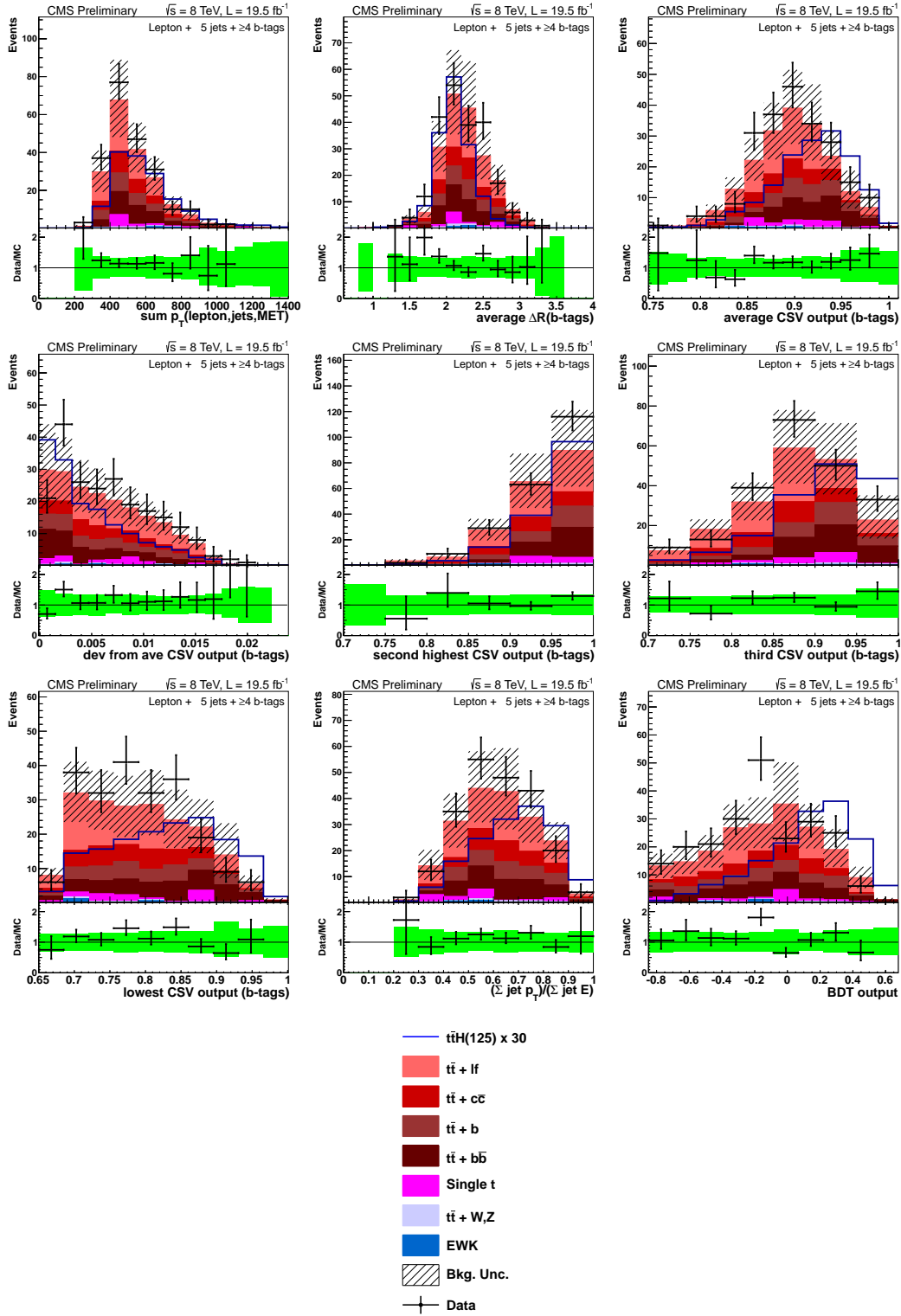


Figure 7.13: Data/MC comparisons for events with one lepton and 5 jets $+ \geq 4$ b-tags. The uncertainty band includes statistical and systematic uncertainties that affect both the rate and shape of the background distributions.

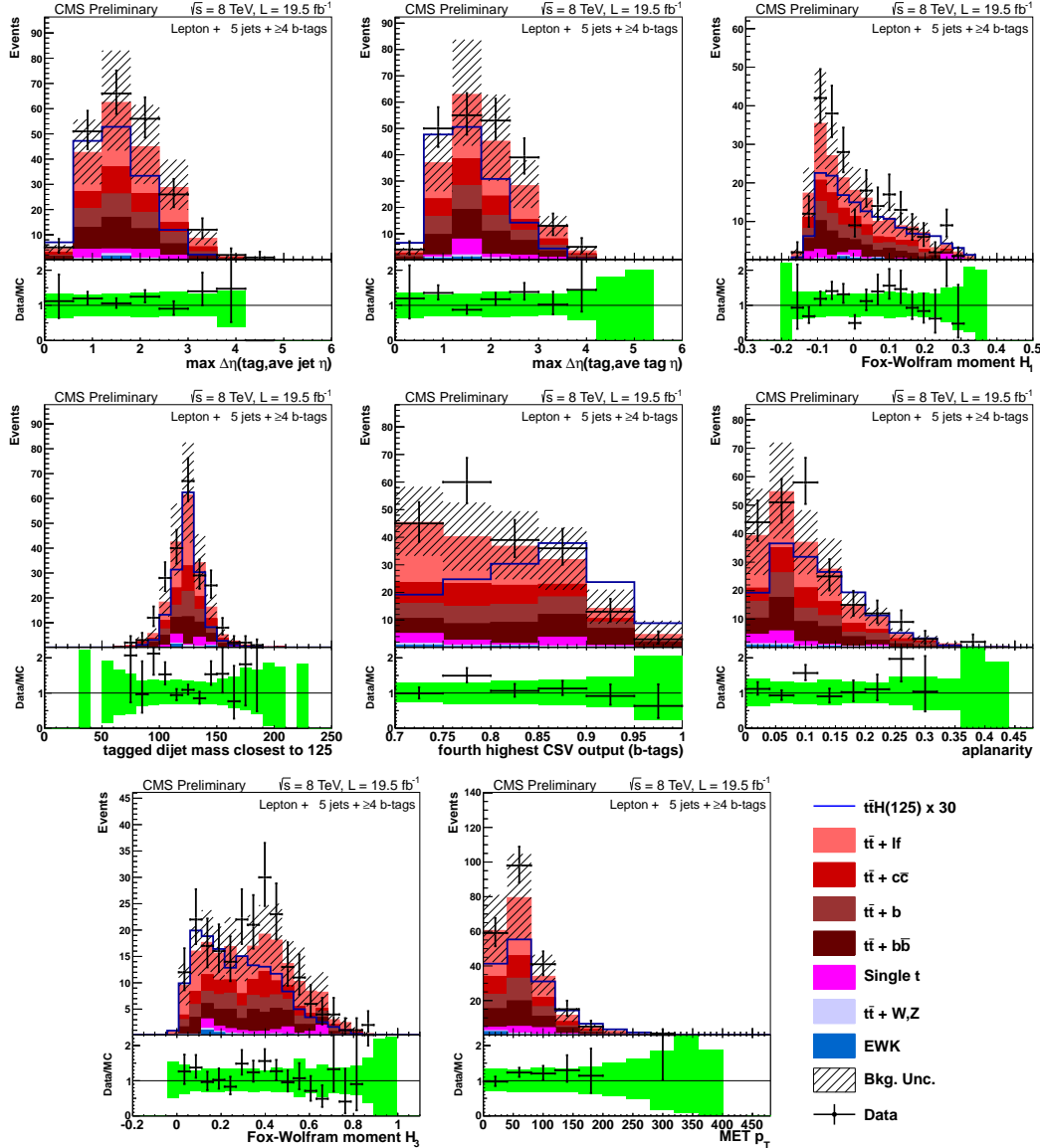


Figure 7.14: Data/MC comparisons for events with one lepton and 5 jets $+ \geq 4$ b-tags. The uncertainty band includes statistical and systematic uncertainties that affect both the rate and shape of the background distributions.

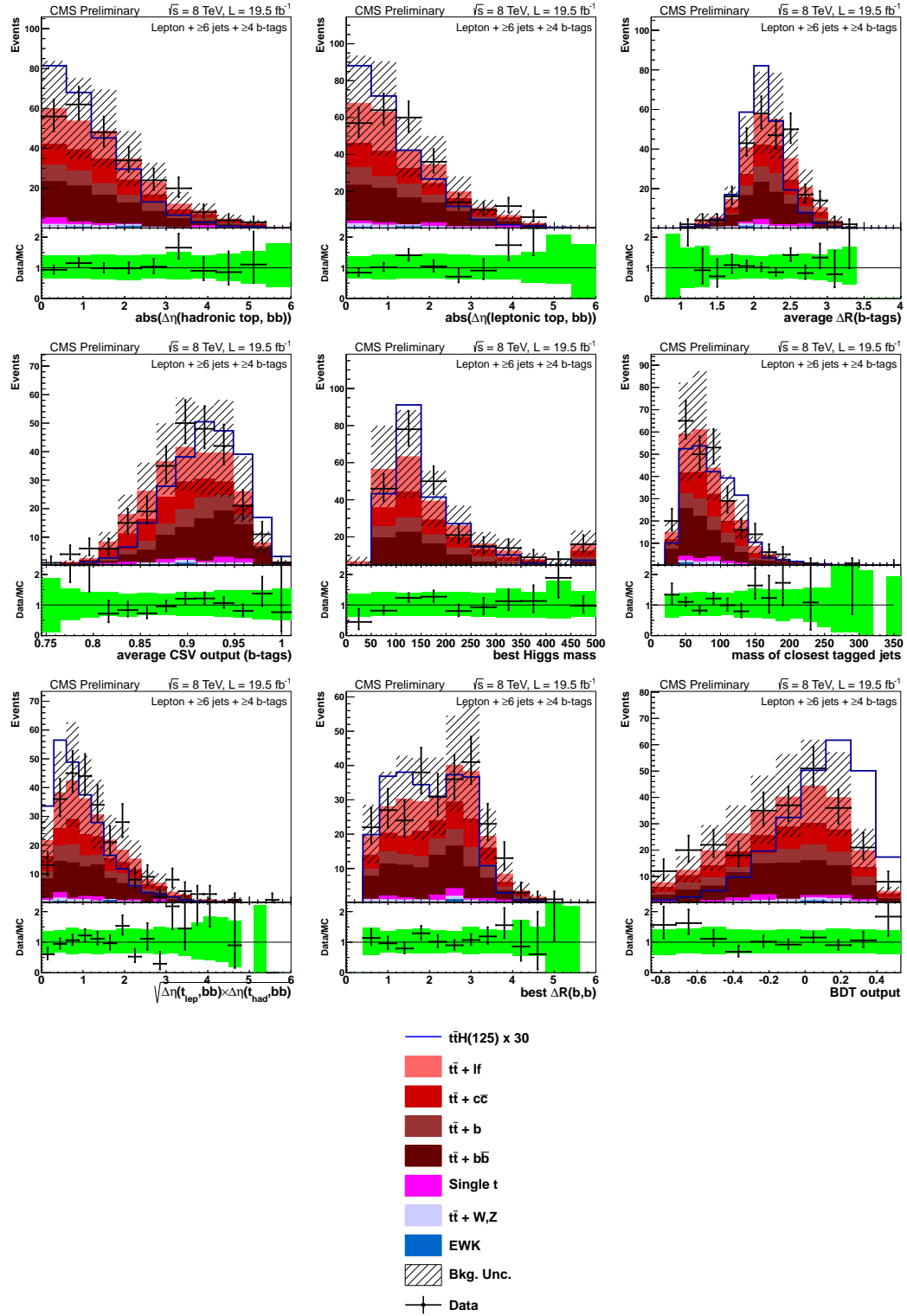


Figure 7.15: Data/MC comparisons for events with one lepton and ≥ 6 jets + ≥ 4 b-tags. The uncertainty band includes statistical and systematic uncertainties that affect both the rate and shape of the background distributions.

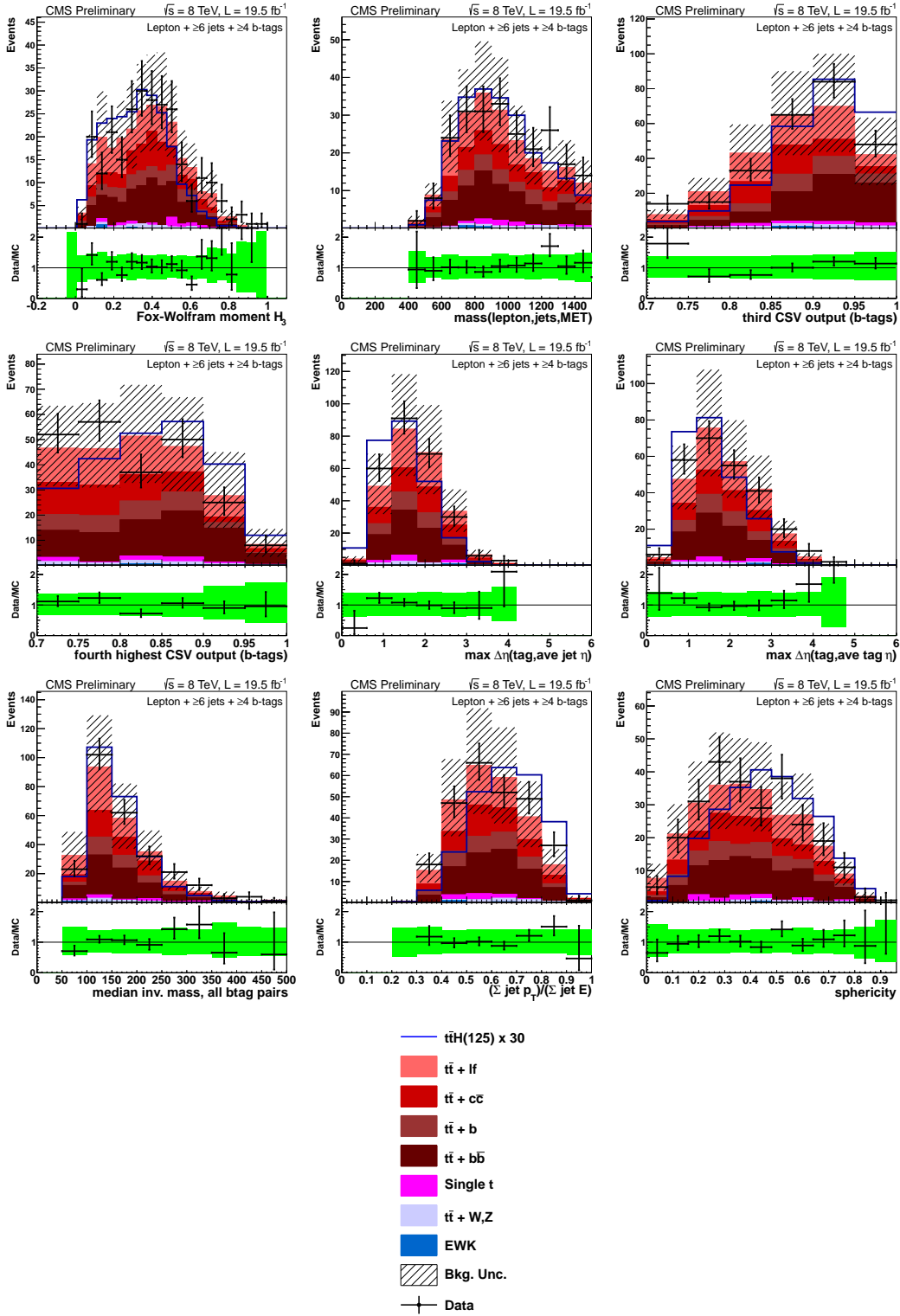


Figure 7.16: Data/MC comparisons for events with one lepton and ≥ 6 jets + ≥ 4 b-tags. The uncertainty band includes statistical and systematic uncertainties that affect both the rate and shape of the background distributions.

2670 7.3.3 MVA Output, Data to Monte Carlo Comparisons

2671 The distributions of the BDT output discriminators in each category are shown in Fig. 7.17. For
 2672 these figures, the uncertainty band includes statistical and systematic uncertainties, e.g. JES
 2673 and b -tag SF uncertainties, that are described in section 7.4.

2674 7.4 Systematic Uncertainties

2675 The evaluation of several of the systematic uncertainties follows the same procedure as described
 2676 in the previous chapter. For these cases, the reader is directed to previous description of the
 2677 uncertainty. Systematic uncertainties that are new to this analysis include those associated with
 2678 the new b -tag calibration method and the top- p_T reweighting. Where appropriate, comparisons
 2679 between the shapes of the nominal and $\pm 1\sigma$ variations are made.

2680 **Jet Energy Scale (JES):** See section 6.4 for a description of the evaluation of this systematic.
 2681 Shape comparisons between the nominal and the $\pm 1\sigma$ variations are shown in figure 7.18.
 2682 Table 7.8 shows the effect on the rate for the ≥ 6 jets + ≥ 4 tags category.

JES systematic yield change			
		lepton+jets	
sys	shift	$t\bar{t}H(125)$	$t\bar{t} + bb$
JES	up	+9.1%	+8.3%
	down	-7.7%	-10.6%

Table 7.8: Relative yield change due to JES shift up/down for the ≥ 3 tag category in the dilepton channel and the ≥ 6 jets + ≥ 4 tags category in the lepton+jets channel.

2683 **Jet Energy Resolution (JER):** See section 6.4 for a description of the evaluation of this
 2684 systematic.

2685 **b -tag Scale Factors:** New scale factors to account for the differences in efficiency between
 2686 data and simulation for the CSV b -tagging algorithm is described in section 7.2.1. There
 2687 are three sources of systematic uncertainty on both the heavy flavor and light flavor scale
 2688 factors: JES, purity, and statistics, and each source of variation is considered separately.
 2689 The b -tag uncertainty associated with the JES is evaluated at the same time the overall
 2690 JES uncertainty is considered. When the JES is shifted for the jet kinematics up or down
 2691 by 1σ , the b -tag scale factor values, which depend on the p_T of the jet in question, shift as
 2692 well. This correlates the b -tag uncertainty from JES with the overall JES uncertainty. The
 2693 other two sources of b -tag uncertainty are each evaluated independently for light-flavor and
 2694 heavy-flavor. The purity uncertainty is controlled by a separate nuisance parameter for
 2695 light and heavy flavor. Variation of this parameter is associated with changing the pre-

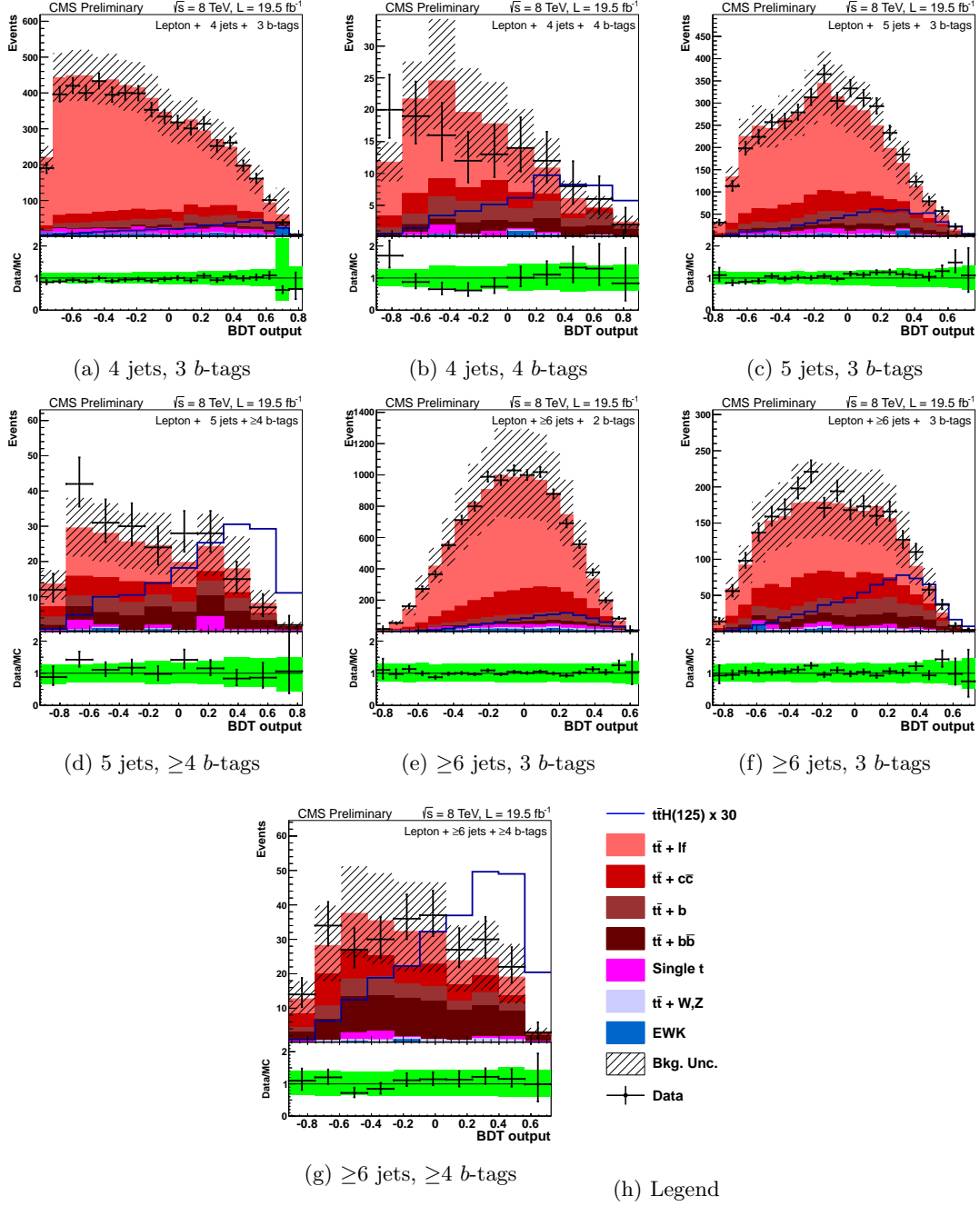


Figure 7.17: Final BDT output for lepton + jet events. Background-like events have a low BDT output value. Signal-like events have a high BDT output value. The uncertainty band includes statistical and systematic uncertainties that affect both the rate and shape of the background distributions. The top, middle and, bottom rows are events with 4, 5, and ≥ 6 jets, respectively, while the left, middle, and right-hand columns are events with 2, 3, and ≥ 4 b -tags, respectively. The $t\bar{t}H$ signal ($m_H = 125$ GeV) is normalized to $30 \times$ SM expectation.

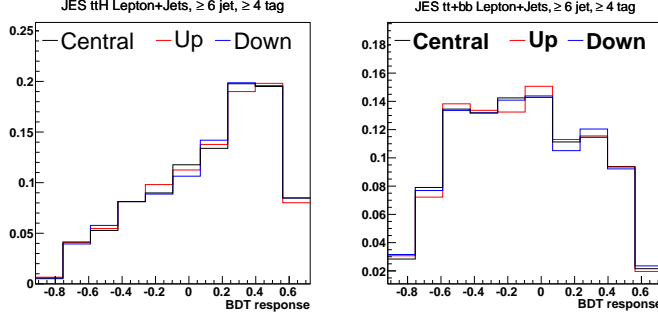


Figure 7.18: Comparison of the MVA discriminator for JES shift upwards (red) and downwards (blue) relative to the nominal (black) shape for the $t\bar{t}H(125)$ signal (left) and the main background sample $t\bar{t} + b\bar{b}$ (right). The plots are from the ≥ 6 jet ≥ 4 tag category in the lepton+jets channel. All plots are normalized to unit area.

2696 diction of simulated heavy-flavor events in the light-flavor control region, and visa versa.
 2697
 2698 Figures 7.19 and 7.20 and Table 7.9 show the effect of this uncertainty on the final BDT
 2699 shapes. The impact of statistical uncertainties associated with the scale factor determina-
 2700 tion are controlled by means of four total nuisance parameters, two for heavy-flavor and
 2701 two for light-flavor. For each jet flavor, the first nuisance parameter controls distortions in
 2702 the CSV distribution corresponding to an overall tilt. This is consistent with a migration
 2703 of events from one end of the CSV range to the other. The second nuisance parameter
 2704 controls distortions of a more complicated nature, where the upper and lower ends of the
 2705 distribution change relative to the center. Figures. 7.21 and 7.22, and Table 7.9 show the
 2706 size of the shape and rate impact on the final BDT shape. For charm jets scale factors, the
 2707 overall relative uncertainty is retained from the heavy flavor scale factors, doubled in size
 2708 and used to construct two separate nuisance parameters to control the uncertainties. These
 2709 two uncertainties associated with charm jets scale factors are not correlated with respect
 2710 to all the uncertainties for the heavy flavor and light flavor scale factors. Figure 7.23 and
 2711 Table 7.9 show the size of the shape and rate impact on the final BDT shape.

2711 **Electron and Muon ID and Trigger Scale Factors:** A rate uncertainty of 1.4% is assigned
 2712 for single-lepton events. A single nuisance parameter is used for all lepton-related and is
 2713 correlated between muons and electrons. Uncertainties for electrons and muons are treated
 2714 identically, and in the case where there is a difference, the larger uncertainty is used.
 2715 Uncertainties from ID and isolation as fully uncorrelated and are combined in quadrature
 2716 for the value of the nuisance parameter.

2717 The total lepton efficiency uncertainty is composed of two parts. Both parts were measured
 2718 using the method described in [172], which is a "tag and probe" method based on lepton
 2719 events near the Z boson mass resonance. The first part is a 1% uncertainty on the lepton

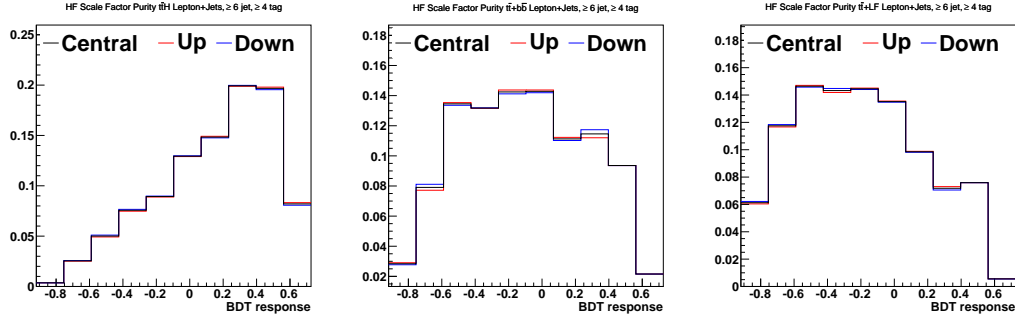


Figure 7.19: Comparison of the MVA discriminator when shifting the light flavor contamination in the heavy flavor scale factor determination shift upwards (red) and downwards (blue) relative to the nominal (black) shape for the $t\bar{t}H(125)$ signal (top row) and $t\bar{t} + b\bar{b}$ and $t\bar{t} + \text{LF}$ background samples (middle row and bottom row respectively). The plots are from the $\text{LJ} \geq 6 \text{ jet} \geq 4$ category. All plots are normalized to unit area.

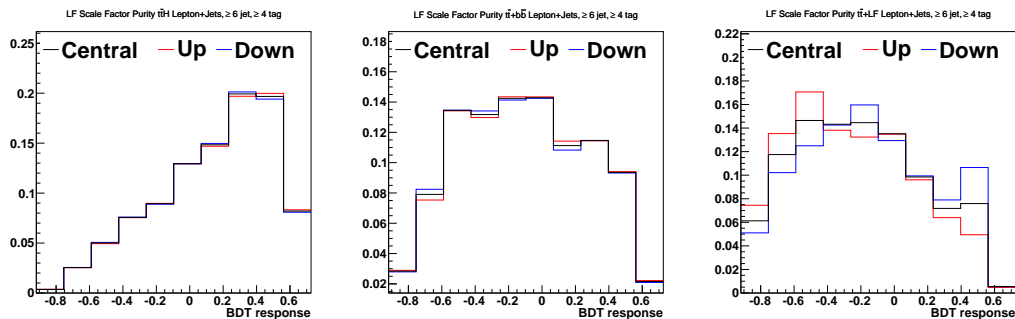


Figure 7.20: Comparison of the MVA discriminator when shifting the heavy flavor contamination in the light flavor scale factor determination shift upwards (red) and downwards (blue) relative to the nominal (black) shape for the $t\bar{t}H(125)$ signal (top row) and $t\bar{t} + b\bar{b}$ and $t\bar{t} + \text{LF}$ background samples (middle row and bottom row respectively). The plots are from the $\text{LJ} \geq 6 \text{ jet} \geq 4$ category. All plots are normalized to unit area.

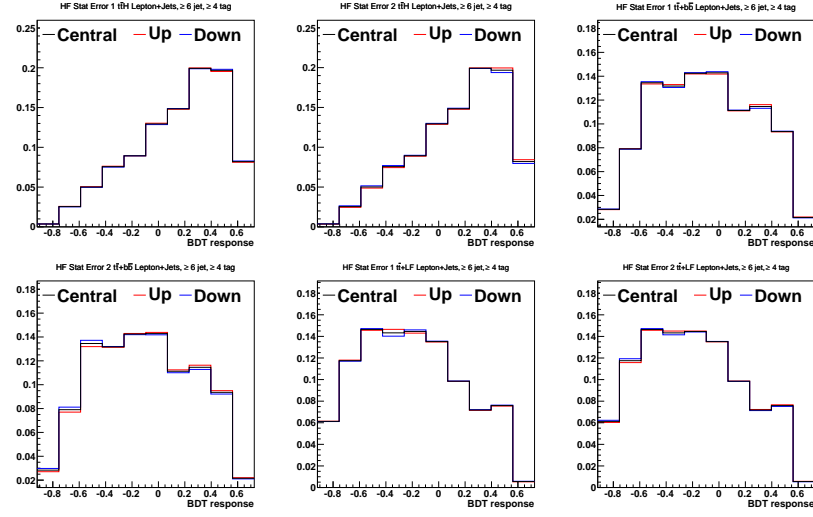


Figure 7.21: Comparison of the MVA discriminator when shifting to account for the statistical uncertainty on the heavy flavor scale factor extraction. Two classes of distortion in the scale factor are considered: linear distortions (labeled “Stat. Error 1”) and nonlinear distortions (labeled “Stat. Error 2”). Both shift upwards (red) and downwards (blue) relative to the nominal (black) shape for the $t\bar{t}H(125)$ signal (top row) and $t\bar{t} + b\bar{b}$ and $t\bar{t} + \text{LF}$ background samples (middle row and bottom row respectively) are shown. The plots are from the ≥ 6 jet ≥ 4 tag category. All plots are normalized to unit area.

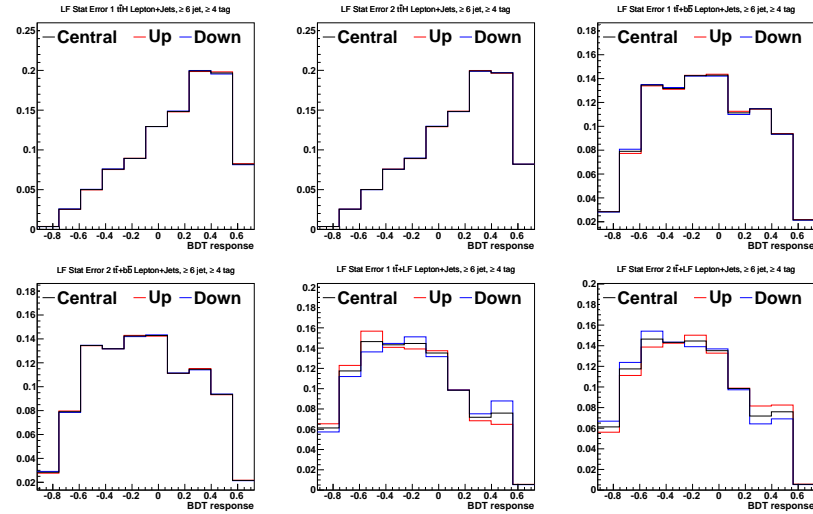


Figure 7.22: Comparison of the MVA discriminator when shifting to account for the statistical uncertainty on the light flavor scale factor extraction. Two classes of distortion in the scale factor are considered: linear distortions (labeled “Stat. Error 1”) and nonlinear distortions (labeled “Stat. Error 2”). Both shift upwards (red) and downwards (blue) relative to the nominal (black) shape for the $t\bar{t}H(125)$ signal (top row) and $t\bar{t} + b\bar{b}$ and $t\bar{t} + \text{LF}$ background samples (middle row and bottom row respectively) are shown. The plots are from the ≥ 6 jet ≥ 4 tag category. All plots are normalized to unit area.

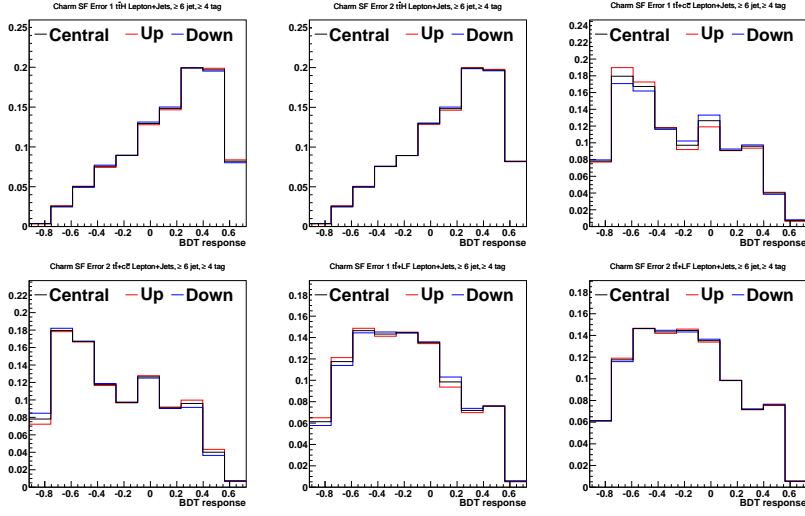


Figure 7.23: Comparison of the MVA discriminator when shifting to account for the uncertainty on the charm jets scale factor extraction. Two classes of distortion in the scale factor are considered: linear distortions (labeled “Error 1”) and nonlinear distortions (labeled “Error 2”). Both shift upwards (red) and downwards (blue) relative to the nominal (black) shape for the $t\bar{t}H(125)$ signal (top row) and $t\bar{t} + c\bar{c}$ and $t\bar{t} + \text{LF}$ background samples (middle row and bottom row respectively) are shown. The plots are from the ≥ 6 jet ≥ 4 tag category. All plots are normalized to unit area.

<i>b</i> -tag systematic yield change					
		lepton+jets			
sys	shift	$t\bar{t} H(125)$	$t\bar{t} + \text{LF}$	$t\bar{t} + bb$	
Heavy Flavor SF Purity	up	+13.2%	+7.4%	+13.3%	
	down	-12.1%	-7.2%	-12.1%	
Light Flavor SF Purity	up	-3.4%	-32.2%	-4.4%	
	down	+3.4%	+43.9%	+4.4%	
Heavy Flavor SF Stat. Err. 1	up	-12.1%	-6.6%	-11.8%	
	down	+13.3%	+6.8%	+12.9%	
Heavy Flavor SF Stat. Err. 2	up	+8.9%	+5.0%	+9.1%	
	down	-8.3%	-4.9%	-8.5%	
Light Flavor SF Stat. Err. 1	up	+0.5%	-15.6%	+0.1%	
	down	-0.5%	+17.7%	-0.1%	
Light Flavor SF Stat. Err. 2	up	+1.8%	+10.1%	+2.1%	
	down	-1.7%	-8.9%	-2.0%	
sys	shift	$t\bar{t} H(125)$	$t\bar{t} + \text{LF}$	$t\bar{t} + cc$	
Charm jets SF Err. 1	up	+5.1%	-3.4%	-5.6%	
	down	-5.1%	+3.3%	+5.0%	
Charm jets SF Err. 2	up	+6.0%	+4.2%	+12.7%	
	down	-5.9%	-4.2%	-11.7%	

Table 7.9: This table summarizes the rate effect of the six independent nuisance parameters that characterize the *b*-tag uncertainties. (Note: The *b*-tag rate uncertainties associated with JES variations are already included with the JES rate uncertainties in Table 6.14. The impact of statistical uncertainties is in the heavy-flavor and light-flavor scale factor extraction is incorporated using two separate nuisance parameters, as described above. The uncertainty labeled “Stat. Err. 1” represents statistical uncertainties resulting a linear distortion of the CSV scale factor, while the one labeled “Stat. Err. 2” corresponds to nonlinear distortions.

identification and isolation scale factor. The second part of the total lepton efficiency uncertainty is a 1% trigger scale factor uncertainty.

Pileup Reweighting: See section 6.4 for a description of the evaluation of this systematic.

Top Quark p_T Reweighting: The systematic uncertainty on the top p_T reweighting is assessed as follows: the uncorrected Monte Carlo shapes are used as -1σ systematic uncertainty, and doubling the correction factor gives the $+1\sigma$ variation. This creates a deviation that is the same size as the original observed difference between data and Monte Carlo. This uncertainty is shown in Fig. 7.2. Fig. 7.24 shows the effects of the uncertainty on the top quark p_T on the BDT shape and Table 7.10 shows the effect on the rates.

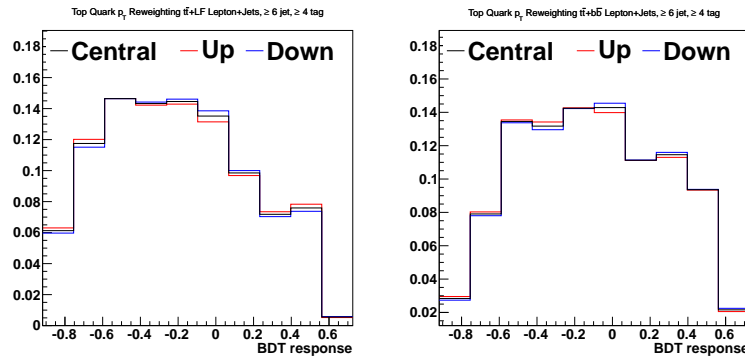


Figure 7.24: Comparison of the MVA discriminator for shifts in top quark p_T reweighting upwards (red) and downwards (blue) relative to the nominal (black) shape for the $t\bar{t}$ +LF background (left) and the $t\bar{t}$ + $b\bar{b}$ (right). The plots are from the ≥ 6 jets + ≥ 4 tags category in the lepton+jets channel. All plots are normalized to unit area.

Top quark p_T reweighing systematic yield change			
		lepton+jets	
sys	shift	$t\bar{t}$	$t\bar{t} + b\bar{b}$
Top quark p_T Reweighting	up	-5.2%	-7.0%
	down	+5.2%	+7.0%

Table 7.10: Relative yield change due to varying the top quark p_T reweighting. The “up” variation corresponds to apply twice as much correction to the top quark p_T distribution as the nominal, while the “down” correction corresponds to applying no correction to the default MC top quark p_T distribution.

Cross Sections: See section 6.4 for a description of the evaluation of this systematic. Uncertainties affecting these normalizations are summarized in Table 7.11.

Luminosity: The uncertainty on the luminosity estimate is 2.2%. This affects all rates.

Madgraph Q^2 Uncertainty: See section 6.4 for a description of the evaluation of this systematic.

Process	pdf			QCD Scale			
	gg	qb	qg	$t\bar{t}$	V	VV	$t\bar{t}H$
$t\bar{t}H$	9%						12.5%
$t\bar{t} + \text{jets}$	2.6%			3%			
$t\bar{t} + W$		7%		15%			
$t\bar{t} + Z$	9%			15%			
Single top			4.6%	2%			
$W + \text{jets}$		4.8%			1.3%		
$Z + \text{jets}$		4.2%			1.2%		
Dibosons						3.5%	

Table 7.11: Cross section uncertainties used for the limit settings. Each column in the table is an independent source of uncertainty, except for the last column which represents uncertainties uncorrelated with any others. Uncertainties in the same column for two different processes (different rows) are completely correlated.

2734 Figure 7.25 shows the shape and Table 7.12 shows the rate variations for selected event
 2735 categories.

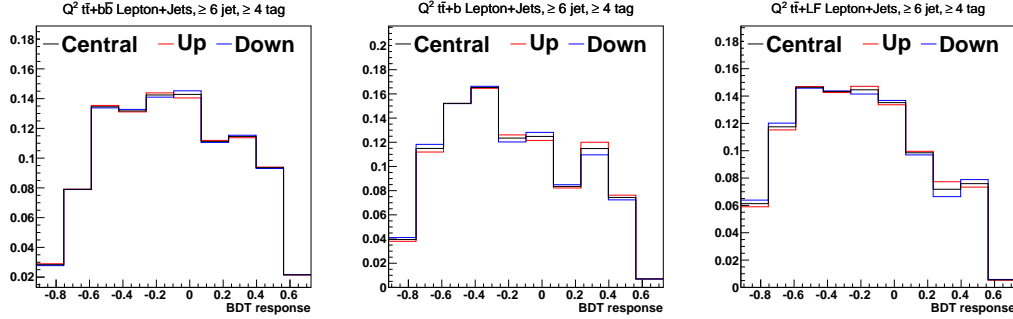


Figure 7.25: Comparison of the MVA discriminator when shifting the Q^2 scale up and down by its uncertainties. Shown are the shift upwards (red) and downwards (blue) relative to the nominal (black) shape for the $t\bar{t} + b\bar{b}$ (top row) $t\bar{t} + b$ (middle row) and $t\bar{t} + \text{LF}$ (bottom) background samples. The plots are from the $LJ \geq 6$ jet ≥ 4 category. All plots are normalized to unit area.

Q^2 systematic yield change					
		lepton+jets			
sys	shift	$t\bar{t} + \text{LF}$	$t\bar{t} + b$	$t\bar{t} + b\bar{b}$	
Q^2 Uncertainty	up	-13.8%	-16.1%	-17.6%	
	down	+17.6%	+20.8%	+23.3%	

Table 7.12: This table summarizes the rate effect of shifting Q^2 scale uncertainty for Madgraph. Note that the shifts are made independently for the following topologies: $t\bar{t} + 0p$, $t\bar{t} + 1p$, $t\bar{t} + 2p$, $t\bar{t} + c\bar{c}$, $t\bar{t} + b$, and $t\bar{t} + b\bar{b}$.

2736 **MC Statistics Uncertainty:** See section 6.4 for a description of the evaluation of this sys-
 2737 tematic.

2738 **Extra $t\bar{t}$ +HF Rate Uncertainty:** See section 6.4 for a description of the evaluation of this sys-
 2739 tematic.

2740 Table 7.13 summarizes the systematic uncertainties assessed on the signal and backgrounds
2741 for this analysis. It describes how each systematic is treated in the fit used for signal extraction.

Source	Shape?	Notes
Luminosity	No	Signal and all backgrounds
Lepton ID/Trig	No	Signal and all backgrounds
Pileup	No	Signal and all backgrounds
Jet Energy Resolution	No	Signal and all backgrounds
Jet Energy Scale	Yes	Signal and all backgrounds
<i>b</i> -Tag HF fraction	Yes	Signal and all backgrounds
<i>b</i> -Tag HF stats (linear)	Yes	Signal and all backgrounds
<i>b</i> -Tag HF stats (quadratic)	Yes	Signal and all backgrounds
<i>b</i> -Tag LF fraction	Yes	Signal and all backgrounds
<i>b</i> -Tag LF stats (linear)	Yes	Signal and all backgrounds
<i>b</i> -Tag LF stats (quadratic)	Yes	Signal and all backgrounds
<i>b</i> -Tag Charm (linear)	Yes	Signal and all backgrounds
<i>b</i> -Tag Charm (quadratic)	Yes	Signal and all backgrounds
QCD Scale ($t\bar{t}H$)	No	Scale uncertainty for NLO $t\bar{t}H$ prediction
QCD Scale ($t\bar{t}$)	No	Scale uncertainty for NLO $t\bar{t}$ and single top predictions
QCD Scale (V)	No	Scale uncertainty for NNLO W and Z prediction
QCD Scale (VV)	No	Scale uncertainty for NLO diboson prediction
pdf (gg)	No	Pdf uncertainty for gg initiated processes ($t\bar{t}, t\bar{t}Z, t\bar{t}H$)
pdf ($q\bar{q}$)	No	Pdf uncertainty for $q\bar{q}$ initiated processes ($t\bar{t}W, W, Z$).
pdf (qg)	No	Pdf uncertainty for qg initiated processes (single top)
Madgraph Q^2 Scale ($t\bar{t} + 0p, 1p, 2p$)	Yes	Madgraph Q^2 scale uncertainty for $t\bar{t} + jets$ split by parton number. There is one nuisance parameter per parton multiplicity and they are uncorrelated.
Madgraph Q^2 Scale ($t\bar{t} + b\bar{b}/c\bar{c}$)	Yes	Madgraph Q^2 scale uncertainty for $t\bar{t}+jets/b\bar{b}/c\bar{c}$.
Madgraph Q^2 Scale (V)	No	Varies by jet bin.
τ Energy Scale	Yes	Tau signal and background
τ ID efficiency	Yes	Tau signal and background
τ Jet Fake Rate	Yes	Tau signal and background
τ Electron Fake Rate	Yes	Tau signal and background

Table 7.13: Summary for the of the systematic uncertainties considered on the inputs to the limit calculation. Except where noted, each row in this table will be treated as a single, independent nuisance parameter.

2742 Table 7.14 shows the results of the comparing the variation in rate for the sum of $t\bar{t} + lf + b\bar{b} + c\bar{c}$
2743 backgrounds. The systematic that produces the largest variation of the backgrounds is the QCD
2744 scale uncertainty on the $t\bar{t} + b\bar{b}$ background. The next largest variation comes from: the amount
2745 of $t\bar{t} + b\bar{b}$, the *b*-tagging efficiency and fake rate, and the jet energy scale. The next most important
2746 effect is the top quark p_T correction, and it is more than three times smaller than the QCD scale
2747 uncertainty on $t\bar{t} + b\bar{b}$.

2748 7.5 Statistical Methods

2749 The same procedure that was used in the previous analysis, and desrcied in section 6.5.

Uncertainties on the sum of $t\bar{t} + \text{lf}$, $t\bar{t} + b$, $t\bar{t} + b\bar{b}$, and $t\bar{t} + c\bar{c}$ events with ≥ 6 jets and ≥ 4 b-tags		
Source	Rate	Shape?
QCD Scale ($t\bar{t} + b\bar{b}$)	17%	No
b -Tag HF contamination	17%	Yes
QCD Scale ($t\bar{t} + c\bar{c}$)	11%	No
Jet Energy Scale	11%	Yes
b -Tag LF contamination	9.6%	Yes
b -Tag HF stats (linear)	9.1%	Yes
QCD Scale ($t\bar{t} + b$)	7.1%	No
Madgraph Q^2 Scale ($t\bar{t} + b\bar{b}$)	6.8%	Yes
b -Tag Charm Uncertainty (quadratic)	6.7%	Yes
Top Pt Correction	6.7%	Yes
b -Tag HF stats (quadratic)	6.4%	Yes
b -Tag LF stats (linear)	6.4%	Yes
Madgraph Q^2 Scale($t\bar{t} + 2$ partons)	4.8%	Yes
b -Tag LF stats (quadratic)	4.8%	Yes
Luminosity	4.4%	No
Madgraph Q^2 Scale ($t\bar{t} + c\bar{c}$)	4.3%	Yes
Madgraph Q^2 Scale ($t\bar{t} + b$)	2.6%	Yes
Lepton ID/Trig	1.4 (2.8)%	No
QCD Scale ($t\bar{t}$)	3%	No
pdf (gg)	2.6%	No
Jet Energy Resolution	1.5%	No
Pileup	1%	No
b -Tag Charm Uncertainty (linear)	0.6%	Yes

Table 7.14: Specific effect of systematics on predicted background yields for events with ≥ 6 jets and ≥ 4 b-tags. Here we only consider the sum of the largest backgrounds, $t\bar{t} + \text{lf}$, $t\bar{t} + b$, $t\bar{t} + b\bar{b}$, and $t\bar{t} + c\bar{c}$. These three backgrounds account for 94% of all background events. The signal is 3.5% of the yield of the three main backgrounds. The signal fraction is directly comparable to the variations of the background in the table. The table shows that the signal is much smaller than many of the background variations.

2750 7.6 Results and Conclusions

2751 In the lack of a significant excess of events in data, upper limits are once again set on the
 2752 $t\bar{t}H$ production rate. The shape of the BDT discriminator distribution is used to fit the simulated
 2753 signal and backgrounds samples to the data. Besides the BDT discriminator shapes for data,
 2754 background and signal, inputs to the limit setting include the number of events passing the
 2755 selection for each process. Systematics that are used are nuisance parameters are described in
 2756 the previous section. The Higgs mass points we set limits for are: 110, 115, 120, 125, 130, 135
 2757 and 140 GeV/c^2 . For the lepton+jets channel, the limits are shown in Tab. 7.15 and Fig. 7.26.

Higgs Mass	Observed	Median	Expected 68% C.L. Range	Expected 95% C.L. Range
110 GeV/c^2	3.6	3.3	[2.4,4.7]	[1.8,6.6]
115 GeV/c^2	4.1	3.5	[2.4,4.9]	[1.8,6.9]
120 GeV/c^2	4.3	4.0	[2.9,5.8]	[2.1,8.1]
125 GeV/c^2	4.9	4.7	[3.3,6.7]	[2.5,9.4]
130 GeV/c^2	6.8	6.0	[4.3,8.6]	[3.2,12.0]
135 GeV/c^2	7.4	7.1	[5.0,10.2]	[3.7,14.2]
140 GeV/c^2	9.0	9.6	[6.9,13.7]	[5.2,18.9]

Table 7.15: Expected and observed upper limits for SM Higgs for lepton + jets channel using the 2012 dataset. These limits were extracted using the asymptotic method.

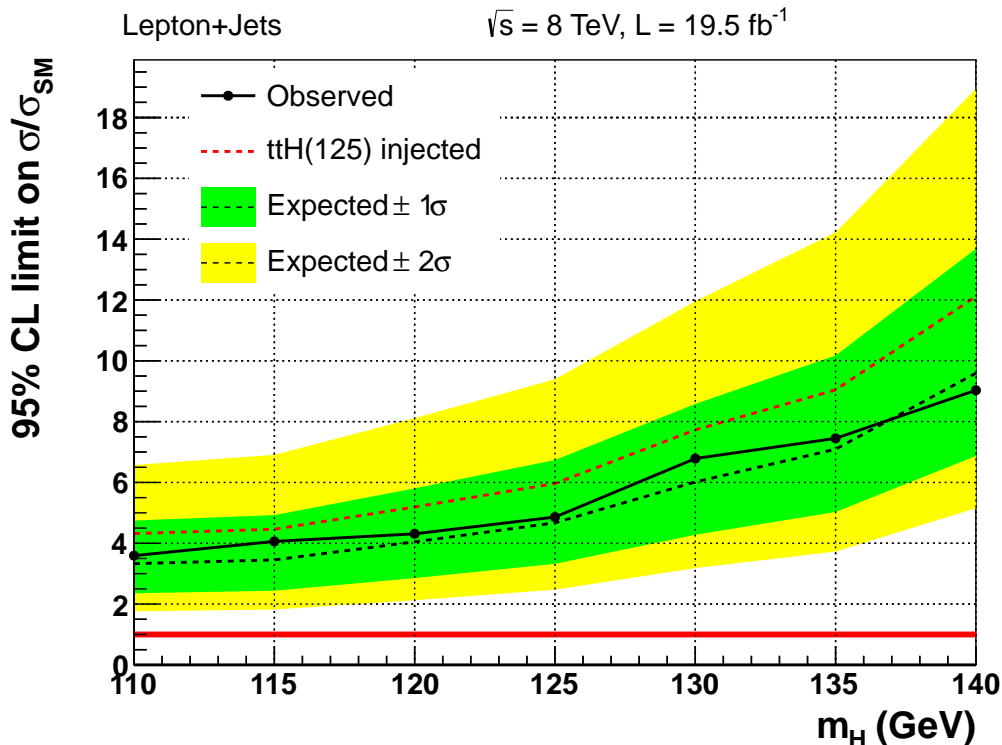


Figure 7.26: The expected and observed 95% CL upper limits on the signal strength parameter $\mu = \sigma/\sigma_{SM}$ for the lepton+jets channel using the 2012 dataset. These limits were extracted using the asymptotic method.

2758 For the full 19.4 fb^{-1} of 8 TeV data collected by the CMS detector, an updated search

for the Standard Model Higgs boson produced in association with top-quark pairs has been performed. The increase in expected sensitivity did not increase by a factor of ~ 2 that one would naively expect from increasing the statistics by a factor of ~ 4 . This is because, largely due to the different set of systematic uncertainties used, the analysis entered a regime where statistical uncertainty was no longer the dominant factor that degraded sensitivity. If this data set was repeatedly collected, allowing for statistical fluctuations, it should be expected that, for a Standard Model Higgs boson, with mass, $m_H = 125 \text{ GeV}$, that 95% of the results would fail to observe the $t\bar{t}H$ signal unless its cross-section was modified by a factor of 4.9. From simulations alone, this expected factor is 4.7, a difference of less than 1σ from the observed data.

The results of this analysis were combined with previous results in this channel from 7 TeV data and with di-lepton, same-sign di-lepton, hadronic tau, di-photon, and multi-lepton final state channels and published in the Journal of High Energy Physics (JHEP) in September of 2014 [173]. The combined analytical power of all of the channels allowed for an upper limit of 4.5 times the predicted Standard Model cross section. This is slightly more than 2σ away from the expected factor of 1.8 from simulations alone.

Relative the previous analysis, which was primarily driven by my efforts, the addition of new members to our research group and the conclusion of the 7 TeV analysis allowed me to focus on specific tasks in greater detail. The validation of the b-tagging calibration factors involved extensive investigations, selecting both light and heavy-flavour enriched events, using a χ^2 minimization technique to identify $t\bar{t} + \text{jets}$ events and $Z + \text{jets}$ events, in order to compare the simulations to data. I also was responsible for comparisons of this analysis to the results provided by ATLAS. This involved reproducing the ATLAS event selection and signal extraction techniques, then producing an exact account of the effect that each of the different choices made on the upper limits of this analysis. The results of the comparisons will be used to guide the design of the analysis in Run 2.

2784 **Chapter 8**

2785 **Analysis Improvements**

2786 The analyses described in the previous two chapters use sophisticated multivariate analysis
2787 (MVA) techniques to perform signal extraction and limit setting. However, there are several
2788 improvements that can still be made to optimize signal extraction and increase sensitivity. The
2789 following section will describe the implementation of the latest simulation techniques in order
2790 to improve the modeling the signal and background processes. The final section will discuss
2791 variables from these new simulations that can be used to enhance the identification of final state
2792 jets with their roles in the $t\bar{t}$ system.

2793 **8.1 aMC@NLO, MadSpin, and Pythia8 Monte Carlo**

2794 One of the largest sources of uncertainty in each analysis comes from the theoretical uncertainty
2795 of the Leading Order (LO) monte carlo sample used to estimate background rates and shapes.
2796 In order to accurately model the high jet-multiplicity environment of the $t\bar{t}H$ final state, higher-
2797 order calculations in perturbation theory are necessary. Recently, the aMC@NLO framework
2798 has been released, and is an automated tool for event generation that utilizes Next-to-Leading
2799 Order (NLO) QCD predictions [174]. This framework takes advantage of recent theoretical
2800 developments in the automation of calculating spin-entangled decays from heavy resonances,
2801 which is packaged in the program MadSpin [175]. The event generator, aMC@NLO, using
2802 MadSpin to calculate the decays of the top quark, W and Z bosons, is then interfaced to Pythia
2803 8 to framework perform the parton shower and hadronization [176]. Each stage of this event
2804 generation process uses the latest technological developments in monte carlo simulation, which
2805 were unavailable at the time of the previous analyses.

2806 For process where additional jets are simulated in the final state, there will be an additional
2807 complication since the parton shower and hadronization are performed separately and the con-

tributions for NLO processes will be double counted in several cases. This occurs when a process with an additional jet in the final state is created in the matrix element level by aMC@NLO and later, another event is created with no additional jets in the final state at the matrix element level, but when the parton shower occurs in Pythia 8, an additional jet can be generated, creating two events from a single underlying theoretical contribution. The removal of these overlapping events is carried out by a method known as FXFX merging [177]. This algorithm tracks the heritage of final state jets, in order to determine whether it was created as part of the matrix element or later during the parton shower. Due to the higher accuracy of modeling the kinematics of partons calculated in the matrix element stage, the algorithm removes events where additional jets are created in the parton shower, ensuring that the underlying process with an additional final state jets are created at the matrix element level, utilizing the NLO QCD calculations in aMC@NLO.

The utilization of these event generation techniques to simulate $t\bar{t}H$ and $t\bar{t}+jets$ backgrounds will improve the kinematic modeling of these high-jet multiplicity processes. A dedicated $t\bar{t}+b\bar{b}$ sample with a large number of events generated with this framework would improve the modeling of the irreducible background. Unfortunately, these event generation tools were only recently released and the computational time required to generate samples with the equivalent statistical power of those used in the previous analyses is prohibitive on the time scale of this dissertation. However, each of the following samples were created using the process described above with 500,000 events each:

- $t\bar{t} + 0, 1, \text{ and } 2$ additional jets

- $t\bar{t} + b\bar{b}$

- $t\bar{t}H + 0, \text{ and } 1$ additional jets

The number of events generated is not sufficient to create a control region to assess calibrations of jet energy, b -tag efficiency, or lepton identification and reconstruction efficiency. However, since all of these processes are generated in an identical framework, it is reasonable to assume that calibrations applied will be similar for each, and as such comparisons amongst the samples can still provide insight into how they can be used to improve the analysis. Figure 8.1 shows a comparison between the number of reconstructed jets and b -tagged jets that pass the selection used in the previous analysis, with a lowered p_T threshold of 25 GeV. As before, the jet multiplicity of $t\bar{t}H$ has a much longer distribution than the $t\bar{t}+jets$ backgrounds, making it very important that these high-multiplicity events are modeled with the highest precision available.

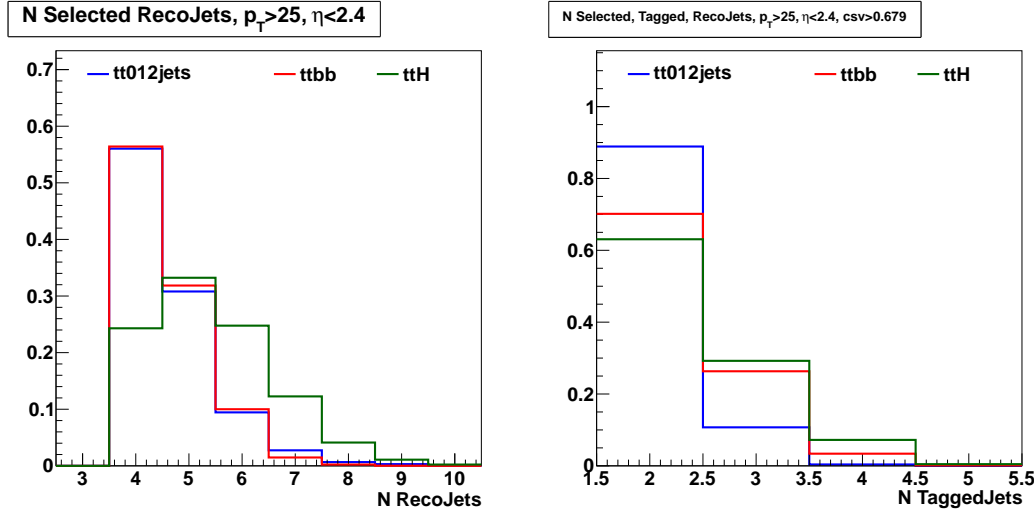


Figure 8.1: The number of reconstructed jets passing selection (left) and that have additionally been b -tagged (right) for $t\bar{t}H$, $t\bar{t} + jets$, and $t\bar{t} + b\bar{b}$ samples generated with the aMC@NLO and Pythia 8 framework

2840 8.2 Analysis Techniques Under Development

2841 One of the most difficult challenges of the $t\bar{t}H$ final state is the combinatorics of possible b -jet
 2842 candidates coming from the Higgs decay. The correct associate of jets to their roles in the decay
 2843 of the top quarks would greatly reduce the number of jets as candidates for Higgs daughters.
 2844 This is done, in some degree, in the analyses described in previous chapters via the "best Higgs
 2845 mass" variable. This is a χ^2 minimization that relies only on the masses of the top quark, W and
 2846 Higgs bosons in the event, to decide which jets are associated to the decays of which particles.
 2847 These mass variables will be useful in identifying jets from the $t\bar{t}$ system. Figure 8.2 shows the
 2848 case for the W boson mass evaluated for jets which have been correctly associated to the MC
 2849 truth generated partons in blue, and for the incorrect associations in green.

2850 The implementation of Madspin in the aMC@NLO framework allows for the highest precision
 2851 on the spin correlations of the decay products from the $t\bar{t}H$ and $t\bar{t}$ systems. The angular
 2852 relationships among the decay products provide additional discrimination power for the correct
 2853 association of jets to their roles in the $t\bar{t}H$ and $t\bar{t}$ systems. The spin correlations of the decay
 2854 products are enhanced by boosting to a reference frame that is more sensitive to differences in
 2855 the angles between the correctly and incorrectly associated objects in the event. The reference
 2856 frame of choice is formed by first identifying all of the potential candidates of the semi-leptonic
 2857 $t\bar{t}$ decay:

- 2858 • \bar{b} -quark coming from the t -quark
- 2859 • b -quark coming from \bar{t} -quark
- 2860 • up-type quark from hadronic W boson decay

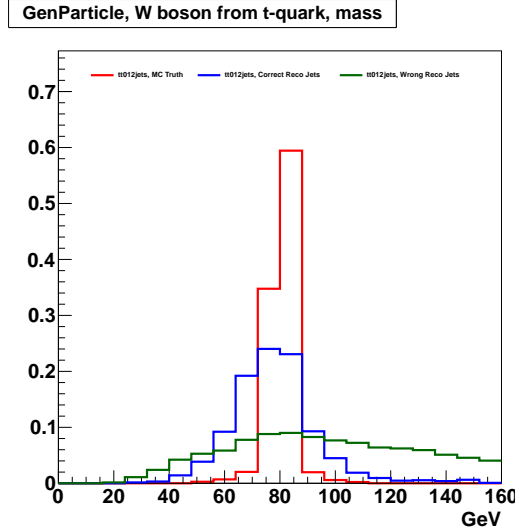


Figure 8.2: The invariant mass of the W boson in the $t\bar{t}$ decay for the case of the MC truth (red), correctly associated reconstructed jets (blue), and incorrectly associated reconstructed jets (green)

- 2861 • down-type quark from the hadronic W boson decay

2862 The four-vector of the entire $t\bar{t}$ system can be formed, and the hadronic candidates are
 2863 boosted to a frame where the $t\bar{t}$ system itself is at rest. Then, the t -quark, and its daughters
 2864 are boosted to a frame such that the t -quark is at rest. Finally, the \bar{t} -quark, and its daughters
 2865 are boosted to a frame such that the \bar{t} -quark is at rest. Then the angles between their decay
 2866 products is evaluated. Typically, these studies are performed in the di-lepton channel since the
 2867 angular resolution is much better in leptons than in jets. Figure 8.3 shows the cosine of the
 2868 momentum 3-vector between the b -quarks from t and \bar{t} , the lepton and the up-type W -boson
 2869 daughter, and the lepton and the down-type W -boson daughter.

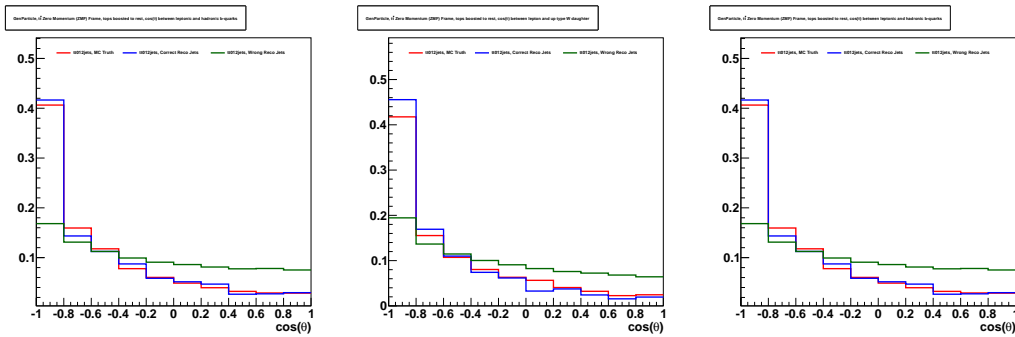


Figure 8.3: The cosine of the angle between the momentum three-vectors for the b -quarks from the top decays (left), the lepton and the up-type W boson daughter (center), and the lepton and the down-type W boson daughter (right)

- 2870 All three distributions have peaking values that provide discrimination between the jets correctly
 2871 associated to the MC truth generator-level partons of the $t\bar{t}$ decay, and the jets which are
 2872 incorrectly associated. In each plot, the green represents the incorrect associations, while the

blue represents the correct associations, and the red represents the MC truth from the generated parton. An additional angle of interest is the difference in the ϕ coordinate between daughters of the $t\bar{t}$ decay. Figure 8.4 shows the distributions for the $\Delta\phi$ between the b -quarks from the top decays, the lepton and up-type W -boson daughter, and the lepton and the down-type W -boson daughter. The case of the correctly associated jets has two sharp peaks near $\phi = \pm 2$, where the distribution is more uniform for incorrectly associated jets.

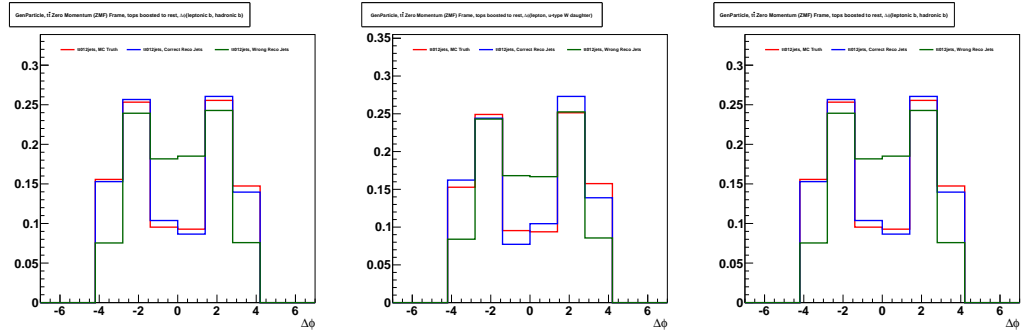


Figure 8.4: The difference in the ϕ coordinate between the momentum three-vectors for the b -quarks from the top decays (left), the lepton and the up-type W boson daughter (center), and the lepton and the down-type W boson daughter (right)

A final variable of interest for jet association would be the charge of lepton multiplied against the charge of the b -quark that is associated with the same top-quark. These two values, due to charge conservation, will always be negative when multiplied. The charge of the jet is calculated from a p_T weighted sum of the tracks contained in the cluster, where the curvature of each track tells the charge of the hadron creating the signature. Since there are many hadrons clustered together to form a jet, there is a large degradation on resolution of the charge of the jet, however for the peak of this distribution is negative for correctly associated jets, and positive for incorrect jets, as shown in figure 8.5.

A jet association algorithm can be formed by using an MVA technique to provide a discriminant for how likely a certain combination of jets from an event are correctly associated to their roles in the decay of the $t\bar{t}$ system. A training sample of correctly and incorrectly associated jets can be trained using the following variables:

- Invariant Mass of the Hadronic W boson
- Invariant Mass of the Leptonic W boson
- Invariant Mass of the Hadronic top-quark
- Invariant Mass of the Leptonic top-quark
- $\cos\theta_{b,\bar{b}}$ in the frame where $t\bar{t}$ system and t -quarks are at rest respectively

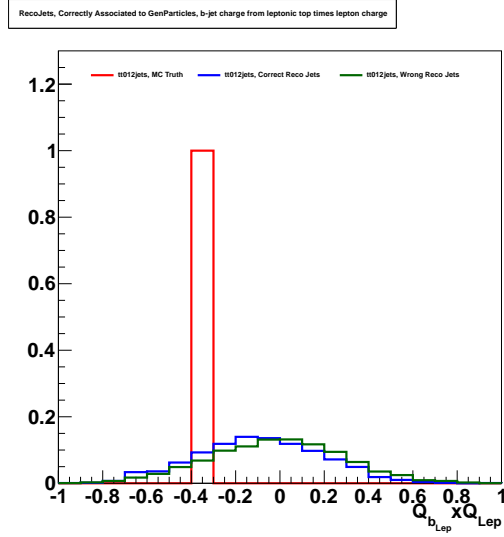


Figure 8.5: Jet times lepton charge, for the b -jet associated with the same top as the lepton. Green shows incorrectly associated reconstructed jets, blue shows correctly associated jets, and red is the MC truth

- $\cos \theta_{\text{lep}, \text{up-type}W\text{daughter}}$ in the frame where $t\bar{t}$ system and t -quarks are at rest respectively

- $\cos \theta_{\text{lep}, \text{down-type}W\text{daughter}}$ in the frame where $t\bar{t}$ system and t -quarks are at rest respectively

- $\Delta\phi(\theta_{b,\bar{b}})$ in the frame where $t\bar{t}$ system and t -quarks are at rest respectively

- $\Delta\phi(\theta_{\text{lep}, \text{up-type}W\text{daughter}})$ in the frame where $t\bar{t}$ system and t -quarks are at rest respectively

- $\Delta\phi(\theta_{\text{lep}, \text{down-type}W\text{daughter}})$ in the frame where $t\bar{t}$ system and t -quarks are at rest respectively

- The product of the lepton and b -quark associated with the same t -quark

An additional improvement to the analysis will rely on a dedicated MVA for each of the $t\bar{t} + X$ backgrounds, where X is light flavor, single c , $c\bar{c}$, single b , and $b\bar{b}$. A dedicated $t\bar{t} + b\bar{b}$ and even a $t\bar{t} + c\bar{c}$ sample with sufficiently large enough events to train an MVA would be ideal. The discriminants from each of the backgrounds would be combined as input variables to a second MVA, in order to produce a discriminant for how likely the event is from a $t\bar{t}H$ decay.

2910 **Chapter 9**

2911 **Conclusions and Summary**

2912 In 2012, the Large Hadron Collider (LHC) produced the highest energy proton-proton collisions,
2913 with center of mass energies of 8 TeV. Protons, with humble beginnings in a bottle of Hydrogen,
2914 travel through a multi-stage accelerator complex, before being injected into the 27.6 km LHC
2915 ring as two counter-rotating beams. Superconducting radio-frequency cavities accelerate the
2916 beams during each revolution, constrained to the circular path by more than a thousand 8 T
2917 superconducting dipole magnets, as each beam is brought to an energy of 4 TeV.

2918 At one of the four points on the LHC ring where the proton beams are squeezed together
2919 to produce collisions, sits the Compact Muon Solenoid (CMS) experiment, a general purpose
2920 particle detector designed to elucidate the mechanism of electroweak symmetry breaking, and
2921 explore physics interactions at the TeV energy scale. This 14,000 ton, 15 m tall device, provides
2922 hermetic, 4π , coverage of the interaction region, and is composed of a system of sub-detectors,
2923 with a cylindrical symmetry about the beam-line and interaction region, which work in parallel
2924 to identify and measure the kinematic properties of particles produced during pp collisions.
2925 The inner tracking system is composed of more than 70 million silicon pixel and strip detectors
2926 that provide μm spatial resolution on the trajectory of charged particles. An electromagnetic
2927 calorimeter (ECAL) surrounds the inner tracker, and is composed of more than 75,000
2928 lead-tungstate crystals, which absorb energy from electromagnetically interacting particles, with
2929 electrons and photons depositing almost all of their energy in this sub-detector. The hadronic
2930 calorimeter (HCAL) surrounds the ECAL, absorbing the energy of charged and neutral hadrons
2931 with stacks of brass absorber material with layers of plastic scintillator to sample the energy
2932 in between. The outermost system are the muon chambers, which utilize three different types
2933 of detector technologies to provide fast timing to trigger measurements and excellent spatial
2934 resolution on muons, an important signature for many TeV energy scale processes. Hardware
2935 and firmware installed on the detector provide an instant, but basic reconstruction of a collision,

allowing for the amount of collisions recorded to be reduced from a rate of 40 MHz down to 10 kHz. Events are additionally filtered through the use of software to a manageable rate of 100 Hz.

Once the first 5.1 fb^{-1} of 8 TeV data was collected by the CMS detector, a search for the Standard Model Higgs boson, produced in association with top-quark pairs ($t\bar{t}H$) was performed in the final state with a single lepton, at least 4 jets and at least 2 *b*-tags. The search region was divided into categories based on the jet and *b*-tag multiplicity of the final state, and a Clermont-Ferrand Multi-Layer Perceptron Artificial Neural Network (CFMlpANN) was trained to provide a one-dimensional discriminant for how likely the event is to be from the $t\bar{t}H$ signal, or one of the $t\bar{t} + \text{jets}$ backgrounds. No significant excess of events in the data was observed, and an observed (expected) upper limit on the production rate of $t\bar{t}H$ at 9.5 (5.4) times the rate predicted by the Standard Model. This final state was combined with a di-lepton final state, and the previous results from the 7 TeV dataset collected in 2011, produce an observed (expected) upper limit on the $t\bar{t}H$ process as 5.8 (5.2) times the Standard Model rate and published in the Journal of High Energy Physics (JHEP) in May of 2013.

A second analysis was performed on the full 19.5 fb^{-1} dataset of 8 TeV data collected by CMS. This also used a final state with a single lepton, at least 4 jets, and at least 2 *b*-tags, and a search region divided into categories based on the jet and *b*-tag multiplicity of the final state. A different multivariate analysis (MVA) technique was employed: a Boosted Decision Tree (BDT) was trained to separate the $t\bar{t}H$ signal from the $t\bar{t} + \text{jets}$ background for each of the jet/tag categorizations. Once again, no significant excess of events is observed, and an observed (expected) upper limit on the $t\bar{t}H$ production rate is set at 4.9 (4.7) times the Standard Model prediction. This analysis was combined with same and opposite sign di-lepton, multi-lepton, and hadronic tau final states to produce an observed (expected) upper limit of 4.5 (2.5) time the predicted rate of $t\bar{t}H$ production.

In preparation to perform this search in the next dataset collected by CMS, several investigations have been performed on ways to improve the sensitivity of the analysis to the $t\bar{t}H$ signal. One of the most important improvements will be the incorporation of next-to-leading order (NLO) QCD effects into the simulation of $t\bar{t}H$ signal and $t\bar{t} + \text{jets}$ background. This will improve the modeling of high jet-multiplicity events, which characterize both the signal and background in this analysis. These improved simulations will also incorporate the latest techniques to calculate the spin-correlations of the decay products from heavy resonances in top-quark and *W* boson decays, via the MadSpin framework. This will allow the angular correlations of the daughters of the $t\bar{t}$ system to be used to correctly associate jets in an event to their roles in the $t\bar{t}$ decay, thereby reducing the combinatorics of jets that can possibly be associated with jets from the

²⁹⁷¹ Higgs decay.

²⁹⁷² With the experience gained in previous analyses, and improvements already underway, the
²⁹⁷³ observation of a $t\bar{t}H$ signal will be increasingly likely in the larger statistics, higher-energy
²⁹⁷⁴ datasets collected in the future by $t\bar{t}H$. In the lack of an observation, now or in the future, these
²⁹⁷⁵ upper limits can be used to constrain future models involving physics beyond the Standard Model
²⁹⁷⁶ (BSM) that would predict enhancements to final states explored in these first two $t\bar{t}H$ analyses.

²⁹⁷⁷ Bibliography

- ²⁹⁷⁸ [1] S. Bethke, “The 2009 World Average of alpha(s)”, *Eur.Phys.J.* **C64** (2009) 689–703,
²⁹⁷⁹ doi:10.1140/epjc/s10052-009-1173-1, arXiv:0908.1135.
- ²⁹⁸⁰ [2] “Image, Higgs Potential”.
²⁹⁸¹ URL <http://inspirehep.net/record/1086544/files/higgspotential.png>.
- ²⁹⁸² [3] “Image, CMS Standard Model Processes”.
²⁹⁸³ URL <https://twiki.cern.ch/twiki/bin/view/CMSPublic/PhysicsResultsSMP>.
- ²⁹⁸⁴ [4] “Image, Hierarchy Problem”. URL <http://upload.wikimedia.org/wikipedia/commons/thumb/6/68/Hqmc-vector.svg/300px-Hqmc-vector.svg.png>.
²⁹⁸⁵
- ²⁹⁸⁶ [5] “LHC Aerial View”.
²⁹⁸⁷ URL <http://www.coepp.org.au/files/coepp/images/cern-aerial2.jpg>.
- ²⁹⁸⁸ [6] “LHC, Delivered Luminosity”. URL http://cms-service-lumi.web.cern.ch/cms-service-lumi/publicplots/int_lumi_cumulative_pp_2.png.
²⁹⁸⁹
- ²⁹⁹⁰ [7] J.-L. Caron, “The LHC injection complex.. L’ensemble d’injection du LHC.”, (May,
²⁹⁹¹ 1993). AC Collection. Legacy of AC. Pictures from 1992 to 2002.
- ²⁹⁹² [8] L. Evans and P. Bryant, “LHC Machine”, *JINST* **3** (2008) S08001,
²⁹⁹³ doi:10.1088/1748-0221/3/08/S08001.
- ²⁹⁹⁴ [9] M. Barnes et al., “Injection and extraction magnets: Kicker magnets”,
²⁹⁹⁵ arXiv:1103.1583.
- ²⁹⁹⁶ [10] “Image, Klystron operations”.
²⁹⁹⁷ URL <http://upload.wikimedia.org/wikipedia/commons/a/aa/Klystron.enp.gif>.
- ²⁹⁹⁸ [11] “Image, Klystron operations”. URL <http://cds.cern.ch/record/43017?ln=en>.
- ²⁹⁹⁹ [12] “Image, CERN LHC, Layout of the 5 cryogenic islands”. URL <http://d29qn7q9z0j1p6.cloudfront.net/content/roypta/370/1973/3887/F12.medium.gif>.
³⁰⁰⁰

- 3001 [13] P. Lebrun, “Large Cryogenic Helium Refrigeration System for the LHC”, Technical
 3002 Report LHC-Project-Report-629. CERN-LHC-Project-Report-629, CERN, Geneva, Feb,
 3003 2003. revised version number 1 submitted on 2003-02-19 11:44:11.
- 3004 [14] “Image, CERN LHC, Beam Screen”. URL http://home.web.cern.ch/sites/home.web.cern.ch/files/image/engineering_page/2013/01/beam-screen_0.jpg.
- 3005 [15] CMS Collaboration, “The CMS experiment at the CERN LHC”, *JINST* **3** (2008)
 3007 S08004, doi:10.1088/1748-0221/3/08/S08004.
- 3008 [16] “Image, CMS, Static Slice with tracks”. URL https://cms-docdb.cern.ch/cgi-bin/PublicDocDB/RetrieveFile?docid=4172&version=2&filename=CMS_Slice.gif.
- 3010 [17] “Image, CMS, Tracker cross-section”. URL <http://cms.web.cern.ch/sites/cms.web.cern.ch/files/styles/small/public/field/image/Barrel.gif?itok=dc1cYUp->.
- 3012 [18] “Image, CMS, Tracker Pixel Resolution”. URL https://twiki.cern.ch/twiki/pub/CMSPublic/PixelOfflinePlots2013/207487_h420.png.
- 3014 [19] “Image, CMS, ECAL crystal shower evolution simulation”.
 3015 URL http://www.lepp.cornell.edu/rsrcc/Home/Research/CMS/EventReconstruction/fe24elwhite_small.gif.
- 3017 [20] “Image, CMS, HCAL built from Russian naval shells”.
 3018 URL http://cms.web.cern.ch/sites/cms.web.cern.ch/files/styles/small/public/field/image/navy-shells-image_0095.jpg?itok=0tSvdvLx.
- 3020 [21] “Image, CMS, Muon chamber RPCs, exploded view”.
 3021 URL <http://cms.web.cern.ch/sites/cms.web.cern.ch/files/styles/small/public/field/image/RPClayers.jpg?itok=qtLqtQ89>.
- 3023 [22] CMS Collaboration Collaboration, “Energy calibration and resolution of the CMS
 3024 electromagnetic calorimeter in pp collisions at $\sqrt{s} = 7$ TeV”, *J. Instrum.* **8** (Jun, 2013)
 3025 P09009. 51 p. Comments: Submitted to JINST.
- 3026 [23] “Image, CMS, ECAL LED pulsing calibration results”. URL https://twiki.cern.ch/twiki/pub//CMSPublic/EcalDPGResultsCMSDP2013007/histories_2011-2012.png.
- 3028 [24] CMS Collaboration Collaboration, “Particle-Flow Event Reconstruction in CMS and
 3029 Performance for Jets, Taus, and MET”, Technical Report CMS-PAS-PFT-09-001,
 3030 CERN, 2009. Geneva, Apr, 2009.

- [25] M. Cacciari, G. P. Salam, and G. Soyez, “The Anti-k(t) jet clustering algorithm”, *JHEP* **0804** (2008) 063, doi:10.1088/1126-6708/2008/04/063, arXiv:0802.1189.
- [26] CMS Collaboration Collaboration, “Commissioning of the Particle-Flow reconstruction in Minimum-Bias and Jet Events from pp Collisions at 7 TeV”, Technical Report CMS-PAS-PFT-10-002, CERN, Geneva, 2010.
- [27] “Image, b-Tagging”. URL http://www-d0.fnal.gov/Run2Physics/top/singletop_observation/b_tagging_graphic.png.
- [28] “Image, basic ANN”. http://upload.wikimedia.org/wikipedia/commons/thumb/4/46/Colored_neural_network.svg/300px-Colored_neural_network.svg.png.
- [29] “Image, CMS Higgs Physics Results, H- ν ZZ- ν l Inv. Mass”. URL https://twiki.cern.ch/twiki/pub/CMSPublic/Hig13002PubTWiki/ZZMass_7Plus8TeV_70-1000_3GeV.pdf.
- [30] “Image, CMS Higgs Physics Results, H- ν GammaGamma Inv. Mass”. URL https://twiki.cern.ch/twiki/pub/CMSPublic/Hig13001PubTWiki/Fig_19.pdf.
- [31] CMS Collaboration, “Observation of a new boson at a mass of 125 GeV with the CMS experiment at the LHC”, *Phys.Lett.B* (2012) arXiv:1207.7235.
- [32] ATLAS Collaboration, “Observation of a new particle in the search for the Standard Model Higgs boson with the ATLAS detector at the LHC”, *Phys.Lett.B* (2012) arXiv:1207.7214.
- [33] M. E. Peskin and D. V. Schroeder, “An Introduction to Quantum Field Theory”. Westview Press, URL <http://www.westviewpress.com>, 1995.
- [34] K. G. Wilson, “Renormalization Group and Critical Phenomena. I. Renormalization Group and the Kadanoff Scaling Picture”, *Phys. Rev. B* **4** (Nov, 1971) 3174–3183, doi:10.1103/PhysRevB.4.3174.
- [35] K. G. Wilson, “Renormalization Group and Critical Phenomena. II. Phase-Space Cell Analysis of Critical Behavior”, *Phys. Rev. B* **4** (Nov, 1971) 3184–3205, doi:10.1103/PhysRevB.4.3184.
- [36] H. Weyl, “The theory of groups and quantum mechanics”. Dover Press, URL <https://ia700807.us.archive.org/20/items/ost-chemistry-quantumtheoryofa029235mbp/quantumtheoryofa029235mbp.pdf>, 1930.

- 3061 [37] C. N. Yang and R. L. Mills, “Conservation of Isotopic Spin and Isotopic Gauge
3062 Invariance”, *Phys. Rev.* **96** (Oct, 1954) 191–195, doi:10.1103/PhysRev.96.191.
- 3063 [38] M. Gell-Mann, “A Schematic Model of Baryons and Mesons”, *Phys.Lett.* **8** (1964)
3064 214–215, doi:10.1016/S0031-9163(64)92001-3.
- 3065 [39] G. Zweig, “An SU₃ model for strong interaction symmetry and its breaking; Version 1”,
3066 Technical Report CERN-TH-401, CERN, Geneva, Jan, 1964.
- 3067 [40] G. Zweig, “An SU₃ model for strong interaction symmetry and its breaking; Version 2”,.
- 3068 [41] O. W. Greenberg, “Spin and Unitary-Spin Independence in a Paraquark Model of
3069 Baryons and Mesons”, *Phys. Rev. Lett.* **13** (Nov, 1964) 598–602,
3070 doi:10.1103/PhysRevLett.13.598.
- 3071 [42] P. Higgs, “Broken symmetries, massless particles and gauge fields”, *Physics Letters* **12**
3072 (1964), no. 2, 132 – 133, doi:[http://dx.doi.org/10.1016/0031-9163\(64\)91136-9](http://dx.doi.org/10.1016/0031-9163(64)91136-9).
- 3073 [43] S. Weinberg, “A Model of Leptons”, *Phys. Rev. Lett.* **19** (Nov, 1967) 1264–1266,
3074 doi:10.1103/PhysRevLett.19.1264.
- 3075 [44] S. L. Glashow, “Partial-symmetries of weak interactions”, *Nuclear Physics* **22** (1961),
3076 no. 4, 579 – 588, doi:[http://dx.doi.org/10.1016/0029-5582\(61\)90469-2](http://dx.doi.org/10.1016/0029-5582(61)90469-2).
- 3077 [45] A. Salam and J. Ward, “Electromagnetic and weak interactions”, *Physics Letters* **13**
3078 (1964), no. 2, 168 – 171, doi:[http://dx.doi.org/10.1016/0031-9163\(64\)90711-5](http://dx.doi.org/10.1016/0031-9163(64)90711-5).
- 3079 [46] Nobelprize.org, “The Nobel Prize in Physics 1957”.
3080 URL http://www.nobelprize.org/nobel_prizes/physics/laureates/1957/.
- 3081 [47] N. Cabibbo, “Unitary Symmetry and Leptonic Decays”, *Phys. Rev. Lett.* **10** (Jun,
3082 1963) 531–533, doi:10.1103/PhysRevLett.10.531.
- 3083 [48] M. Kobayashi and T. Maskawa, “CP Violation in the Renormalizable Theory of Weak
3084 Interaction”, *Prog.Theor.Phys.* **49** (1973) 652–657, doi:10.1143/PTP.49.652.
- 3085 [49] S. L. Glashow, J. Iliopoulos, and L. Maiani, “Weak Interactions with Lepton-Hadron
3086 Symmetry”, *Phys. Rev. D* **2** (Oct, 1970) 1285–1292, doi:10.1103/PhysRevD.2.1285.
- 3087 [50] G. Arnison et al., “Experimental observation of isolated large transverse energy electrons
3088 with associated missing energy at s=540 GeV”, *Physics Letters B* **122** (1983), no. 1,
3089 103 – 116, doi:[http://dx.doi.org/10.1016/0370-2693\(83\)91177-2](http://dx.doi.org/10.1016/0370-2693(83)91177-2).

- [51] G. Arnison et al., “Experimental observation of lepton pairs of invariant mass around 95 GeV/c² at the {CERN} {SPS} collider”, *Physics Letters B* **126** (1983), no. 5, 398 – 410, doi:[http://dx.doi.org/10.1016/0370-2693\(83\)90188-0](http://dx.doi.org/10.1016/0370-2693(83)90188-0).
- [52] M. Banner et al., “Observation of single isolated electrons of high transverse momentum in events with missing transverse energy at the {CERN} pp collider”, *Physics Letters B* **122** (1983), no. 56, 476 – 485, doi:[http://dx.doi.org/10.1016/0370-2693\(83\)91605-2](http://dx.doi.org/10.1016/0370-2693(83)91605-2).
- [53] P. Bagnaia et al., “Evidence for Z0e+e at the {CERN} pp collider”, *Physics Letters B* **129** (1983), no. 12, 130 – 140, doi:[http://dx.doi.org/10.1016/0370-2693\(83\)90744-X](http://dx.doi.org/10.1016/0370-2693(83)90744-X).
- [54] The ALEPH, DELPHI, L3, OPAL, SLD Collaborations, the LEP Electroweak Working Group, the SLD Electroweak and Heavy Flavour Groups, “Precision Electroweak Measurements on the Z Resonance”, *Phys. Rept.* **427** (2006) 257, arXiv:[hep-ex/0509008](https://arxiv.org/abs/hep-ex/0509008).
- [55] The ALEPH, DELPHI, L3, OPAL Collaborations, the LEP Electroweak Working Group, “Electroweak Measurements in Electron-Positron Collisions at W-Boson-Pair Energies at LEP”, *Phys. Rept.* **532** (2013) 119, arXiv:[1302.3415](https://arxiv.org/abs/1302.3415).
- [56] “Image, LEP ZPole”. URL <http://lepewwg.web.cern.ch/LEPEWWG/1/Nnu.eps>.
- [57] “Image, CDF Top Quark Mass”. URL http://www-cdf.fnal.gov/physics/new/top/public_mass.html.
- [58] TEVNPH (Tevatron New Phenomena and Higgs Working Group), CDF, D0 Collaboration, “Combined CDF and D0 Upper Limits on Standard Model Higgs Boson Production with up to 8.6 fb⁻¹ of Data”, arXiv:[1107.5518](https://arxiv.org/abs/1107.5518).
- [59] “Image, CMS Higgs Mass”. URL http://cms-higgs-results.web.cern.ch/cms-higgs-results/Comb/HIG-14-009-Paper/sqr_mass_all.pdf.
- [60] F. Abe et al., “Observation of Top Quark Production in $\bar{p}p$ Collisions with the Collider Detector at Fermilab”, *Phys. Rev. Lett.* **74** (Apr, 1995) 2626–2631, doi:[10.1103/PhysRevLett.74.2626](https://doi.org/10.1103/PhysRevLett.74.2626).
- [61] S. Abachi et al., “Search for High Mass Top Quark Production in $p\bar{p}$ Collisions at $\sqrt{s} = 1.8$ TeV”, *Phys. Rev. Lett.* **74** (Mar, 1995) 2422–2426, doi:[10.1103/PhysRevLett.74.2422](https://doi.org/10.1103/PhysRevLett.74.2422).

- [62] LHC Higgs Cross Section Working Group Collaboration, “Handbook of LHC Higgs Cross Sections: 3. Higgs Properties”, doi:10.5170/CERN-2013-004, arXiv:1307.1347.
- [63] W. Beenakker et al., “Higgs radiation off top quarks at the Tevatron and the LHC”, *Phys.Rev.Lett.* **87** (2001) 201805, doi:10.1103/PhysRevLett.87.201805, arXiv:hep-ph/0107081.
- [64] W. Beenakker et al., “NLO QCD corrections to t anti-t H production in hadron collisions”, *Nucl.Phys.* **B653** (2003) 151–203, doi:10.1016/S0550-3213(03)00044-0, arXiv:hep-ph/0211352.
- [65] R. Frederix et al., “Scalar and pseudoscalar Higgs production in association with a top-antitop pair”, *Phys.Lett.* **B701** (2011) 427–433, doi:10.1016/j.physletb.2011.06.012, arXiv:1104.5613.
- [66] M. Garzelli, A. Kardos, C. Papadopoulos, and Z. Trocsanyi, “Standard Model Higgs boson production in association with a top anti-top pair at NLO with parton showering”, *Europhys.Lett.* **96** (2011) 11001, doi:10.1209/0295-5075/96/11001, arXiv:1108.0387.
- [67] S. Dawson, L. Orr, L. Reina, and D. Wackerlo, “Associated top quark Higgs boson production at the LHC”, *Phys.Rev.* **D67** (2003) 071503, doi:10.1103/PhysRevD.67.071503, arXiv:hep-ph/0211438.
- [68] T. Gleisberg et al., “Event generation with SHERPA 1.1”, *JHEP* **0902** (2009) 007, doi:10.1088/1126-6708/2009/02/007, arXiv:0811.4622.
- [69] P. Artoisenet, R. Frederix, O. Mattelaer, and R. Rietkerk, “Automatic spin-entangled decays of heavy resonances in Monte Carlo simulations”, *JHEP* **1303** (2013) 015, doi:10.1007/JHEP03(2013)015, arXiv:1212.3460.
- [70] F. Cascioli, P. Maierhofer, and S. Pozzorini, “Scattering Amplitudes with Open Loops”, *Phys.Rev.Lett.* **108** (2012) 111601, doi:10.1103/PhysRevLett.108.111601, arXiv:1111.5206.
- [71] F. Krauss, R. Kuhn, and G. Soff, “AMEGIC++ 1.0: A Matrix element generator in C++”, *JHEP* **0202** (2002) 044, doi:10.1088/1126-6708/2002/02/044, arXiv:hep-ph/0109036.
- [72] T. Gleisberg and F. Krauss, “Automating dipole subtraction for QCD NLO calculations”, *Eur.Phys.J.* **C53** (2008) 501–523, doi:10.1140/epjc/s10052-007-0495-0, arXiv:0709.2881.

- [73] Planck Collaboration, “Planck 2013 results. I. Overview of products and scientific results”, *Astron.Astrophys.* **571** (2014) A1, doi:10.1051/0004-6361/201321529, arXiv:1303.5062.
- [74] V. Rubin, N. Thonnard, and J. Ford, W.K., “Rotational properties of 21 SC galaxies with a large range of luminosities and radii, from NGC 4605 /R = 4kpc/ to UGC 2885 /R = 122 kpc/”, *Astrophys.J.* **238** (1980) 471, doi:10.1086/158003.
- [75] Super-Kamiokande Collaboration Collaboration, “Measurements of the solar neutrino flux from Super-Kamiokande’s first 300 days”, *Phys.Rev.Lett.* **81** (1998) 1158–1162, doi:10.1103/PhysRevLett.81.1158, arXiv:hep-ex/9805021.
- [76] KamLAND Collaboration Collaboration, “Measurement of neutrino oscillation with KamLAND: Evidence of spectral distortion”, *Phys.Rev.Lett.* **94** (2005) 081801, doi:10.1103/PhysRevLett.94.081801, arXiv:hep-ex/0406035.
- [77] MINOS Collaboration Collaboration, “Observation of muon neutrino disappearance with the MINOS detectors and the NuMI neutrino beam”, *Phys.Rev.Lett.* **97** (2006) 191801, doi:10.1103/PhysRevLett.97.191801, arXiv:hep-ex/0607088.
- [78] S. P. Martin, “A Supersymmetry primer”, *Adv.Ser.Direct.High Energy Phys.* **21** (2010) 1–153, doi:10.1142/9789814307505_0001, arXiv:hep-ph/9709356.
- [79] J. Aguilar-Saavedra, R. Benbrik, S. Heinemeyer, and M. Prez-Victoria, “Handbook of vectorlike quarks: Mixing and single production”, *Phys.Rev.* **D88** (2013), no. 9, 094010, doi:10.1103/PhysRevD.88.094010, arXiv:1306.0572.
- [80] G. Burdman, M. Perelstein, and A. Pierce, “Large Hadron Collider tests of a little Higgs model”, *Phys.Rev.Lett.* **90** (2003) 241802, doi:10.1103/PhysRevLett.90.241802, arXiv:hep-ph/0212228.
- [81] M. Perelstein, M. E. Peskin, and A. Pierce, “Top quarks and electroweak symmetry breaking in little Higgs models”, *Phys.Rev.* **D69** (2004) 075002, doi:10.1103/PhysRevD.69.075002, arXiv:hep-ph/0310039.
- [82] H.-C. Cheng, I. Low, and L.-T. Wang, “Top partners in little Higgs theories with T parity”, *Phys. Rev. D* **74** (Sep, 2006) 055001, doi:10.1103/PhysRevD.74.055001.
- [83] H.-C. Cheng, B. A. Dobrescu, and C. T. Hill, “Electroweak symmetry breaking and extra dimensions”, *Nucl.Phys.* **B589** (2000) 249–268, doi:10.1016/S0550-3213(00)00401-6, arXiv:hep-ph/9912343.

- [84] M. S. Carena, E. Ponton, J. Santiago, and C. E. Wagner, “Light Kaluza Klein States in Randall-Sundrum Models with Custodial SU(2)”, *Nucl.Phys.* **B759** (2006) 202–227, doi:10.1016/j.nuclphysb.2006.10.012, arXiv:hep-ph/0607106.
- [85] C. T. Hill, “Topcolor: Top quark condensation in a gauge extension of the standard model”, *Phys.Lett.* **B266** (1991) 419–424, doi:10.1016/0370-2693(91)91061-Y.
- [86] R. Contino, L. Da Rold, and A. Pomarol, “Light custodians in natural composite Higgs models”, *Phys.Rev.* **D75** (2007) 055014, doi:10.1103/PhysRevD.75.055014, arXiv:hep-ph/0612048.
- [87] “CERN Linac2 Duoplasmatron Schematic”. URL <http://linac2.home.cern.ch/linac2/sources/source.htm>.
- [88] “CERN Linac2 Duoplasmatron Image”. URL <http://linac2.web.cern.ch/linac2/CF002521-ProtonSourceDuoplasmatronRichardChristianss.jpg>.
- [89] “RFQ Schematic”. URL http://www.lnl.infn.it/images/acc_fig14.jpg.
- [90] “Example RFQ Image”. URL http://www.toyama-en.com/accelerator/images/rfq_downstream_webLarge.jpg.
- [91] “Inside an Alvarez Tube”. URL https://cds.cern.ch/record/1281668/files/DTL_proto_assembled_image.jpg?subformat=icon.
- [92] “CERN Linac2 Alvarez Tubes”. URL http://www.toyama-en.com/accelerator/images/rfq_downstream_webLarge.jpg.
- [93] M. Benedikt et al., “LHC Design Report Vol3 - The Injection Chain”. CERN, Geneva, 2004.
- [94] C. Hill et al., “Tests of the CERN proton linac performance for LHC - type beams”, *eConf* **C000821** (2000) TUD17, arXiv:physics/0008102.
- [95] “Image, CERN PSbooster injection from Linac2”. URL http://www.lhc-facts.ch/img/psb/psb_injektion.jpg.
- [96] “Image, CERN PSbooster is 4 vertically stacked synchotrons”. URL <http://www.lhc-facts.ch/img/psb/psb.jpg>.
- [97] “Image, CERN PSbooster Layout”. URL <http://psb-machine.web.cern.ch/psb-machine/layout.gif>.

- 3213 [98] “Image, CERN PSbooster Section 10 Layout”.
 3214 URL <http://psb-machine.web.cern.ch/psb-machine/sectors/sect10.gif>.
- 3215 [99] “Image, CERN PSbooster CO2 RF Cavity”. URL http://cern-accelerators-optics.web.cern.ch/cern-accelerators-optics/PS_BOOSTER/Pictures/P10L1.JPG.
- 3216
 3217 [100] “Image, CERN PSbooster 2 batch filling scheme of the PS”.
 3218 URL <http://ps-div.web.cern.ch/ps-div/LHC-PS/schindlrf.gif>.
- 3219 [101] K. S. Klaus Hanke, and Michel Chanel.
- 3220 [102] “Image, CERN PSbooster Layout”.
 3221 URL <http://psb-machine.web.cern.ch/psb-machine/>.
- 3222 [103] S. Baird, “Accelerators for pedestrians; rev. version”, Technical Report
 3223 AB-Note-2007-014. CERN-AB-Note-2007-014. PS-OP-Note-95-17-Rev-2.
 3224 CERN-PS-OP-Note-95-17-Rev-2, CERN, Geneva, Feb, 2007.
- 3225 [104] “Image, CERN PS Layout”.
 3226 URL <http://psring.web.cern.ch/psring/psring/pscomplex.gif>.
- 3227 [105] “Image, CERN PS Dipoles”.
 3228 URL <http://home.web.cern.ch/sites/home.web.cern.ch/files/styles/medium/public/image/accelerator/2013/01/accelerators-ps.jpg?itok=5E3Tp4Q0>.
- 3229
 3230 [106] “Image, CERN SPS, Layout”.
 3231 URL <https://espace.cern.ch/be-dep/0P/sps/pictures/sps2.PNG>.
- 3232 [107] “Image, CERN SPS Beamline”.
 3233 URL <http://home.web.cern.ch/sites/home.web.cern.ch/files/styles/medium/public/image/accelerator/2013/01/sps.jpg?itok=iLnNGjdI>.
- 3234
 3235 [108] “Image, CERN SPS, Inside 200 MHz RF Cavity”.
 3236 URL <http://rsta.royalsocietypublishing.org/content/roypta/370/1973/3887/F24.large.jpg?width=800&height=600&carousel=1>.
- 3237
 3238 [109] “Image, CERN SPS 200 MHz RF Cavity”. URL <https://cds.cern.ch/record/969086/files/7505156X.jpg?subformat=icon-1440>.
- 3239
 3240 [110] “CERN Website, Super Proton Synchrotron”.
 3241 URL <http://home.web.cern.ch/about/accelerators/super-proton-synchrotron>.
- 3242
 3243 [111] G. Dme, “The SPS acceleration system travelling wave drift-tube structure for the
 CERN SPS”,.

- 3244 [112] O. S. Brning et al., “LHC Design Report Vol1 - The Main Ring”. CERN, Geneva, 2004.
- 3245 [113] “CERN, List of All LHC Magnets”. URL http://lhc-machine-outreach.web.cern.ch/lhc-machine-outreach/components/magnets/types_of_magnets.htm.
- 3247 [114] M. Barnes, J. Borburgh, B. Goddard, and M. Hourican, “Injection and extraction
3248 magnets: septa”, [arXiv:1103.1062](https://arxiv.org/abs/1103.1062).
- 3249 [115] “Image, CERN LHC, Dipole Magnet, Dual Bore”.
3250 URL http://lhc-machine-outreach.web.cern.ch/lhc-machine-outreach/components/magnets_files/image002.jpg.
- 3252 [116] “Image, CERN LHC, Dipole Magnet, field”. URL <http://lhc-machine-outreach.web.cern.ch/lhc-machine-outreach/images/dipole-field.gif>.
- 3254 [117] J. Beauquis, “LHC Dipole Geometry Parameters, Comparisons between Producers”,
3255 *eConf C04100411* (2004) 046.
- 3256 [118] “Image, CERN LHC, Dipole Magnet, Staging Area”. URL https://cds.cern.ch/record/994212/files/transp-2001-001_05.jpg?subformat=icon-1440.
- 3258 [119] “Image, CERN LHC, Quadrupole Magnet, Cross Section Schematic”.
3259 URL <https://cds.cern.ch/record/841485>.
- 3260 [120] “Image, CERN LHC, Quadrupole Magnet, Staging Area”. URL <http://www.triumf.ca/sites/default/files/images/twinquadrupolemagnets.preview.jpg>.
- 3262 [121] “Image, CERN LHC, Quadrupole Magnet, Focusing Schematic”.
3263 URL http://www.lhc-closer.es/img/subidas/4_6_3_3.png.
- 3264 [122] “Image, CERN LHC, Multipole Magnet, Focusing Schematic”.
3265 URL <http://www.lhc-closer.es/img/subidas/Multipoles.jpg>.
- 3266 [123] “Image, CERN LHC, Magnetic Cell Layout”.
3267 URL http://www.lhc-closer.es/img/subidas/4_6_3_4.png.
- 3268 [124] “Image, CERN LHC, Interaction Region Schematic”.
3269 URL http://www.lhc-closer.es/img/subidas/4_6_3_6.jpg.
- 3270 [125] J.-L. Caron, “Superconducting cavity with its cryostat. Cavit supraconductrice dans son
3271 cryostat.”, May, 1994. AC Collection. Legacy of AC. Pictures from 1992 to 2002.
- 3272 [126] “Image, CERN LHC, Superconducting RF Cavities, Staged”.
3273 URL http://www.lhc-closer.es/img/subidas/4_7_2_2.jpg.

- 3274 [127] “Image, CERN LHC, Superconducting RF Cavities, Installed”.
 3275 URL http://home.web.cern.ch/sites/home.web.cern.ch/files/image/engineering_page/2013/01/rf-cavity.jpg.
- 3277 [128] “Outreach, CERN LHC, Cryogenic System”. URL <http://home.web.cern.ch/about/engineering/cryogenics-low-temperatures-high-performance>.
- 3278
 3279 [129] “The challenge of keeping cool”,.
- 3280 [130] “Outreach, CERN LHC, Vacuum System”. URL <http://home.web.cern.ch/about/engineering/vacuum-empty-interplanetary-space>.
- 3281
 3282 [131] “Image, CMS, Tracker Strip Efficiency”. URL https://twiki.cern.ch/twiki/pub//CMSPublic/DPGResultsTRK/efficiency_end2010.png.
- 3283
 3284 [132] “Image, CMS, Tracker Strip Resolution”. URL <https://twiki.cern.ch/twiki/pub//CMSPublic/DPGResultsTRK/StripHitRes2.gif>.
- 3285
 3286 [133] “Image, CMS, ECAL VPT with pen for scale”.
 3287 URL http://hepwww.rl.ac.uk/CMSecal/Meetings/2005/VPT_RIE_front.jpg.
- 3288 [134] R. M. Brown et al., “The vacuum phototriodes for the CMS electromagnetic
 3289 calorimeter”, *PoS HEP2001* (2001) 255.
- 3290 [135] CMS Collaboration, “Description and performance of track and primary-vertex
 3291 reconstruction with the CMS tracker”, *JINST* **9** (2014), no. 10, P10009,
 3292 doi:10.1088/1748-0221/9/10/P10009, arXiv:1405.6569.
- 3293 [136] R. Fruhwirth, “Application of Kalman filtering to track and vertex fitting”,
 3294 *Nucl.Instrum.Meth.* **A262** (1987) 444–450, doi:10.1016/0168-9002(87)90887-4.
- 3295 [137] CMS Electromagnetic Calorimeter Group Collaboration, “Intercalibration of the barrel
 3296 electromagnetic calorimeter of the CMS experiment at start-up”, *JINST* **3** (2008)
 3297 P10007, doi:10.1088/1748-0221/3/10/P10007.
- 3298 [138] K. Cankocak, Y. Onel, P. de Barbaro, and D. Vishnevskiy, “CMS HCAL Installation and
 3299 Commissioning”, Technical Report CMS-CR-2008-047, CERN, Geneva, Jul, 2008.
- 3300 [139] CMS Collaboration Collaboration, “Commissioning of the CMS ECAL calibration with
 3301 muons from cosmic rays and beam dumps”, Technical Report CMS-CR-2009-339, CERN,
 3302 Geneva, Nov, 2009.
- 3303 [140] CMS Collaboration Collaboration, “Performance of the CMS Hadron Calorimeter with
 3304 Cosmic Ray Muons and LHC Beam Data”, *J. Instrum.* **5** (Nov, 2009) T03012 . 35 p.

- 3305 [141] CMS Collaboration Collaboration, “HCAL performance from first collisions data”,,
- 3306 [142] “Image, CMS, Muon Particle-Flow Commissioning”.
- 3307 URL <https://twiki.cern.ch/twiki/bin/view/CMSPublic/PhysicsResultsMU0>.
- 3308 [143] CMS Collaboration Collaboration, “Particle-flow commissioning with muons and
- 3309 electrons from J/Psi and W events at 7 TeV”, Technical Report CMS-PAS-PFT-10-003,
- 3310 CERN, 2010. Geneva, 2010.
- 3311 [144] W. Adam, R. Frhwirth, A. Strandlie, and T. Todor, “Reconstruction of Electrons with
- 3312 the Gaussian-Sum Filter in the CMS Tracker at the LHC”,,
- 3313 [145] “Image, CMS, Electron Particle-Flow Commissioning”. URL <https://twiki.cern.ch/twiki/bin/view/CMSPublic/EGMElectronsMoriond2010>.
- 3315 [146] CMS Collaboration, “Electromagnetic calorimeter calibration with 7 TeV data”,,
- 3316 [147] Particle Data Group Collaboration, “Review of Particle Physics”, *Chin.Phys. C***38**
- 3317 (2014) 090001, doi:[10.1088/1674-1137/38/9/090001](https://doi.org/10.1088/1674-1137/38/9/090001).
- 3318 [148] A. Schalicke et al., “Geant4 electromagnetic physics for the LHC and other HEP
- 3319 applications”, *J.Phys.Conf.Ser.* **331** (2011) 032029,
- 3320 doi:[10.1088/1742-6596/331/3/032029](https://doi.org/10.1088/1742-6596/331/3/032029).
- 3321 [149] “MET Optional Filters”.
- 3322 URL <https://twiki.cern.ch/twiki/bin/view/CMS/MissingETOptionalFilters>.
- 3323 [150] CMS Collaboration, “Jet Energy Resolution in CMS at sqrt(s)=7 TeV”,,
- 3324 [151] C. Weiser, “A Combined Secondary Vertex Based B-Tagging Algorithm in CMS”,
- 3325 Technical Report CMS-NOTE-2006-014, CERN, Geneva, Jan, 2006.
- 3326 [152] “Operating Points for *b*-Tag Algorithms”.
- 3327 URL <https://twiki.cern.ch/twiki/bin/viewauth/CMS/BTagPerformanceOP>.
- 3328 [153] “*b*-Jet Identification in the CMS Experiment”,,
- 3329 [154] VHbb Team, “Search for the SM Higgs Boson Produced in Association with W or Z and
- 3330 Decaying to Bottom Quarks (ICHEP 2012)”, CMS Note 2012/181, 2012.
- 3331 [155] A. Hocker et al., “TMVA - Toolkit for Multivariate Data Analysis”, *PoS ACAT* (2007)
- 3332 040, arXiv:[physics/0703039](https://arxiv.org/abs/physics/0703039).
- 3333 [156] J. D. Bjorken and S. J. Brodsky, “Statistical Model for Electron-Positron Annihilation
- 3334 into Hadrons”, *Phys. Rev. D* **1** (1970) 1416, doi:[10.1103/PhysRevD.1.1416](https://doi.org/10.1103/PhysRevD.1.1416).

- 3335 [157] G. C. Fox and S. Wolfram, “Event Shapes in e^+e^- Annihilation”, *Nucl. Phys. B* **149**
 3336 (1979) 413, doi:10.1016/0550-3213(79)90003-8.
- 3337 [158] “Jet Energy Scale Uncertainties”. <https://twiki.cern.ch/twiki/bin/view/CMSPublic/WorkBookJetEnergyCorrections>.
- 3338
- 3339 [159] “Jet Energy Resolution Uncertainties”.
 3340 <https://twiki.cern.ch/twiki/bin/view/CMS/JetResolution>.
- 3341 [160] “ b -Tag Scale Factor Uncertainties”.
 3342 <https://twiki.cern.ch/twiki/bin/viewauth/CMS/BtagPOG>.
- 3343 [161] T. Peiffer., “ Q^2 Systematic MC Samples re-weighting”. <https://indico.cern.ch/getFile.py/access?contribId=5&resId=0&materialId=slides&confId=177717>, 2012.
- 3344
- 3345 [162] R. Barlow and C. Beeston, “Fitting using finite Monte Carlo samples”, *Computer
 3346 Physics Communications* **77** (1993) 219–228.
- 3347 [163] J. S. Conway, “Incorporating Nuisance Parameters in Likelihoods for Multisource
 3348 Spectra”, (2011). arXiv:1103.0354.
- 3349 [164] A. Bredenstein, A. Denner, S. Dittmaier, and S. Pozzorini, “NLO QCD corrections to
 3350 top anti-top bottom anti-bottom production at the LHC: 2. full hadronic results”,
 3351 (2010). arXiv:1001.4006.
- 3352 [165] The ATLAS Collaboration, The CMS Collaboration, The LHC Higgs Combination
 3353 Group Collaboration, “Procedure for the LHC Higgs boson search combination in
 3354 Summer 2011”, Technical Report CMS-NOTE-2011-005. ATL-PHYS-PUB-2011-11,
 3355 CERN, Geneva, Aug, 2011.
- 3356 [166] J. Conway, “Incorporating Nuisance Parameters in Likelihoods for Multisource Spectra”,
 3357 arXiv:1103.0354.
- 3358 [167] G. Cowan, K. Cranmer, E. Gross, and O. Vitells, “Asymptotic formulae for
 3359 likelihood-based tests of new physics”, *Eur.Phys.J.* **C71** (2011) 1554,
 3360 doi:10.1140/epjc/s10052-011-1554-0, 10.1140/epjc/s10052-013-2501-z,
 3361 arXiv:1007.1727.
- 3362 [168] CMS Collaboration, “Search for the standard model Higgs boson produced in association
 3363 with a top-quark pair in pp collisions at the LHC”, *JHEP* **1305** (2013) 145,
 3364 doi:10.1007/JHEP05(2013)145, arXiv:1303.0763.

- 3365 [169] CMS Collaboration, “Measurement of the differential top-quark pair production cross
 3366 section in the dilepton channel in pp collisions at $\sqrt{s} = 8$ TeV.”, CMS PAS TOP-12-028,
 3367 2012.
- 3368 [170] CMS Collaboration, “Measurement of the differential top-quark pair production cross
 3369 section in the lepton+jets channel in pp collisions at $\sqrt{s} = 8$ TeV.”, CMS PAS
 3370 TOP-12-027, 2012.
- 3371 [171] CMS Collaboration, “Calibration of the Combined Secondary Vertex b-Tagging
 3372 discriminant using dileptonic ttbar and Drell-Yan events”, CMS Note 2013/130, 2013.
- 3373 [172] CMS Collaboration, “Dilepton trigger and lepton identification efficiencies for the top
 3374 quark pair production cross section measurement at 8 TeV in the dilepton decay
 3375 channel.”, CMS AN AN-12-389, 2012.
- 3376 [173] CMS Collaboration, “Search for the associated production of the Higgs boson with a
 3377 top-quark pair”, *JHEP* **1409** (2014) 087,
 3378 doi:10.1007/JHEP09(2014)087, 10.1007/JHEP10(2014)106, arXiv:1408.1682.
- 3379 [174] J. Alwall et al., “The automated computation of tree-level and next-to-leading order
 3380 differential cross sections, and their matching to parton shower simulations”, *JHEP*
 3381 **1407** (2014) 079, doi:10.1007/JHEP07(2014)079, arXiv:1405.0301.
- 3382 [175] P. Artoisenet, R. Frederix, O. Mattelaer, and R. Rietkerk, “Automatic spin-entangled
 3383 decays of heavy resonances in Monte Carlo simulations”, *JHEP* **1303** (2013) 015,
 3384 doi:10.1007/JHEP03(2013)015, arXiv:1212.3460.
- 3385 [176] T. Sjostrand, S. Mrenna, and P. Z. Skands, “A Brief Introduction to PYTHIA 8.1”,
 3386 *Comput.Phys.Commun.* **178** (2008) 852–867, doi:10.1016/j.cpc.2008.01.036,
 3387 arXiv:0710.3820.
- 3388 [177] R. Frederix and S. Frixione, “Merging meets matching in MC@NLO”, *JHEP* **1212**
 3389 (2012) 061, doi:10.1007/JHEP12(2012)061, arXiv:1209.6215.

³³⁹⁰ List of Acronyms

³³⁹¹ **ATLAS** A Toroidal LHC Apparatus

³³⁹² **BSM** Beyond the Standard Model

³³⁹³ **CERN** European Center for Nuclear Research

³³⁹⁴ **CMS** Compact Muon Solenoid

³³⁹⁵ **ECAL** Electromagnetic Calorimeter

³³⁹⁶ **FSR** Final State Radiation

³³⁹⁷ **HCAL** Hadronic Calorimeter

³³⁹⁸ **ISR** Initial State Radiation

³³⁹⁹ **JHEP** Journal of High Energy Physics

³⁴⁰⁰ **LHC** Large Hadron Collider

³⁴⁰¹ **LO** Leading Order

³⁴⁰² **MVA** Multi-Variate Analysis

³⁴⁰³ **NLO** Next to Leading Order

³⁴⁰⁴ **QCD** Quantum Chromodynamics

³⁴⁰⁵ **QED** Quantum Electrodynamics

³⁴⁰⁶ **QFT** Quantum Field Theory

³⁴⁰⁷ **SM** Standard Model